TECHNISCHE UNIVERSITÄT MÜNCHEN

Physik-Department

Lehrstuhl für Topologie korrelierter Systeme

Arbeitsgebiet stark korrelierte Elektronensysteme

Forschungsneutronenquelle Heinz Maier-Leibnitz (FRM II)

Experimental Studies of Ultraslow Magnetisation Dynamics

Steffen Säubert, M. Sc.

Vollständiger Abdruck der von der Fakultät für Physik der Technischen Universität München zur Erlangung des akademischen Grades eines

Doktors der Naturwissenschaften (Dr. rer. nat.)

genehmigten Dissertation.

Vorsitzender:		Prof. Dr. Frank Pollmann
Prüfer der Dissertation:	1.	Prof. Dr. Christian Pfleiderer
	2.	Prof. Dr. Rudolf Gross

Die Dissertation wurde am 12.07.2018 bei der Technischen Universität München eingereicht und durch die Fakultät für Physik am 13.11.2018 angenommen.

Abstract

The present work reports the study of ultraslow magnetisation dynamics in the vicinity of magnetic phase transitions. Namely, low-temperature magnetisation processes in the pyrochlore oxide $Yb_2Ti_2O_7$, spin wave excitations and dispersions in the archetypal ferromagnet Fe, and spin relaxation processes in the spin-glass Fe_xCr_{1-x}. The spin dynamics in these systems were addressed by means of vibrating coil magnetometry (VCM) and neutron resonance spin echo spectroscopy (NRSE) in the MIEZE mode (modulation of intensity with zero effort).

VCM was employed to investigate $Yb_2Ti_2O_7$. The ground state was found to be of ferrimagnetic order, with spins splayed away from the $\langle 100 \rangle$ axes. The magnetic phase diagram for applied field shows an unusual field dependence. Applying a field initially increases the ordering temperature when applied along the $\langle 111 \rangle$ or $\langle 110 \rangle$ axes. This field dependence is absent for field along $\langle 100 \rangle$. A Potts model for cubic ferromagnets describes the low temperature behaviour of $Yb_2Ti_2O_7$. However, the estimates do not model the field strength of the phase transitions found in experiment. Frustrated interactions and quantum effects might significantly renormalise the critical field, and might not only account for the experimentally found critical temperatures, but also explain the reentrant type phase diagram.

Spin waves in Fe and spin relaxations in Fe_xCr_{1-x} were addressed by MIEZE. To measure magnetisation dynamics in the vicinity of magnetic phase transitions, ultra high energy resolution is indispensable. The highest resolution is achieved by neutron spin echo spectrometers. Since instrumental development at the spin echo beamline RESEDA was part of the present work, technical progress, development of instrument control and data analysis software, and measures to reduce instrumental background are reported.

In Fe, the focus was on the inelastic excitations in the ferromagnetic phase, i.e. spin wave excitation and dispersion. It was found that there is a clear deviation from the classical Heisenberg ferromagnet, where the spin wave energy depends quadratic on q. Due to the large magnetic moment of Fe, dipolar interactions had to be taken into account to describe the observed spin wave dispersion.

In Fe_xCr_{1-x}, the ferromagnetism of Fe and the antiferromagnetism of Cr can be suppressed by changing the Fe content x, and a putative quantum critical point is covered by a dome of spin-glass behaviour. Three samples with antiferromagnetic, paramagnetic, and ferromagnetic states above the spin-glass were investigated. The spin echo measurements showed a broad distribution of spin relaxation times in and around the spin-glass phase. This indicates the formation of different-sized domains, fluctuating on different time scales, before freezing out at lowest temperatures.

Kurzdarstellung

Die vorliegende Arbeit behandelt ultralangsame Magnetisierungsdynamiken in der Nähe zu magnetischen Phasenübergängen. Erforscht wurden Magnetisierungsprozesse im Pyrochloroxid $Yb_2Ti_2O_7$ bei tiefen Temperaturen, Anregungen und Dispersionen von Spinwellen im Ferromagneten Fe, sowie Spinrelaxationsprozesse im Spinglas Fe_xCr_{1-x}. Die Spindynamiken in diesen Systemen wurden dabei mittels Spulenvibrationsmagnetometrie (VCM) und Neutronen Resonanz Spin Echo Spektroskopie (NRSE) im MIEZE Modus (modulation of intensity with zero effort) untersucht.

Der Grundzustand in $Yb_2Ti_2O_7$ wurde mittels VCM als Ferrimagnet identifiziert. Dabei sind die Spins weg von den $\langle 100 \rangle$ Richtungen leicht verkippt. Für angelegtes Feld zeigt das magnetische Phasendiagramm eine unübliche Feldabhängigkeit. Anlegen eines Feldes führt zu einer Erhöhung der Ordnungstemperatur, sofern es entlang der $\langle 111 \rangle$ oder der $\langle 110 \rangle$ Achsen angelegt ist. Für Feld entlang $\langle 100 \rangle$ wird diese Feldabhängigkeit nicht beobachtet. Das Tieftemperaturverhalten von $Yb_2Ti_2O_7$ konnte mit einem Potts Modell für kubische Ferromagneten beschrieben werden, welches jedoch die Feldstärken der Phasenübergänge nicht exakt erklärt. Das kritische Feld könnte durch frustrierte Wechselwirkungen und Quanteneffekte stark renormalisiert sein, was nicht nur die Abweichung zu den beobachteten kritischen Feldern beschreiben könnte, sondern auch die unübliche Feldabhängigkeit.

MIEZE wurde genutzt um Spinwellen in Fe sowie die Spinrelaxationen in Fe_xCr_{1-x} zu untersuchen. Um Magnetisierungsdynamiken in der Nähe magnetischer Phasenübergängen zu beobachten, braucht es eine ultrahohe Energieauflösung. Die höchste Energieauflösung in der Neutronenstreuung hat ein Neutronen Spin Echo Spektrometer. Die vorliegende Arbeit beinhaltet Entwicklungen am Spin Echo Instrument RESEDA. Technischer Fortschritt, Entwicklungen der Instrumentensteuer- sowie Datenanalysesoftware, und die Maßnahmen zur Reduzierung des instrumentellen Untergrunds werden berichtet.

In Fe lag der Fokus auf inelastischen Anregungen in der ferromagnetischen Phase, i.e. Spinwellenanregung und -dispersion. Dabei wurde eine klare Abweichung zum klassischen Heisenberg Ferromagneten beobachtet, in welchem die Spinwellenenergie quadratisch in q ist. Um die Spinwellendispersion zu beschreiben, mussten, aufgrund des großen magnetischen Moments von Fe, dipolare Wechselwirkungen berücksichtigt werden.

In Fe_xCr_{1-x} wird der Ferromagnetismus von Fe, sowie der Antiferromagnetismus von Cr, durch Änderung des Fe Anteils x unterdrückt. Dabei wird ein möglicher Quantenkritischer Punkt durch eine Spinglas Phase verdeckt. Die Spin Echo Messungen zeigten eine breite Verteilung von Spinrelaxationszeiten in der Umgebung der Spinglasphase. Dies deutet auf die Bildung verschieden großer Domänen hin, welche alle auf unterschiedlichen Zeitskalen fluktuieren, bevor sie bei tiefsten Temperaturen ausfrieren.

Contents

1. Ultraslow Magnetisation Dynamics

Magnetism in condensed matter arises as a collective quantum phenomenon of magnetic moments interacting with one another and is fundamentally different from the magnetic behaviour of single atoms or molecules. With the discovery of new magnetic materials, exotic forms of electronic and magnetic order emerge. To develop new applications in solid state science exploiting these exotic states, it is necessary to explore and understand the underlying physical phenomena. Determined from their interaction energies via Heisenberg's uncertainty principle

$$\Delta E \Delta \tau \geq \frac{\hbar}{2}, \tag{1.1}$$

a plethora of magnetic phenomena occur on various characteristic time scales. These may range from a few femtoseconds for the exchange interaction between magnetic moments, to several years for spin relaxation processes in frustrated magnets. Fig. 1.1 illustrates the characteristic time scales of magnetisation dynamics for different physical phenomena.

In course of the present work, aspects of the magnetism in three different systems were investigated, namely, low-temperature magnetisation processes in the pyrochlore oxide $Yb_2Ti_2O_7$, spin wave excitations and dispersions in the archetypal ferromagnet iron, and spin relaxation processes in the spin-glass Fe_xCr_{1-x}. The time scales of the dynamical processes investigated in these systems are marked in Fig. 1.1. Two different measurement methods were chosen to address the spin dynamics. In the quasi-static limit of milliseconds to seconds, measurements of the magnetisation using a bespoke vibrating coil magnetometer were used to study the magnetic phase diagram and ground state of $Yb_2Ti_2O_7$. For measurements of spin waves in iron on the nanosecond scale, the neutron spin echo method MIEZE was employed. The MIEZE technique was also used for investigating spin relaxation processes in Fe_xCr_{1-x}.

The remainder of this chapter will discuss the emergence of unconventional magnetic phenomena, briefly introduce the investigated systems, and give an outline of the present work.

Figure 1.1.: Characteristic time scales of the magnetisation dynamics for various physical phenomena ranging from $1\,\mathrm{fs}$ to several years. Marked in red are the time scales of the systems investigated during the present work. The magnetic phase diagram and magnetic ground state of $Yb_2Ti_2O_7$ was measured using vibrating coil magnetometry. The spin waves in iron and the spin relaxation processes in Fe_xCr_{1-x} were investigated with the neutron spin echo technique MIEZE. Figure adapted from Ref. [1, 2].

1.1. Exotic Forms of Electronic and Magnetic Order

The magnetic properties of a system are primarily determined by the kind of interaction between its magnetic moments. If the moments in a material are not interacting with one another, the system shows dia- or paramagnetic behaviour. An interaction between the magnetic moments may lead to an ordered ferro-, antiferro-, or ferrimagnetic state. The latter three may be understood fundamentally by quantum mechanical exchange interactions between the magnetic moments due to the Coulomb correlation of electrons obeying the Pauli principle. In these materials, magnetic ordering is observed below a material-specific temperature.

According to Ehrenfest, classical transitions between two phases can be classified as first-order or second-order phase transitions. A phase transition can be characterised by introducing an order parameter which is finite below some critical value of a control parameter, and zero above [3, 4]. Characteristic for a first-order phase transition is a coexistence of the two phases at the transition, and a discontinuously vanishing order

parameter. While fluctuations of the order parameter typically are irrelevant in a first-order phase transition, they are at the heart of second-order phase transitions. In a second-order phase transition, there is no phase coexistence, and the macroscopic order is destroyed continuously by fluctuations, hence, the order parameter vanishes continuously.

In some systems, the critical temperature of a second-order phase transition can be suppressed by a non-thermal control parameter, like applied magnetic field or external pressure, terminating in a quantum critical point at zero temperature. The phase transition is then driven by quantum rather than thermal fluctuations. Detailed reviews on these so-called quantum phase transitions can be found in the literature, cf. Ref. [5–12]. In other systems, putative quantum critical points are covered by a dome of emerging order, such as the unconventional superconductivity in UGe_2 [13], or the spin-glass behaviour in Fe_xCr_{1-x} alloys [14, 15].

The emergence of exotic forms of electronic or magnetic order is often linked to a competition between different phases, such as the classical or quantum transition between magnetically ordered and disordered states. Hence, exotic phenomena are generally observed when materials with strong electronic correlations are subject to extreme conditions like low temperatures, applied magnetic field, or external pressure. Examples are high-temperature superconductivity in cuprates [16, 17], unconventional superconductivity in heavy fermion systems [18–21], the breakdown of the model of electrons in a metal, namely the Fermi liquid theory [22–26], or complex forms of magnetic order, for instance spin-glasses [27] or spin-liquids [28, 29].

Besides the critical behaviour in the vicinity of classical and quantum phase transitions, frustrated magnetic systems are good candidates for harbouring exotic ordering phenomena. Frustration arises from competing interactions of the magnetic moments or from the structure of the lattice of the solid, that may prevent the simultaneous satisfaction of all interactions, leaving the system in a highly degenerate state. Systems with competing interactions often attempt to resolve the underlying frustration by developing non-trivial spatial correlations, resulting in a plethora of exotic ordering phenomena [28]. Examples for exotic magnetic states in frustrated systems are classical spin-ice with magnetic monopole excitations [30–36], or quantum spin-liquids, a state of matter where quantum fluctuations prevent the spins from entering a phase with magnetic long-range order even at zero temperature, with photon-like excitations [29, 37–39].

1.2. Outline of this Thesis

In the present work, aspects of the magnetism in three different systems were investigated, employing two different measurement methods. Vibrating coil magnetometry,

briefly introduced in Ch. 2, allows investigating magnetisation processes at millikelvin temperatures. It was used to investigate the low temperature magnetisation process in the pyrochlore oxide $Yb_2Ti_2O_7$.

To address the spin dynamics in the vicinity of magnetic phase transitions in iron and Fe_xCr_{1-x}, respectively, neutron resonance spin echo spectroscopy was used. As the energy scale of quantum effects is very small, an ultra high energy resolution is indispensable for studying magnetisation dynamics in the vicinity of classical and quantum phase transitions. The highest energy resolution among neutron spectroscopy is achieved by neutron spin echo spectrometers. Neutron spin echo uses the precession of neutrons to encode the flight time of individual neutrons, thus achieving the ultra high energy resolution [40, 41]. A modification of neutron spin echo allows utilising a technique called modulation of intensity with zero effort (MIEZE) [42–46]. In MIEZE, all neutron spin manipulation is completed prior to the sample, making the method insensitive for beam depolarisation at the sample position. The MIEZE method is ideally suited to study magnetisation dynamics in the vicinity of magnetic phase transitions, thereby covering large time scales from a few femto- to tens of nanoseconds. Since instrumental development of the spin echo spectrometer RESEDA was part of the present work, Ch. 3 gives a more detailed introduction into the fundamentals of neutron scattering, focusing on neutron spin echo techniques.

The magnetic pyrochlore oxide $Yb_2Ti_2O_7$, the topic of Ch. 4, received a lot of attention in recent years, as strong quantum fluctuations significantly influence the system, and since the nature of its ground state is still under debate to host a quantum spin-liquid state at low temperatures [28, 37, 38]. The present work presents a detailed study of the magnetic phase diagram and the transitions in and out of the ground state as a first step to understand the physics in $Yb_2Ti_2O_7$. Thereby, the ground state was found to be of ferrimagnetic order, with spins slightly splayed away from one of the six $\langle 100 \rangle$ cubic directions. The magnetic phase diagram for applied magnetic field shows an unusual field dependence of a first-order phase boundary, notably an applied field initially increases the ordering temperature when applied parallel to the crystalline $\langle 111 \rangle$ or $\langle 110 \rangle$ axes. This unusual field dependence is absent for field along $\langle 100 \rangle$.

In Ch. 5, the present work continues a recent study where the prototypical continuous phase transition from the para- to the ferromagnetic phase in iron was reported [47]. The focus of the present study was on the inelastic excitations in the ferromagnetic phase, i.e. spin wave excitation and dispersion. It was found that there is a clear deviation from the classical Heisenberg ferromagnet, where the spin wave energy depends quadratic on q. Due to the large magnetic moment of iron, dipolar interactions had to be taken into account to describe the observed spin wave dispersion.

Ch. 6 discusses the spin relaxation processes in a series of Fe_xCr_{1-x} alloys. In Fe_xCr_{1-x}, the ferromagnetic phase transition of iron, and the antiferromagnetic phase transition of chromium, respectively, can be suppressed to lower temperatures, where a dome of spin-glass behaviour covers a putative quantum critical point. The samples were chosen so that the phase at temperatures above the spin-glass state is of antiferromagnetic, paramagnetic, and ferromagnetic order, respectively. For all samples, the spin echo measurements showed a broad distribution of relaxation times in and just above the spin-glass state. This indicates the formation of different-sized domains, fluctuating on different time scales, before freezing out at lowest temperatures. At higher temperatures, the distribution of spin relaxation times depends on the iron concentration, and is broadest for the samples with the lowest iron concentration, i.e. on the antiferromagnetic site.

In the final Ch. 7, a conclusion of the present work is drawn, and an outlook to future work is given.

2. Vibrating Coil Magnetometry

The magnetisation of $Yb_2Ti_2O_7$ as a function of temperature and field was measured by means of a bespoke vibrating coil magnetometer (VCM) as combined with an Oxford Instruments TL-400 top-loading dilution refrigerator [48, 49]. This chapter gives an overview of the experimental methods used for the magnetisation measurements. The basic concepts of a dilution refrigerator and its technical realisation, in particular of the Oxford Instruments TL-400, are described in Sec. 2.1. A more detailed description of the working principle of dilution refrigerators can be found in textbooks by, for instance, Lounasmaa [50], Betts [51], or Enns and Hunklinger [52]. The integration of the vibrating coil magnetometer into the Oxford Instruments TL-400 dilution refrigerator is described in Sec. 2.2, cf. Ref. [48, 49, 53] for more details about the refurbishment and upgrades of the TL-400 dilution refrigerator and the VCM. The chapter concludes with a detailed description of the magnetisation data treatment in Sec. 2.3.

2.1. Dilution Refrigerator

Evaporation cryostats cool a liquid by pumping the vapour above it. Using ^{3}He as refrigerant and exploiting its very high vapour pressure, temperatures as low as $0.24\,\mathrm{K}$ can be achieved [54]. The dilution refrigerator is a more sophisticated variant of the evaporation cryostat, making use of the unusual properties of dilute ^{3}He/^{4}He mixtures. The fundamental idea using a mixture of the two isotopes ^{3}He and ^{4}He for cooling was first suggested by London in 1951 [55]. Developments of the technique within the last decades nowadays allow standard dilution refrigerators to reach temperatures below $0.01\,\mathrm{K}$ continuously [50]. The Oxford Instruments TL-400 cryostat used in this work is equipped with a $5\,\mathrm{T}$ superconducting magnet and possesses an integrated vibrating coil magnetometer. The cryostat has a nominal cooling power of $400\,\mathrm{\mu W}$ at $0.1\,\mathrm{K}$, and can reach temperatures below $0.01\,\mathrm{K}$.

2.1.1. ^{3}He/^{4}He Dilution

In a dilution refrigerator the cooling power is provided by the enthalpy of mixing the two helium isotopes ^{3}He and ^{4}He. Fig. 2.1 shows the phase diagram of a mixture of liquid ^{3}He and ^{4}He as a function of the ^{3}He concentration $c_3 = n_3/(n_3 + n_4)$. Pure ^{4}He ($c_3 = 0$) becomes superfluid at a temperature of $T_\lambda = 2.177\,\text{K}$. The Lambda transition, separating the superfluid and normal-fluid ^{3}He/^{4}He mixtures, gets suppressed in temperature with increasing ^{3}He concentration and ends in a tricritical point at $T = 0.87\,\text{K}$ and $c_3 = 0.675$. At this point, the Lambda transition line meets an area in the phase diagram where the ^{3}He and ^{4}He phases separate entirely. In this miscibility gap one phase is rich in ^{3}He while the other is rich in ^{4}He, where the less dense ^{3}He-rich phase is floating atop the ^{4}He-rich phase. By further decreasing the temperature below the tricritical point, the concentrations of the two separated phases ($c_{3,\text{c}}$ ^{3}He-rich (concentrated) and $c_{3,\text{d}}$ ^{4}He-rich (diluted)) follow the phase-separation line. For $T \to 0$, the amount of ^{3}He in the concentrated phase goes to $c_{3,\text{d}}|_{T=0} = 1$ whereas for the dilute phase the concentration of ^{3}He reaches a constant value of $c_{3,\text{d}}|_{T=0} = 0.064$.

The finite solubility results from the different properties of the He isotopes: ^{3}He carries a spin $S = 1/2$, and hence, as a fermion, obeys the Fermi-Dirac statistic, while ^{4}He with $S = 0$ is a boson and obeys the Bose-Einstein statistic. At temperatures below
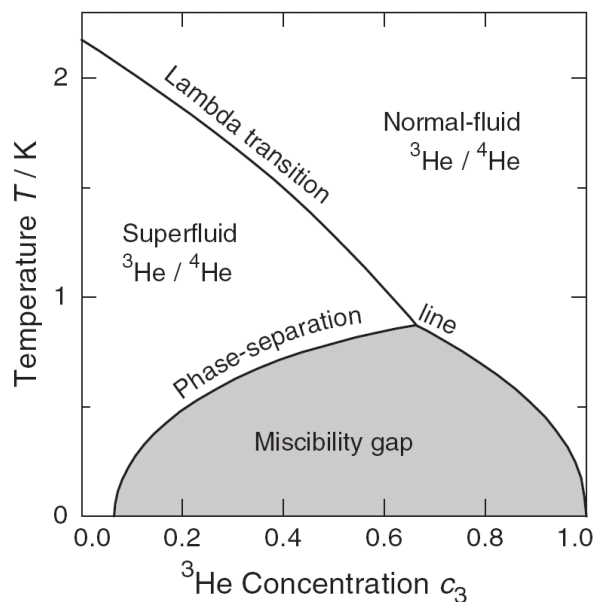

Figure 2.1.: Phase diagram of liquid mixtures of ^{3}He and ^{4}He. The Lambda transition gets suppressed in temperature with increasing ^{3}He concentration, and ends in a tricritical point where it meets the miscibility gap, i.e. where the solution separates into two distinct phases. Figure taken from Ref. [52].

several hundred millikelvin, ^{4}He is in its quantum mechanical ground state, and hence can be treated as thermal and hydrodynamic inert. This is not the case for the ^{3}He where the concentrated and dilute phases behave differently. The ^{3}He in the dilute phase is a Fermi liquid, whereas the ^{3}He in the concentrated phase can be seen as a Fermi gas under a pressure equal to the osmotic pressure of the ^{3}He in the dilute phase. This leads to a system of ^{3}He quasi particles with increased mass m^*. In equilibrium, the chemical potentials of ^{3}He in both phases are equal with

$$\mu_c(T, c_{3,c}) = \mu_d(T, c_{3,d}). \tag{2.1}$$

At absolute zero temperature, the concentrated phase consists of pure ^{3}He. The energy to remove a single ^{3}He atom from the concentrated phase is given by the latent heat per atom

$$L_3/N_A = -\mu_c/N_A, \tag{2.2}$$

with the Avogadro constant N_A. The energy necessary to add a ^{3}He to the dilute phase, however, depends on two factors. It consists of the released binding energy $\epsilon_3(c_{3,d})$ of a single atom and of the energy cost to fill an unoccupied state in the Fermi gas. The latter is given by the Fermi energy $E_F = k_B T_F(c_{3,d})$ with the Fermi temperature $T_F(c_{3,d})$. The chemical potential per atom in the dilute phase is therefore given by

$$\mu_d(c_{3,d})/N_A = -\epsilon_d(c_{3,d}) + k_B T_F(c_{3,d}). \tag{2.3}$$

And finally, for equilibrium at $T = 0$ follows

$$L_3/N_A = \epsilon_d(c_{3,d}) - k_B T_F(c_{3,d}). \tag{2.4}$$

The dependence of the binding energy ϵ_3 from the ^{3}He concentration in the dilute phase $c_{3,d}$ can be determined from experimental data or theory. At absolute zero, Eq. (2.4) then gives with $c_{3,d}(T = 0) = 0.0648$ a finite solubility as a consequence of the fermionic properties of ^{3}He. The finite solubility obeys the third law of thermodynamics, since at $T = 0$ only the ground state is occupied with $\Gamma = 1$ being the number of states; hence, the entropy is given by $S = k_B \ln(\Gamma) = 0$ [50].

2.1.2. The Cooling Principle

The equilibrium of the ^{3}He/^{4}He mixture can be brought out of balance by removing ^{3}He atoms from the dilute phase. To restore equilibrium, ^{3}He atoms diffuse from the concentrated towards the dilute phase which provides cooling, since the enthalpy of ^{3}He in the two phases is different. The enthalpy as a function of temperature is given by

$$H(T) = H(0) + \int_0^T C_3(T) \mathrm{d}T, \tag{2.5}$$

with the enthalpy $H(0)$ at $T = 0$. With experimental determined specific heat values for $T < 40\,\mathrm{mK}$, the enthalpy for the concentrated phase is

$$H_\mathrm{c} = H_\mathrm{c}(0) + 12T^2\,\mathrm{J/molK^2} \tag{2.6}$$

and for the dilute phase

$$H_\mathrm{d} = H_\mathrm{d}(0) + 96T^2\,\mathrm{J/molK^2}. \tag{2.7}$$

The process of a ^{3}He atom diffusing from the concentrated to the dilute phase is endothermic. From Eq. (2.6) and Eq. (2.7) follows $\Delta H < 0$, hence this process removes heat from the environment leading to an effective cooling. It can be seen as ^{3}He atoms evaporate into the ^{3}He gas of the dilute phase, and is equivalent to an evaporation of a liquid into vacuum.

In a dilution refrigerator, a continuous cooling process is realised by permanently pumping ^{3}He from the dilute phase into the concentrated phase. Thereby, the cooling power is proportional to the ^{3}He particle flux and the difference in enthalpy of the two phases

$$\frac{\mathrm{d}Q}{\mathrm{d}t} = \frac{\mathrm{d}n}{\mathrm{d}t}\,\Delta H = \frac{\mathrm{d}n}{\mathrm{d}t}\left(H_\mathrm{d}\left(T_\mathrm{MC}\right) - H_\mathrm{c}\left(T_\mathrm{hx}\right)\right), \tag{2.8}$$

where the T_MC is the temperature in the mixing chamber and T_hx the temperature of the ^{3}He entering the mixing chamber. The enthalpy of ^{3}He in the dilute phase can be seen as $H_\mathrm{d}(0) + T\Delta S$ where $T\Delta S = \Delta Q$ is the energy necessary for the evaporation process.

2.1.3. Technical Realisation

A schematic of a dilution refrigerator is shown in Fig. 2.2 (a). The cold part of the ^{3}He/^{4}He circulation, essentially consisting of the mixing chamber (MC), the still and multiple counterflow heat exchanger (hx), is located in a vacuum chamber immersed in a ^{4}He bath. The dilution refrigerator used during the present work further possesses a superconducting magnet, also immersed in the ^{4}He bath, as well as a liquid nitrogen jacket around the whole unit, functioning as a radiation shield. Fig. 2.2 (b) shows the dilution unit of the TL-400 Oxford Instruments refrigerator based on the principle shown in Fig. 2.2 (a).

The circulation is driven by continuously pumping the still, which is heated to $\sim$0.7 K to increase efficiency of the pumping. Even though the ^{3}He concentration of the liquid in the still is only about 1%, due to its higher vapour pressure mainly ^{3}He is evaporated. Before the ^{3}He is fed back into the system, it is purified and pre-cooled by a liquid nitrogen trap, followed by a helium trap. The latter is also located in the helium bath of the unit. The ^{3}He then enters a thin capillary, the condenser, where it is liquefied and further pre-cooled by the 1 K pot, which is a bath of liquid ^{4}He that is pumped to a temperature of
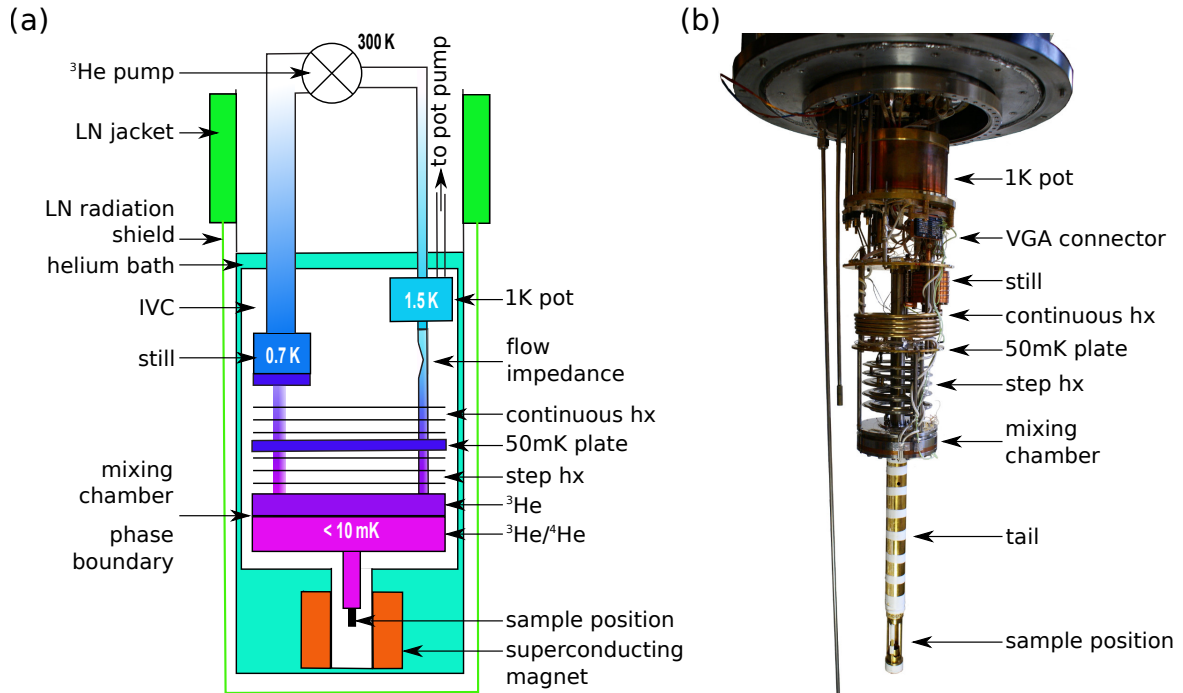
Figure 2.2.: Working principle of a dilution refrigerator. (a) Detailed schematic drawing of a dilution refrigerator. Schematic taken from Ref. [56]. (b) Dilution unit of the Oxford Instruments TL-400 dilution refrigerator.

about $1.5\,\mathrm{K}$. The necessary pressure for liquefying the gas is maintained sufficiently high by using a flow impedance. After the still, the ^{3}He is led through two different types of counterflow heat exchanger. The first one is a continuous heat exchanger and is made of coiled concentric tubes. The second one is a step heat exchanger and consists of several units made of sintered silver to increase the thermal contact area. After passing through the heat exchangers, the ^{3}He enters the concentrated phase in the mixing chamber. The return line to the still starts below the phase boundary in the dilute phase. On its way back to the still, the ^{3}He again flows through the heat exchangers, and this way cooling the incoming ^{3}He, completing the cycle. Continuously pumping the still leads to a concentration gradient, and, in turn, to an osmotic pressure, causing ^{3}He flowing from the mixing chamber to the still. The only possibility for the ^{3}He to reach the still is by crossing the phase boundary in the mixing chamber, which leads to cooling.

2.2. **Vibrating Coil Magnetometer**

Most methods to measure the magnetisation of a material are based on Faraday's law of induction, where a time-varying magnetic field will always accompany a spatially-varying electric field, and vice versa, according to the Maxwell-Faraday equation

$$\nabla \times \boldsymbol{E} \, = \, \frac{\partial \boldsymbol{B}}{\partial t}. \tag{2.9}$$

In such magnetometers the stray fields of a magnetic sample are detected by a set of coils. Consider a magnetic sample magnetised by a homogeneous external magnetic field $\mu_0 H$ generating a dipole field. A coil, parallel to $\mu_0 H$ and to the magnetisation of the sample m, with N windings is placed in a distance z_0 away from the centre of the dipole field. Changing the distance z_0 between sample and coil directly changes the magnetic flux Φ through the surface of the coil due to the gradient of the dipole field. According to Faraday's law of induction a voltage U_{ind} is induced in the coil. The induced voltage is directly proportional to the magnetic moment of the sample, $U_{\mathrm{ind}} \propto m$. In a vibrating sample magnetometer (VSM) or vibrating coil magnetometer (VCM) the change in z_0 is an oscillatory movement with

$$z(t) \, = \, z_0 + A \sin\left(\omega t\right), \tag{2.10}$$

and the induced voltage is

$$U_{\mathrm{ind}} \, = \, -\left(\frac{\mathrm{d}\Phi}{\mathrm{d}z}\right)_{z_0} \frac{\mathrm{d}z}{\mathrm{d}t} \, \propto \, m. \tag{2.11}$$

Fig. 2.3 shows the working principles of a VSM in (a) and a VCM in (b), respectively. The vibrating sample magnetometer, developed by Foner in 1959 [57], is the most common implementation. Here, the detection coil is placed in the gradient of the dipole field of an oscillating sample. The oscillatory movement of the sample induces a voltage in the coil directly proportional to the magnetic moment of the sample according to Eq. (2.11).

However, vibrating sample magnetometer are not suitable for magnetisation measurements in the millikelvin regime. This is due to the mechanical movement of the sample causing parasitic heating. A vibrating coil magnetometer, as suggested by Smith in 1956 [58], avoids this problem by moving the detection coils rather than the sample. It therefore allows measurements at much lower temperatures. Further developments in the 1960ies made an effort to adapt the VCM technique to ultra-low temperatures. For example, to avoid heat leaks the drive unit was placed at low temperatures [59].

In 2010, Legl *et al.* reported the development of a VCM as combined with a top-loading dilution refrigerator for measurements of the magnetisation down to millikelvin
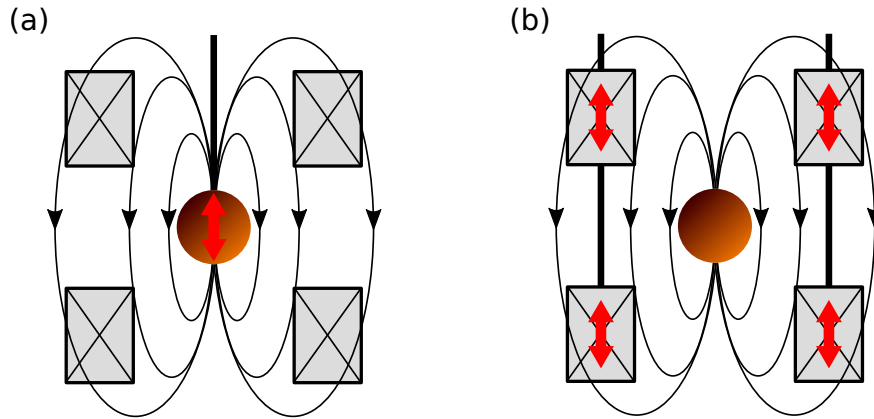
Figure 2.3.: Working principle of a vibrating sample magnetometer (VSM) (a) and vibrating coil magnetometer (VCM) (b). In a VSM the sample is oscillating and the coils are at rest, while in a VCM the coils are moving and the sample is at rest.

temperatures [48, 49]. Fig. 2.4 shows schematically the VCM integrated in the Oxford Instruments TL-400 dilution refrigerator. The VCM is composed of three parts [48]. (i) The vibration drive of the VCM below the mixing chamber, located in the zero-field region of the superconducting sample magnet. It is attached to the inner vacuum chamber (IVC), and therefore thermally coupled to the He bath of the cryostat and decoupled from the mixing chamber and the sample holder. (ii) A transmission mechanism below the drive unit composed of a a carbon-fibre tube. (iii) The detection coils in the centre of the sample magnet.

As its main advantage, the VCM offers excellent thermal coupling without risk of mechanical vibrations with respect to the applied magnetic field, which is highly homogeneous. This contrasts Faraday force magnetometers, in which the sample is exposed to a field gradient, or extraction magnetometers, such as a VSM, where the sample is moved with respect to the field.

The Oxford Instruments TL-400 dilution refrigerator is equipped with a $5\,\mathrm{T}$ superconducting magnet and has the vibrating coil magnetometer integrated as schematically shown in Fig. 2.4. The cryostat has a nominal cooling power of $400\,\mathrm{\mu W}$ at $0.1\,\mathrm{K}$, and can reach temperatures below $0.01\,\mathrm{K}$. Investigations of the spin-liquid properties of $\mathrm{Tb_2Ti_2O_7}$ [60], and of the first-order metamagnetic transition in $\mathrm{Ho_2Ti_2O_7}$ [61], established the vibrating coil magnetometry as an ideal technique for measurements of the magnetisation at millikelvin temperatures.
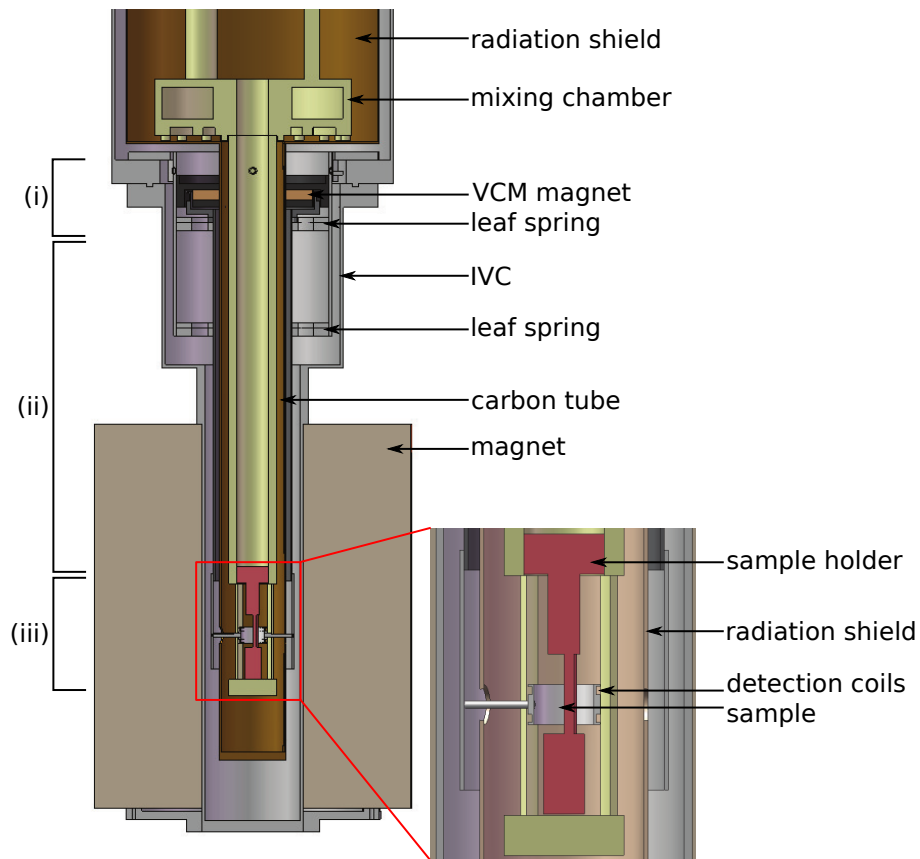
Figure 2.4.: Schematic of the vibrating coil magnetometer (VCM) integrated in the Oxford Instruments TL-400 dilution refrigerator. The vibration drive (i) is below the mixing chamber, located in the zero field region of the superconducting sample magnet. The vibration of the drive unit is transmitted via a carbon-fibre tube (ii) to the detection coils in the centre of the sample magnet (iii). The inset shows the area (iii), where the detection coils and the sample holder with the sample are mounted. Schematic taken from Ref. [48].

2.3. Post-Measurement Data Treatment

For determination of the signal contribution of the sample, the empty sample holder was remeasured and the background signal subtracted from the data. The signal of the empty sample holder was found to be small, with a highly reproducible field dependence and an essentially negligible temperature and sweep rate dependence. Fig. 2.5 shows typical data of the induced voltage of the empty sample holder in the VCM as a function of the applied magnetic field. Already for slightly higher fields, the background shows a linear like behaviour. Non-linearities and the hysteresis around zero field are attributed to magnetic impurities in the sample holder. The inset in Fig. 2.5 further shows two features. First, a shift of the centre of the data to parasitic voltages. Second, a difference between the zero-field cooled data, recorded at $15\,\mathrm{mT\,min^{-1}}$ and $25\,\mathrm{mT\,min^{-1}}$, respectively. The
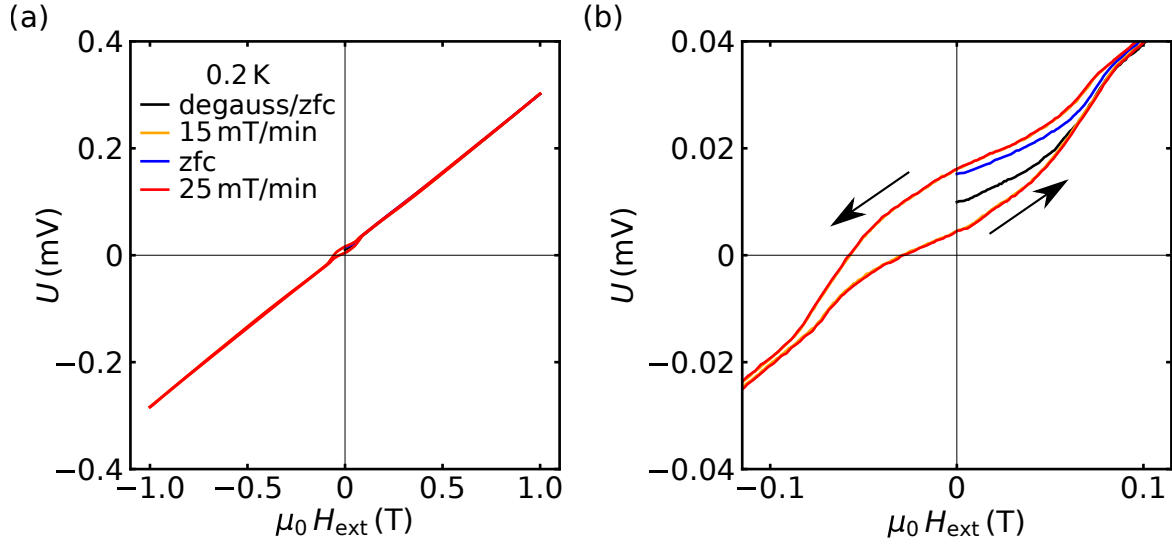
Figure 2.5.: Background signal of the empty VCM at $0.2\,\mathrm{K}$ and for sweep rates of $15\,\mathrm{mT\,min^{-1}}$ and $25\,\mathrm{mT\,min^{-1}}$, respectively. (a) Background signal for a hysteresis loop from $0 \rightarrow 1 \rightarrow -1 \rightarrow 1\,\mathrm{T}$. The yellow and the red curve lie on top of each other. A zoom of the plot in (a) is shown in (b), where an offset around the axis origin and a difference between the two zero-field cooled measurements can be seen. The zfc data of the $15\,\mathrm{mT\,min^{-1}}$ measurement were taken after eliminating the remnant field by degaussing. The zfc data of the $25\,\mathrm{mT\,min^{-1}}$ were taken after heating up to $\sim 1\,\mathrm{K}$ and cooling back down to $0.2\,\mathrm{K}$, without degaussing. The background is highly reproducible, linear for higher fields, and independent of the sweep rate.

zfc data of the measurement at $15\,\mathrm{mT\,min^{-1}}$ were recorded after degaussing. The zfc data of the $25\,\mathrm{mT\,min^{-1}}$ were recorded after heating to $\sim 1\,\mathrm{K}$ and cooling back down to $0.2\,\mathrm{K}$, without degaussing. This shows that the sample holder background changes slightly after the first field sweep. To account for this effect, data recorded directly after mounting the sample were corrected with the background measurement recorded after degaussing, and data recorded thereafter were corrected with the background measurement recorded without degaussing.

The signal of the sample was calibrated quantitatively at $3\,\mathrm{K}$ against the magnetisation as measured in an Oxford Instruments VSM determined at $3\,\mathrm{K}$. The VSM was calibrated using a Ni sample. Fig. 2.6 illustrates the calibration of the VCM data by means of the VSM measurements. In Fig. 2.6(a) the signal of the VSM is plotted in units $\mu_\mathrm{B}\mathrm{Yb^{-1}}$ against the signal of the VCM. A fit with a second-order polynomial was used as the calibration curve to convert the VCM signal from Volt to μ_B per Ytterbium. The origin of the nonlinearities of the calibration curves were studied in great detail by Duvinage [56]. Fig. 2.6(b) shows typical calibrated VCM data together with the data from the VSM measurement. The quality of the calibration curve may be seen in Fig. 2.3(c), where the difference of the VCM data and the calibrated VSM data is plotted. Deviations are below
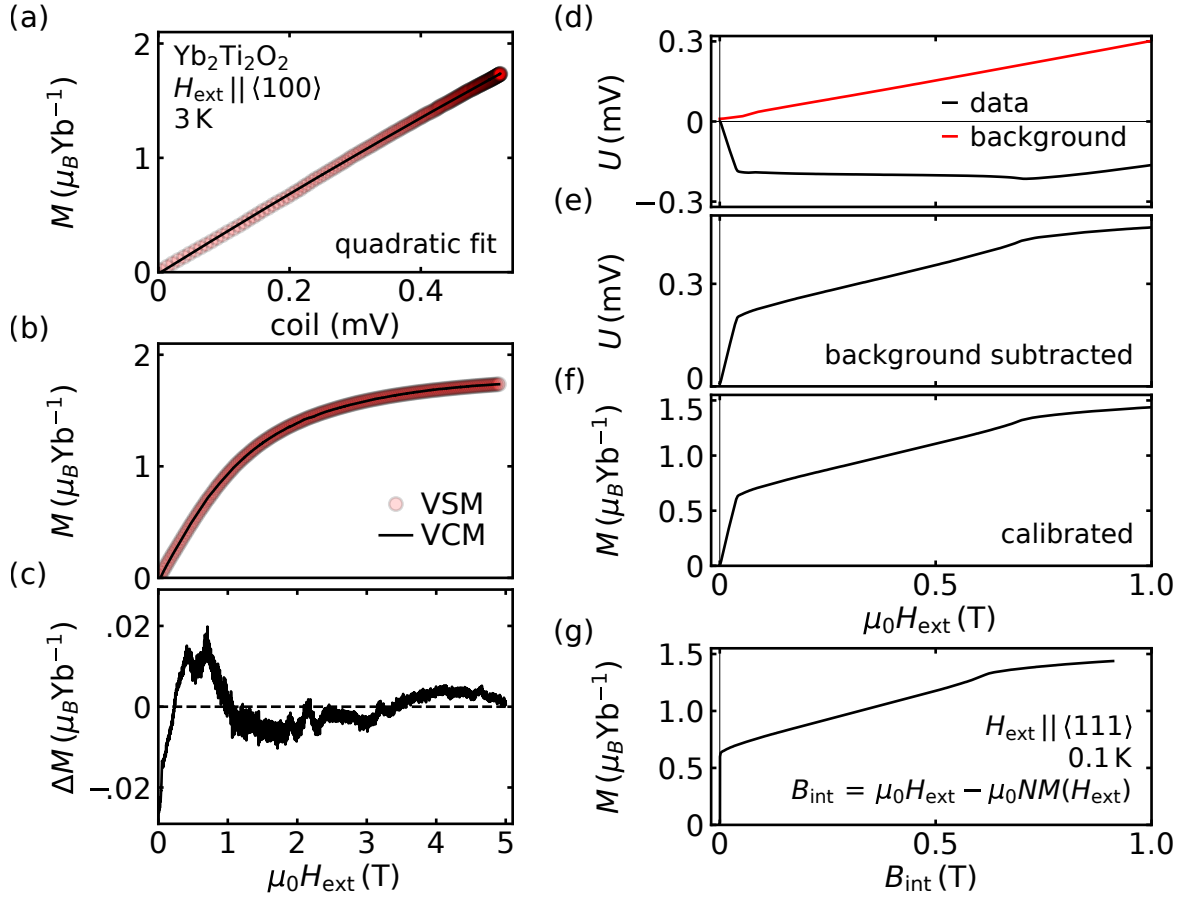
Figure 2.6.: VCM data calibration (a-c) and example data reduction of the magnetisation data taken at $T = 0.1\,\mathrm{K}$ for field along $\langle 111 \rangle$ (d-g). (a) Calibration of the VCM data of $Yb_2Ti_2O_7$ against a Ni measurement in the VSM at $3\,\mathrm{K}$. (b) Calibrated VCM data converted from V to $\mu_B Yb^{-1}$ together with the VSM data. (c) Absolute difference of the VSM data and the calibrated VCM data shown in (b). (d) Raw data of the VCM signal induced by the empty sample holder (red), and by the sample holder with mounted sample (black). (e) Contribution of the sample to the signal, after the signal from the empty sample holder, i.e. background, was subtracted. (f) Sample signal calibrated by means of a Ni standard and the magnetisation of the $Yb_2Ti_2O_7$ sample as measured at $3\,\mathrm{K}$ in an Oxford Instruments VSM. (g) Final data after correction for demagnetising effects.

$0.1\,\%$. It should be noted that in Fig. 2.3(a) and (b) only every 50 data point was plotted for clarity.

For the uniformly magnetised spherical sample, demagnetising effects were corrected and the internal field calculated as follows

$$B_{\mathrm{int}} = \mu_0 H_{\mathrm{ext}} - \mu_0 N M(H_{\mathrm{ext}}), \tag{2.12}$$

where N is the demagnetisation factor and M the magnetisation. For the spherical

sample studied, the demagnetisation factor is $N = 1/3$. Fig. 2.6(d-g) illustrates the steps of data treatment for typical data. The raw sample and background signals are plotted in Fig. 2.6(d). After background subtraction (e), the data are calibrated (f) as described above and shown in Fig. 2.6(a-c). Finally, demagnetising fields are taken into account (g). A background signal was also subtracted from the measured signal during temperature scans. Features found in the temperature dependence were also corrected for demagnetising effects.

3. Neutron Resonance Spin Echo Spectroscopy

The critical spin wave dynamics in Fe and the spin relaxation processes in Fe_xCr_{1-x} were studied by a modification of neutron spin echo spectroscopy. This chapter gives an overview of neutron scattering and the techniques used for the studies in the present work. It starts with a short introduction into the theory of neutron scattering in Sec. 3.1, following Ref. [62–65]. As the energy scale of quantum effects is very small, an ultra high energy resolution is indispensable for studying magnetisation dynamics in the vicinity of classical and quantum phase transitions. The highest energy resolution among neutron spectrometry is achieved by neutron spin echo spectrometers (NSE). Sec. 3.2 introduces the basis of classical neutron spin echo, and its modifications neutron resonance spin echo (NRSE) and modulation of intensity with zero effort (MIEZE). It is followed by a detailed description of the process of spin echo data reduction in Sec. 3.3. Sec. 3.4 is dedicated to the neutron resonance spin echo spectrometer RESEDA at the Heinz Maier-Leibnitz Zentrum (MLZ), where the experiments were carried out.

3.1. Theoretical Background

Neutron scattering is a very powerful tool for investigating structures and excitations in solid state physics, thanks to the unique character of the neutron. Neutron scattering is highly complementary to X-ray scattering.

One of the properties of the neutron is that it is uncharged and, hence, interacts directly with the atomic nucleus since there is no Coulomb barrier to overcome, and not with the electronic shell as X-rays do. Therefore, the scattering cross section does not depend on the atomic number of the chemical element. This not only allows to distinguish atoms of comparable atomic number, but also to distinguish isotopes of the same element. The neutrality also allows a large penetration depth. This is beneficial not only for the study of bulk properties, but also to study under extreme conditions such as very low or very high temperature, high pressure, or high magnetic or electric fields, where the neutron beam must penetrate sophisticated sample environments. The wavelength of

cold and thermal neutrons are of the order of interatomic distances in solids. Further, the energy of cold and thermal neutrons is of the same order as that of many elementary excitations in condensed matter. Last but not least, the neutron carries a magnetic moment, allowing the interaction with magnetic structures and magnetic excitations. For all these reasons, neutrons are ideally suited to investigate the structure and excitations in solid state physics under extreme conditions.

A neutron scattering experiment aims to determine the probability that a neutron with incident wave vector $\boldsymbol{k}_i$ and spin state $\boldsymbol{\sigma}_i$ is scattered into a state with wave vector $\boldsymbol{k}_f$ and spin state $\boldsymbol{\sigma}_f$. Thereby, the scatterer changes its state from λ_i to λ_f. The momentum transfer during a scattering process is described by

$$\hbar\boldsymbol{q} \,=\, \hbar\left(\boldsymbol{k}_i - \boldsymbol{k}_f\right), \tag{3.1}$$

with the scattering vector $\boldsymbol{q}$. The corresponding energy transfer is given by

$$\hbar\omega \,=\, \frac{\hbar^2}{2m}\left(k_i^2 - k_f^2\right). \tag{3.2}$$

For the scattering process, the momentum and energy are conserved. The probability of the scattering process from above can be described by the neutron scattering cross-section, which corresponds to the number of neutrons scattered per second into a small solid angle with a certain energy transfer, divided by the incident neutron flux. Starting from a system where an initial state λ_i goes to a final state λ_f with the transition probability described by Fermi's Golden Rule, the double differential scattering cross-section follows to

$$\frac{\mathrm{d}^2\sigma}{\mathrm{d}\Omega\mathrm{d}\omega} \,=\, \left(\frac{m}{2\pi\hbar^2}\right)^2 \frac{k_f}{k_i} \sum_{\lambda_f,\sigma_f} \sum_{\lambda_i,\sigma_i} p_{\lambda_i} p_{\sigma_i} \left|\langle \boldsymbol{k}_f, \boldsymbol{\sigma}_f, \lambda_f | \hat{U} | \boldsymbol{k}_i, \boldsymbol{\sigma}_i, \lambda_i \rangle\right|^2 \delta\left(\hbar\omega + E_{\lambda_i} - E_{\lambda_f}\right),$$

$$\tag{3.3}$$

where λ_i is the initial state of the scatterer with energy E_{λ_i}, and the probability to find the scatterer in this state p_{λ_i}. λ_f denotes the final state of the scatterer. The spin states of the incoming and scattered neutrons are $\boldsymbol{\sigma}_i$ and $\boldsymbol{\sigma}_f$, respectively, with the probability p_{σ_i} to find the spin state in $\boldsymbol{\sigma}_i$. The energy distribution of the scattered neutrons is described by a δ-function including the conservation of energy. The interaction between scatterer and neutron is described by the potential $\hat{U}$. This interaction potential depends on the specific scattering process, which can be nuclear or magnetic.

3.1.1. Nuclear Scattering

For neutron scattering from nuclei at fixed positions $\boldsymbol{R}_j$, the interaction potential is well approximated by the Fermi pseudopotential

$$\hat{U}(\boldsymbol{r}) = \frac{2\pi\hbar^2}{m} \sum_j b_j \delta(\boldsymbol{r} - \boldsymbol{R}_j), \tag{3.4}$$

where $\boldsymbol{r}$ is the position of the neutron, and b_j is the scattering length depending on the nuclei and is of the order 10^{-15} m. The incoming and outgoing neutrons may be described by plane waves

$$|\boldsymbol{k}_i\rangle = \exp\{(i\boldsymbol{k}_i \cdot \boldsymbol{r})\} \tag{3.5}$$

$$\tag{3.6}$$

and

$$|\boldsymbol{k}_f\rangle = \exp\{(i\boldsymbol{k}_f \cdot \boldsymbol{r})\}. \tag{3.7}$$

Considering an unpolarised neutron beam, therefore neglecting $\boldsymbol{\sigma}_i$ and $\boldsymbol{\sigma}_f$ in Eq. (3.3), and introducing Heisenberg operators, the final cross-section formula for nuclear scattering of an unpolarised beam is given by

$$\frac{\mathrm{d}^2\sigma}{\mathrm{d}\Omega\mathrm{d}\omega} = \frac{1}{2\pi\hbar} \frac{k_f}{k_i} \sum_{j,j'} b_j b_{j'} \int_{-\infty}^{+\infty} \langle \exp\{-i\boldsymbol{q} \cdot \hat{\boldsymbol{R}}_{j'}(0)\} \exp\{-i\boldsymbol{q} \cdot \hat{\boldsymbol{R}}_j(t))\}\rangle \exp\{-i\omega t\} \, \mathrm{d}t. \tag{3.8}$$

Various properties of the scattering system are included in the correlation functions introduced by Van Hove in 1954 [66]. The operator part in Eq. (3.8) corresponds to the intermediate pair correlation function, or intermediate scattering function,

$$I(\boldsymbol{q}, t) = \frac{1}{N} \sum_{j,j'} \langle \exp\{-i\boldsymbol{q} \cdot \hat{\boldsymbol{R}}_{j'}(0)\} \exp\{-i\boldsymbol{q} \cdot \hat{\boldsymbol{R}}_j(t))\}\rangle, \tag{3.9}$$

where N is the number of nuclei in the scattering system. The space-time pair correlation function is defined as

$$G(\boldsymbol{r}, t) = \frac{1}{(2\pi)^3} \int I(\boldsymbol{q}, t) \exp\{-i\boldsymbol{q} \cdot \boldsymbol{r}\} \, \mathrm{d}\boldsymbol{q}. \tag{3.10}$$

The intermediate scattering function is the Fourier transform of Eq. (3.10) in space. The scattering function of the system, also known as the dynamical structure factor or the scattering law, as it is directly related to the cross section in Eq. (3.8), is the Fourier transformation of Eq. (3.9) in time, and the Fourier transform of Eq. (3.10) in space and time. It is given by

$$S(\boldsymbol{q}, \omega) = \frac{1}{2\pi\hbar} \int I(\boldsymbol{q}, t) \exp\{-i\omega t\} \, \mathrm{d}t. \tag{3.11}$$

3.1.2. Magnetic Scattering

Due to the magnetic moment of the neutron, a magnetic interaction between the neutron and the unpaired electrons in the atom occur. The operator of the magnetic dipole moment of the neutron is given by

$$\boldsymbol{\mu}_\mathrm{n} = -\gamma\mu_\mathrm{N}\boldsymbol{\sigma} \tag{3.12}$$

with the nuclear magneton

$$\mu_\mathrm{N} = \frac{e\hbar}{2m_\mathrm{p}}, \tag{3.13}$$

the mass of the neutron m_n and proton m_p, respectively, the gyromagnetic ratio $\gamma = 1.913$, and the Pauli spin operator for the neutron $\boldsymbol{\sigma}$. Analogous, the operator of the magnetic dipole moment of the electron is

$$\boldsymbol{\mu}_\mathrm{e} = -2\mu\mathrm{B}\boldsymbol{s}, \tag{3.14}$$

where

$$\mu_\mathrm{B} = \frac{e\hbar}{2m_\mathrm{e}} \tag{3.15}$$

is the Bohr magneton, m_e is the mass of the electron, and $\boldsymbol{s}$ is the spin angular momentum operator for the electron in units of $\hbar$.

The interaction potential is given by

$$\hat{U} = \boldsymbol{\mu}_\mathrm{n} \cdot \boldsymbol{H} = -\gamma\mu_\mathrm{N}\boldsymbol{\sigma} \cdot \boldsymbol{H}, \tag{3.16}$$

where the neutron interacts with the magnetic field $\boldsymbol{H}$, generated by the unpaired electrons in the sample. A single electron with velocity v_e generates a magnetic field at a point $\boldsymbol{R}$ from the electron with

$$\boldsymbol{H} = \boldsymbol{H}_\mathrm{S} + \boldsymbol{H}_\mathrm{L} = \nabla \times \left(\frac{\boldsymbol{\mu}_\mathrm{e} \times \boldsymbol{R}}{|\boldsymbol{R}|^3}\right) - \frac{e}{c}\frac{\boldsymbol{v}_\mathrm{e} \times \boldsymbol{R}}{|\boldsymbol{R}|^3}, \tag{3.17}$$

where e is the elementary charge, and c is the speed of light. The first term in Eq. (3.17), $\boldsymbol{H}_\mathrm{S}$, comes from the magnetic dipole moment of the electron, and the second term, $\boldsymbol{H}_\mathrm{L}$, arises from its orbital motion.

The calculation of the matrix element in Eq. (3.3), using the interaction potential in Eq. (3.16), is calculated in detail in Ref. [62, 65]. The magnetic scattering cross section for unpolarised neutrons and spin-only scattering by ions with localised electrons is given by

$$\frac{\mathrm{d}^2\sigma}{\mathrm{d}\Omega\mathrm{d}\omega} = (\gamma r_0)^2 \frac{k_f}{k_i} F^2(\boldsymbol{q}) \exp\{-2W(\boldsymbol{q})\} \sum_{\alpha,\beta}\left(\delta_{\alpha\beta} - \frac{Q_\alpha Q_\beta}{Q^2}\right) S^{\alpha\beta}(\boldsymbol{q},\omega), \tag{3.18}$$

where $F(\boldsymbol{q})$ is the magnetic form factor, $\exp\{-2W(\boldsymbol{q})\}$ the Debye-Waller factor, and γr_0 takes the same role as the scattering length b for nuclear scattering. $S^{\alpha\beta}(\boldsymbol{q},\omega)$ is the magnetic scattering function:

$$S^{\alpha\beta}(\boldsymbol{q},\omega) = \sum_{j,j'}\exp\{i\boldsymbol{q}(\boldsymbol{R}_j - \boldsymbol{R}_{j'})\}\sum_{\lambda_i,\lambda_f}p_{\lambda_i}\langle\lambda_i|\hat{S}^{\alpha}_{j'}|\lambda_f\rangle\langle\lambda_f|\hat{S}^{\beta}_j|\lambda_i\rangle\delta\left(\hbar\omega + E_{\lambda_i} - E_{\lambda_f}\right),$$
(3.19)

where $\hat{S}^{\alpha}_j$ $(\alpha = x, y, z)$ is the spin operator of the jth ion at site $\boldsymbol{R}_j$.

Besides the magnetic scattering function, Eq. (3.8) is governed by the magnetic form factor $F(\boldsymbol{q})$ and the polarisation factor $(\delta_{\alpha\beta} - Q_\alpha Q_\beta/Q^2)$. The latter states that the neutron can only couple to magnetic moments or spin fluctuations perpendicular to $\boldsymbol{q}$. The strength of the magnetic cross section is of the order of the nuclear cross section.

So far, spin-only scattering was described where the orbital angular momentum of the magnetic ions was regarded as zero. A theoretical treatment of scattering by ions considering both, spin and orbital angular momentum, was given by Johnston in 1966 [67]. The calculation is quite tedious and, therefore, only the result will be quoted here. For more detail see Ref. [62, 65, 67]. The scattering function in Eq. (3.19) translates to

$$S^{\alpha\beta}(\boldsymbol{q},\omega) = \frac{1}{2\pi\hbar}\sum_{j,j'}\int_{-\infty}^{+\infty}\exp\{i\boldsymbol{q}(\boldsymbol{R}_j - \boldsymbol{R}_{j'})\}\langle\hat{S}^{\alpha}_j(0)\hat{S}^{\beta}_{j'}(t)\rangle\exp\{-i\omega t\}\,\mathrm{d}t, \qquad (3.20)$$

with the spin operator

$$\hat{S}^{\alpha}_j = \frac{1}{2}g\hat{J}^{\alpha}_j, \tag{3.21}$$

the thermal average of the time-dependent spin operators $\langle\hat{S}^{\alpha}_j(0)\hat{S}^{\beta}_{j'}(t)\rangle$, the Landé splitting factor g, and an effective angular momentum operator $\hat{J}^{\alpha}_j$. Eq. (3.20) gives the probability that, if the magnetic moment of the j'th ion at $\boldsymbol{R}_{j'}$ at $t = 0$ has some specific value, the magnetic moment of the jth ion at $\boldsymbol{R}_j$ has some other specific value at the time t. It corresponds to the van Hove pair correlation function introduced in Sec. 3.1.1. This allows to connect the magnetic scattering function in Eq. (3.19) to the fluctuation-dissipation theorem

$$S^{\alpha\beta}(\boldsymbol{q},\omega) = \frac{N\hbar}{\pi}\left(1 - \exp\left\{-\frac{\hbar\omega}{k_\mathrm{B}T}\right\}\right)^{-1}\mathrm{Im}\chi^{\alpha\beta}(\boldsymbol{q},\omega), \tag{3.22}$$

where N is the total number of magnetic ions and $\chi^{\alpha\beta}$ the generalised susceptibility tensor. Physically speaking, the neutron may be considered a magnetic probe generating a perturbing magnetic field $H^{\beta}(\boldsymbol{q},\omega)$ in the scatterer, and detecting its response $M^{\alpha}(\boldsymbol{q},\omega)$ to the generated field by the relation

$$M^{\alpha}(\boldsymbol{q},\omega) = \chi^{\alpha\beta}(\boldsymbol{q},\omega)H^{\beta}(\boldsymbol{q},\omega). \tag{3.23}$$

3.1.3. Spin Polarisation

The neutron spin with quantum number $s = 1/2$ is described by the spin operator

$$\hat{\boldsymbol{S}} = (S_x, S_y, S_z) \tag{3.24}$$

with the two eigenvalues $\pm\,\hbar/2$ with respect to an arbitrary quantisation axis. The eigenvalue condition can be written as

$$\hat{\boldsymbol{S}}|\chi\rangle = \pm\frac{\hbar}{2}|\chi\rangle, \tag{3.25}$$

where $|\chi\rangle$ describe the spin state. The operator $\hat{\boldsymbol{\sigma}} = 2\hat{\boldsymbol{S}}/\hbar$ is represented by the Pauli matrices

$$\sigma_x = \begin{pmatrix} 0 & 1 \\ 1 & 0 \end{pmatrix}, \qquad \sigma_y = \begin{pmatrix} 0 & -i \\ i & 0 \end{pmatrix}, \qquad \sigma_z = \begin{pmatrix} 1 & 0 \\ 0 & -1 \end{pmatrix}, \tag{3.26}$$

and can therefore be written as

$$\hat{\boldsymbol{S}} = \frac{\hbar}{2}\hat{\boldsymbol{\sigma}}, \tag{3.27}$$

with $\hat{\boldsymbol{\sigma}} = (\sigma_x, \sigma_y, \sigma_z)$. The general spin wave function of a neutron can be written as

$$\chi = a|\chi_\uparrow\rangle + b|\chi_\downarrow\rangle = a\begin{pmatrix} 1 \\ 0 \end{pmatrix} + b\begin{pmatrix} 0 \\ 1 \end{pmatrix} = \begin{pmatrix} a \\ b \end{pmatrix}, \tag{3.28}$$

where the two complex quantities a and b must fulfil the normalisation condition

$$\chi^\dagger\chi = |a|^2 + |b|^2 = 1. \tag{3.29}$$

The spin states $|\chi_\uparrow\rangle$ and $|\chi_\downarrow\rangle$ correspond to the spin up and spin down states with eigenvalues $+1$ and -1 for the operator σ_z, therefore the z-axis was chosen as polarisation and quantisation axis. The polarisation of a single neutron is defined as the expectation value of the spin operator

$$\boldsymbol{p} = \langle\frac{2\hat{\boldsymbol{S}}}{\hbar}\rangle = \langle\hat{\boldsymbol{\sigma}}\rangle. \tag{3.30}$$

For a single neutron the polarisation is always $|\boldsymbol{P}| = 1$. Considering a neutron beam, the polarisation is given by the average over the individual polarisation of the neutrons

$$\boldsymbol{P} = \frac{1}{N}\sum_j \boldsymbol{p}_j, \tag{3.31}$$

with $0 \leq |\boldsymbol{p}| \leq 1$. For a beam partly polarised along the z-direction without a component along the x- and y-direction, the fraction of neutrons in the $|\chi_{\uparrow}\rangle$ state is given by

$$n^+ = \frac{1 + P_z}{2},$$ (3.32)

and the fraction of neutrons in the $|\chi_{\downarrow}\rangle$ state is given by

$$n^- = \frac{1 - P_z}{2},$$ (3.33)

with

$$P_z = n^+ - n^-.$$ (3.34)

3.1.4. Neutrons in a Magnetic Field

In an external magnetic field the magnetic moment of the neutron will perform a Larmor precession about the external magnetic field $\boldsymbol{H}$. The spin-1/2 system is again represented by the Pauli matrices in Eq. (3.26). The spin operator and the general spin wave function obeying the normalisation condition are also as described in Sec. 3.1.3, Eq. (3.27) through Eq. (3.29). The consequence of a magnetic field on the spin operator is described by the Hamiltonian

$$\hat{H} = \gamma \boldsymbol{H} \cdot \hat{\boldsymbol{S}},$$ (3.35)

where γ is the gyromagnetic ratio of the neutron. With the external magnetic field along the z-direction, i.e. $\boldsymbol{H} = H\hat{z}$, the Schrödinger equation for the spin component χ,

$$-i\hbar \frac{\partial}{\partial t}\chi = \hat{H}\chi$$ (3.36)

can be solved using the ansatz

$$a = \alpha \exp\{i\omega_a t\} \qquad \text{and} \qquad b = \beta \exp\{i\omega_b t\},$$ (3.37)

resulting in

$$\omega_a = \frac{\gamma H}{2} \qquad \text{and} \qquad \omega_b = -\frac{\gamma H}{2}.$$ (3.38)

With the spin wave function in Eq. (3.28), the expectation value of the spin operator is
given by

$$\langle \boldsymbol{S} \rangle = \langle \chi^\star | \hat{\boldsymbol{S}} | \chi \rangle = \frac{\hbar}{2} \langle \begin{pmatrix} a \\ b \end{pmatrix}^\star | \boldsymbol{\sigma} | \begin{pmatrix} a \\ b \end{pmatrix} \rangle \tag{3.39}$$

$$= \begin{pmatrix} \alpha\beta \left(\exp\{-i\omega_a - \omega_b t\} + \exp\{i\omega_a - \omega_b t\} \right) \\ i\alpha\beta \left(\exp\{i\omega_a - \omega_b t\} - \exp\{-i\omega_a - \omega_b t\} \right) \\ \alpha^2 - \beta^2 \end{pmatrix} \tag{3.40}$$

$$= \begin{pmatrix} 2\alpha\beta \cos\left(\omega_L t\right) \\ -2\alpha\beta \sin\left(\omega_L t\right) \\ \alpha^2 - \beta^2 \end{pmatrix}, \tag{3.41}$$

introducing the Larmor frequency

$$\omega_L = \omega_a - \omega_b = \gamma H. \tag{3.42}$$

Choosing $2\alpha\beta = \sin(\theta)$ and $\alpha^2 - \beta^2 = \cos(\theta)$ gives

$$\langle \boldsymbol{S} \rangle = \begin{pmatrix} \sin(\theta) \cos(\omega_L t) \\ -\sin(\theta) \sin(\omega_L t) \\ \cos(\theta) \end{pmatrix}. \tag{3.43}$$

Therefore, $\langle \boldsymbol{S} \rangle$ is a vector whose azimuth is precessing about the z-axis at a fixed incli-
nation angle θ.

   If the direction of the magnetic field is changing as the neutrons travel through it, two
different cases have to be considered. First, if the transition frequency ω_H, at which the
field changes from $\boldsymbol{H}$ to $\boldsymbol{H'}$, is much larger than the Larmor frequency of the precession,
the precession vector will follow the magnetic field if they were parallel before. If the
precession vector was tilted away from the magnetic field with a finite angle, its precession
cone will follow the magnetic field during the transition. This transition is called adiabatic
and shown in Fig. 3.1(a). If the change of the magnetic field is fast compared to the Larmor
frequency of the precession, the polarisation will start to precess about the new magnetic
field direction. This is called non-adiabatic transition and shown in Fig. 3.1(b). Neutron
spin manipulation via both, adiabatic and non-adiabatic transitions, are crucial for the
realisation of the spin echo technique, as will become apparent in the following Sec. 3.2.

3.2. Principles of Neutron Spin Echo Techniques

Neutron Spin Echo (NSE) spectroscopy, proposed by Mezei in 1972 [40, 41], is a time-of-
flight technique where information about the flight time of individual neutrons is encoded
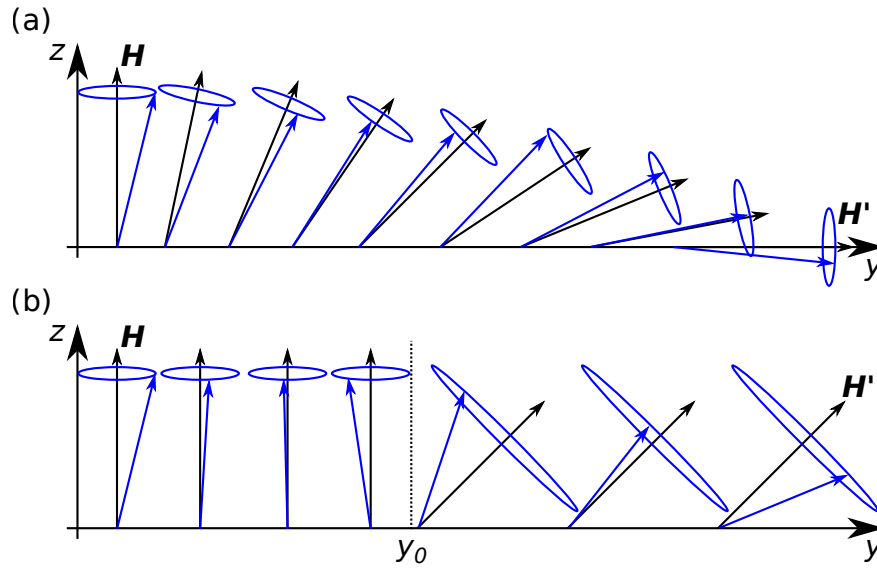
Figure 3.1.: Polarised neutron beam in an external magnetic field. (a) Adiabatic transition of a neutron beam in a magnetic field changing from $\boldsymbol{H}$ to $\boldsymbol{H}'$ with $\omega_H \ll \omega_L$. The polarisation vector follows the changing field. (b) Non-adiabatic transition. The field direction changes rapidly at y_0 from $\boldsymbol{H}$ to $\boldsymbol{H}'$. The polarisation vector starts precessing about the new field direction.

in the Larmor precession phases in known magnetic fields before and after the scattering process. A NSE spectrometer possesses an extremely high energy resolution and allows to investigate large domains in time and space. Since its invention in 1972, the method has been further developed, increasing the field of application. In 1987, Golub and Gähler proposed to replace the highly homogeneous constant field regions in NSE by a combination of a constant and an oscillating field, a method called Neutron Resonance Spin Echo (NRSE) [42]. A major disadvantage of classical NSE and NRSE is that depolarising conditions at the sample position lead to a loss of information of the spin phase. A modification of NRSE overcoming this obstacle is the Modulation of IntEnsity with Zero Effort (MIEZE) [43–46]. In MIEZE all neutron spin manipulation is completed prior to the sample, making the method insensitive for beam depolarisation at the sample position.

3.2.1. Neutron Spin Echo Spectroscopy (NSE)

Fig. 3.2(a) schematically shows a depiction of a neutron spin echo spectrometer. An incoming neutron with velocity v_1 travels along the y-direction of the spectrometer. After being polarised along the z-axis, it enters the first homogeneous and static magnetic field region of length L_1 and field B_1. According to the Larmor precession, the neutron spin
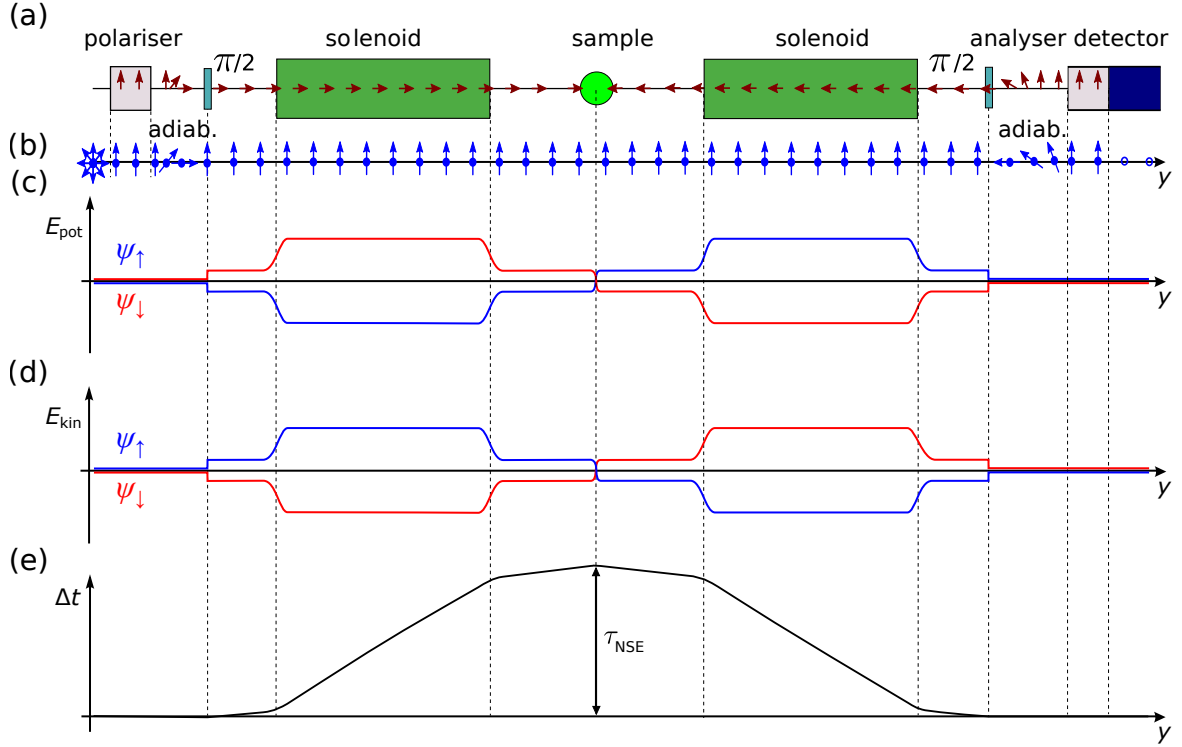
Figure 3.2.: Schematic of a NSE spectrometer. (a) The neutron beam travels along the y-axis of the spectrometer, passing the polariser, the first and second precession field, and the analyser before reaching the detector. (b) Polarisation of the neutron beam throughout its flight path. (c) Splitting of the potential energy E_{pot} of the spin up ($\chi_\uparrow$) and spin down ($\chi_\downarrow$) eigenstates of the neutron along the flight path due to the presence of a static magnetic field B_0. (d) Splitting of the kinetic energy E_{kin} of the eigenstates compensating the splitting of the potential energy so that the total energy is conserved. (e) Flight time difference Δt of the up and down eigenstates along the flight path. The magnitude of the splitting at the sample position determines the time resolution of the spectrometer τ_{NSE}. Figure adapted from Ref. [68].

starts to precess about the external magnetic field, thereby accumulating a spin phase ϕ_1 which is proportional to the time spent in the field region,

$$\phi_1 = \gamma B_1 t_1 = \gamma B_1 \frac{L_1}{v_1}. \tag{3.44}$$

After the first spectrometer arm the neutron travels through the sample region before entering the second magnetic field region of length L_2 and field B_2. In the second spectrometer arm the neutron accumulates a spin phase ϕ_2 of

$$\phi_2 = \gamma B_2 t_2 = \gamma B_2 \frac{L_2}{v_2}, \tag{3.45}$$

before getting analysed along the z-axis, and finally reaching the detector. The total spin phase that the neutron accumulates while travelling through the instrument is therefore given by

$$\phi = \phi_1 + \phi_2 = \gamma\, BL \left(\frac{1}{v_1} - \frac{1}{v_2} \right), \tag{3.46}$$

with $B_1 = -B_2 = B$ and $L_1 = L_2 = L$. Considering an elastic scattering process, or no interaction with the sample at all, the total spin phase for $v_1 = v_2 = v$ is

$$\phi = \gamma\, BL \left(\frac{1}{v} - \frac{1}{v} \right) = 0. \tag{3.47}$$

The initial neutron polarisation is recovered, completing the spin echo. It becomes apparent that this is also true for a neutron beam with a finite velocity distribution, as the recovering of the polarisation is made for each neutron individually. Therefore, the resolution for measuring the change in velocity after quasi- or inelastic scattering can be much better than the resolution of the width of the incident beam. This is why spin echo spectrometers use a velocity selector at the entrance of the instrument, selecting a wavelength band with a width of about $\frac{\Delta\lambda}{\lambda} = 10 - 20\%$. This allows a very high resolution while maintaining a high intensity, and is one of the greatest advantages of NSE over spectrometers depending on well defined monochromatic neutron beams.

Assuming an exchange of energy with the sample, the neutron velocity upon entering the second field region has changed to $v_2 = v + \Delta v$. The total spin phase is then given by

$$\phi = \gamma\, BL \left(\frac{1}{v} - \frac{1}{v + \Delta v} \right) = \gamma BL \left(\frac{\Delta v}{v^2 + v\Delta v} \right). \tag{3.48}$$

In a quasielastic scattering process the energy change is small, and hence is the change in velocity $\Delta v \ll v$. This allows to Taylor expand Eq. (3.48) to

$$\phi = \gamma BL \left(\frac{\Delta v}{v^2 + v\Delta v} \right) \approx \gamma BL \frac{\Delta v}{v^2}. \tag{3.49}$$

The change in velocity due to the scattering process in terms of energy transfer

$$\Delta E = \hbar\omega = \frac{m_{\rm n}}{2} \left((v + \Delta v)^2 - v^2 \right) \tag{3.50}$$

$$= \frac{m_{\rm n}}{2} \left(2v\Delta v + \Delta v^2 \right) \tag{3.51}$$

$$\approx m_{\rm n} v \Delta v \tag{3.52}$$

allows to rewrite the total spin phase in Eq. (3.49) to

$$\phi = \gamma BL \frac{\hbar}{m_{\rm n} v^3} \omega =: \omega\tau_{\rm NSE}, \tag{3.53}$$

with the spin echo time defined as

$$\tau_{\text{NSE}} = \frac{\gamma \hbar B L}{m_{\text{n}} v^3}. \tag{3.54}$$

The spin echo time is a measure for the resolution of a spin echo spectrometer and incorporates the key instrumental parameter, i.e. the magnetic field integral BL. For high resolution, i.e. large spin echo times τ_{NSE}, large magnetic field integrals are required, and a larger neutron wavelength is of advantage.

In the following, the whole neutron beam rather than a single neutron is considered. The polarisation of the neutron beam along a particular direction is given by the average of all spin phases in the beam. In the schematic shown in Fig. 3.2(a), the neutron beam is polarised along z, hence

$$P_z = \langle \cos(\phi) \rangle = \int S(\boldsymbol{q}, \omega) \cos(\omega \tau_{\text{NSE}}) \, \mathrm{d}\omega, \tag{3.55}$$

where the probability that a neutron is scattered with the energy transfer $\hbar \omega$ is given by the scattering function $S(\boldsymbol{q}, \omega) \, \mathrm{d}\omega$. The cosine of the spin phase describes the projection of the spin onto the polarisation axis. The expression in Eq. (3.55) is the Fourier transform of $S(\boldsymbol{q}, \omega)$ in space and time, known as the intermediate scattering function $S(\boldsymbol{q}, \tau)$. The scattering functions were introduced in Sec. 3.1, and will be discussed in more detail in Sec. 3.3.1.

Neutron spin echo can also be explained from a semi-classical point of view, delivering a more intuitive explanation of the spin echo principle. From a quantum mechanical point of view a neutron is a spin-1/2 particle with two spin eigenstates with respect to any quantisation axis defined by an external magnetic field. Assuming the neutron beam is fully polarised along z, hence all neutrons are in one of the eigenstates. If the magnetic field is applied perpendicular to the polarisation axis, all neutrons are in a mixed state. With the quantisation axis along x the initial spin state is given by

$$\chi_{\uparrow}^{z} = \frac{1}{\sqrt{2}} \left(\chi_{\uparrow}^{x} + \chi_{\downarrow}^{x} \right). \tag{3.56}$$

The up eigenstate $\chi_{\uparrow}^{x}$ has a magnetic moment anti-parallel to the constant magnetic field B_0, while the down eigenstate $\chi_{\downarrow}^{x}$ has a magnetic moment parallel to B_0. This leads to a splitting of the potential energies of the two eigenstates in the magnetic field

$$E_{\text{pot}}^{\uparrow/\downarrow} = \pm \frac{\Delta E}{2} = \pm \frac{\hbar \omega_L}{2} = \pm \frac{\hbar}{2} \gamma B. \tag{3.57}$$

The splitting of the potential energies is shown in Fig. 3.2(b). Since the total energy in a magnetic field which is constant in time is conserved, this shift in potential energy is accompanied by a shift in kinetic energy, see Fig. 3.2(c),

$$E_{\text{kin}}^{\uparrow/\downarrow} = E_0 - E_{\text{pot}}^{\uparrow/\downarrow} = E_0 \left(1 - \frac{E_{\text{pot}}^{\uparrow/\downarrow}}{E_0} \right), \tag{3.58}$$

with the total energy

$$E_0 = \frac{m_{\mathrm{n}} v_0^2}{2}. \tag{3.59}$$

Regarding the two spin states as individual wave packets, the spin-up state is delayed by a magnetic field region, while the spin-down state is accelerated. From the different kinetic energies for each spin state, the difference in velocity is given by

$$v^{\uparrow/\downarrow} = \sqrt{2\frac{E_{\mathrm{kin}}^{\uparrow/\downarrow}}{m_{\mathrm{n}}}} = \sqrt{2\frac{E_0 - E_{\mathrm{pot}}^{\uparrow/\downarrow}}{m_{\mathrm{n}}}} = v_0\sqrt{1 - \frac{E_{\mathrm{pot}}^{\uparrow/\downarrow}}{E_0}}. \tag{3.60}$$

Since $E_{\mathrm{pot}} \ll E_0$, Taylor expanding the square root yields

$$v^{\uparrow/\downarrow} \approx v_0\left(1 - \frac{E_{\mathrm{pot}}^{\uparrow/\downarrow}}{2E_0}\right). \tag{3.61}$$

Therefore, the temporal splitting of the two spin states at the sample position is given by the different flight time through the magnetic field region with length L

$$t^{\uparrow/\downarrow} = \frac{L}{v^{\uparrow/\downarrow}} \approx \frac{L}{v_0}\left(1 + \frac{E_{\mathrm{pot}}^{\uparrow/\downarrow}}{2E_0}\right), \tag{3.62}$$

to

$$t^{\uparrow} - t^{\downarrow} = \frac{L}{v_0}\left(\frac{E_{pot}^{\downarrow} - E_{pot}^{\uparrow}}{2E_0}\right) = \frac{\gamma \hbar B L}{m_{\mathrm{n}} v_0^3} = \tau_{\mathrm{NSE}}, \tag{3.63}$$

which is equal to the spin echo time defined in Eq. (3.54). The temporal splitting at the sample position is shown in Fig. 3.2(d).

From this semi-classical point of view it becomes apparent that, by regarding the neutron beam as wave packets, the first magnetic field region coherently splits the wave packets. The second field region coherently reverses the splitting, leading to a constructive interference of the two states. The polarisation is restored. If the sample structure changes in the time interval between scattering of the first and second split wave packet, the interference will not be perfect, resulting in a loss of polarisation.

3.2.2. Neutron Resonance Spin Echo Spectroscopy (NRSE)

Neutron resonance spin echo is a modification of NSE, where the energetic splitting of the spin states is induced by resonantly oscillating magnetic fields in combination with a static field and, therefore, the precession field regions can be replaced by zero field regions. A schematic of a NRSE spectrometer is shown in Fig. 3.3(a). Each spectrometer

arm possesses two resonant spin flipper coils, known as NRSE coils, separated by the distance L. Such a spin flipper consists of a constant magnetic field B_0 perpendicular to the precession plane, and a rotating magnetic field B_{rf}, rotating with frequency ω in the precession plane. Upon entering the spectrometer, the neutron beam is again polarised along the z-axis. The magnetic field vector inside a NRSE coil is given by

$$\boldsymbol{B} = \begin{pmatrix} B_{\mathrm{rf}} \cos{(\omega t)} \\ B_{\mathrm{rf}} \sin{(\omega t)} \\ B_0 \end{pmatrix}. \tag{3.64}$$

Neutrons entering the NRSE coil start to precess about B_0. The effect of the rotating field $\boldsymbol{B}_{\mathrm{rf}}$ can be understood by assuming a reference frame rotating around the z-axis with frequency ω. If this field rotates with a frequency equal to the Larmor frequency of the neutron, i.e. $\gamma B_0 = \omega_{\mathrm{L}} = \omega$, the field in the reference frame of the rotation reduces to

$$\boldsymbol{B} = \begin{pmatrix} B_{\mathrm{rf}} \\ 0 \\ 0 \end{pmatrix}. \tag{3.65}$$

In the rotating reference frame the neutron spin precesses about the x-axis. The total spin phase depends on the accumulated precession phase during the flip, and on the time spent in the rf-field. The accumulated precession phase with respect to the z-axis after a π-flip around $\boldsymbol{B}_{\mathrm{rf}}$ is twice the phase difference between spin and field. Therefore, the total spin phase is

$$\phi = \phi_0 + 2\left(\phi_1 - \phi_0\right) + \omega t = 2\phi_1 + \omega t - \phi_0, \tag{3.66}$$

with the phase of the rf-field ϕ_1, the phase of the incoming spins ϕ_0, and the time t spent in the rotating field with frequency ω. The accumulated spin phase at the sample position is determined by considering two rf-flippers separated by a distance L. Thereby, the phase of the incoming spins for the second rf-flipper is the phase accumulated in the first flipper

$$\phi = 2\phi_2 + \omega t - \left(2\phi_1 + \omega t - \phi_0\right) = \phi_0 + 2\left(\phi_2 - \phi_1\right), \tag{3.67}$$

and the phase change depends only on the difference of the phases of the oscillating fields

$$\Delta\phi = 2\left(\phi_2 - \phi_1\right). \tag{3.68}$$

Under the assumption that both rf-fields are oscillating in phase lock, ϕ_2 is given by the flight time between the two rf-fields:

$$\Delta\phi = 2\left(\phi_1 + \omega\frac{L}{v} - \phi_1\right) = 2\,\frac{\omega L}{v} = 2\frac{\gamma B_0 L}{v}. \tag{3.69}$$
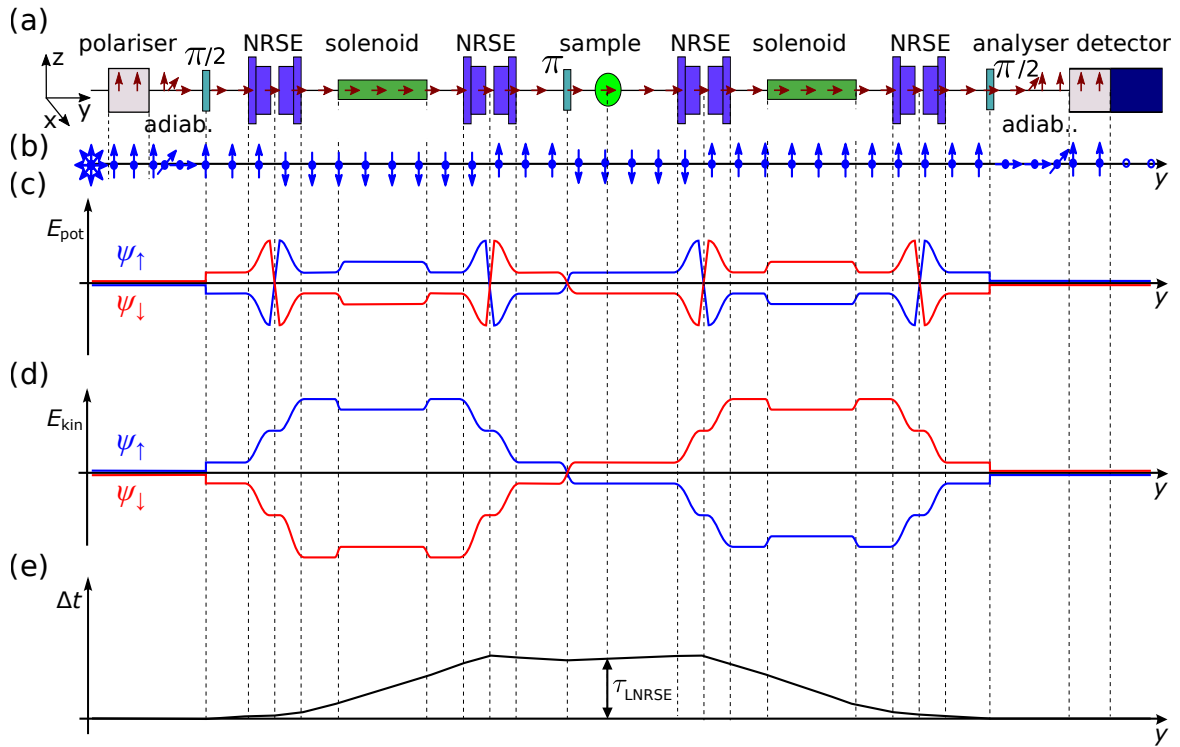
Figure 3.3.: Schematic of a NRSE spectrometer. (a) The neutron beam travels along the y-axis of the spectrometer, passing the polariser, the first and second precession region, and the analyser before reaching the detector. In contrast to NSE, the precession regions consist of two resonant spin flippers rather than a solenoid. (b) Polarisation of the neutron beam throughout its flight path. (c) Splitting of the potential energy E_{pot} of the spin up ($\chi_\uparrow$) and spin down ($\chi_\downarrow$) eigenstates of the neutron along the flight path due to the superposition of a static magnetic field B_0 and a rotating magnetic field B_{rf} in the π-flippers. (d) Splitting of the kinetic energy E_{kin} of the eigenstates. Energy is transferred in form of resonant emission of absorption of photons from the radiation field. (e) Flight time difference Δt of the up and down eigenstates along the flight path. The magnitude of the splitting at the sample position determines the time resolution of the spectrometer τ_{NRSE} and is analogous to τ_{NSE} for NSE. Figure adapted from Ref. [68].

Comparing to classical NSE where the neutron travels through a constant magnetic field B_0 of length L, cf. Eq. (3.44), travelling through the precession regions of two NRSE coils with the same constant field B_0 and the same distance L gives twice the precession angle.

The precession angle is determined by the amplitude of the rotating field and the flight time inside the rf-field, and is tuned so that the neutron performs a π-flip. From a quantum mechanical point of view, two conditions must be fulfilled for the neutron to perform a π-flip. First, the resonance condition

$$\omega = \omega_L = \gamma B_0, \tag{3.70}$$

and, second, the π-flip condition

$$\pi \overset{!}{=} \gamma B_{\mathrm{rf}} t = \gamma B_{\mathrm{rf}} \frac{l}{v} \quad \Rightarrow \quad B_{\mathrm{rf}} = \frac{\pi v}{\gamma l}, \tag{3.71}$$

with the length of the rf-field l, and the velocity of the neutron v.

If the initial polarisation is perpendicular to the quantisation axis given by the static field B_0, the up and down spin eigenstates are equally populated. With both above mentioned conditions fulfilled, the two spin states are flipped: the spin eigenstate initially in the down state is now in the up state and vice versa. Fig. 3.3(b) shows the difference in potential energy between the two states given by the static field B_0. Due to the difference in potential energy, energy is transferred in form of resonant emission or absorption of photons from the radiation field. Therefore, the two states travel with different kinetic energies through the region between the two rf-flippers, see Fig. 3.3(b). At the second rf-flipper coil, the spin states are flipped again, and the energy split is reversed. This can be seen as a simulated magnetic field of strength $2B_0$ and length L. Following Eq. (3.57) through (3.63) gives the spin echo time for NRSE, analogous to that for classical NSE,

$$\tau_{\mathrm{NRSE}} = \frac{2\gamma\hbar BL}{m_{\mathrm{n}}v^3} = \frac{2\hbar\omega L}{m_{\mathrm{n}}v^3} = 2\tau_{NSE}. \tag{3.72}$$

The temporal splitting of the two spin states is shown in Fig. 3.3(d).

3.2.3. Modulation of Intensity with Zero Effort (MIEZE)

Modulation of intensity with zero effort (MIEZE) is a spin echo option, and only feasible with resonantly oscillating magnetic field coils, therefore limited to NRSE spectrometers. The MIEZE set-up is schematically shown in Fig. 3.4(a) and consists of two NRSE coils in the first spectrometer arm, separated by the distance L_1. The distance between the second rf-coil and the detector is L_2, and the distance between sample and detector is L_{SD}. In contrast to NRSE, the two rf-fields run at different frequencies ω_A and ω_B, with corresponding rotating fields $B_{\mathrm{rf},A}$ and $B_{\mathrm{rf},B}$, and static fields $B_{0,A}$ and $B_{0,B}$. Both NRSE coils are tuned to perform a π-flip in the neutron.

The calculation of the phase difference for MIEZE is analogues to the calculation for NRSE. From Eq. (3.66), the phase $\phi_{A'}$ after the first rf-flipper is

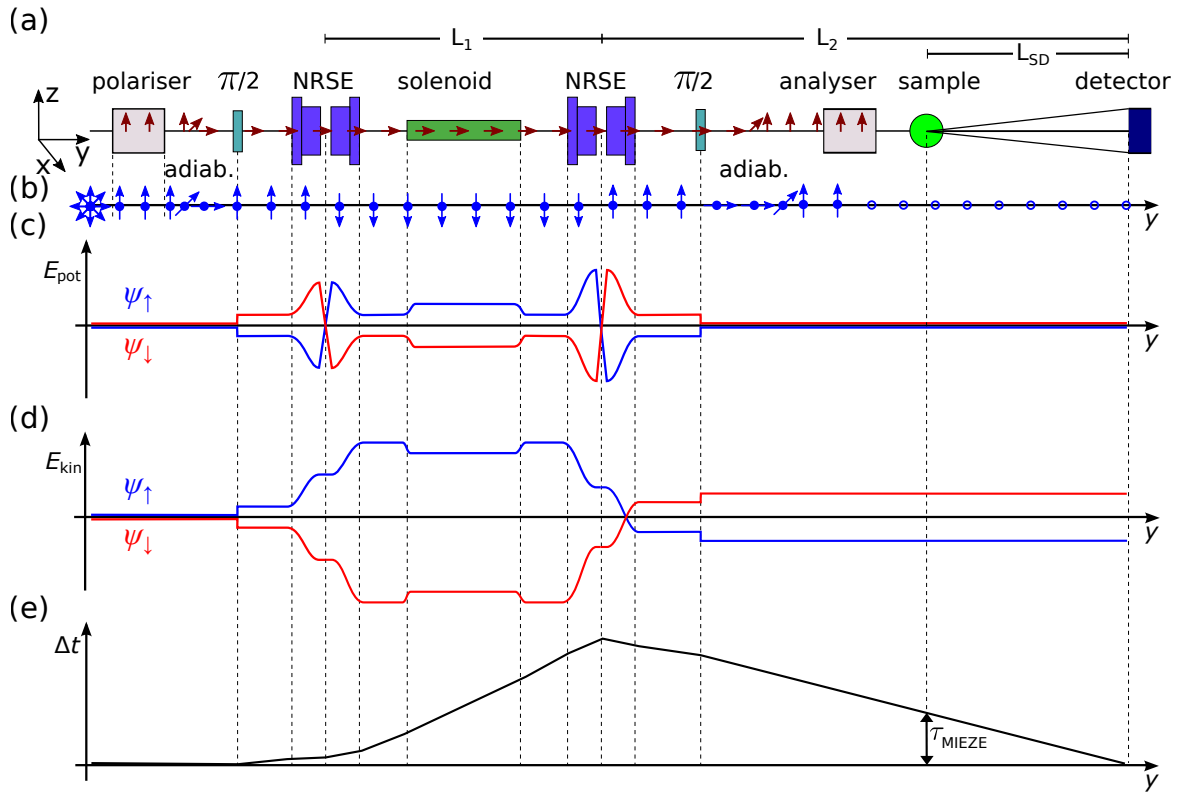$$\phi_{A'} = 2\phi_A + \omega_A t - \phi_0, \tag{3.73}$$

Figure 3.4.: Schematic of a MIEZE spectrometer. (a) The neutron beam travels along the y-axis of the spectrometer, passing the polariser, the precession region, and the analyser before reaching the detector. (b) Polarisation of the neutron beam throughout its flight path. (c) Splitting of the potential energy E_{pot} of the spin up ($\chi_\uparrow$) and spin down ($\chi_\downarrow$) eigenstates of the neutron along the flight path due to the superposition of a static magnetic field B_0 and a rotating magnetic field B_{rf} in the π-flippers. The potential energy splitting is overcompensated in the second π-flipper. (d) Splitting of the kinetic energy E_{kin} of the eigenstates. Energy is transferred in form of resonant emission of absorption of photons from the radiation field. (e) Flight time difference Δt of the up and down eigenstates along the flight path. The magnitude of the splitting at the sample position determines the time resolution of the spectrometer τ_{MIEZE}. In contrast to NSE and NRSE, the overcompensation of the potential energy leads to a maximal temporal splitting at the second π-flipper, which is only compensated when the detector position is reached. Figure adapted from Ref. [68].

with the phase of the rf-field ϕ_A, the phase of the incoming spins ϕ_0, and the time t spent in the rotating field with frequency ω_A. The spin phase after the second rf-flipper follows to

$$\phi_{B'} = 2\phi_B + \omega_B t - \phi_{A'} \tag{3.74}$$

$$= 2\left(\phi_B - \phi_A\right) + t\left(\omega_B - \omega_A\right) + \phi_0, \tag{3.75}$$

where the time spent in ω_A and ω_B are equal with $t = \frac{l}{v}$, l being the length of a rf-field.

With $\phi_A = \omega_A t_A$ and $\phi_B = \omega_B t_B = \omega_B(t_A + L_1/v)$, the total accumulated spin phase after the second rf-flipper is given by

$$\phi_{B'} = 2t_A (\omega_B - \omega_A) + 2\omega_B \frac{L_1}{v} + \frac{l}{v}(\omega_B - \omega_A) + \phi_0 \tag{3.76}$$

$$= 2t_A \Delta\omega + 2\omega_B \frac{L_1}{v} + \frac{l}{v}\Delta\omega + \phi_0. \tag{3.77}$$

Thereby, t_A and t_B are the times the neutron arrives at the rf-field A and B, respectively.

The MIEZE condition is given by the fact that at a certain point D, where the detector will be placed, at a distance L_2 from the second rf-flipper, all velocity dependent contributions to the spin phase must cancel out. The time the neutron arrives at this position is given by

$$t_D = t_A + \frac{L_1}{v} + \frac{L_2}{v}, \tag{3.78}$$

and, therefore, the spin phase at D is

$$\phi_D = 2t_D \Delta\omega + 2\omega_A \left(\frac{L_1}{v} + \frac{L_2}{v}\right) - 2\omega_B \frac{L_2}{v} + \frac{l}{v}\Delta\omega + \phi_0. \tag{3.79}$$

With the above mentioned condition for MIEZE

$$2\omega_A \left(\frac{L_1}{v} + \frac{L_2}{v}\right) - 2\omega_B \frac{L_2}{v} + \frac{l}{v}\Delta\omega \overset{!}{=} 0, \tag{3.80}$$

and by choosing

$$\frac{\Delta\omega}{\omega_A} = \frac{L_1}{L_2 - l/2}, \tag{3.81}$$

all velocity dependent contributions to the spin phase cancel out.

With $\phi_0 = 0$ remains a rotating polarisation at position D, dependent only on the difference between the frequencies of the two flippers and the time of flight between the second flipper and the detector,

$$\phi_D = 2t_D (\omega_B - \omega_A) = 2t_D \Delta\omega. \tag{3.82}$$

Placing a spin analyser somewhere between second coil and detector converts the rotating polarisation to a modulated intensity, given by the cosine projection of the polarisation on the analyser axis. This results in an intensity oscillation in time

$$I(t) = \frac{I_0}{2}(\cos(2\Delta\omega t) + 1), \tag{3.83}$$

with the probability of a neutron transmitting through the analyser

$$T = \frac{1}{2}(\cos(\phi) + 1). \tag{3.84}$$

For a totally depolarised beam the cosine is zero and half of the neutrons are transmitted. For full polarisation along the quantisation axis the cosine is one and all neutrons are transmitted, while for full polarisation against the quantisation axis the cosine is minus one and no neutron gets through.

Considering a sample being placed at a position L_{SD} upstream of the detector, as shown in Fig. 3.4(a). Further, assuming quasielastic scattering given by the scattering function $S(\boldsymbol{q}, \omega)$ with an energy transfer $\hbar\omega \ll \frac{1}{2}mv^2$ and being symmetric around $\omega = 0$. This leads to a delayed time of arrival as a function of flight distance L_{SD}

$$\Delta t = \frac{L_{\mathrm{SD}}}{v - \Delta v/2} - \frac{L_{\mathrm{SD}}}{v + \Delta v/2} = \frac{L\Delta v/v^2}{1 - (\Delta v/v)^2}, \tag{3.85}$$

and for $\Delta v \ll v$ Taylor expansion gives

$$\Delta t \approx \frac{L_{\mathrm{SD}}\Delta v}{v^2} = \frac{L_{\mathrm{SD}}\hbar\omega}{m_{\mathrm{n}}v^3}. \tag{3.86}$$

The altered time of flight from sample to detector results in a deviation from the spin echo condition, ultimately leading to a decrease in intensity. Introducing the time delay due to the scattering process into the oscillating intensity in Eq. (3.83) gives

$$I(t_D) = \frac{I_0}{2}\left(\cos\left(2\Delta\omega t_D + 2\Delta\omega\Delta t\right) + 1\right). \tag{3.87}$$

Further, introducing the scattering process $S(\boldsymbol{q}, \omega)$ results in

$$I(t_D) = \frac{I_0}{2}\int\left(\cos\left(2\Delta\omega t_D + 2\Delta\omega\Delta t\right) + 1\right)S(\boldsymbol{q}, \omega)\,\mathrm{d}\omega \tag{3.88}$$

$$= \frac{I_0}{2}\int\left(\cos\left(2\Delta\omega t_D\right)\cos\left(2\Delta\omega\Delta t\right) + 1\right)S(\boldsymbol{q}, \omega)\,\mathrm{d}\omega \tag{3.89}$$

$$= \frac{I_0}{2}\left(\int\cos\left(2\Delta\omega t_D\right)\cos\left(2\Delta\omega\Delta t\right)S(\boldsymbol{q}, \omega)\,\mathrm{d}\omega + 1\right). \tag{3.90}$$

Due to the symmetry of the scattering function, Eq. (3.88) can be rewritten to Eq. (3.89). From Eq. (3.89) to Eq. (3.90) it is used that $\int S(\boldsymbol{q}, \omega)\,\mathrm{d}\omega = 1$.

Comparing Eq. (3.90) with Eq. (3.83), there is a reduction in contrast of the oscillation given by

$$C := \frac{\int\cos\left(2\Delta\omega t_D\right)\cos\left(2\Delta\omega\Delta t\right)S(\boldsymbol{q}, \omega)\,\mathrm{d}\omega}{\cos\left(2\Delta\omega t_D\right)} \tag{3.91}$$

$$= \int\cos\left(2\Delta\omega\Delta t\right)S(\boldsymbol{q}, \omega)\,\mathrm{d}\omega \tag{3.92}$$

$$= \int\cos\left(2\Delta\omega\frac{\hbar L_{\mathrm{SD}}}{m_{\mathrm{n}}v^3}\omega\right)S(\boldsymbol{q}, \omega)\,\mathrm{d}\omega \tag{3.93}$$

$$= \int\cos\left(\tau_{\mathrm{MIEZE}}\omega\right)S(\boldsymbol{q}, \omega)\,\mathrm{d}\omega, \tag{3.94}$$

with the time resolution of a MIEZE spectrometer defined as

$$\tau_{\text{MIEZE}} = \frac{2\hbar}{m_\text{n} v^3} L_{\text{SD}} \Delta\omega = \frac{m_\text{n}^2}{\pi h^2} \lambda^3 L_{\text{SD}} \ \Delta\omega. \tag{3.95}$$

The contrast is the Fourier transform of $S(\boldsymbol{q}, \omega)$ in space and time, and takes the role of the polarisation in NSE, cf. Eq. (3.55).

Following the quantum mechanical approach as for NRSE, a simple energetic consideration also delivers the MIEZE condition and the time resolution of a MIEZE spectrometer. The difference in potential and kinetic energy of the two spin states is shown in Fig. 3.4(b-c). The change in velocity for the two spin states due to the presence of a magnetic field from Eq. (3.60) is

$$\Delta v = v \frac{E_{\text{pot}}}{2 E_0} = \frac{\hbar\omega}{m_\text{n} v}, \tag{3.96}$$

for a simulated magnetic field with frequency ω. This leads to a temporal splitting as function of flight distance L of

$$\Delta t = \frac{L}{v - \Delta v} - \frac{L}{v + \Delta v} = \frac{2L\Delta v / v^2}{1 - (\Delta v / v)^2}, \tag{3.97}$$

and for $\Delta v \ll v$ Taylor expansion gives

$$\Delta t \approx \frac{2L\Delta v}{v^2} = \frac{2L\hbar\omega}{m_\text{n} v^3}. \tag{3.98}$$

For fulfilling the MIEZE condition, the temporal splitting must be zero at the position of the detector,

$$\Delta t = \frac{2L_1 \hbar \omega_A}{m_\text{n} v^3} - \frac{2L_2 \hbar \Delta\omega}{m_\text{n} v^3} \overset{!}{=} 0 \tag{3.99}$$

$$\Rightarrow \quad \frac{\Delta\omega}{\omega_A} = \frac{L_1}{L_2}. \tag{3.100}$$

Comparing this result with the MIEZE condition obtained earlier, in Eq. (3.81) the thickness of the NRSE coils are taken into account, while it is neglected here. While the temporal splitting is zero at the detector position, it is finite at the position of the sample and defines the time resolution of a MIEZE spectrometer, shown in Fig. 3.4(d). The MIEZE time is defined by the temporal splitting at the sample position in consideration of the MIEZE condition in Eq. (3.100),

$$\Delta t = \frac{2\hbar}{m v^3} \left(L_1 \omega_A - (L_2 - L_{\text{SD}}) \Delta\omega \right), \tag{3.101}$$

$$\text{with} \quad \frac{\Delta\omega}{\omega_A} = \frac{L_1}{L_2}$$

$$\Rightarrow \quad \tau_{\text{MIEZE}} = \frac{2\hbar}{m_\text{n} v^3} L_{\text{SD}} \Delta\omega = \frac{m_\text{n}^2}{\pi h^2} \lambda^3 L_{\text{SD}} \ \Delta\omega. \tag{3.102}$$

(i). MIEZE and Large Energy Transfers

The considerations made so far were under the assumption of quasielastic scattering with an energy transfer between neutron and sample much smaller than the energy of the incoming neutron, i.e. $\Delta v \ll v$, giving the expression of the approximated spin echo time in Eq. (3.102). In case of a larger energy transfers, the spin echo approximation fails.

Starting with the spin phase after the second rf-flipper in Eq. (3.76),

$$\phi_{B'} = 2t_A (\omega_B - \omega_A) + 2\omega_B \frac{L_1}{v} + \frac{l}{v} (\omega_B - \omega_A) + \phi_0. \tag{3.103}$$

The time the neutron arrives at the detector is given by

$$t_D = t_A + \frac{L_1}{v} + \frac{L_{2S}}{v} + \frac{L_{SD}}{v + \Delta v}, \tag{3.104}$$

where L_{2S} is the distance between second rf-flipper and sample. The spin phase at the detector is therefore written as

$$\phi_D = 2(\omega_B - \omega_A) \left(t_D - \frac{L_1 + L_{2S}}{v} - \frac{L_{SD}}{v + \Delta v} \right) + 2\omega_B \frac{L_1}{v} + (\omega_B - \omega_A)\frac{l}{v} - \phi_{sub} + \phi_0, \tag{3.105}$$

introducing a field subtraction coil between the two rf-flippers giving the contribution ϕ_{sub} to the spin phase. This additional accumulated spin phase is generated by a DC magnetic field, and hence given by

$$\phi_{sub} = \frac{\gamma B l_{sub}}{v} = \frac{\gamma J_{sub}}{v}, \tag{3.106}$$

with the length of the field subtraction coil l_{sub}, the field generated by the coil B, the neutron velocity v, and the gyromagnetic ratio of the neutron $\gamma = 29.16 \, \text{MHz T}^{-1}$. This field subtraction coil allows easier tuning of a MIEZE spectrometer and gives access to the smallest spin echo times. With $\phi_0 = 0$ and neglecting the length of the rf-flippers $l \approx 0$, the expression in Eq. (3.105) reduces to

$$\phi_D = 2(\omega_B - \omega_A) \left(t_D - \frac{L_1 + L_{2S}}{v} - \frac{L_{SD}}{v + \Delta v} \right) + 2\omega_B \frac{L_1}{v} - \Phi_{sub}. \tag{3.107}$$

The MIEZE condition is again given by the fact that at the detector all velocity dependent contributions to the spin phase must cancel out,

$$2\omega_A \frac{L_1 + L_{2S}}{v} - 2\omega_B \frac{L_{2S}}{v} - 2(\omega_B - \omega_A)\frac{L_{SD}}{v + \Delta v} \overset{!}{=} 0, \tag{3.108}$$

which is true for

$$L_1 + L_{2S} = \frac{\omega_B L_1}{\omega_B - \omega_A} - L_{SD}. \tag{3.109}$$

With Eq. (3.109), the spin phase at the detector in Eq. (3.107) follows to

$$\phi_D = 2(\omega_B - \omega_A)\left(t_D + \frac{L_{\mathrm{SD}}}{v} - \frac{L_{\mathrm{SD}}}{v + \Delta v}\right) - \frac{\gamma J_{\mathrm{sub}}}{v}. \tag{3.110}$$

Introducing the time delay due to the scattering process into the oscillating intensity in Eq. (3.83) gives

$$I(t_D) = \frac{I_0}{2}\left(\cos\left(2(\omega_B - \omega_A)\left(t_D + \frac{L_{\mathrm{SD}}}{v} - \frac{L_{\mathrm{SD}}}{v + \Delta v}\right) - \frac{\gamma J_{\mathrm{sub}}}{v}\right) + 1\right) \tag{3.111}$$

$$= \frac{I_0}{2}\left(\cos\left(2(\omega_B - \omega_A)\left(t_D + \frac{L_{\mathrm{SD}}}{v} - \frac{L_{\mathrm{SD}}}{\sqrt{\frac{2\hbar\omega}{m_{\mathrm{n}}} + v^2}}\right) - \frac{\gamma J_{\mathrm{sub}}}{v}\right) + 1\right), \tag{3.112}$$

with the energy transfer

$$\hbar\omega = \frac{m_{\mathrm{n}}}{2}\left((v + \Delta v)^2 - v^2\right) \tag{3.113}$$

$$\Leftrightarrow \quad \Delta v = \sqrt{\frac{2\hbar\omega}{m_{\mathrm{n}}} + v^2} - v. \tag{3.114}$$

A comparison between the explicit calculation of the spin phase in Eq. (3.110) and Eq. (3.112), and the simpler case under the assumption of the spin echo approximation in Eq. (3.82) and Eq. (3.87), is conducted in Sec. 3.3.2.

3.3. Spin Echo Data Reduction

Recording the intermediate scattering function $S(\boldsymbol{q}, \tau)$ is measuring the polarisation P or contrast C for NSE and NRSE or MIEZE, respectively. Throughout this section, polarisation and contrast will be treated synonymously. Spin echo data must be normalised with the instrumental resolution and corrected for instrumental background to extract the sample contribution to the measured signal.

3.3.1. Spin Echo Group and Intermediate Scattering Function

The polarisation is measured by measuring its projection onto the analyser axis. After passing through the analyser, the intensity of the neutron beam is given by

$$I(\Delta J) = \frac{I_0}{2}\left(1 + C\cos\left(\phi(\Delta J)\right)\right). \tag{3.115}$$

The intensity is a function of an additional spin phase ϕ due to a field integral ΔJ the neutron experiences throughout the spectrometer. The spin echo group, i.e. the intensity as a function of the field integral, is recorded by an asymmetric scan of the field integral in one spectrometer arm for NSE and NRSE. In the case of MIEZE, the spin echo group is recorded by changing the frequency of one NRSE coil in the primary spectrometer arm, hence scanning the field integral. The spin echo point is defined for $\Delta J = 0$. With Eq. (3.55), and assuming a monochromatic beam, the intensity can be written as

$$I(\tau, \Delta J) = \frac{I_0}{2} \left(1 + \cos\left(\phi(\Delta J)\right) \int S(\boldsymbol{q}, \omega) \cos\left(\omega\tau\right) \mathrm{d}\omega \right), \tag{3.116}$$

introducing the scattering function of the system. The extra spin phase comes from the energy transfer in the scattering process, leading to a reduction of contrast/polarisation. For a finite wavelength distribution of the incoming neutron beam, Eq. (3.115) becomes

$$I(\tau, \Delta J) = \frac{I_0}{2} \left(1 + \int f(\lambda) \mathrm{d}\lambda \cos\left(\phi(\Delta J)\right) \int S(\boldsymbol{q}, \omega) \cos\left(\omega\tau\right) \mathrm{d}\omega \right). \tag{3.117}$$

The integral over the wavelength distribution envelopes the spin echo group described by the field integral. The second integral describes the physics in the sample and gives the amplitude of the oscillation, i.e. the contrast/polarisation. Fig. 3.5(a) shows the spin echo group for a monochromatic neutron beam after a purely elastic scattering process, i.e. polarisation is one. Considering a triangular shaped wavelength distribution, as it is the case for the velocity selector at RESEDA, the spin echo group for an elastic scattering process is shown in Fig. 3.5(b). The triangular wavelength distribution envelopes the spin echo group for a width of the distribution of $\Delta\lambda/\lambda = 0.12$ and 0.2, respectively.

To measure the reduction of the polarisation by the sample, the amplitude of the spin echo group must be determined. Since measuring the whole spin echo group is time consuming, the spectrometer is tuned so that the spin echo point is known precisely. The amplitude is now determined by measuring several points of one oscillation of the spin echo group around the spin echo point and fitting a sinus to these points. The frequency of the oscillation is defined by instrumental parameters and, hence, known precisely. At least four points separated by $\pi/2$ are required to determine the amplitude and phase of the oscillation, shown in Fig. 3.5(b). Kindervater *et al.* discussed the advantages of the 2-, 4- and 20-point-echo methods, finding the 4-point-echo method the most efficient for NSE and NRSE [69].

In case of the MIEZE method, where the intensity is modulated in time, a time resolved detector measures 16 points in one oscillation to obtain amplitude and phase of the oscillation. The contrast is then given by

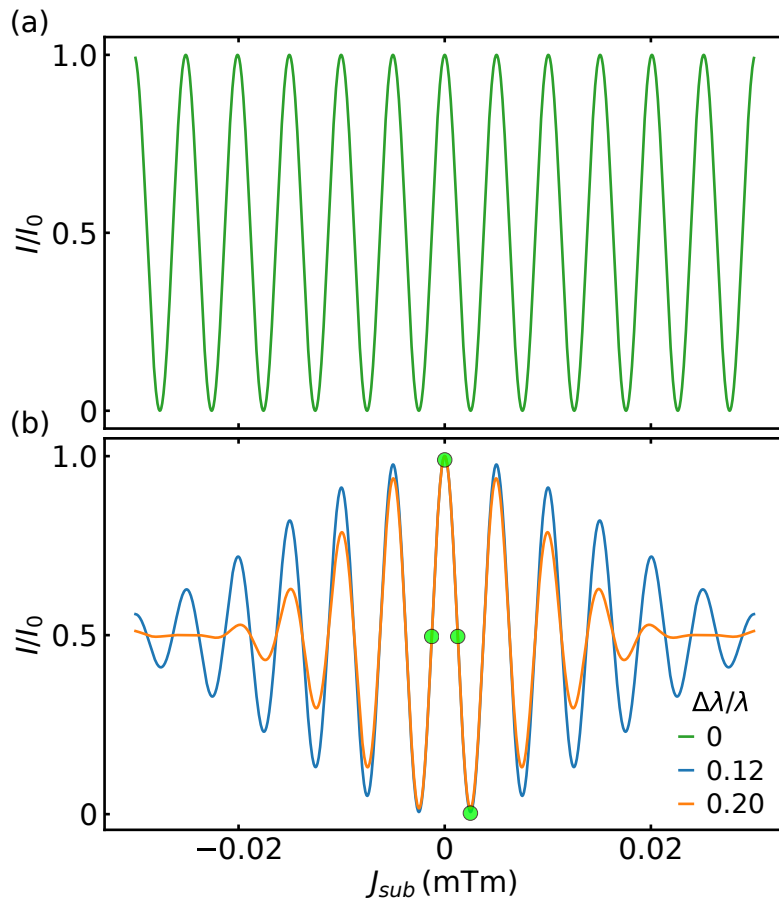$$C(\tau) = \frac{A}{B}, \tag{3.118}$$

(a)

(b)

Figure 3.5.: Modulated intensity signal for mono- and polychromatic neutron beams. (a) Spin echo group for a monochromatic neutron beam. (b) Spin echo group for a triangular shaped wavelength distribution, centred at $\lambda = 6\,\text{Å}$ with a width of the distribution of $\Delta\lambda/\lambda = 0.12$ and 0.2, respectively. Increasing the width of the wavelength distribution decreases the width of the spin echo group. The green markers are four points separated by $\pi/2$ measured during the 4-point-echo method.

where A is the amplitude of the oscillation and B the average count rate.

In most cases, the intensity in Eq. (3.117) can be seen as the intermediate scattering function $S(\boldsymbol{q}, \tau)$. It is the spatial Fourier transform of the time-dependent pair-correlation function of the scattering system, cf. Eq. (3.9) and Eq. (3.10). From the intermediate scattering function, the scattering function $S(\boldsymbol{q}, \omega)$ is obtained by the time Fourier transform in Eq. (3.11). Measuring the intermediate scattering function hence allows to directly observe the life-time of excitations in a system, as the measurement takes place in the time domain. To obtain a full spin echo data set, the intermediate scattering function, i.e. the contrast/polarisation, is measured as a function of spin echo time τ. Fig. 3.6 shows on
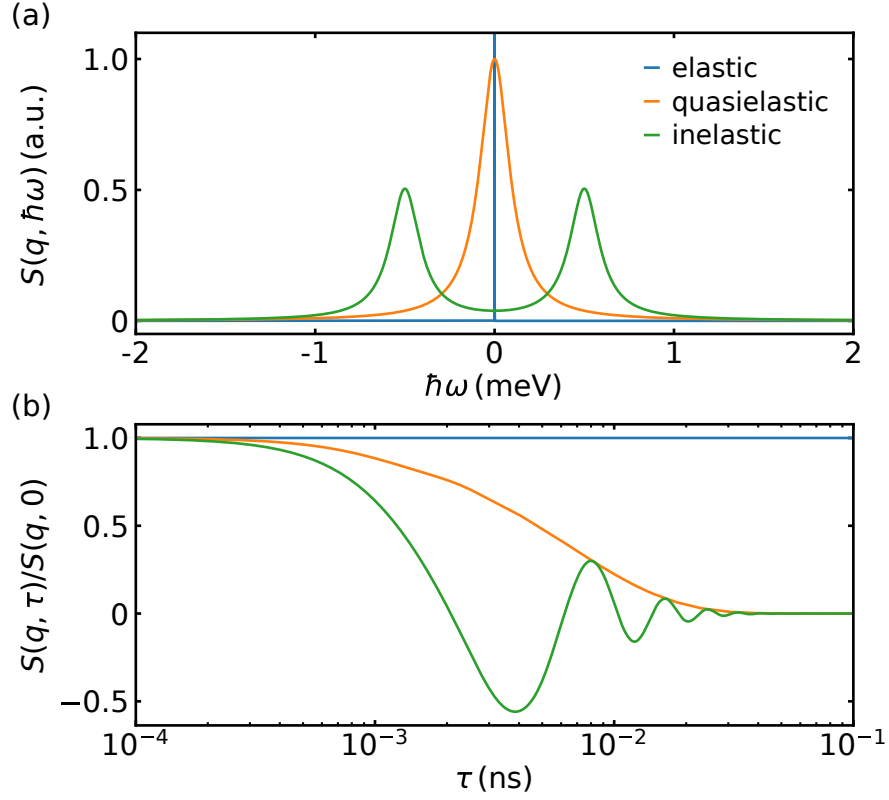
Figure 3.6.: Scattering function $S(\boldsymbol{q}, \omega)$ and intermediate scattering function $S(\boldsymbol{q}, \tau)$ for different scattering processes. (a) $S(\boldsymbol{q}, \omega)$ as function of energy transfer $\hbar\omega$ for an elastic, a quasielastic, and an inelastic scattering process. (b) $S(\boldsymbol{q}, \tau)$ as a function of Fourier time τ. The intermediate scattering function can be directly measured in neutron spin echo spectroscopy.

an example a comparison between a measurement in the energy- and time-domain for an elastic, a quasielastic, and an inelastic scattering process:

$$\text{elastic}: S(\boldsymbol{q}, \omega) \propto \delta(\omega = 0) \qquad \xleftrightarrow{\text{FT}} S(\boldsymbol{q}, \tau) \propto 1 \qquad (3.119)$$

$$\text{quasielastic}: S(\boldsymbol{q}, \omega) \propto \frac{\Gamma}{\omega^2 + \Gamma^2} \qquad \xleftrightarrow{\text{FT}} S(\boldsymbol{q}, \tau) \propto \exp\{-\Gamma\tau\} \qquad (3.120)$$

$$\text{inelastic}: S(\boldsymbol{q}, \omega) \propto \frac{\Gamma}{(\omega \pm \omega_0)^2 + \Gamma^2} \qquad \xleftrightarrow{\text{FT}} S(\boldsymbol{q}, \tau) \propto \exp\{-\Gamma\tau\} \cos(\omega_0\tau). \quad (3.121)$$

Without an energy transfer, an elastic scattering process is a delta-function at zero energy transfer in the energy-domain. In the time-domain, this becomes a constant contrast/polarisation of 1, shown as blue lines in Fig. 3.6. Quasielastic scattering shows a Lorentzian centred around zero energy transfer in the energy-domain. Its Fourier transform into the time-domain gives a single exponential decay, shown as orange lines in Fig. 3.6. In case of an inelastic scattering process, the energy-domain shows Lorentzian peaks at $\pm\omega_0 \neq 0$. This results in an oscillation damped by an exponential decay in the time-domain, shown as green lines in Fig. 3.6.

3.3.2. Spin Echo Approximation vs Explicit Calculation in MIEZE

As already mentioned in Sec. (i), the spin echo approximation in Eq. (3.98) breaks down for large energy transfers, where $\Delta v \ll v$ is not valid any more. To quantify where the spin echo approximation is still valid, the additional spin phase the neutron collects due to an energy transfer during the scattering process has to be regarded, comparing the spin echo approximation with the explicit calculation. From Eq. (3.82) and Eq. (3.98) follows the additional spin phase due to scattering with small energy transfers, i.e. $\Delta v \ll v$, to

$$\phi_{\text{approx.}} = 2 \frac{L_{\text{SD}} \hbar \omega}{m v^3} \Delta \omega. \tag{3.122}$$

Explicitly calculating the additional spin phase, i.e. using Eq. (3.110), gives

$$\phi_{\text{explicit}} = 2 L_{\text{SD}} \left(\frac{1}{v} - \frac{1}{\sqrt{\frac{2\hbar\omega}{m} + v^2}} \right) \Delta \omega. \tag{3.123}$$

Fig. 3.7 shows the difference in the spin phase as function of energy transfer for different MIEZE frequencies for the approximated and explicit calculation, respectively. The calculations are for a monochromatic neutron beam with $\lambda = 6\,\text{Å}$, which gives a neutron energy of $E_{\text{n}} = 2.27\,\text{meV}$, and a sample to detector distance of $L_{\text{SD}} = 2.25\,\text{m}$. The spin echo approximation can be used for small MIEZE frequencies. From the calculation it further becomes apparent that in the proximity of $\hbar\omega \approx 0$, the spin echo approximation is valid with $\phi_{\text{approx.}} \approx \phi_{\text{explicit}}$. The explicit calculation of the spin phase becomes important for large energy transfers, and also for increasing MIEZE frequencies.

To illustrate the importance of the explicit calculation of the spin phase, Fig. 3.8 compares the differences between spin echo approximation and explicit calculation on the example of inelastic scattering processes with energies of the excitations ranging from $0.2\,\text{meV}$ to $1.3\,\text{meV}$. The intermediate scattering function was calculated with

$$S(\boldsymbol{q}, \tau) = \int_{\lambda_0(1-\Delta\lambda/\lambda_0)}^{\lambda_0(1+\Delta\lambda/\lambda_0)} \int_{-E(\lambda)}^{\infty} f(\lambda) I(t_D) S(\boldsymbol{q}, E) \, \mathrm{d}E \, \mathrm{d}\lambda, \tag{3.124}$$

assuming a triangular wavelength distribution $f(\lambda)$ with $\lambda_0 = 6\,\text{Å}$, which gives a neutron energy of $E_{\text{n}} = 2.27\,\text{meV}$, a width of the wavelength distribution of $\Delta\lambda/\lambda_0 = 0.12$, and a sample to detector distance of $L_{\text{SD}} = 2.25\,\text{m}$. $I(t_D)$ is given by Eq. (3.87) in case of the spin echo approximation, and by Eq. (3.112) in case of the explicit calculation. Fig. 3.8(a) shows the scattering function $S(\boldsymbol{q}, \omega)$ for inelastic scattering with $\hbar\omega_q = 0.2\,\text{meV}$, $0.6\,\text{meV}$ and $1.3\,\text{meV}$ and a width of $\Gamma_q = 0.1\,\text{meV}$, $0.2\,\text{meV}$ and $0.3\,\text{meV}$, respectively. Fig. 3.8(b-d) show the intermediate scattering function $S(\boldsymbol{q}, \tau)$ for the three different inelastic scattering processes, comparing spin echo approximation and explicit calculation. For an energy
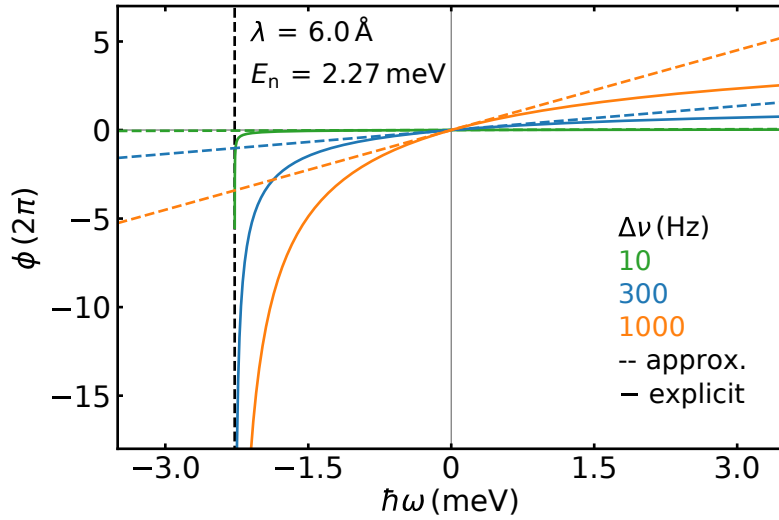
Figure 3.7.: Spin phase as function of energy transfer for different MIEZE frequencies $\Delta\nu = \nu_2 - \nu_1$. Comparison between spin echo approximation (dashed) and explicit calculation (solid) of the spin phase for MIEZE frequencies of $10\,\mathrm{Hz}$, $300\,\mathrm{Hz}$ and $1000\,\mathrm{Hz}$, respectively. The dashed vertical line shows the neutron energy of $E_\mathrm{n} = 2.27\,\mathrm{meV}$, corresponding to a wavelength of $\lambda = 6\,\mathrm{\mathring{A}}$ as used for the calculation.

transfer of $0.2\,\mathrm{meV}$, Fig. 3.8(b), approximation and explicit calculation are almost identical. For an energy transfer of $0.6\,\mathrm{meV}$, Fig. 3.8(c), the approximation already started to fail. Fig. 3.8(d) shows the case for an energy transfer of $1.3\,\mathrm{meV}$, where the energy transfer during the scattering process is in the same order of magnitude as the energy of the incoming neutron, i.e. $\Delta v \approx v$. The differences between approximation and explicit calculation are severe, showing that the explicit calculation is indispensable for large energy transfers.

3.3.3. Normalisation and Background Correction

Depolarisation effects such as imperfect tuning, field inhomogeneities, or beam divergence lead to a reduced polarisation even in the absence of a sample. At very small spin echo times, due to small frequencies, the polarisation can be further reduced due to the fail of the rotating wave approximation [70]. The polarisation obtained so far includes both, the sample contribution and the instrumental contribution

$$P_\mathrm{sample} = S(\boldsymbol{q}, \tau) P_\mathrm{res}(\boldsymbol{q}, \tau), \qquad (3.125)$$

where $P_\mathrm{res}(\boldsymbol{q}, \tau)$ is the contribution of the instrument, which can be obtained by measuring an elastic scatterer under the same conditions as the investigated sample. The dynamic

(a)

(b)

(c)

(d)
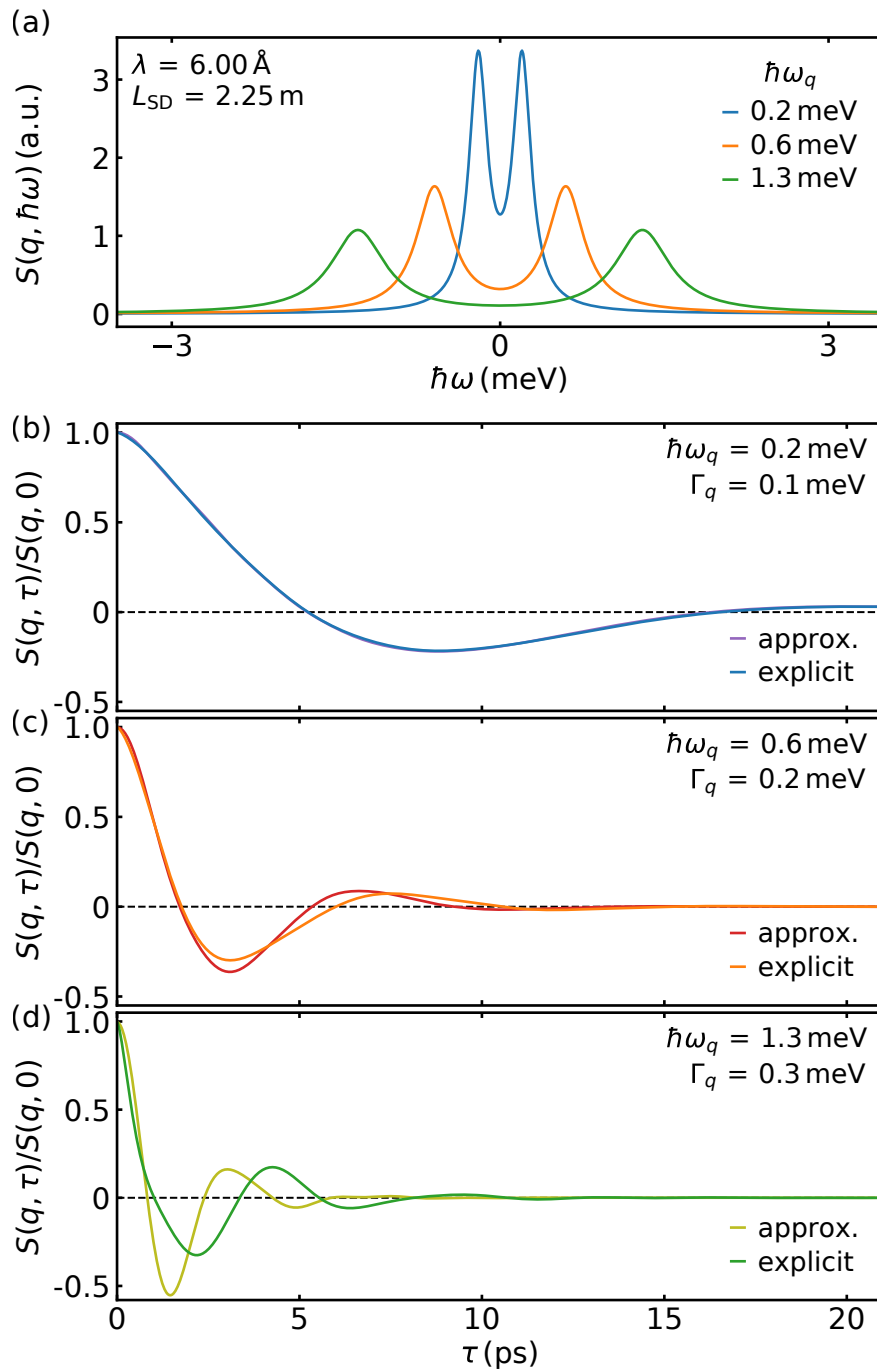
Figure 3.8.: Scattering law $S(\boldsymbol{q}, \omega)$ and intermediate scattering function $S(\boldsymbol{q}, \tau)$ for three inelastic scattering processes. For the calculation a wavelength of $6\,\text{Å}$ and a sample to detector distance of $2.25\,\text{m}$ was chosen. (a) Scattering law $S(\boldsymbol{q}, \omega)$ with $\hbar\omega_q = 0.2\,\text{meV}$, $0.6\,\text{meV}$ and $1.3\,\text{meV}$ and a width of $\Gamma_q = 0.1\,\text{meV}$, $0.2\,\text{meV}$ and $0.3\,\text{meV}$, respectively. (b-d) Intermediate scattering function $S(\boldsymbol{q}, \tau)$ for the three inelastic scattering processes in (a). $S(\boldsymbol{q}, \tau)$ is calculated with the spin echo approximation and explicitly. A comparison shows that the explicit calculation becomes indispensable for large energy transfers.

structure factor $S(\boldsymbol{q}, \omega)$ of an elastic scatterer can be assumed as a delta-function, yielding $S(\boldsymbol{q}, \tau) = 1$, reducing the measured signal to

$$P_{\text{res}} = P_{\text{res}}(\boldsymbol{q}, \tau), \tag{3.126}$$

directly giving the contribution of the instrument. Accounting for the instrumental contribution, the normalised intermediate scattering function is given by

$$\frac{S(\boldsymbol{q}, \tau)}{S(\boldsymbol{q}, 0)} = \frac{P_{\text{sample}}}{P_{\text{res}}} = \frac{A_{\text{sample}}/B_{\text{sample}}}{A_{\text{res}}/B_{\text{res}}}. \tag{3.127}$$

The instrumental background can be obtained by measuring under the same conditions without any scatterer at the sample position. The neutron beam should either be attenuated so that after the sample position the beam intensity is equal to the transmitted intensity through the sample, or the background measurement should be corrected for the transmission through the sample. Background subtraction can be performed in two ways: (i) Combining the raw counts and fitting the spin echo group after the subtraction. This only works if the phase for each spin echo time is fixed. (ii) First fitting the sample data and the background data and combining the spin echo amplitude and average counts. The statistics in the background data must be sufficient to allow fitting. This ultimately gives the background corrected and normalised intermediate scattering function to

$$\frac{S(\boldsymbol{q}, \tau)}{S(\boldsymbol{q}, 0)} = \frac{(A_{\text{sample}} - A_{\text{bg}})/(B_{\text{sample}} - B_{\text{bg}})}{(A_{\text{res}} - A_{\text{bg}})/(B_{\text{res}} - B_{\text{bg}})}. \tag{3.128}$$

Fig. 3.9 shows the contrast of one spin echo time in on an example MIEZE data set, taken just above the Curie temperature in the paramagnetic phase of iron. The instrumental resolution (a), the sample (b), and the background (c) are shown at $\tau = 0.016\,\text{ns}$. The intensity of the sample and resolution measurements are in the same order of magnitude, while the contrast of the sample at $\tau = 0.016\,\text{ns}$ has already dropped, as compared to the resolution. The background signal is smaller by three orders of magnitude. A full MIEZE data set is obtained by measuring the contrast of the instrumental background resolution, the sample, and the background at all desired spin echo times τ.

Fig. 3.10 shows the data reduction on an example MIEZE data set. The contrast was measured as described in Sec. 3.3.1 and shown in Fig. 3.9 for a set of spin echo times in a resolution sample, i.e. an elastic scatterer, and the sample. Since the instrumental background is smaller by three orders of magnitude, subtracting the background would not be necessary. Background subtraction becomes very important for samples with poor signal to noise ratios. The contrast measured in the resolution function shown in Fig. 3.10(a) is almost constant over the whole dynamic range, while the contrast measured in the sample drops to zero between $10^{-3}\,\text{ns}$ and $10^{-1}\,\text{ns}$. The normalised intermediate
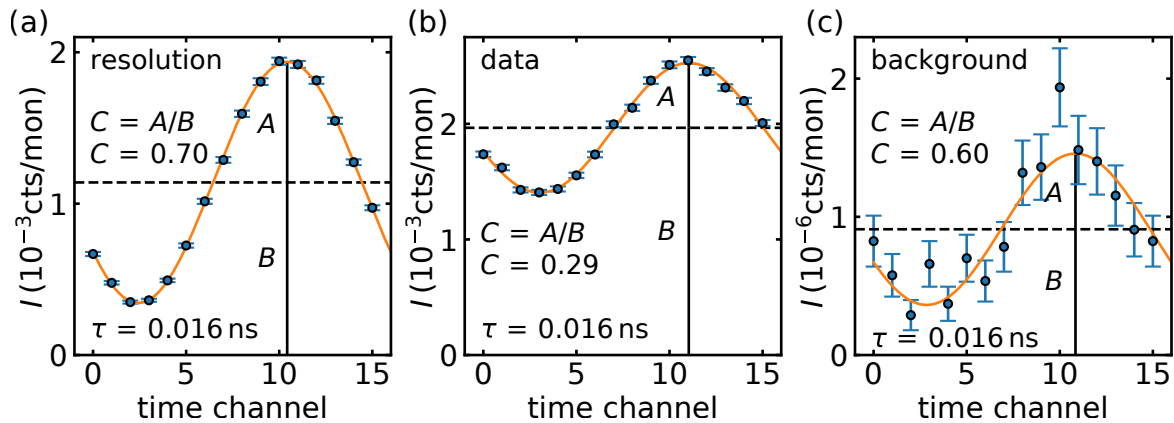
Figure 3.9.: MIEZE signal evaluated at 0.026 Å^{-1} and $\tau = 0.016 \text{ ns}$ for an example data set. The signal of the (a) resolution, (b) sample, and (c) background was measured at a detector with 16 time channels set to record one full oscillation. The solid lines are fits to the data yielding the amplitude and phase of the oscillation as well as the average count rate. The contrast C is given by the ratio of the amplitude A of the oscillation and the average count rate B of the spin echo group.

scattering function of the sample is shown in Fig. 3.10(b). The dashed line in Fig. 3.10(a) and (b) indicates the spin echo time for the example determination of the contrast shown in Fig. 3.9.

3.3.4. Grouping Pixels on a Position Sensitive Detector

A time resolved CASCADE area detector is used during MIEZE measurements, allowing the study of dynamic processes on a large range in reciprocal space. This is very important for instance for the investigation of critical scattering in the vicinity of second-order phase transitions, as the q-dependence of the inverse lifetime of the fluctuation provides important information on the critical behaviour.

As the count rate in a single pixel during one measurement can be very low, combining several pixels can be used to get meaningful statistics. Combining several pixels to one region requires that the phase of the spin echo is not varying over that region. The count rate in each pixel, or the desired region, must be large enough to allow a reliable fit to the MIEZE signal. Two types of grouping routines were used for analysing the MIEZE data. In a pre-grouping (i), the count rate of all pixels in the desired region are summed up, and then fitted. In a post-grouping (ii), each pixel is fitted separately, and all amplitudes and average counts of the pixels in the group are summed up. Both routines can be combined. In a first step, the detector is pre-grouped using a mask summing the counts of arrays of, e.g. 5×5 pixels each. The MIEZE signal is then fitted to these combined counts to extract
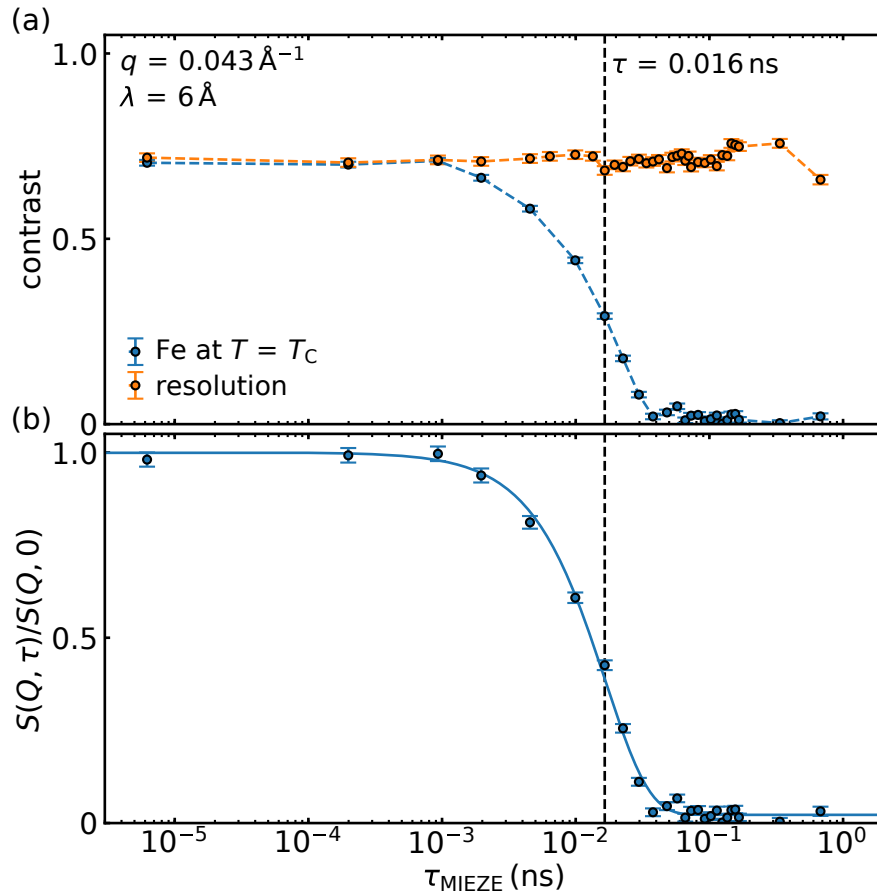
Figure 3.10.: Example reduction of a spin echo data set. (a) Contrast of the resolution measured in a graphite sample and the critical scattering from iron at T_c. Dashed lines connecting the data points are guides to the eye. Data were measured with the MIEZE set-up at RESEDA. (b) Normalised intermediate scattering function of the data from iron in (a), after subtracting the background and correcting for the instrumental resolution. The solid line is a fit to the data using an exponential decay. The vertical dashed line indicate the spin echo time for the example determination of the contrast shown in Fig. 3.9.

amplitude and average counts with sufficient statistics. Finally, amplitude and average counts are summed in areas as defined by the post-grouping. This procedure of pre- and post-grouping allows to extract the intermediate scattering function with sufficient statistics, while keeping a high MIEZE contrast. The reduction of data from area sensitive detectors using pre- and post-grouping is also discussed in Ref. [47, 71–73].

3.4. The NRSE/MIEZE Spectrometer RESEDA

High resolution spin echo measurements were performed at the REsonance Spin Echo for Diverse Applications beamline RESEDA at the Heinz Maier-Leibnitz Zentrum (MLZ) [74].

The spectrometer is operated by the Technical University of Munich (TUM) and installed at the cold neutron guide NL5-S in the neutron guide hall west of the MLZ. The neutron guide provides the instrument with a cold wavelength spectrum ranging from $3.5\,\text{Å}$ to $15\,\text{Å}$. A mechanical velocity selector at the entrance of the spectrometer allows adjusting a wavelength bandwidth of a triangular distribution with $\Delta\lambda/\lambda = 8.8-17.2\%$. The original set-up of RESEDA consisted of one primary and two identical secondary spectrometer arms, allowing to measure at two scattering vectors simultaneously [75]. This set-up employed transversal NRSE coils, i.e. the constant field in the NRSE coils is perpendicular to the neutron beam, making it necessary to shield the flight path between the NRSE coils with mu-metal to preserve the spin polarisation. In 2013/2014, the instrument was extensively reconstructed, and the transverse NRSE was replaced by longitudinal NRSE [76, 77]. This set-up was based on the demonstrations by Häußler *et al.* at the beamline IN11 of the Institute Laue-Langevin (ILL) [78–80]. There are several major advantages of longitudinal NRSE over transverse NRSE. The biggest is the self-correction of beam divergence due to the symmetrical geometry of the fields. Another major point is the possibility of using longitudinal guide fields preserving the polarisation, making the mu-metal shielding obsolete. Further, longitudinal NRSE allows field integral subtraction, making very small spin echo times accessible [80]. With implementing longitudinal NRSE, this second set-up was further upgraded with the MIEZE option [46].

In the last years, the instrument was again reconstructed to a more reliable and permanent longitudinal NRSE/MIEZE set-up. Among other developments, primary goals were to increase the dynamic range, increase the intensity at the sample position, and drastically lower the instrumental background. The following sections discuss the current state of the art at RESEDA.

3.4.1. NRSE and MIEZE Options at RESEDA

The primary spectrometer arm for both, the NRSE and MIEZE option, is identical until after the second NRSE coil. In case of MIEZE, a nose is attached to the primary spectrometer arm carrying the spin analyser and a collimator. The secondary spectrometer arms for NRSE and MIEZE, respectively, are shown in Fig. 3.11. The secondary spectrometer arm for NRSE in Fig. 3.11(a) is the mirrored primary spectrometer arm with an analyser and helium-3 detector at the end.

Fig. 3.11(b) shows the secondary spectrometer arm for the MIEZE option. Since all neutron spin manipulation is completed prior to the sample, the secondary spectrometer arm only consists of flight tubes, collimation, and the detector. For MIEZE, a detec-

tor with a very high time resolution is required. RESEDA utilises a position sensitive CASCADE detector which covers an area of $20 \times 20\,\mathrm{cm}$ with 128×128 pixels [81–83].

RESEDA can choose wavelengths between $3.5\,\text{Å} \leq \lambda \leq 15\,\text{Å}$, with a wavelength spread of $0.088 \leq \Delta\lambda/\lambda \leq 0.172$. The maximum flux is at $\lambda = 4.5\,\text{Å}$. With the current set-up, RESEDA covers a dynamic range of up to $1.8\,\mathrm{ns}$ at $6\,\text{Å}$, and a large reciprocal space of $0.01\,\text{Å}^{-1} \leq q \leq 1.8\,\text{Å}^{-1}$, whereas the strength of RESEDA is on small scattering angles $q < 0.1\,\text{Å}^{-1}$.

(a)
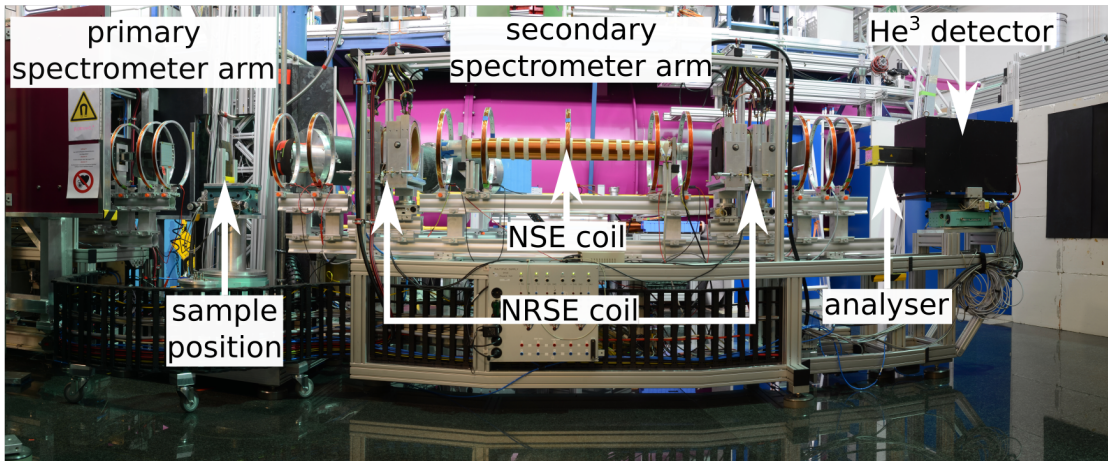
(b)
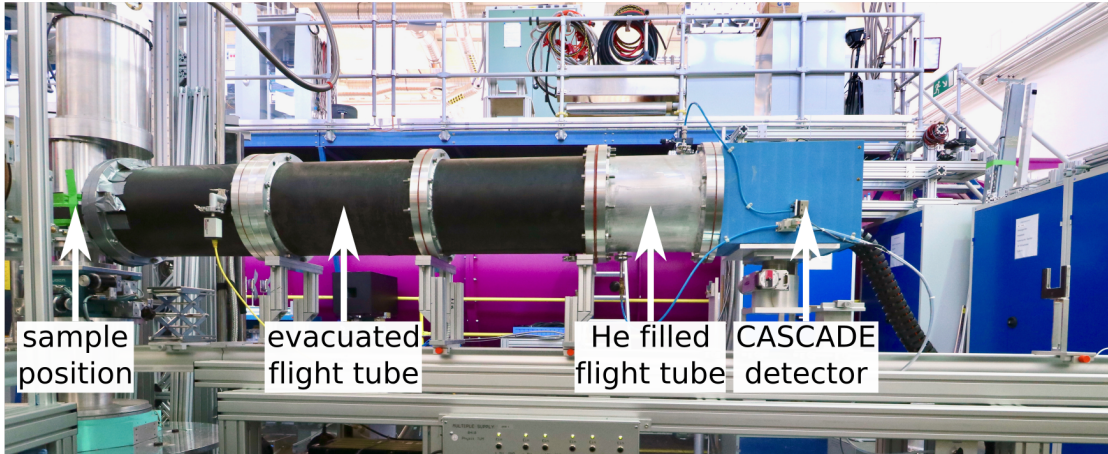
Figure 3.11.: Secondary spectrometer arms at RESEDA. (a) NRSE set-up. The secondary arm has the same components as the primary spectrometer arm, i.e. NRSE coils, NSE coils, flippers, and guide fields. The neutron spin is flipped at the end of the arm before being analysed and detected by a ^{3}He detector. (b) MIEZE set-up. Since all neutron spin manipulation is completed prior to the sample position, the secondary arm only needs the CASCADE detector. For reducing the background, the arm is equipped with an evacuated flight tube, covering most of the neutron flight path. The distance between the evacuated flight tube and the detector is flooded with helium, since a pressure difference between vacuum and detector can break the detector window.

3.4.2. RESEDA 3.0

Instrumental developments over the last decade required RESEDA to be a very flexible
construction, with parts easy replaceable and modifiable. With the establishment of the
longitudinal NRSE and MIEZE methods in the last years, RESEDA was reconstructed
as a permanent longitudinal NRSE/MIEZE instrument. Besides the technical progress,
software for instrumental control and data analysis was developed. Further, a major focus
was on the reduction of background signal.

(i). Reconstruction of the Spectrometer

In course of the reconstruction, the primary spectrometer arm and the two secondary
spectrometer arms, i.e. NRSE and MIEZE, were build up new, fitting the requirements
for NRSE and MIEZE, respectively. The new spectrometer arms now allow a reproducible
switching between NRSE and MIEZE.

Among the most recent improvements on RESEDA are new hardware components. A
new polariser at the entrance of the spectrometer now provides an increased polarisation,
a cleaner beam, and a reduced background. Further, the new polariser now allows to
use wavelengths of up to 15 Å. Compared to the old analyser, which cut off wavelengths
above 10 Å, this upgrade increases the dynamic range of the spectrometer significantly.
For the MIEZE set-up, a new transmission bender analyser was installed. Compared
to the old 5-V-cavity analyser, the transmission bender gives a higher polarisation, a
cleaner beam, and has less parasitic scattering. Both, the "stripes" on the beam profile
and a lot of parasitic scattering came from the 5-V-cavity edges of the old analyser.
Neutron guides were installed in the first spectrometer arm to increase the flux at the
sample position. The guides are evacuated and covered with sapphire windows to reduce
background. Since neutron guides increases the beam divergence, optional collimation can
be installed for studies requiring very low beam divergence. New power supplies now allow
a higher precision and better control of the neutron phase. The detector electronics for
the CASCADE, the monitor, and the ^{3}He-detector were rewired and optically decoupled,
which significantly reduced noise.

(ii). Background Reduction

In a spectrometer, where the investigated signal often becomes very small, it is of utmost
importance to reduce the background to a minimum. This is of highest priority especially
when using the MIEZE method, as a lot of parasitic scattering is scattered under small
angles, contaminating the signal.

Several studies at RESEDA showed a sample independent drop to a constant, lower than expected, contrast at about 0.01 ns, cf. Fig. 3.12. This spurious loss of contrast is more pronounced for weaker sample signal, and vanishes for very high signal to noise ratios. Both suggest that this feature is a sample independent, constant instrumental background. Fig. 3.12(a) shows this step in an example data set, i.e. $Fe_{0.175}Cr_{0.825}$ at $q = 0.032 \mathring{A}^{-1}$ for temperatures between 4 K to 100 K. In this system, the spins are expected to be frozen out in the observed dynamic range at low temperatures. Nonetheless, the measurement at 4 K drops from $\sim$0.7 to a contrast of $\sim$0.2. The resolution measurement on a graphite sample does not show the step, which is due to the much better signal to noise ratio as compared to the Fe_xCr_{1-x} sample. Therefore, correcting for instrumental resolution with a resolution sample is not possible. This can be seen in Fig. 3.12(b), where the intermediate scattering function, obtained by using the graphite measurement as instrumental resolution, still shows the pronounced step. Correcting for the instrumental resolution by measuring the same sample in a static state, i.e. where the dynamics are frozen, allows to correct also for the spurious loss of contrast. However, this kind of resolution correction is only possible in samples which become static at a temperature accessible during the measurements.

There are several possible causes for background and, especially, for the spurious loss of contrast. Components in the neutron beam lead to parasitic background scattering in the small angle regime. In contrast to a dedicated SANS instrument, where almost nothing is in the neutron beam, a NRSE spectrometer has to have key components placed in the neutron flight path, i.e. NRSE coils, spin flippers, and spin analyser. The contribution to the background of some of these components was investigated at SANS-1 at MLZ [84], showing only a reasonable contribution to the background. Another major cause for background is air scattering. The above mentioned step in the MIEZE measurements is not a loss of contrast over the full dynamic range, but only from a certain point on. This leads to the assumption that the background causing this feature is dynamic, and the most probable cause is air humidity.

To reduce the background, parasitic scattering from instrument components and air, which is scattered out of the neutron beam flight path, is removed by a set of apertures throughout the primary spectrometer arm. Air scattering is drastically reduced by evacuating the neutron guides. A flight tube on the secondary spectrometer arm allows to evacuate the space between sample and detector. It was found that already a few centimetres of air hit by the direct beam between the exit of the flight tube and the entrance of the detector cause a huge background. Therefore, flight tube and detector were connected, and the space between them filled with helium at atmospheric pressure. It is not possible to evacuate this space, since the window of the detector is very thin and might break under pressure.
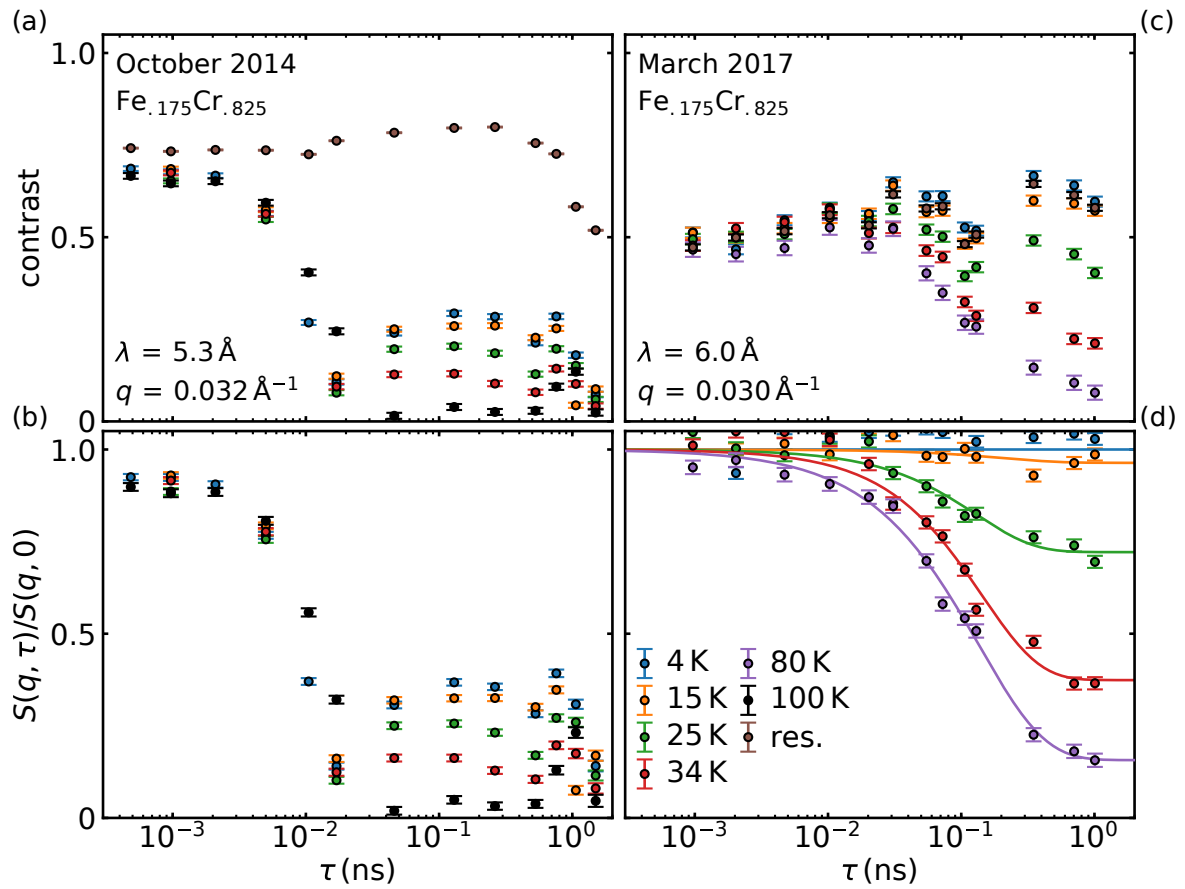
Figure 3.12.: Comparison of spin echo curves before and after the reduction of the instrumental background. (a) Data taken in October 2014, before reducing the background of the instrument. Spurious background signal leading to a step in the spin echo curve of the data at $\sim 10^{-2}\,\mathrm{ns}$. Due to a much higher signal to noise ratio, the resolution (brown) shows the tuned contrast. At low temperatures, i.e. at $4\,\mathrm{K}$, the spins in $\mathrm{Fe}_x\mathrm{Cr}_{1-x}$ are expected to be frozen out and, therefore, the spin echo curve at this temperature should lie on top of the resolution measurement. (b) Data in (a) corrected for instrumental resolution by measuring a graphite standard sample, not allowing to correct for the spurious loss of contrast. (c) Data taken in March 2017, after reducing the background of the instrument significantly. The spurious background is gone and no step in the spin echo signal is observed. As expected, the low temperature measurement lies on top of the resolution measurement. (d) Data in (c) corrected for instrumental resolution by measuring a graphite standard sample. Solid lines are fits to the data using an exponential decay.

Further, a very strong direct beam hitting the detector leads to false signal readouts of the detector close to pixels with very high count rates. Therefore, each experiment uses an individual beam stop placed close to the detector, blocking the direct beam and simultaneously allowing to investigate under very small scattering angles.

(iii). Software

The IGOR Pro software for data analysis was completely rewritten in Python. The improved code is now more transparent and much faster. It allows to visualise each step of the complex data treatment process. New data fitting options were implemented, including the explicit calculation of the spin phase, cf. Sec. 3.3.2. Another feature is summing of CASCADE detector foils during MIEZE, tremendously increasing the intensity [85, 86].

Parallel to the IGOR Pro instrument control software, the Python based NICOS instrument control was implemented. This upgrade significantly improves RESEDA as it allows for a more reliable control of the instrument. In NICOS, a simultaneous control of multiple devices is possible, resulting in a significant saving of time during measurements. Further, monitoring of instrumental device statuses and live feeds of data collection is possible. Moreover, NICOS is supported by the FRM II instrument control software group.

4. Magnetic Phase Diagram of Yb$_2$Ti$_2$O$_7$

The magnetic pyrochlore oxide Yb$_2$Ti$_2$O$_7$ received a lot of attention in recent years, as strong transverse quantum fluctuations significantly influence the system, and since the nature of its ground state is still under debate to host a spin-liquid quantum state at low temperatures [28, 37, 38]. This chapter discusses the orientation dependence of the magnetic phase diagram of Yb$_2$Ti$_2$O$_7$, inferred from magnetometry down to millikelvin temperatures, and further addresses the question of the ground state of Yb$_2$Ti$_2$O$_7$. The magnetic phase diagram for applied magnetic field shows an unusual field dependence of a first-order phase boundary, notably an applied field initially increases the ordering temperature when applied parallel to the crystalline $\langle 111 \rangle$ or $\langle 110 \rangle$ axes. This unusual field dependence is absent for field along $\langle 100 \rangle$. Further, a theoretical model describing the low-temperature magnetisation data was proposed by Tchernyshyov and collaborators at Johns Hopkins University in Baltimore. An introduction to the materials class of magnetic pyrochlore oxides, in particular Yb$_2$Ti$_2$O$_7$, in Sec. 4.1, is followed by a brief description of the Potts model describing cubic ferromagnets in Sec. 4.2. The experimental set-up and the experimental results are presented in Sec. 4.3 and Sec. 4.4, respectively. The chapter concludes with a summary of the present study and an outlook, cf. Sec. 4.5.

4.1. Geometric Frustration in Pyrochlore Systems

The magnetism of pyrochlore oxides often shows unconventional behaviour connected to geometric frustration [31, 87]. Pyrochlore oxides are described by the chemical formula A$_2$B$_2$O$_7$, where the A site is occupied by a magnetic rare-earth ion and the B site by a non-magnetic transition metal. The sites A and B form each a sub-lattice of corner sharing tetrahedra, inter-penetrating each other. Pyrochlore oxides crystallise in the face-centred cubic (fcc) structure with $Fd\bar{3}m$ symmetry, i.e. space group number 227, illustrated in Fig. 4.1.

In the following Sec. 4.1.1, the concept of frustration will be introduced. The realisation of a geometrical frustrated system in the family of rare-earth pyrochlore oxides will be

(a)

(b)

rare-earth
ion

transition
metal
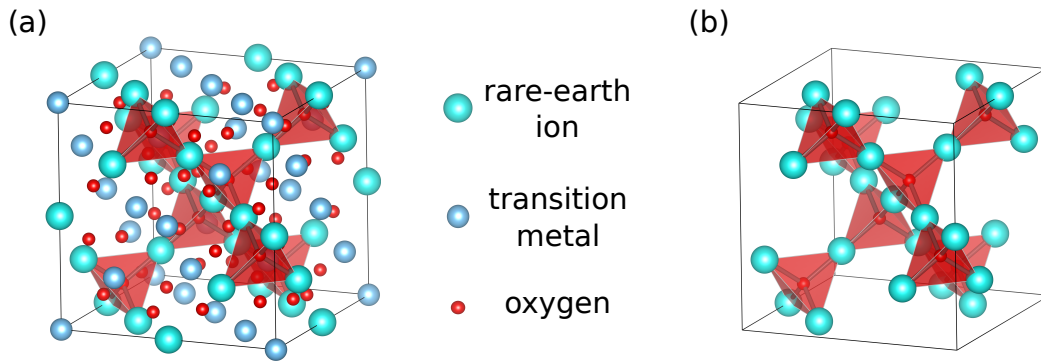
oxygen

Figure 4.1.: Unit cell of the pyrochlore structure with chemical formula A$_2$B$_2$O$_7$. (a) All atoms in the unit cell. The A site (green) is occupied by a magnetic rare-earth ion, and the B site (blue) by a non-magnetic transition metal. The oxygen atoms are shown in red. A and B form each a sub-lattice of corner-sharing tetrahedra, inter-penetrating each other. (b) Atoms in the unit cell reduced to the magnetic ions. The magnetic behaviour of rare-earth pyrochlore oxides is governed by the magnetic ion and the crystal electric field of the oxygen in the centre of the tetrahedra.

presented, thereby addressing the exotic properties emerging in spin-ice, cf. Sec. 4.1.2, and quantum spin-ice, cf. Sec. 4.1.3. Sec. 4.1.4 summarises the current state of research in Yb$_2$Ti$_2$O$_7$, focussing on the debate about the nature of its ground state.

4.1.1. Forms of Frustration Effects

At low temperatures, magnetic materials typically develop long-range order, such as ferromagnetic, ferrimagnetic, and/or antiferromagnetic order [88, 89]. In frustrated magnetic systems, however, material-specific properties prevent the simultaneous satisfaction of all interactions, leaving the system in a highly degenerate state. Frustration originates from two primary causes: frustration of interactions, also known as random frustration, and geometrical frustration.

An example for the first case are diluted spin-glasses, such as Au$_{1-x}$Fe$_x$ or Cu$_{1-x}$Mn$_x$ [90, 91], where the random distribution of the magnetic ions leads to a competition between ferromagnetic and antiferromagnetic interactions due to the oscillatory RKKY-interactions (Ruderman-Kittel-Kasuya-Yosida) between the Fe and Mn atoms, respectively [27, 92]. Random frustration will be addressed later in Ch. 6 in the context of spin-glasses.

In contrast, in geometrically frustrated systems, the structure of the lattice precludes

simultaneous satisfaction of the magnetic interactions. Regarding the classical isotropic nearest-neighbour Heisenberg exchange Hamiltonian given by

$$\mathcal{H} = -J \sum_{\langle ij \rangle} \boldsymbol{S}_i \cdot \boldsymbol{S}_j. \tag{4.1}$$

The model with 1, 2, and 3 components of the spin $\boldsymbol{S}$ corresponds to the Ising, XY, and Heisenberg model, respectively. The nearest-neighbour exchange constant is $J > 0$ for ferromagnetic interactions and $J < 0$ for antiferromagnetic interactions. Fig. 4.2(a) shows Ising spins, i.e. spins that can only be in one of two states, up and down, with nearest-neighbour ferromagnetic interactions on the corners of a two dimensional triangular lattice. In this case, all interactions are satisfied simultaneously. An important example for geometric frustration is shown in Fig. 4.2(b), where the Ising spins are interacting with a nearest-neighbour antiferromagnetic exchange on the same triangular lattice. If one antiferromagnetic interaction is satisfied with two spins anti-parallel, it is impossible for the third spin to satisfy both antiferromagnetic bonds with its two neighbours. This concept was first introduced by Wannier in 1950 describing that, in case of antiferromagnetic interactions on a two dimensional triangular Ising net, no transition into a magnetically ordered state is predicted down to lowest temperatures, due to geometric frustration [93, 94]. The degree of frustration in magnetic systems may be measured in terms of the ratio

$$f = \frac{|\theta_{\mathrm{CW}}|}{T^{\star}}, \tag{4.2}$$

with the Curie-Weiss temperature θ_{CW}, characterising the nature and strength of the magnetic interactions, and $T^{\star}$ being the transition temperature to an ordered or glassy state [95]. Strong geometrical frustrated systems show $f > 10$ [95].

In three dimensions, geometric frustration may be realised by magnetic moments on the corners of a tetrahedron, as shown in Fig. 4.2(c) and (d). An antiferromagnetic interaction between the spins, cf. Fig. 4.2(c), leads to frustration, since it is not possible to arrange the spins in a way all interactions are satisfied. The absence of long-range magnetic order in three dimensions was first reported by Anderson in 1956 in an Ising pyrochlore antiferromagnet [96]. In 1979, Villain observed the absence of long-range order in the Heisenberg pyrochlore antiferromagnet [97]. Mean field theory [98], Monte Carlo simulation [99], and numerical studies [100, 101] confirmed the absence of long-range order in the studies of Anderson [96] and Villain [97].

In a system with ferromagnetic nearest-neighbour interactions, as it is the case shown in Fig. 4.2(d), geometric frustration is possible when the spins are arranged in a non-collinear way, when the spins directly point either towards or away from the centre of the tetrahedron. This is the case in rare-earth pyrochlore oxides, where long-range dipolar
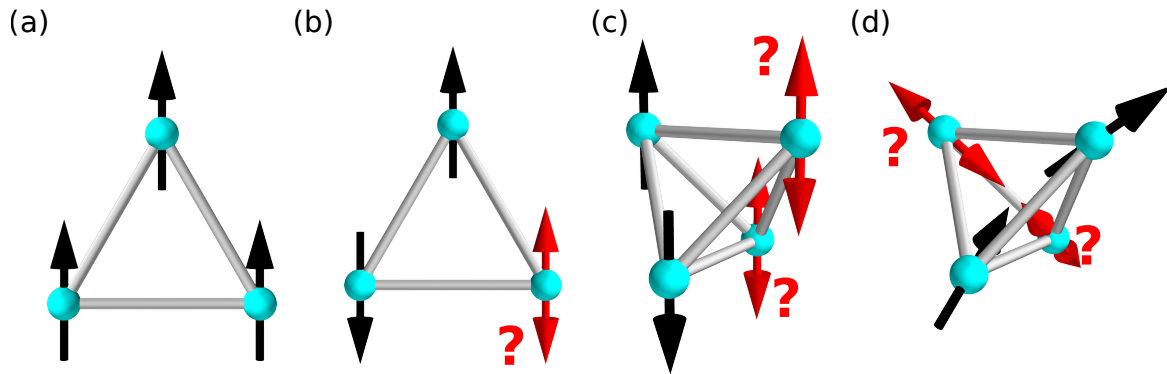
Figure 4.2.: Illustration of geometrical frustration in two and three dimensions. (a) Ferromagnetic nearest-neighbour interactions between spins on a two dimensional triangular lattice does not lead to frustration. Anti-ferromagnetic nearest-neighbour interactions between spins on a two dimensional triangular lattice (b) and on a three dimensional tetrahedron (c) frustrate the system. The system shown in (d), where the spins point either towards or away from the centre of the tetrahedron, frustrates for ferromagnetic nearest-neighbour interactions.

interactions lead to ferromagnetic coupling, and strong local $\langle 111 \rangle$-Ising anisotropy arranges the spins [28]. On a pyrochlore lattice with cubic symmetry, the Ising and XY models are only physically sensible, when a local Ising direction z_i or local XY plane normal to z_i parallel to a local $\langle 111 \rangle$ is regarded.

The ground state of frustrated systems is highly degenerate and no magnetic order is predicted down to absolute zero temperature, leading to a residual entropy. This violates the third law of thermodynamics, and the system eventually must find a ground state. In this case, perturbative interactions lead to the development of order out of the spin-liquid state [28]. The magnetic ground state of the pyrochlore oxides is therefore governed by the nature of the exchange interactions between the nearest-neighbour and further neighbour spins, the character of the spin anisotropy, dipolar interactions, and anisotropic exchange. These numerous physical aspects influencing the nature of the ground state might lead to quantum spin fluctuations and unconventional exotic magnetic phases such as spin-glasses [102], classical [30, 31, 33] and quantum spin-ices [37, 103], or quantum spin-liquids [29, 38].

4.1.2. Classical Spin Ice

The most prominent example among the pyrochlore oxides is classical spin-ice first identified in Ho$_2$Ti$_2$O$_7$ and Dy$_2$Ti$_2$O$_7$ [30–34]. The spins in these systems can be described as Ising-like along the local $\langle 111 \rangle$ due to strong crystal electric fields, giving rise to a strong magnetic anisotropy. To describe the interactions in the classical nearest-neighbour spin-

ice model (CSI), Eq. (4.1) further includes easy axis anisotropy, and the Hamiltonian reads as

$$\mathcal{H}_{\mathrm{CSI}} = -J_{zz} \sum_{\langle ij \rangle} \boldsymbol{S}_i^z \cdot \boldsymbol{S}_j^z - \Delta \sum_{K,\kappa} \left(\boldsymbol{\delta}_\kappa \cdot \boldsymbol{S}_{K,\kappa} \right)^2 , \qquad (4.3)$$

where Δ is the strength of the easy axis anisotropy. The easy axes $\boldsymbol{\delta}_\kappa$, with κ running over the number of easy axes directions, i.e. four in case of a local $\langle 111 \rangle$ symmetry, and the spin on the corner κ of the tetrahedron K is given by $\boldsymbol{S}_{K,\kappa}$.

Compared to an antiferromagnetic nearest-neighbour Heisenberg exchange coupling on the pyrochlore lattice, cf. Eq. (4.1) and Fig. 4.2(b), which leads to frustration [96], an antiferromagnetic nearest-neighbour exchange in the case of the classical spin-ice model leads to an ordered ground state [104, 105]. This ground state is two-fold degenerate, with either all four spins pointing in or out of one tetrahedron (all-in/all-out) as depicted in Fig. 4.3(a). The frustration in the classical spin-ice model arises from nearest-neighbour ferromagnetic interactions, cf. Fig. 4.2(d). The ferromagnetic exchange energy is minimised when two spins point in and two spins point out of one tetrahedron (two-in/two-out), as shown schematically on two adjacent tetrahedra in Fig. 4.3(b). Even though there are six equivalent spin configurations fulfilling the two-in/two-out constraint in a single tetrahedron, there is an infinite number of ground states for a macroscopic sample, resulting in a ground state residual entropy.

The similarity of the spin configuration to the proton structure in water ice, which is also degenerate and shows a high residual entropy [106–108], gives the spin-ice its name.
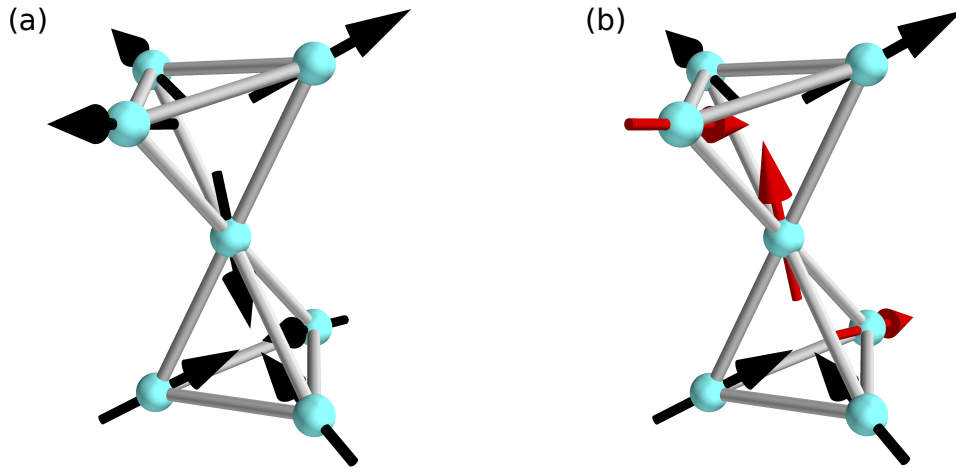
Figure 4.3.: Ground state in the classical spin-ice model on the pyrochlore lattice, where strong Ising anisotropy force spins on local $\langle 111 \rangle$-axes. (a) Antiferromagnetic nearest-neighbour exchange leads to an all-in/all-out ground state. (b) For ferromagnetic nearest-neighbour exchange, the magnetic moments obey the two-in/two-out spin-ice constraint.

$Ho_2Ti_2O_7$ and $Dy_2Ti_2O_7$ both have pre-dominant ferromagnetic interactions, in agreement with a positive Curie-Weiss temperature θ_{CW} of $1.9\,K$ [30] and $0.5\,K$ [32], respectively, and classical spins with a strong Ising anisotropy. According to Eq. (4.3), ferromagnetic interactions and a strong Ising anisotropy lead to the spin-ice configuration. However, trivalent rare-earth ions possess a large magnetic moment resulting in dipolar interactions being relatively strong compared to the weak exchange interactions inferred from the Curie-Weiss temperature. Including dipolar interactions, the classical spin-ice Hamiltonian in Eq. (4.3) is written as

$$\mathcal{H}_{DSIM} = -J_{zz} \sum_{\langle ij \rangle} \boldsymbol{S}_i^{z_i} \cdot \boldsymbol{S}_j^{z_j} + Dr_{nn}^3 \sum_{j>i} \frac{\boldsymbol{S}_i^{z_i} \cdot \boldsymbol{S}_j^{z_j}}{|\boldsymbol{r}_{ij}|^3} - \frac{3(\boldsymbol{S}_i^{z_i} \cdot \boldsymbol{r}_{ij})(\boldsymbol{S}_j^{z_j} \cdot \boldsymbol{r}_{ij})}{|\boldsymbol{r}_{ij}|^5}, \qquad (4.4)$$

with the dipole energy scale $D = (\mu_0/4\pi)g^2\mu^2/r_{nn}^3$, and the distance between nearest-neighbours r_{nn}. The nearest-neighbour exchange energy is given by $J_{nn} = J/3$, and the nearest-neighbour dipole-dipole interaction by $D_{nn} = 5D/3$. For $Ho_2Ti_2O_7$ and $Dy_2Ti_2O_7$ the constants are $J_{nn} \sim -1.2\,K$ and $D_{nn} \sim 2.35\,K$ [104, 105]. Given that, the nearest-neighbour exchange is antiferromagnetic, and the nearest-neighbour dipole-dipole interaction is ferromagnetic. If the antiferromagnetic exchange dominates, the system undergoes a phase transition into an all-in/all-out ground state, cf. Fig. 4.3(a). For a dominating ferromagnetic exchange, however, the system displays a spin-ice state, cf. Fig. 4.3(b). A critical value of $J_{nn}/D_{nn} \sim -0.9$ between the all-in/all-out and the spin-ice state was determined by mean-field theory and Monte Carlo simulations [109, 110]. Therefore, both $Ho_2Ti_2O_7$ and $Dy_2Ti_2O_7$ are spin-ices with a two-in/two-out ground state and may be described by the dipolar spin-ice model (DSIM) in Eq. (4.4).

Excitations in spin-ice were first introduced by Ryzhkin as quasiparticle-like [111]. In 2008, Castelnovo *et al.* described excitations above the ground-state manifold in spin-ices as magnetic monopoles with Coulomb interactions between them [35]. Such an excitation is obtained when flipping one spin on the pyrochlore lattice, locally violating the two-in/two-out ice rule in Fig. 4.3(b). The spin flip generates a three-in/one-out state in one tetrahedron, and a one-in/three-out state in the adjoining tetrahedron, as shown in Fig. 4.4(a). If each spin is seen as a pair of opposite magnetic charges, such a spin flip generates a monopoles-antimonopole pair in the two adjacent tetrahedra. Once created, the two monopoles can diffuse through the magnetic sub-lattice away from each other by flipping the spins on their way. This creates a ferromagnetic chain of spins connecting the pair of separated monopoles shown in Fig. 4.4(b), which is known as a Dirac string [35, 36].

Exciting monopoles in spin-ices is achieved by applying a magnetic field along a $\langle 111 \rangle$ crystallographic direction. A field along $\langle 111 \rangle$ first partially magnetises the system, retaining the two-in/two-out ground state. Increasing the field further breaks the ice rule,
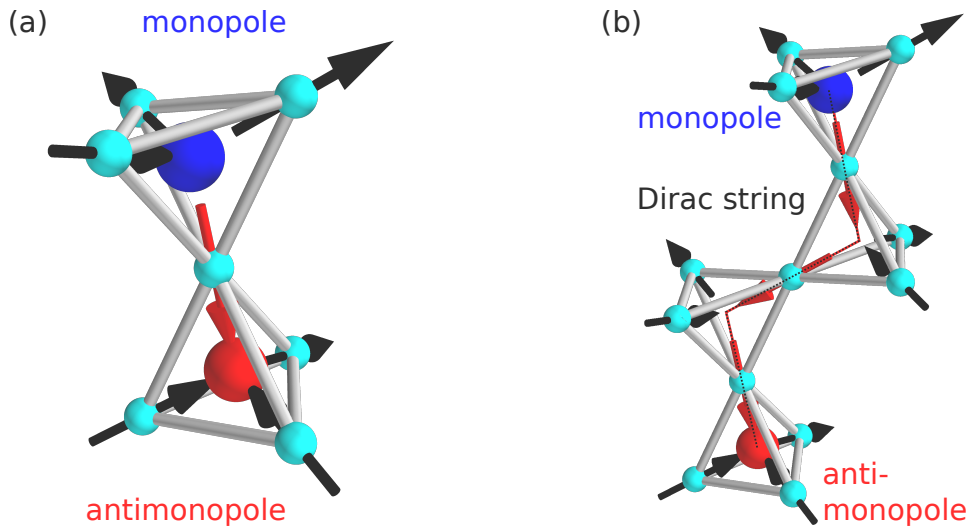
Figure 4.4.: Magnetic monopoles in spin-ice. (a) A spin flip violates the two-in/two-out spin-ice constraint, creating a monopole-antimonopole pair. (b) The two monopoles can diffuse through the lattice by additional flipping of spins, generating a chain of inverted spins known as Dirac string.

flipping one spin to the three-in/one-out (one-in/three-out) state in all tetrahedra. This spin flips may be viewed as the condensation of emergent magnetic monopoles [35, 61, 111], what may explain the first-order phase transition for field along $\langle 111 \rangle$ found in $Dy_2Ti_2O_7$ by Sakakibara *et al.* [112], and later in $Ho_2Ti_2O_7$ by Krey *et al.* [61].

4.1.3. Quantum Spin Liquid and Quantum Spin Ice

In a spin-liquid state the spins are highly correlated due to interactions between them, but do not order at very low or even zero temperature [38]. In classical spin-ice, as discussed in the previous section, the frustration of the magnetic moments give rise to a classical spin-liquid with Coulombic interactions and emergent electrostatic charges, the magnetic monopoles [35, 36, 113]. By lowering the temperature, the spins in classical spin-ice freeze at some finite temperature. This is due to the energy barrier between the different spin-ice states, which can not be overcome by the weak quantum effects [29, 34].

A quantum spin-liquid (QSL), on the other hand, is a state of matter where quantum fluctuations prevent the spins from entering a phase with magnetic long-range order even at zero temperature [37]. If quantum fluctuations perturbing a spin-ice state, the ground state is a quantum spin-liquid with a $U(1)$ gauge symmetry, and the same properties as the classical spin-ice, i.e. Ising anisotropy along the local $\langle 111 \rangle$ directions, fulfilling the ice rule constraint two-in/two-out [37, 114]. This state of matter is called quantum spin-ice (QSI).

The ice rule constraint two-in/two-out is equivalent to stating that a spin field $\boldsymbol{B}$ is divergence-free on each tetrahedron: $\nabla \cdot \boldsymbol{B} = 0$. This divergence-free constraint can be viewed as an emergent gauge invariance $\boldsymbol{B} = \nabla \times \boldsymbol{A}$, with a vector potential $\boldsymbol{A}$ that leaves the divergent free condition invariant. Spin flips out of the spin-ice manifold break this divergent free condition and create a field source of magnetic charges that interact with the emergent electromagnetic field [37]. Hence, these charges behave like particles of light [37].

To describe quantum spin-ice, the classical nearest-neighbour spin-ice model in Eq. (4.3) could be extended by transverse nearest-neighbour exchange couplings, in addition to the longitudinal Ising exchange. This gives a minimal model for a quantum spin-ice, containing quantum dynamics within the spin-ice and reads as

$$
\begin{aligned}
\mathcal{H}_{\mathrm{QSI}} &= \mathcal{H}_{\mathrm{CSI}} + \mathcal{H}_{\perp} \\
&= \mathcal{H}_{\mathrm{CSI}} - J_{\pm} \sum_{\langle ij \rangle} \left(S_i^+ S_j^- + S_i^- S_j^+ \right),
\end{aligned} \tag{4.5}
$$

with $J_{\pm} \ll J_{zz}$, so that the ice rule is obeyed with spins slightly canted away from the local $\langle 111 \rangle$ direction. The $J_{\pm}$ is a perturbation of the classical spin-ice ground state, lifting the degeneracy of the classical spin-ice.

The hierarchy of energy scales in rare-earth pyrochlore oxides make them ideal candidates for quantum spin-ice behaviour. In such materials the spin-orbit coupling is stronger than the crystal electric field, hence the ground state is well protected, and the spin is highly anisotropic. Further, the ground states often are well-isolated low-energy doublets where the spin dynamics may be reduced to that of spin-1/2 moments [37]. Especially for odd-numbered electron ions, i.e. Kramers, the ground state is very robust, and other nearest-neighbour couplings lead to strong quantum effects [37]. Therefore, the low-temperature properties can be described by an effective pseudospin-1/2 Hamiltonian including all the symmetry-allowed nearest-neighbour couplings. The most general nearest-neighbour symmetry-allowed anisotropic Hamiltonian on the pyrochlore lattice is then given by [37, 103]

$$
\begin{aligned}
\mathcal{H}_{\mathrm{eff}, \frac{1}{2}} = \sum_{\langle ij \rangle} \Big\{ &J_{zz} S_i^z S_j^z - J_{\pm} \left(S_i^+ S_j^- + S_i^- S_j^+ \right) \\
&+ J_{\pm\pm} \left(\gamma_{ij} S_i^+ S_j^+ + \gamma_{ij}^* S_i^- S_j^- \right) \\
&+ J_{z\pm} \left(S_i^z \left(\zeta_{ij} S_j^+ + \zeta_{ij}^* S_j^- \right) + i \leftrightarrow j \right) \Big\},
\end{aligned} \tag{4.6}
$$

where $\langle ij \rangle$ describes the nearest-neighbour sites of the pyrochlore lattice, γ_{ij} is a 4×4 complex unimodular matrix, with $\zeta = -\gamma^*$, describing the cubic rotations and local bases of the pyrochlore lattice [103]. The first term, proportional to J_{zz}, describes the classical

Ising spin-ice. The other terms, i.e. $J_\pm$, $J_{\pm\pm}$, and $J_{z\pm}$, are additional nearest-neighbour terms allowed by the symmetry on the pyrochlore lattice, that do not commute with the classical spin-ice term and, hence, lead to quantum dynamics within the classical spin-ice [37]. Discussing the physical origin, besides the Ising term, the other three nearest-neighbour interactions can be seen as follows [37, 115, 116]: $J_\pm$ as isotropic interactions of the form $J_{\mathrm{iso}}\boldsymbol{S}_i \cdot \boldsymbol{S}_j$, $J_{\pm\pm}$ as pseudo-dipolar exchange interactions $J_{\mathrm{pd}}(\boldsymbol{S}_i \cdot \boldsymbol{S}_j - 3\boldsymbol{S}_i \cdot \hat{\boldsymbol{r}}_{ij}\hat{\boldsymbol{r}}_{ij} \cdot \boldsymbol{S}_j)$, and $J_{z\pm}$ as Dzyaloshinskii-Moriya interactions $J_{\mathrm{DM}}(\hat{\boldsymbol{d}}_{ij} \cdot \boldsymbol{S}_i \times \boldsymbol{S}_j)$.

The effective pseudospin-1/2 Hamiltonian in Eq. (4.6) was analysed by means of gauge mean-field theory (gMFT), and the zero temperature phase diagram was computed for systems with Kramers ions [117] and non-Kramers ions [118]. Fig. 4.5(a) shows the calculated phase diagram for Kramers ions in the space of nearest-neighbour couplings, where phases emerge from the classical spin-ice point at $J_\pm = 0$ and $J_{z\pm} = 0$. The quantum spin-liquid appears from perturbation theory in the vicinity of the classical spin-ice point at the origin of the phase diagram. The Coulomb ferromagnetic phase (CFM) shows dipolar ferromagnetic long-range order and displays the same excitations as in the quantum spin-ice. The two other phases show ferromagnetic (FM) and antiferromagnetic (AFM) long-range order, where the states are six-fold degenerate with net moments along one of the $\langle 100 \rangle$ directions for the ferromagnetic state, and moments perpendicular to the local $\langle 111 \rangle$ directions for the antiferromagnetic state. It becomes apparent that for $J_\pm$ being the leading perturbation with $J_\pm \ll J_{zz}$, and being sufficiently larger than $J_{\pm\pm}$ and $J_{z\pm}$, there is a region where the quantum spin-liquid is predicted [37, 114, 117–119]. It should
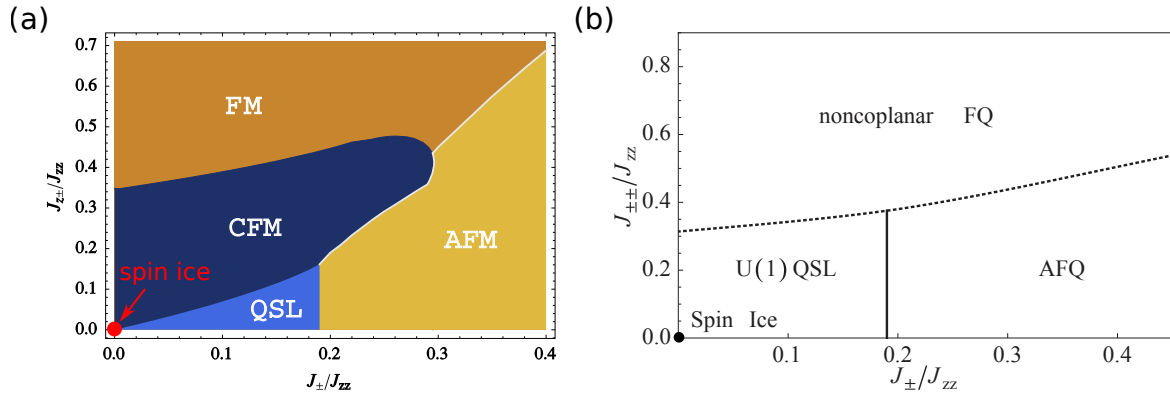
Figure 4.5.: Gauge mean-field phase diagram in the exchange parameter space of the Hamiltonian in Eq. (4.6). (a) For Kramers ions with $J_{\pm\pm} = 0$. The phases are a quantum spin-liquid (QSL), a Coulomb ferromagnet (CFM), a standard ferromagnet (FM), and a standard antiferromagnet (AFM). The classical spin-ice point is at $J_\pm = 0$ and $J_{z\pm} = 0$. Figure taken from Ref. [117]. (b) For non-Kramers ions with $J_{z\pm} = 0$. The phases are a quantum spin-liquid and two quadrupolar phases (FQ and AFQ). The classical spin-ice point is at $J_{\pm\pm} = 0$ and $J_\pm = 0$. Figure taken from Ref. [118].

be noted that Savary and Balents also addressed the finite temperature phase diagram, which will not be discussed here [119]. In case of non-Kramers ions, cf. Fig. 4.5(b), besides the quantum spin-liquid, there exist a long-range ordered ferroquadrupolar (FQ) phase, and a long-range ordered antiferroquadrupolar (AFQ) phase.

Among the pyrochlore oxides, quantum spin-ice candidates are systems with Kramers ions, such as $Yb_2Ti_2O_7$, or with even-numbered electron ions, i.e. non-Kramers, such as $Tb_2Ti_2O_7$, and a magnetic ground state doublet [103, 120–124]. In a pyrochlore oxide with a weaker rare earth moment as compared to $Ho_2Ti_2O_7$ and $Dy_2Ti_2O_7$, dipolar interactions become less important and, as a consequence, exchange interactions become more important. The spin anisotropy, derived from the crystal electric field effects and the hierarchy of energy scales in the pyrochlore oxide, leads to an XY anisotropy in the case of $Yb_2Ti_2O_7$ and $Tb_2Ti_2O_7$ [125].

4.1.4. State of the Art of Quantum Spin Ice Candidate $Yb_2Ti_2O_7$

$Yb_2Ti_2O_7$ is an insulator crystallising in the cubic pyrochlore structure with a lattice constant $a = 10.03\,\text{Å}$ [126]. The magnetic behaviour of $Yb_2Ti_2O_7$ originates from the Yb^{3+} $(4f^{13})$ ions at the vertices of the A sub-lattice of the corner sharing tetrahedra. Since the $3d^0$ Ti^{4+} on the inter-penetrating B sub-lattice has no valence electrons, the magnetic behaviour of the Yb^{3+} ions is isolated from any interfering magnetic interactions. $Yb_2Ti_2O_7$ possesses a single ion ground state doublet protected by Kramers degeneracy, with its ground state Kramers doublet extremely well separated from the first excited state by a crystal field gap of $\Delta \sim 600\,\text{K}$ [103, 123, 127, 128]. The hierarchy of energy scales in $Yb_2Ti_2O_7$, together with the pyrochlore structure, leads to an XY anisotropy of the spins on the rare earth site [125]. The Curie-Weiss temperature is small and positive, with $\theta_{CW} = 0.76\,\text{K}$ [126], suggesting predominantly ferromagnetic interactions [126, 129].

The magnetic properties of $Yb_2Ti_2O_7$ are still under debate. An obstacle in identifying the true ground state of $Yb_2Ti_2O_7$ are the experimental inconsistencies of different samples concerning the measured low-temperature transition. Subtle structural differences and the proximity to magnetic order presumably lead to small perturbation in the exchange parameters, and, hence, significant changes in the nature of the magnetic ground state [119, 130–132]. For instance, Ross *et al.* identified that stuffing of the transition metal ion site in single crystals grown by optical float zoning introduce additional exchange bonds and local lattice deformations, leading to instabilities of the magnetic ground state [133]. Arpino *et al.* suggested that these differences are due to a systematic material discrepancy, indicating that a better and more consistent method of crystal growth is needed [126].

The earliest experimental study on selected magnetic pyrochlore oxides, by Blöte *et al.* in 1969, observed a sharp peak in the specific heat of $Yb_2Ti_2O_7$ at a critical temperature of $\sim 0.214\,K$ [129], suggesting a transition to long-range order. Indeed, a transition into a state with long-range magnetic order was reported by several groups [120, 134–139]. However, several other studies reported a lack of long-range order [121, 140–143].

From a theoretical point of view, the ferromagnetic interactions along the local axis of the tetrahedra together with the well protected ground state Kramers doublet suggest, that $Yb_2Ti_2O_7$ forms a quantum spin-ice at low temperatures [103, 120–123]. The magnetic interactions of $Yb_2Ti_2O_7$ are therefore best described by the nearest-neighbour symmetry-allowed anisotropic effective pseudospin-1/2 Hamiltonian in Eq. (4.6).

The exchange parameter of the Hamiltonian in Eq. (4.6) were determined by Ross *et al.*, and used to compute specific heat, entropy, and magnetisation by means of numerical linked-cluster calculation [120, 121]. However, placing their parameters in the gauge mean-field theory phase diagram calculated by Savary and Balents in Fig. 4.5(a), suggests a ferromagnetic ground state. Robert *et al.* determined the exchange couplings by applying the Hamiltonian to zero-field diffuse scattering, and to the spin wave spectrum in the field polarised state [131]. Their analysis found $Yb_2Ti_2O_7$ at the border between a ferromagnetic and an antiferromagnetic state, hence the ground state to be governed by quantum fluctuations due to phase competition [131]. A recent inelastic neutron scattering study by Thompson *et al.* applied the Hamiltonian to a large set of data and determined the exchange parameters [144]. They identified the transverse exchange $J_{z\pm}$ as leading perturbation, and not $J_{\pm}$ as would be necessary for a quantum spin-liquid according to the gauge mean-field theory by Savary *et al.* [117].

Tab. 4.1 summarises the exchange parameters of the Hamiltonian in Eq. (4.6) obtained for $Yb_2Ti_2O_7$ found in the literature. The couplings J_1, J_2, J_3, and J_4 are linear combinations of the exchange in Eq. (4.6), given by

$$\begin{pmatrix} J_1 \\ J_2 \\ J_3 \\ J_4 \end{pmatrix} = \frac{1}{3} \begin{pmatrix} -1 & 4 & 2 & 2\sqrt{2} \\ 1 & -4 & 4 & 4\sqrt{2} \\ -1 & -2 & -4 & 2\sqrt{2} \\ -1 & -2 & 2 & -\sqrt{2} \end{pmatrix} \begin{pmatrix} J_{zz} \\ J_{\pm} \\ J_{\pm\pm} \\ J_{z\pm} \end{pmatrix}. \tag{4.7}$$

Further, the *g*-tensor for the spins was determined from spin wave theory. It contains the two components g_{zz} along, and g_{xy} transverse to the local $\langle 111 \rangle$ axes. The obtained *g*-tensor components for the different spin wave studies fit well the *g*-tensors obtained from crystal field studies [127, 128, 145]. Their resulting *g*-tensor components all imply local XY anisotropy.

Yan *et al.* determined the expected classical ground state phases for pyrochlore oxides with anisotropic exchange interactions [146]. Fig. 4.6 shows the classical ground state

Table 4.1.: Exchange parameter of the effective pseudospin-$1/2$ Hamiltonian in Eq. (4.6) estimated from experiments on Yb$_2$Ti$_2$O$_7$ by Ross *et al.* [103], Robert *et al.* [131], and Thompson *et al.* [144].

	Ross *et al.*	Robert *et al.*	Thompson *et al.*
J_{zz} (meV)	0.17(4)	0.07	0.026(3)
$J_{\pm}$ (meV)	0.05(1)	0.085	0.074(2)
$J_{\pm\pm}$ (meV)	0.05(1)	0.04	0.048(2)
$J_{z\pm}$ (meV)	$-0.14(1)$	-0.15	$-0.159(2)$
J_1 (meV)	$-0.09(3)$	-0.03	$-0.028(4)$
J_2 (meV)	$-0.22(3)$	-0.32	$-0.326(4)$
J_3 (meV)	$-0.29(2)$	-0.28	$-0.272(4)$
J_4 (meV)	0.01(2)	-0.02	0.049(2)
g_{zz}	1.8	2.06	2.14(3)
g_{xy}	4.32	4.09	4.17(2)

phase diagram in the exchange parameter space for vanishing Dzyaloshinskii-Moriya interactions $J_4 = 0$, as expected for XY pyrochlore oxides. The phase diagram shows four different magnetic phases, with their spin configuration shown schematically on two tetrahedra in Fig. 4.6. The phases are a non-collinear ferromagnetic phase (FM), a Palmer-Chalker antiferromagnetic state (ψ_4), a coplanar antiferromagnetic state (ψ_2), and a non-coplanar antiferromagnetic state (ψ_3). The exchange parameters determined by Ross *et al.*, Robert *et al.*, and Thompson *et al.*, all suggest that the ground state of Yb$_2$Ti$_2$O$_7$ is a non-collinear ferromagnetic phase. All set of parameters place Yb$_2$Ti$_2$O$_7$ in the vicinity to a coplanar antiferromagnetic phase. This suggests that already modest changes to the exchange parameters may change the magnetic ground state [125].

To summarise: Simple mean-field calculations by Ross *et al.* [103], ground state minimisation by Wong *et al.* [147], sophisticated gauge mean-field theory by Savary and Balents [117, 119], a thermodynamic properties study by Hayre *et al.* [121], and neutron scattering studies by Robert *et al.* [131] and Thompson *et al.* [144], all predict conventional long-range ferrimagnetic order. In this ferrimagnetic state, the spins are aligned along one of the six $\langle 100 \rangle$ cubic directions, but slightly splayed away from a perfect alignment. This compares with the magnetic properties of Yb$_2$Sn$_2$O$_7$, another quantum spin-ice candidate [148]. On the basis of these calculations, Yb$_2$Ti$_2$O$_7$ is predicted to be in a semi-classical splayed ferromagnetic (s-FM) state, and might be either very close to long-range antiferromagnetic order [130, 131, 144], or a quantum spin-liquid phase [135, 144, 149]. The close proximity of Yb$_2$Ti$_2$O$_7$ to these different phases arises from dominant quantum ex-
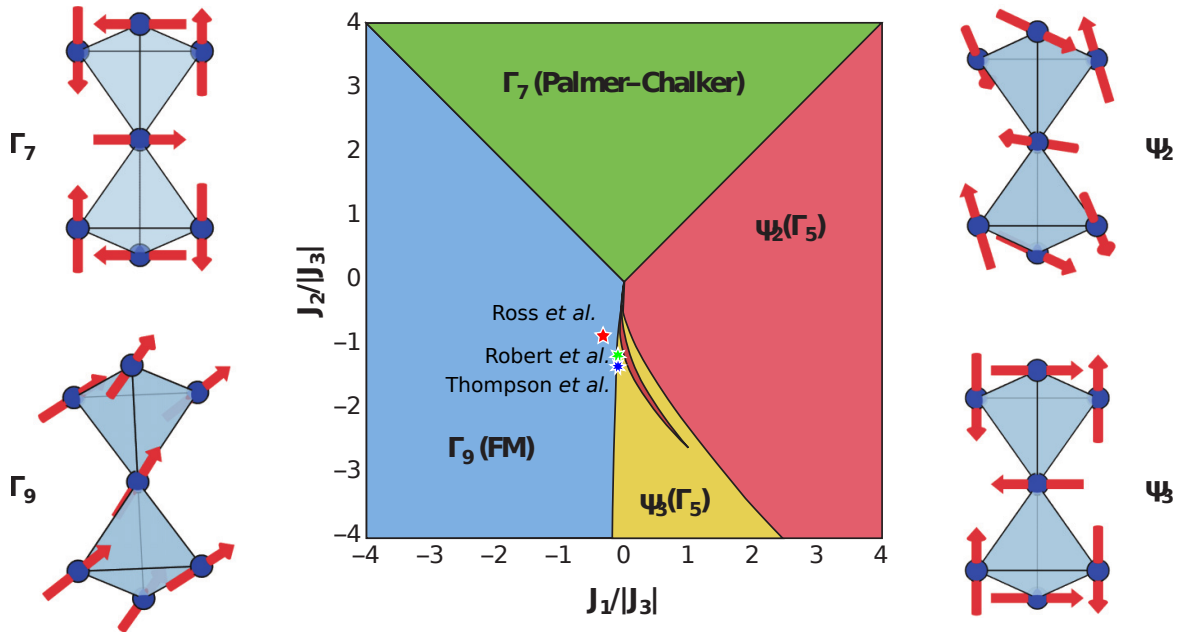
Figure 4.6.: Classical ground state phase diagram of pyrochlore oxides with anisotropic exchange. The phase diagram is shown in exchange parameter space of the nearest-neighbour exchange Hamiltonian in Eq. (4.6) in the limit of vanishing Dzyaloshinskii-Moriya interactions $J_4 = 0$. In the vicinity of the origin, four long-ranged ordered phases emerge. A non-collinear ferromagnetic phase (FM), a Palmer-Chalker antiferromagnetic state (ψ_4), a coplanar antiferromagnetic state (ψ_2), and a non-coplanar antiferromagnetic state (ψ_3). The spin configurations of these phases are depicted on two tetrahedra. Red, green, and blue markers correspond to the exchange parameters for $Yb_2Ti_2O_7$ found by Ross *et al.* [103], Robert *et al.* [131], and Thompson *et al.* [144], respectively. The axes coordinates are linear combinations of the couplings in Eq. (4.6), cf. Eq. (4.7). Figure taken from Ref. [125, 146].

change terms found by Thompson *et al.* [144]. Further, quantum fluctuations reflecting the competition between different phases identify $Yb_2Ti_2O_7$ as a candidate par excellence for a quantum spin-liquid (QSL) [103].

An unresolved issue in $Yb_2Ti_2O_7$ concerns its sensitivity to disorder, such as Yb^{3+} stuffing on Ti^{4+} sites [133]. As the observed amount of disorder and strength exceeds a critical value, the resulting random frustration would be expected to drive the system first to form a semi-classical spin-glass. This was not reported so far [37].

The objective of the work reported in this thesis was to better understand the nature of the ground state of $Yb_2Ti_2O_7$. To advance the understanding, the temperature and field dependence of the magnetisation was measured at millikelvin temperatures. Measurements were carried out on stoichiometric single crystals, grown by the travelling solvent floating zone technique by Arpino *et al.* [126], and carefully polished into a spherical

shape. It was confirmed that the ground state is of ferrimagnetic nature, with spins slightly splayed away from one of the six $\langle 100 \rangle$ cubic directions. Further, differences for applied fields along the three main symmetry directions, i.e. $\langle 111 \rangle$, $\langle 110 \rangle$, and $\langle 100 \rangle$, were determined. A theoretical model was proposed by Tchernyshyov and collaborators based on the Potts model [150–154]. The model allows to describe the low temperature magnetisation data for the three main symmetry directions on the basis of a cubic ferromagnet with six easy $\langle 100 \rangle$ directions.

4.2. The Potts Model of Cubic Ferromagnets

In 1952, Potts suggested a statistical mechanical model to describe the interactions of spins on a crystalline lattice [150]. Thereby, a spin can be in one of q states. The Potts model may be described by a Hamiltonian of the form

$$\mathcal{H}_c = J_c \sum_{i,j} \cos \left(\theta_{s_i} - \theta_{s_j} \right), \tag{4.8}$$

with the discrete angular positions $\theta_n = \frac{2\pi n}{q}$ of the spins on a circle with $n = 1, ..., q$. This is also known as the clock model, a two-dimensional planar model. In the limit $q \to \infty$ the Potts model equals the XY model, where spins choose any state on the easy plane. The standard Potts model is written as [150, 155]

$$\mathcal{H}_p = -J_p \sum_{i,j} \delta(s_i, s_j), \tag{4.9}$$

where $\delta(s_i, s_j)$ is the Kronecker delta. For $q = 2$, Eq. (4.9) describes the Ising model with $J_p = -2J_c$ and, therefore, the Potts model can be regarded a generalisation of the Ising model. For $q = 3$ the Potts model is equivalent to the three-state vector Potts model with $J_p = -\frac{3}{2}J_c$.

Applying an external magnetic field alters the standard Potts Hamiltonian to

$$\mathcal{H}_h = \sum_{i,j} J_{ij} \delta(s_i, s_j) - \beta^{-1} \sum_i h_i s_i, \tag{4.10}$$

where h is an external magnetic field and $\beta = \frac{1}{k_{\mathrm{B}} T}$ the inverse temperature [150].

In theoretical studies by Baxter [156], and Straley and Fisher [157], the two-dimensional ($q \leq 4$)-Potts model exhibits a continuous phase transition in zero field. Landau theory, however, predicts a discontinuous phase transition for the $q = 3$ Potts model [151]. On the other hand, a first-order nature of the phase transition in the theoretical model was confirmed by renormalisation-group calculations and Monte Carlo simulations [158–160]. In 1976, Mukamel *et al.* addressed the question of the order of the phase transition in the Potts model by studying the phase diagram of a cubic ferromagnet [151].

A ferromagnet with cubic anisotropy and the three easy axes [100], [010] and [001] in a magnetic field along [111] realise the three-dimensional $(q = 3)$-Potts model [151]. Fig. 4.7(a) shows the schematic magnetic phase diagram of a cubic ferromagnet at a fixed temperature below T_C within the $(q = 3)$-Potts model. The model was calculated in accordance with mean-field and Landau theories, and was shown to be equivalent to the $(q = 3)$-Potts model [151]. A planar cut through the phase diagram, together with the corresponding magnetisation along the three main symmetry directions, i.e. $\langle 111 \rangle$, $\langle 110 \rangle$, and $\langle 100 \rangle$, is shown in Fig. 4.7(b). The magnetisation was calculated with mean-field theory.
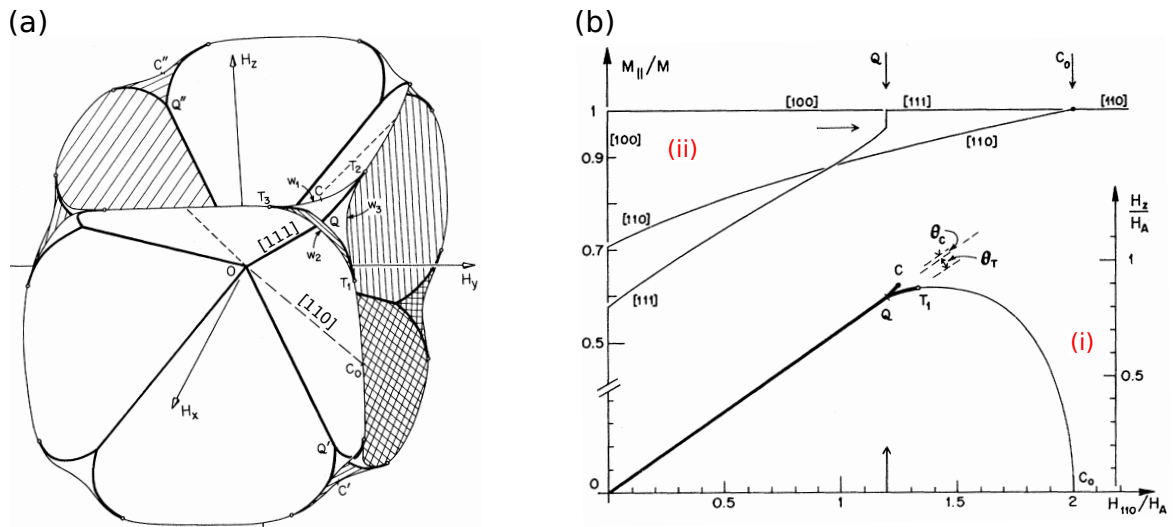
Figure 4.7.: Phase diagram and field dependence of the magnetisation in a cubic ferromagnet. (a) $\boldsymbol{H} = (H_x, H_y, H_z)$ space of the schematic phase diagram. Bold lines denote magnetic triple points, along $\langle 111 \rangle$. Dashed lines are along $\langle 110 \rangle$. The twelve planes are of first-order, and must terminate in critical edges of Ising character, denoted by thin lines. The tricritical points, T_{1-3}, are connected by a bold line to the quadruple points Q. Figure taken from Ref. [151]. (b) In (i), a planar cut through the phase diagram from (a) is shown, where the critical points C and C_0, the tricritical point T_1, and the quadruple point Q are shown. The bold line again represents a first-order, and the thin line a second-order phase transition. In (ii), the corresponding magnetisation for field along the three main symmetry directions is shown, with a first-order phase transition for $\langle 111 \rangle$ at Q, and a second-order phase transition for $\langle 110 \rangle$ at C_0. Figure taken from Ref. [151].

In zero field, the cubic anisotropy selects six ground states with magnetisation along the six equivalent easy directions $\pm \hat{x}$, $\pm \hat{y}$, and $\pm \hat{z}$. The fraction of these domains $n_{\pm \hat{x}}$, $n_{\pm \hat{y}}$, and $n_{\pm \hat{z}}$ add up to 1:

$$n_{+\hat{x}} + n_{-\hat{x}} + n_{+\hat{y}} + n_{-\hat{y}} + n_{+\hat{z}} + n_{-\hat{z}} = 1. \tag{4.11}$$

The average magnetisation is given by

$$\boldsymbol{M} \;=\; M_0\left(n_{+\hat{x}}\hat{x} - n_{-\hat{x}}\hat{x} + n_{+\hat{y}}\hat{y} - n_{-\hat{y}}\hat{y} + n_{+\hat{z}}\hat{z} - n_{-\hat{z}}\hat{z},\right) \tag{4.12}$$

where M_0 is the length of $\boldsymbol{n}$ in a single-domain state, where all these six states are equally represented.

Applying a weak magnetic field $\boldsymbol{H}$ stabilises the easy direction closest to the direction of the external field. Varying $\boldsymbol{H} \, || \, \langle 111 \rangle$ yields a first-order phase transition with a jump in magnetisation [151]. Field along $\langle 110 \rangle$ shows a second-order transition, cf. Fig. 4.7(b).

Tchernyshyov and collaborators at Johns Hopkins University in Baltimore worked out a simple model to describe the behaviour of Yb₂Ti₂O₇ at low temperatures below $0.2\,\mathrm{K}$ and in weak magnetic fields below $0.1\,\mathrm{T}$. The model assumes the above mentioned selection of six ground states within the Potts model, whereas energy of domain walls are negligible. The energy is a sum of the Zeeman energy E_{Z} in an applied magnetic field $\boldsymbol{H}$

$$E_{\mathrm{Z}} \;=\; -\mu_0 \int_V \boldsymbol{M} \cdot \boldsymbol{H}\,\mathrm{d}V \tag{4.13}$$

$$= -\mu_0 \frac{4\pi}{3} R^3 \boldsymbol{M} \cdot \boldsymbol{H}, \tag{4.14}$$

and of the magnetostatic term E_{MS}

$$E_{\mathrm{MS}} \;=\; \frac{1}{6}\mu_0 \int_V \boldsymbol{M}^2 \,\mathrm{d}V \tag{4.15}$$

$$= \frac{4\pi}{3} R^3 \frac{\mu_0 \boldsymbol{M}^2}{6}, \tag{4.16}$$

integrated over the volume of a spherical sample. One third of the magnetostatic energy is stored in a uniform field $\boldsymbol{H} = -\frac{1}{3}\boldsymbol{M}$ inside the sphere, and two thirds in the dipolar field outside. The total energy is then given by

$$E \;=\; E_{\mathrm{Z}} + E_{\mathrm{MS}}$$

$$= -\mu_0 \frac{4\pi}{3} R^3 \boldsymbol{M} \cdot \boldsymbol{H} + \frac{4\pi}{3} R^3 \frac{\mu_0 \boldsymbol{M}^2}{6}. \tag{4.17}$$

Both terms, E_{Z} and E_{MS}, are proportional to the volume of the sphere, which can be divided out. The total energy may then be discussed in terms of energy density

$$U \;=\; -\mu_0 \boldsymbol{H} \cdot \boldsymbol{M} + \frac{\mu_0 \boldsymbol{M}^2}{6}. \tag{4.18}$$

With Eq. (4.12), U in terms of domain fractions is given by

$$U \;=\; \frac{m u_0 M_0^2}{6}\left[\left(n_{\hat{x}} - n_{-\hat{x}} - \frac{3H_x}{M_0}\right)^2 + \left(n_{\hat{y}} - n_{-\hat{y}} - \frac{3H_y}{M_0}\right)^2 + \left(n_{\hat{z}} - n_{-\hat{z}} - \frac{3H_z}{M_0}\right)^2 \right]$$

$$- \left(\frac{3\mu_0}{2}\right)^2 \left(H_x^2 + H_y^2 + H_z^2\right) \tag{4.19}$$

Minimising the energy in Eq. (4.19) with respect to the fractions gives

$$\frac{dU}{d(n_{\hat{a}} - n_{-\hat{a}})} = \frac{\mu_0 M_0^2}{3}\left(n_{\hat{a}} - n_{-\hat{a}} - \frac{3H_a}{M_0}\right) \overset{!}{=} 0$$

$$\Rightarrow \quad (n_{\hat{a}} - n_{-\hat{a}}) = +\frac{3H_a}{M_0} \tag{4.20}$$

with $a = x,\ y,\ z$ and $\hat{a} = \hat{x},\ \hat{y},\ \hat{z}$. Therefore, for any direction of $\boldsymbol{H}$,

$$\boldsymbol{M} = 3\boldsymbol{H}. \tag{4.21}$$

For high enough fields, the fractions reach saturation dependent on the field direction. For field along [100]:

$$\boldsymbol{H} = H\,(1,\,0,\,0)$$

$$n_{\hat{x}} = 1 \quad \text{and} \quad n_{-\hat{x}} = n_{+\hat{y}} = n_{-\hat{y}} = n_{+\hat{z}} = n_{-\hat{z}} = 0$$

the fractions reach saturation, according to Eq. (4.21), for an applied magnetic field of

$$H \geq \frac{M_0}{3}. \tag{4.22}$$

For field along [110]:

$$\boldsymbol{H} = H\left(\frac{1}{\sqrt{2}},\,\frac{1}{\sqrt{2}},\,0\right)$$

$$n_{\hat{x}} = n_{\hat{y}} = \frac{1}{2} \quad \text{and} \quad n_{-\hat{x}} = n_{-\hat{y}} = n_{+\hat{z}} = n_{-\hat{z}} = 0$$

the fractions reach saturation for an applied magnetic field of

$$H \geq \frac{M_0}{3\sqrt{2}}. \tag{4.23}$$

For Field along [111]:

$$\boldsymbol{H} = H\left(\frac{1}{\sqrt{3}},\,\frac{1}{\sqrt{3}},\,\frac{1}{\sqrt{3}}\right)$$

$$n_{\hat{x}} = n_{\hat{y}} = n_{\hat{z}} = \frac{1}{3} \quad \text{and} \quad n_{-\hat{x}} = n_{-\hat{y}} = n_{-\hat{z}} = 0$$

the fractions reach saturation for an applied magnetic field of

$$H \geq \frac{M_0}{3\sqrt{3}}. \tag{4.24}$$

Hence, these saturation fields and spontaneous magnetisation for applied magnetic field $\boldsymbol{H}$ along the three directions $\langle 100 \rangle$, $\langle 110 \rangle$, and $\langle 111 \rangle$ are in ratios

$$H_{\text{ext},\langle 100 \rangle} : H_{\text{ext},\langle 110 \rangle} = M_{0,\langle 100 \rangle} : M_{0,\langle 110 \rangle} = 1 : \frac{1}{\sqrt{2}} \tag{4.25}$$

$$H_{\text{ext},\langle 100 \rangle} : H_{\text{ext},\langle 111 \rangle} = M_{0,\langle 100 \rangle} : M_{0,\langle 111 \rangle} = 1 : \frac{1}{\sqrt{3}}. \tag{4.26}$$

4.2.1. Experimental Challenges

The magnitude of the discontinuity in the order parameter varies depending on the system and also on the field. In the framework of Landau theory, the discontinuity depends on the magnitude of the cubic invariant. If the latter vanishes, the discontinuity becomes continuous.

Mukamel *et al.* considered a ferromagnet with fourth-order anisotropy parameter, determining the jump in magnetisation for field along $\langle 111 \rangle$ to be $3\frac{2}{3}\%$ of M_0 at $T = 0$. Further, their calculation yields that only a misalignment of up to $0.25°$ is acceptable in order to observe the discontinuity at all. Both, detecting such a small discontinuity and aligning the sample with such a high accuracy is very difficult to realise experimentally. In rare-earth systems, however, sixth-order anisotropy has to be included. This quantitatively changes the phase diagram without violating the equivalence with the Potts model, since the model is based upon symmetry considerations only [152].

Based on the theory by Mukamel *et al.*, calculation on DyAl$_2$ predicted a jump of more than 25% at low temperatures [151, 152]. This led to one of the clearest experimental realisation of the Potts model, showing the first-order phase transition in a $\langle 111 \rangle$ field in DyAl$_2$ [152]. Further, the alignment of the external field with respect to the sample orientation is relaxed relative to the case with only fourth-order anisotropy [152]. Other experimental realisations of the $(q = 3)$-Potts model can be found in further RAl$_2$ intermetallic compounds, where the R=Pr, Tb, Dy [152, 161].

To sum up, there are four main challenges to observe the behaviour predicted by the Potts model in real systems. (i) Detecting a very small discontinuity, which depends on the sample. (ii) Accurately aligning the sample with respect to the external field. (iii) Measuring the magnetisation at temperatures well below T_C, i.e. in case of Yb$_2$Ti$_2$O$_7$ $T_\mathrm{C} \sim 0.214\,\mathrm{K}$ [129]. (iv) Scanning the field dependence of the magnetisation with a very high resolution, in order not to miss the tiniest features.

4.3. Experimental Set-up

The magnetisation of Yb$_2$Ti$_2$O$_7$ was measured by means of vibrating coil magnetometry at millikelvin temperatures as described in Ch. 2. This sections presents the sample preparation process in Sec. 4.3.1, and the definition of the protocols for the temperature and field dependent measurements of the magnetisation in Sec. 4.3.2.

4.3.1. Sample Preparation

A high quality single crystal $Yb_2Ti_2O_7$ was grown by the travelling solvent floating zone technique (TSFZ) by Arpino *et al.* The solvent was $30\,wt\%$ rutile TiO_2 and $70\,wt\%$ $Yb_2Ti_2O_7$. The crystal is identical to a single crystal characterised, alongside a doped series of $Yb_{2+x}Ti_{2-x}O_{7-\delta}$ polycrystalline samples, within the study of Arpino *et al.* [126]. The sample is of very high quality, indicated by its clear and colourless appearance. Another sign for the very high quality is a stuffing of Ti on Yb site of only $\sim 0.25\,\%$ to $0.5\,\%$, as determined by X-ray diffraction [162]. All magnetisation measurements were carried out on a $\sim 4.7\,mm$ diameter, $\sim 0.40\,g$ sphere, which was ground from the stoichiometric single crystal and polished into a spherical shape. Fig. 4.8(a) and (b) show the large single crystal and the polished sphere, respectively. A spherical shape was chosen to minimise inhomogeneities of the demagnetising fields, this way also permitting straight forward computation of the internal field values. Further, for the spherical sample shape used, any crystallographic orientation could be studied on the same sample and sample geometry with respect to the applied magnetic field and the detection coils.
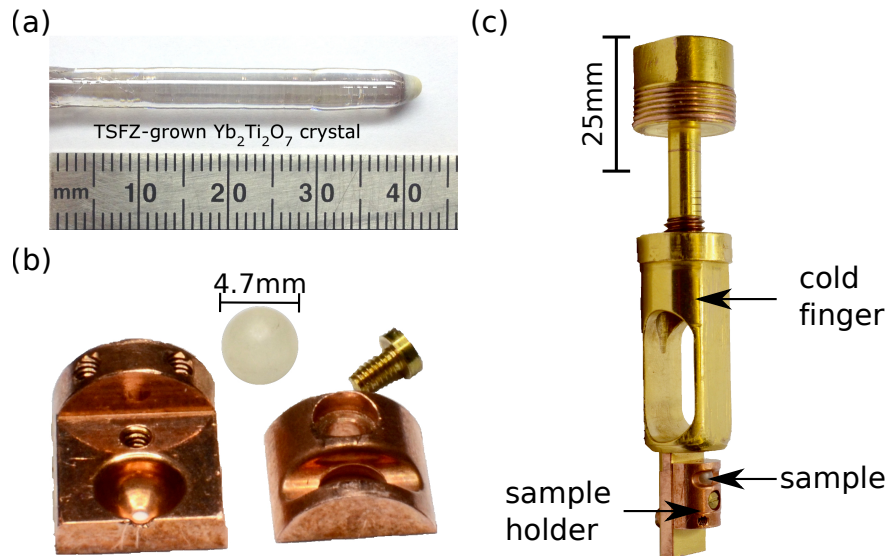
Figure 4.8.: $Yb_2Ti_2O_7$ sample and sample holder for magnetisation measurements. (a) Travelling solvent floating zone technique (solvent $= 30\,wt\%$ rutile TiO_2 and $70\,wt\%$ $Yb_2Ti_2O_7$) produces a large single crystal of $Yb_2Ti_2O_7$ that is clear and colourless. Image taken from Ref. [126]. (b) Spherical sample ground from the stoichiometric single crystal, and the oxygen-free Cu sample holder, composed of two matching sections fitting accurately the size of the sphere. (c) Sample holder mounted on a cold finger, which is then bolted into the Cu tail attached to the mixing chamber of the dilution refrigerator.

The sphere was oriented using a Multiwire Laboratories real time X-ray Laue backscattering camera system, MWL120, with an accuracy better than 0.2°. North Star Orien-

tation software was used for indexing the obtained Laue reflection patterns. Fig. 4.9(a-c) show typical Laue X-ray diffraction patterns obtained for the different orientations in Yb$_2$Ti$_2$O$_7$, together with the indexing calculated by the North Star Orientation software. The diffraction patterns of a cubic lattice, as for Yb$_2$Ti$_2$O$_7$, show for the $\langle 111 \rangle$ direction a three-fold symmetry, cf. Fig. 4.9(a), for the $\langle 110 \rangle$ direction a two-fold symmetry, cf. Fig. 4.9(b), and for the $\langle 100 \rangle$ direction a four-fold symmetry, cf. Fig. 4.9(b). The sample was oriented better than $\sim 0.2°$ for $\langle 111 \rangle$, $\sim 0.4°$ for $\langle 110 \rangle$, and $\sim 0.7°$ for $\langle 100 \rangle$, respectively.

After orientation, the sample was fixed with GE varnish inside the two matching sections of the sample holder, which accurately fit the size of the sphere, see Fig. 4.8(b). The oxygen-free Cu sample holder was then mounted on a cold finger which then was firmly bolted into the Cu tail attached to the mixing chamber of the dilution refrigerator, as shown in Fig. 4.8(c). This provided excellent thermal anchoring of the sample across the entire surface of the sphere during all measurements, while keeping its position rigidly fixed mechanically without exerting strain. The position of the sample holder in Fig. 4.8(c) inside the dilution refrigerator can be seen in the enlarged inset of area (iii) in Fig. 2.4.

4.3.2. Temperature and Field Measurement Protocols

Prior to the work carried out as part of the present thesis, Yb$_2$Ti$_2$O$_7$ was already known to display strong hysteretic behaviour for temperatures below several hundred millikelvin. Therefore, magnetisation data were recorded following well-defined field and temperature histories.

Measurements were performed along the three main symmetry directions $\langle 111 \rangle$, $\langle 110 \rangle$, and $\langle 100 \rangle$. Data were recorded at temperatures down to ~ 0.022 K, and under magnetic fields up to 5 T. The VCM operated at a low excitation frequency of 19 Hz, and a small excitation amplitude of ~ 0.5 mm. The sample temperature was measured with a calibrated RuO$_2$ sensor mounted next to the sample, and additionally monitored with a calibrated RuO$_2$ sensor attached to the mixing chamber in the zero-field region.

Three temperature versus field histories were used: (i) After cooling at zero magnetic field starting at ~ 1 K, the magnetic field was applied at base temperature and data collected while heating monotonically at a rate between 5 mK min^{-1} and 10 mK min^{-1}, depending on the desired measurement. This is referred to as zero-field cooled / field heated (zfc-fh). (ii) Data were recorded while cooling in the same unchanged applied magnetic field starting at ~ 1 K. This is referred to as field cooled (fc). (iii) Following initial cool down in the applied magnetic field, data were recorded while heating monotonically at a rate of 5 mK min^{-1} and 10 mK min^{-1}, respectively, in the same unchanged magnetic field. These data are referred to as field cooled / field heated (fc-fh).
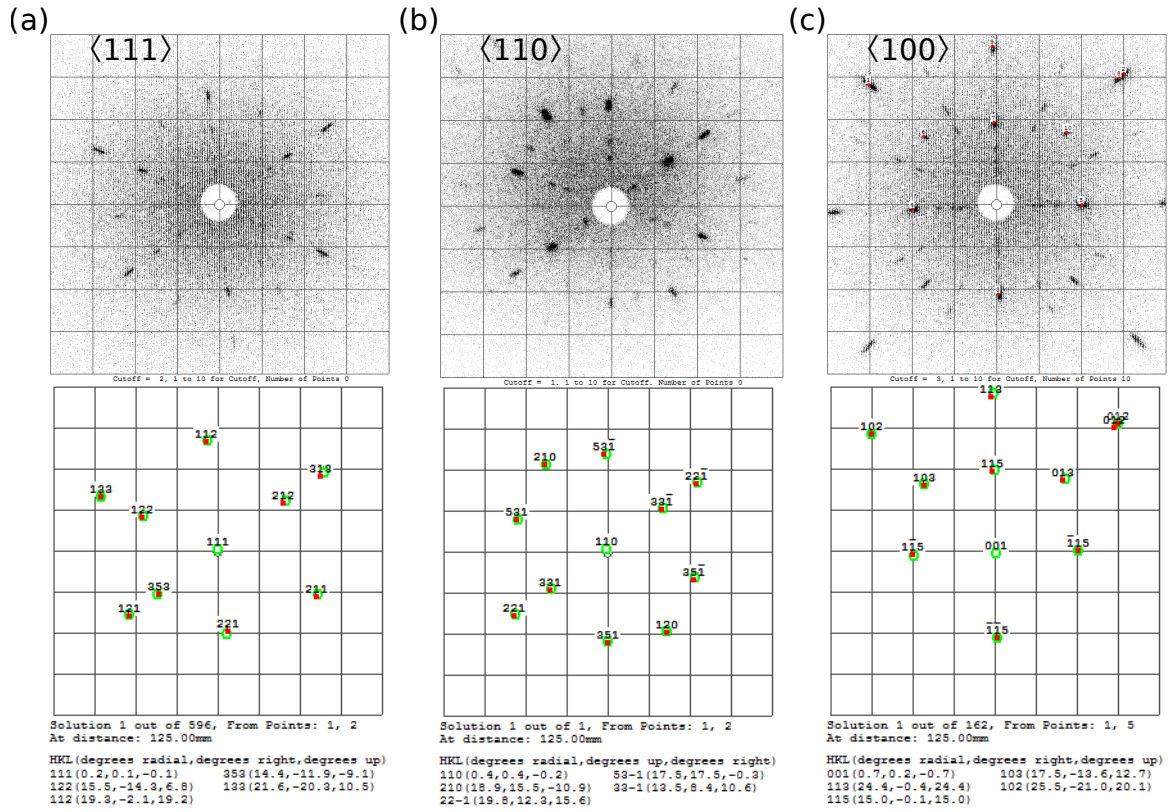
Figure 4.9.: X-ray Laue diffraction pattern and calculated diffraction pattern for $Yb_2Ti_2O_7$ along the three main symmetry directions. (a) Three-fold symmetry for the $\langle 111 \rangle$ direction oriented better than $\pm 0.2°$. (b) Two-fold symmetry for the $\langle 110 \rangle$ direction oriented better than $\pm 0.4°$. (c) Four-fold symmetry for the $\langle 100 \rangle$ direction oriented better than $\pm 0.7°$.

Similarly, the magnetic field dependence was determined according to one of the following three different protocols: (iv) After zero-field cooling, field sweeps were carried out either from $0 \rightarrow 1\,T$ or $0 \rightarrow 5\,T$. They are denoted (A1) and (A1'), respectively. (v) Field sweeps starting at a high field, notably from $1\,T \rightarrow -1\,T$, are denoted (A2). (vi) Related field sweeps from $-1\,T \rightarrow 1\,T$ are denoted (A3).

For temperatures above $0.05\,K$, all data were recorded while sweeping the field continuously at $15\,mT\,min^{-1}$, whereas measurements at the lowest temperatures accessible, i.e. $0.022\,K$ and $0.028\,K$, were carried out at sweep rates of $1\,mT\,min^{-1}$ and $1.5\,mT\,min^{-1}$, respectively, to minimise eddy current heating by the Cu tail. High temperature field sweeps, i.e. for temperatures $\geq 1.5\,K$, were measured continuously with a sweep rate of $30\,mT\,min^{-1}$.

A more detailed list of the measurements performed can be found in App. A.1, Tab. A.1 and A.2 for field along the crystallographic $\langle 111 \rangle$ direction, Tab. A.3 and A.4 for field

along the crystallographic $\langle 110 \rangle$ direction, and Tab. A.5 and A.6 for field along the crystallographic $\langle 100 \rangle$ direction, respectively.

4.4. Experimental Results

In the following, the experimental results of the magnetisation measurements in Yb$_2$Ti$_2$O$_7$ will be presented. The section will first report the orientation dependence of the magnetic phase diagram of Yb$_2$Ti$_2$O$_7$ in Sec. 4.4.1, before turning to the detailed measurements of the temperature and field dependent magnetisation. The temperature dependence will be presented in Sec. 4.4.2, followed by field dependent measurements in Sec. 4.4.3 and Sec. 4.4.4. The section concludes with a comparison of the experimental data with a theoretical model, cf. Sec. 4.4.5.

4.4.1. Phase Diagram

The temperature and field dependence of the magnetic phase diagram of Yb$_2$Ti$_2$O$_7$ was inferred from the magnetisation measurements discussed in detail in Sec. 4.4.2, Sec. 4.4.3, and Sec. 4.4.4. Fig. 4.10 shows the magnetic phase diagram of Yb$_2$Ti$_2$O$_7$ as a function of temperature and internal magnetic field for fields along the three main symmetry directions. For fields along $\langle 111 \rangle$, see Fig. 4.10(a), the high temperature state in zero field is a paramagnet. Cooling the system leads to a first-order phase transition into a splayed ferromagnetic state (s-FM) below $T_C \sim 0.28\,\mathrm{K}$. At a temperature of $\sim 0.1\,\mathrm{K}$ and zero field, an irreversibility reminiscent of spin freezing is observed. Under small fields the spin frozen state vanishes. A magnetic field initially causes the first-order phase boundary to shift up in temperature, reaching a maximum temperature of $\sim 0.43\,\mathrm{K}$ at an internal field of $\sim 0.23\,\mathrm{T}$. The width of the temperature hysteresis at the tip of the nose is $\sim 0.06\,\mathrm{K}$. This hysteresis in the temperature dependence vanishes at a temperature of $\sim 0.24\,\mathrm{K}$ and an internal field of $\sim 0.56\,\mathrm{T}$. The absence of hysteresis, while still being within the splayed ferromagnetic phase pocket, might indicate a change of order in the transition. At $T = 0$, the phase diagram shows a field driven phase transition at $\sim 0.63\,\mathrm{T}$. In high fields, above the upper phase boundary, the system gradually polarises with spins along the applied magnetic field.

The reentrant type of the phase diagram is also present for fields along $\langle 110 \rangle$, shown in Fig. 4.10(b). In zero field, a first-order transition from a para- to a splayed ferromagnet at $\sim 0.28\,\mathrm{K}$ is observed, and a spin frozen state emerges for temperatures below $\sim 0.1\,\mathrm{K}$, which is suppressed already for small applied fields. For field along $\langle 110 \rangle$, the splayed ferromagnetic phase pocket is slightly distorted along the field axis and stretched along
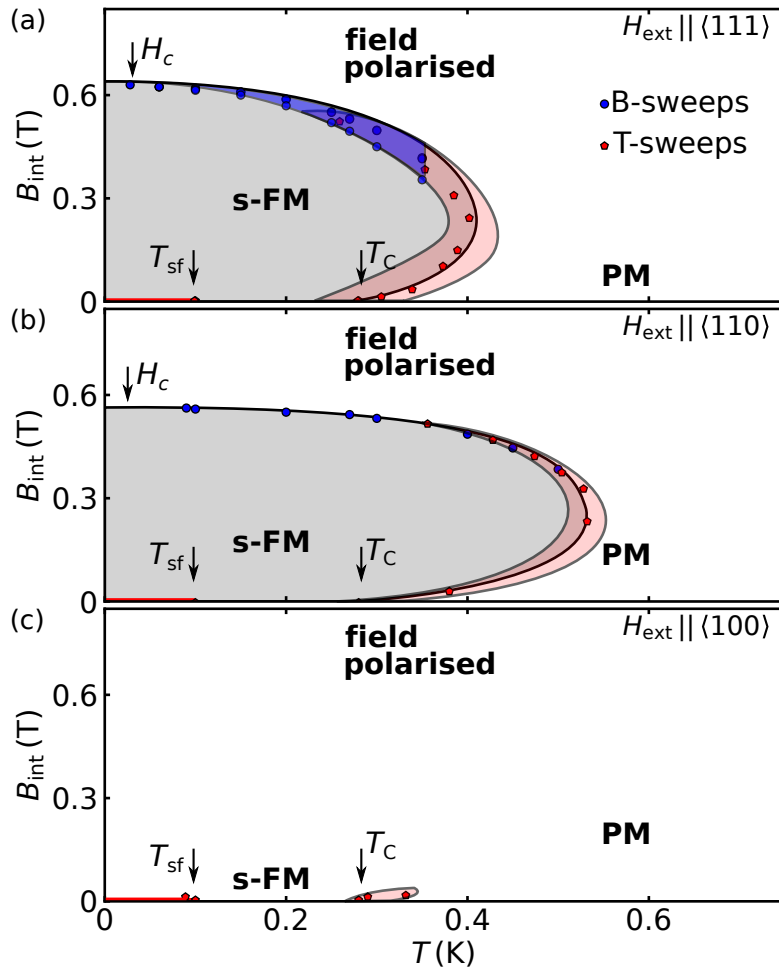
Figure 4.10.: Field orientation dependent magnetic phase diagram of $Yb_2Ti_2O_7$. Fields are applied along $\langle 111 \rangle$ (a), $\langle 110 \rangle$ (b), and $\langle 111 \rangle$ (c). Red markers denote the critical temperature T_C obtained from temperature sweeps, see Fig. 4.11(a,b), whereas the red shaded area indicates the hysteresis upon heating versus cooling during temperature sweeps. The blue markers indicate the critical field obtained from zero-field cooled field sweeps, see Fig. 4.11(c,d). The blue shaded area shows the observed hysteresis in the field loops, see Fig. 4.17. The red line in zero field for $T \leq T_{sf}$ indicate the spin frozen state.

the temperature axis as compared to $\langle 111 \rangle$. The tip of the nose is located at $\sim 0.54\,\mathrm{K}$ $\sim 0.3\,\mathrm{T}$, with a width of $\sim 0.02\,\mathrm{K}$. The hysteresis in the temperature scans closes at a temperature of $\sim 0.38\,\mathrm{K}$ at an internal field of $\sim 0.51\,\mathrm{T}$. A field driven transition is observed at $\sim 0.57\,\mathrm{T}$.

For fields along $\langle 100 \rangle$, cf. Fig. 4.10(c), a clear signature of the transition between splayed ferromagnetic and field polarised state can not be discerned. In zero field, as for the other directions, the system shows a first-order phase transition from a para- to a splayed ferromagnetic state at $\sim 0.28\,\mathrm{K}$. Below a temperature of $\sim 0.1\,\mathrm{K}$, spin freezing occurs, which

is again suppressed in an applied magnetic field. The first-order transition is observed up to an internal field of $\sim$0.07 T at $\sim$0.33 K, where the hysteresis is already very small with a width of $\sim$0.02 K. At slightly higher fields, no transition into the splayed ferromagnetic state is observed.

Fig. 4.11 shows on an example the definition of the transition temperatures and fields, respectively. Fig. 4.11(a) and (b) show the magnetisation as a function of temperature for an applied field of 0.01 T along $\langle 111 \rangle$, where the important features in the temperature sweeps are marked. The inflection points of the field cooled and field heated data are given by T_{C}^+ and T_{C}^-, respectively. Their mean value was defined as the transition temperature T_{C}. The transition temperature T_{C} was determined as long as the temperature scan showed a hysteresis between the field cooled and field heated measurements. Further, the temperature in the zero-field cooled branch below which the magnetisation is changing its slope, indicating spin freezing, T_{sf}, is shown. In Fig. 4.11(c) and (d) the magnetisation as function of internal magnetic field and its numerical derivative are shown, where the kink/jump H_{C} is defined. These feature were tracked in all experimental data throughout this section, cf. Sec. 4.4.2-4.4.4.

4.4.2. Temperature Dependence

The temperature dependence of the magnetisation in Yb$_2$Ti$_2$O$_7$ as a function of an applied magnetic field along the three main symmetry directions $\langle 100 \rangle$, $\langle 110 \rangle$, and $\langle 111 \rangle$ was measured following the measurement protocols described in Sec. 4.3.2 and in App. A.1, Tab. A.1, A.3 and A.5.

Fig. 4.12 shows the magnetisation as a function of temperature for different cooling histories and crystallographic directions. For field along $\langle 111 \rangle$, cf. Fig. 4.12(A1 to A5), data were recorded for temperatures between 0.05 K and 0.9 K and magnetic fields up to 0.9 T, cf. App. A.2, Fig. A.1. For small applied magnetic fields, i.e. 0.01 T, starting at high temperatures, the magnetisation increases monotonically with decreasing temperature. Further cooling reveals a strongly hysteretic transition at $T_{\mathrm{C}} \sim 0.28$ K. The hysteresis in the temperature sweeps suggests a first-order phase transition into a ferromagnetic state, as previously reported in the literature [135, 163]. The transition is accompanied by a jump in the magnetisation. Just below the transition, at $\sim$0.25 K, the zero-field cooled and field cooled magnetisation differ. Whereas the latter increases with decreasing temperature, the zero-field cooled branch decreases. A clear change of slope of the zero-field cooled branch is observed for temperatures below $\sim$0.1 K. Such a behaviour is often attributed to a freezing of domains. In larger magnetic fields, these differences are strongly reduced, becoming fully suppressed for fields greater than 0.05 T.
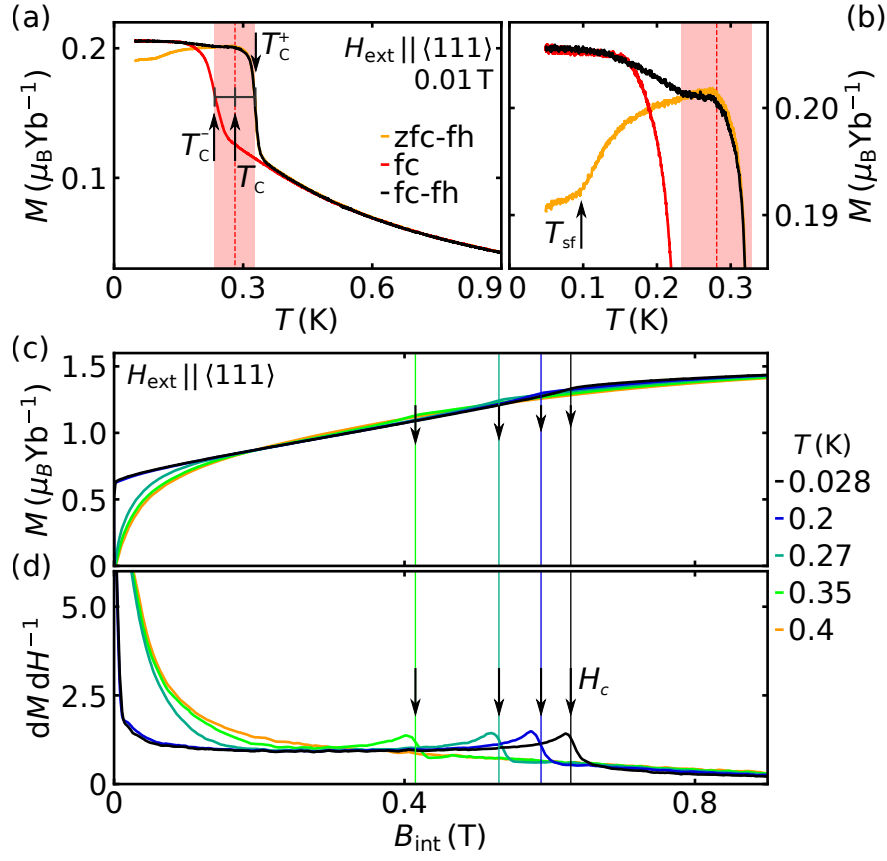
Figure 4.11.: Definition of the transition temperatures and fields in the temperature and field dependence of the magnetisation as illustrated by means of typical data. (a,b) Magnetisation as a function of temperature for an applied field of $0.01\,\mathrm{T}$ along $\langle 111 \rangle$. (a) Temperature scan from $0.05\,\mathrm{K}$ to $0.9\,\mathrm{K}$. (b) Splitting of the zero-field cooled and field cooled branches for low temperatures, and spin freezing feature below $0.1\,\mathrm{K}$. (c) Magnetisation as a function of internal magnetic field along $\langle 111 \rangle$. (d) Susceptibility $\mathrm{d}M\mathrm{d}H^{-1}$ calculated from the magnetisation data.

Further increasing the field initially causes T_{C} to increase, reaching a maximum temperature of $\sim 0.43\,\mathrm{K}$ at an internal field of $\sim 0.23\,\mathrm{T}$ when demagnetisation effects are corrected. At even higher fields, the transition is suppressed again and finally vanishes for fields greater than $\sim 0.6\,\mathrm{T}$. The jump in the magnetisation, found in small fields, at first displays rounding and eventually becomes a kink for higher fields. Here the transition reaches the highest temperature before decreasing again. After this point, the kink becomes a peak and the magnetisation below the transition temperature is slightly lower than before. The transition eventually vanishes at $\sim 0.6\,\mathrm{T}$. In fields higher than $0.6\,\mathrm{T}$, the magnetisation increases monotonically with decreasing temperature. The slope remains finite, down to the lowest temperatures investigated.

For fields along $\langle 110 \rangle$, shown in Fig. 4.12(B1 to B5), data were recorded between $0.05\,\mathrm{K}$ and $0.9\,\mathrm{K}$ for fields up to $0.8\,\mathrm{T}$, cf. App. A.2, Fig. A.2. Cooling down from high temper-
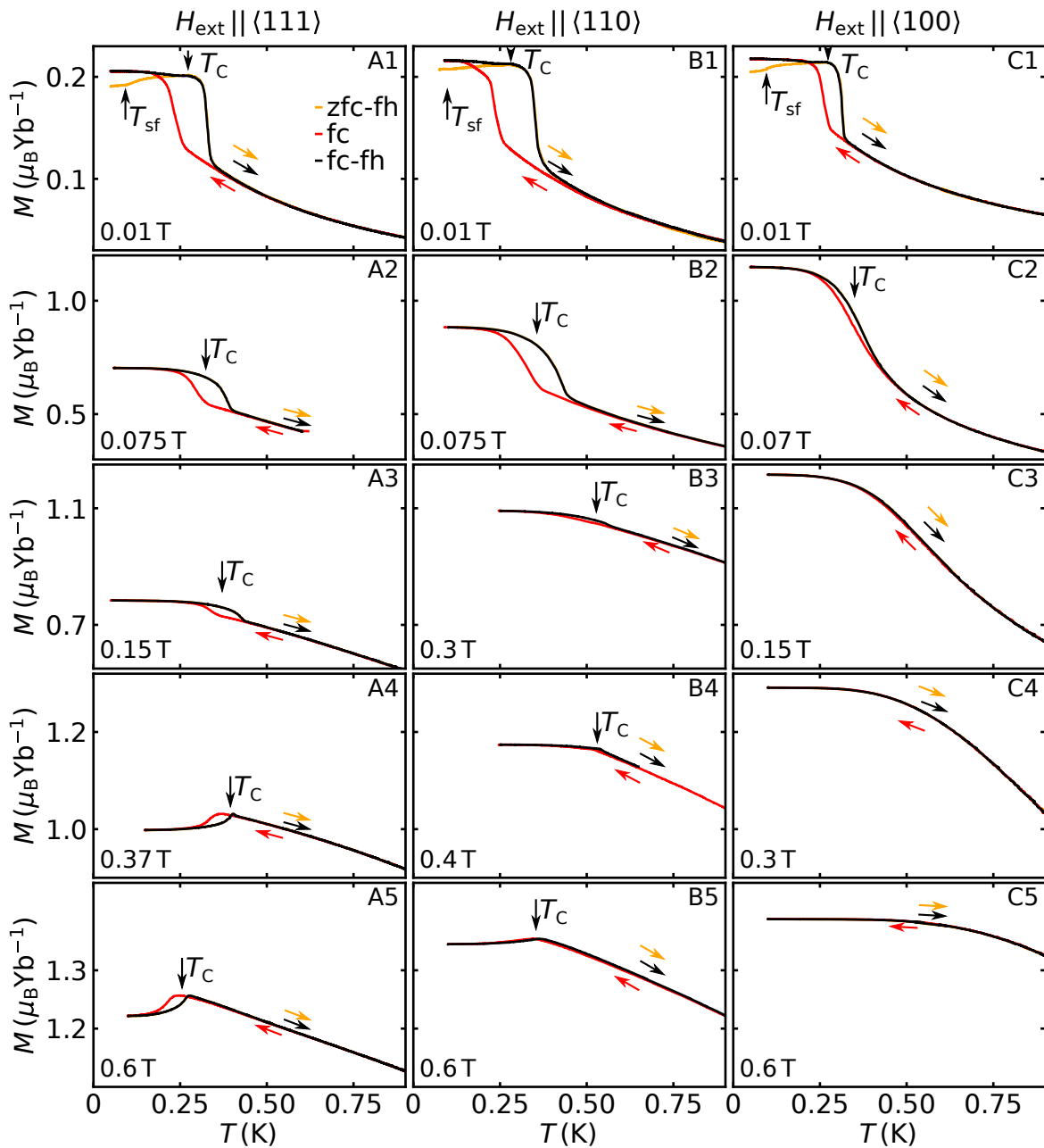
Figure 4.12.: Temperature dependence of the magnetisation of $Yb_2Ti_2O_7$ in applied magnetic fields. (A1-A5) Field along $\langle 111 \rangle$. (B1-B5) Field along $\langle 110 \rangle$. (B1-B5) Field along $\langle 100 \rangle$. In vanishingly small fields, a distinct difference between data recorded under zero-field cooling and field cooling emerges below $\sim 0.25\,\mathrm{K}$. For higher fields, the zero-field cooled and field cooled data are identical. The transition temperature T_C is defined as the mean value of the inflection points of the field cooled and field heated data. The data show a similar behaviour, but on a different temperature and field scale, for fields along $\langle 111 \rangle$ and $\langle 110 \rangle$. For field along $\langle 100 \rangle$, the system behaves different as compared to the other field directions.

atures shows the first-order transition into a ferromagnetic state. The zero-field cooled branch also shows a spin freezing below ∼0.1 K. Under increasing field the transition shifts up in temperature, reaching a maximum value of ∼0.54 K at an internal field of ∼0.3 T before decreasing again. The transition vanishes for fields exceeding ∼0.57 T. Even though the field dependence of the transition is reminiscent of that observed for ⟨111⟩, it does not develop a significant peak for higher fields. Also the kink is not as pronounced, and the hysteresis is slightly smaller. In high field, the magnetisation first grows monotonically and reaches saturation for temperatures below ∼0.25 K.

In Fig. 4.12(C1 to C5), the magnetisation as function of temperature for fields along the ⟨100⟩ direction is shown. Data were recorded between 0.05 K and 0.9 K and fields up to 0.6 T, cf. App. A.2, Fig. A.3. At low fields, the temperature dependence of the magnetisation compares with the other directions, exhibiting a jump at ∼0.28 K. Applying higher fields lead to a different behaviour entirely. In low fields, the zero-field cooled and field cooled branches show again a splitting below ∼0.25 K, with a reduction characteristic of spin freezing in the zero-field cooled branch below ∼0.1 K. The splitting persists up to ∼0.05 T before disappearing. The jump in the magnetisation displays a rounding with a small hysteresis already at ∼0.07 T, without developing a kink. The hysteresis entirely disappears above ∼0.15 T, showing no signs of the reduction at larger fields as observed for ⟨111⟩ and ⟨110⟩. In high fields, the magnetisation grows monotonically for decreasing temperature, and saturates for temperatures below ∼0.5 K.

Comparing the three field directions, the qualitative shape of the curves is the same for all three directions at small fields, showing a strongly hysteretic transition at ∼0.28 K. For field along ⟨100⟩, the hysteresis vanishes below ∼0.15 T, and the system enters a field polarised state already at small fields. The temperature dependent magnetisation behaves similarly for the other two directions up to ∼0.4 T, where the curves develop a peak with a considerable hysteresis observed for field along ⟨111⟩. Below the peak the magnetisation drops to a constant value. This feature is less strongly observed for field along ⟨110⟩, and not observed for field along ⟨100⟩. Further, for ⟨111⟩ the system fully polarises at slightly larger fields as compared to ⟨110⟩, i.e. > 0.63 T for fields along ⟨111⟩ and > 0.57 T for fields along ⟨110⟩.

4.4.3. Field Dependence after Zero-Field Cooling

The magnetic field dependence of the magnetisation in $Yb_2Ti_2O_7$ for field along the three main symmetry directions was measured at various temperatures according to the protocol described in Sec. 4.3.2 and in App. A.1, Tab. A.2, A.4 and A.6.
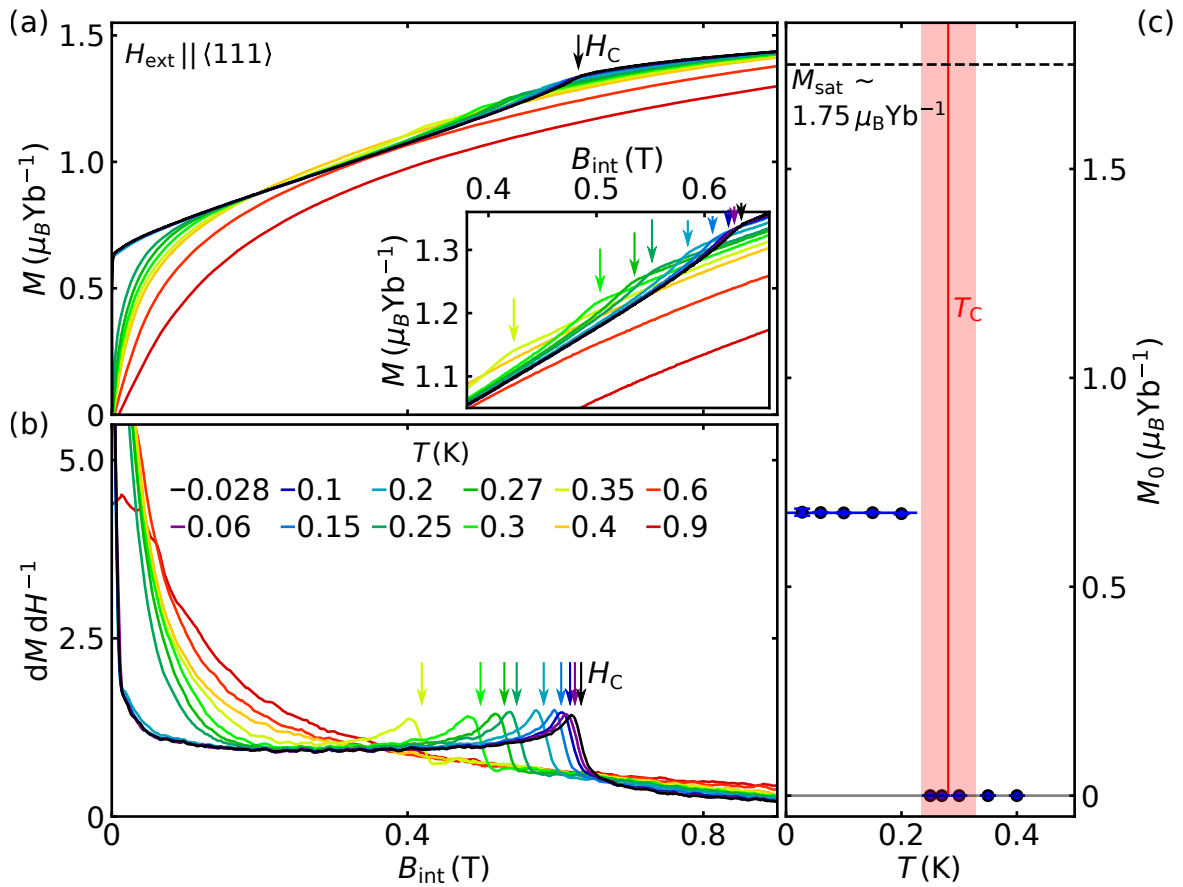
Figure 4.13.: Magnetisation dependence of Yb$_2$Ti$_2$O$_7$ for field along $\langle 111 \rangle$. (a) Magnetisation as a function of internal magnetic field after zero-field cooling and correction of demagnetising fields. The magnetisation has a kink/jump that decreases in field with increasing temperature until it disappears at high temperatures. The inset shows a close-up of the region where the kink/jump appears. (b) Susceptibility $\mathrm{d}M\mathrm{d}H^{-1}$ calculated from the magnetisation data. A discontinuity in the field driven transition is observed. (c) Spontaneous magnetic moment M_0 as a function of temperature. The spontaneous magnetisation is temperature independent and vanishes discontinuously above the same transition temperature T_C observed in the temperature dependence of the magnetisation. The transition temperature in the limit of very small fields is marked in red, with the red shaded area representing the difference of the transition temperature upon heating and cooling.

Besides the magnetisation measurements at low temperatures using the vibrating coil magnetometer, measurements between $3\,\mathrm{K}$ and $50\,\mathrm{K}$ for fields up to $9\,\mathrm{T}$ were performed in a standard Oxford instruments vibrating sample magnetometer. At high temperatures, Yb$_2$Ti$_2$O$_7$ shows typical paramagnetic behaviour in applied magnetic field, that will not be shown and discussed in detail.

Fig. 4.13(a,b) shows the field dependence of the magnetisation and its calculated deriva-

tive, i.e. the magnetic susceptibility $\mathrm{d}M\mathrm{d}H^{-1}$, for temperatures between $0.028\,\mathrm{K}$ and $0.9\,\mathrm{K}$ and field along $\langle 111 \rangle$. The data shown were recorded after zero-field cooling. Following correction of demagnetising fields, data is plotted against internal magnetic field B_{int}. Apart from shifting characteristic features in the magnetisation towards lower fields, demagnetisation effects do not affect the conclusions presented in the following. At low temperatures, below the first-order phase transition observed in the temperature dependence, a temperature independent spontaneous magnetic moment is observed that vanishes for temperatures above the transition temperature as shown in Fig. 4.13(c). This supports the formation of a ferromagnetic state. The spontaneous magnetisation was obtained by extrapolating the low field behaviour of the zero-field cooled magnetisation data linearly to zero field. The red line represents the transition temperature determined by the temperature dependence of the magnetisation at vanishingly small field, and the red shaded area indicates the difference in the transition temperature upon heating versus cooling. The initial jump in magnetisation reaches a value of $M_0 \sim 0.68\,\mu_{\mathrm{B}}\mathrm{Yb}^{-1}$. A discussion about the strength of the spontaneous magnetic moment as a function of field direction will be presented at the end of this section, together with a comparison with theoretical predictions.

After the initial jump, the magnetisation increases monotonically with increasing field. For fields between $\sim 0.25\,\mathrm{T}$ and $\sim 0.45\,\mathrm{T}$, a cross-over between the different temperatures is observed. This cross-over is reversed after the magnetisation shows a kink that defines H_{C}. Above H_{C}, the magnetisation increases monotonically with a smaller slope as for fields below H_{C}. The kink defining H_{C} can be seen as a smeared out jump in the magnetisation, which is supported by regarding the calculated magnetic susceptibility shown in Fig. 4.13(b). This discontinuity suggests a first-order transition at $\sim 0.63\,\mathrm{T}$ for the lowest temperature. For increasing temperature, this phase transition shifts towards smaller fields, before it vanishes for temperatures above $0.35\,\mathrm{K}$. This field driven phase transition is still present for temperatures above the transition temperature found in the temperature dependence, which is consistent with the initial increase in the ordering temperature under applied fields. For temperatures above T_{C}, no spontaneous magnetic moment is observed in the field dependence. At highest temperatures, the magnetisation asymptotically approaches the saturation magnetisation for increasing fields, without any field driven phase transition.

Shown in Fig. 4.14(a,b) is the field dependence of the magnetisation and the magnetic susceptibility for temperatures between $0.090\,\mathrm{K}$ and $0.6\,\mathrm{K}$, and field along $\langle 110 \rangle$. In contrast to the measurements for field along $\langle 111 \rangle$ in Fig. 4.13, data for field along $\langle 110 \rangle$ in Fig. 4.14 were recorded without zero-field cooling, after finding no significant differences between data recorded with and without zero-field cooling when swept in the same direc-

tion. The data is plotted against internal magnetic field. The field dependence compares qualitatively with that observed for $\langle 111 \rangle$, showing a spontaneous magnetic moment for temperatures below the transition temperature T_C as inferred from the temperature dependence of the magnetisation. The spontaneous moment M_0 as function of temperature, shown in Fig. 4.14(c), is with $M_0 \sim 0.83 \, \mu_B \text{Yb}^{-1}$ slightly larger than M_0 observed for $\langle 111 \rangle$.

The magnetisation increases monotonically with increasing field, and shows a kink that defines H_C. In contrast to the magnetisation for fields along $\langle 111 \rangle$, the kink does not show a discontinuity in the magnetisation, as can be seen in the calculated magnetic susceptibility shown in Fig. 4.14(b).

For fields along $\langle 100 \rangle$ the system behaves differently compared to the other field directions, i.e. $\langle 111 \rangle$ and $\langle 110 \rangle$, consistent with the temperature dependence presented above. Fig. 4.15(a,b) shows the field dependence of the magnetisation and its calculated magnetic susceptibility for temperatures between $0.065 \, \text{K}$ and $0.9 \, \text{K}$. Data were recorded after zero-field cooling and is plotted as a function of internal magnetic field. At low temperatures, below T_C inferred from the temperature dependence, the magnetisation jumps to a spontaneous magnetic moment of $M_0 \sim 1.20 \, \mu_B \text{Yb}^{-1}$. This is significantly larger than the values observed for fields along $\langle 111 \rangle$ and $\langle 110 \rangle$. The spontaneous moment M_0 as function of temperature is shown in Fig. 4.15(c). For increasing fields, the magnetisation is approaching its saturation asymptotically, without a field driven phase transition.

Fig. 4.16(a) compares the field dependence of the magnetisation and the calculated susceptibility for applied fields up to $5 \, \text{T}$ along $\langle 111 \rangle$, $\langle 110 \rangle$, and $\langle 100 \rangle$, respectively. Following the change of slope for field along $\langle 111 \rangle$ and $\langle 110 \rangle$, respectively, the magnetisation reaches the same value and has the same slope as for field along $\langle 100 \rangle$. This suggests that at these points, for field along $\langle 111 \rangle$ and $\langle 110 \rangle$, respectively, the system enters the same state as for field along $\langle 100 \rangle$. Beyond the change of slope, the magnetisation shows no further features. For field along $\langle 100 \rangle$, no field driven feature can be seen, which is also supported by the calculated susceptibility of the data. At an applied field of $5 \, \text{T}$, the magnetisation is not yet saturated.

Magnetisation measurements at $3 \, \text{K}$ for applied fields up $9 \, \text{T}$ using a vibrating sample magnetometer along the three main symmetry directions are shown in Fig. 4.16(b). The magnetisation for temperatures at and above $3 \, \text{K}$ is identical for the three main symmetry directions. At $9 \, \text{T}$, the magnetisation has reached a value of $\sim 1.75 \, \mu_B \text{Yb}^{-1}$, but still shows a very small, but finite, slope. This suggests, that the system is almost saturated at $\sim 1.75 \, \mu_B \text{Yb}^{-1}$, which is in excellent agreement with Lhotel *et al.* for compacted powder of Yb$_2$Ti$_2$O$_7$ in fields up to $7 \, \text{T}$ [137].

For any field direction, the magnetisation increases asymptotically towards saturation,
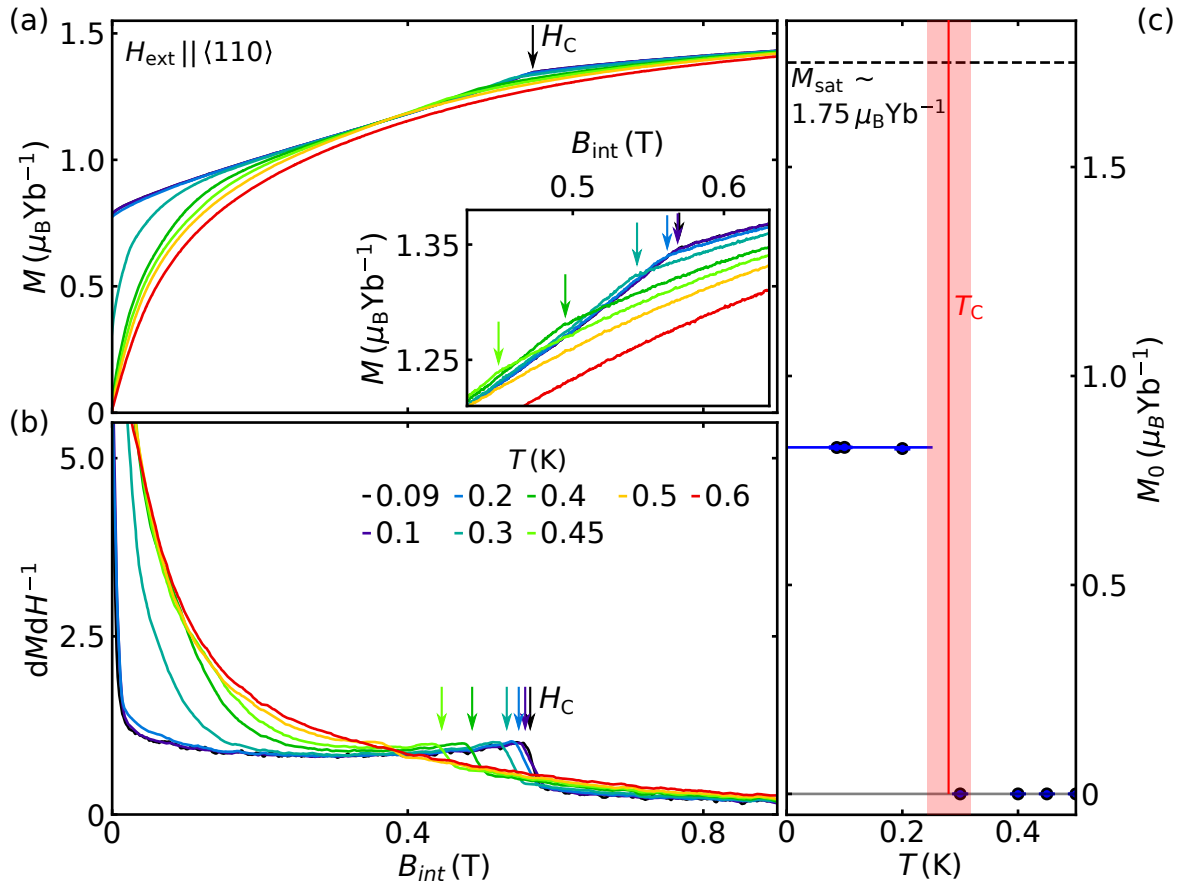
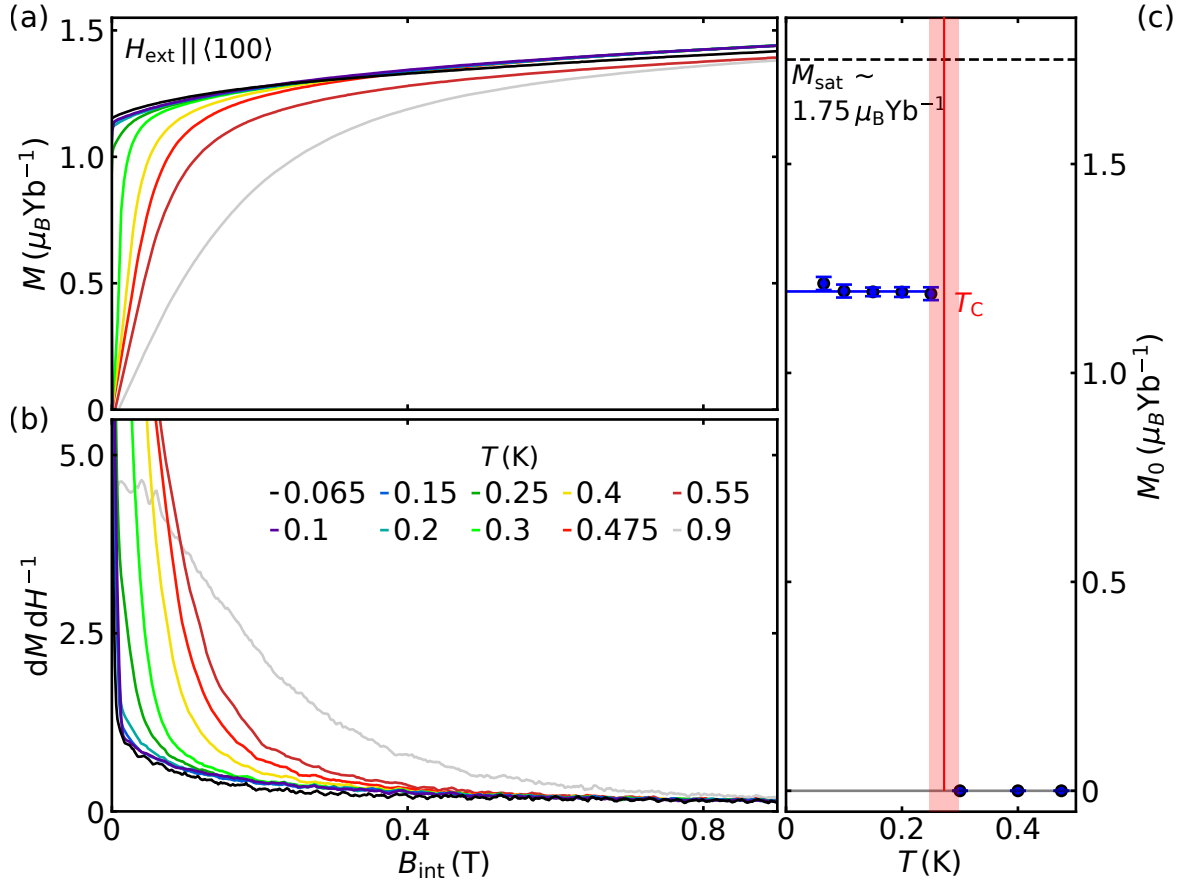**Figure 4.14.:** Magnetisation dependence of $Yb_2Ti_2O_7$ for field along $\langle 110 \rangle$. (a) Magnetisation as a function of internal magnetic field after correction of demagnetising fields. The magnetisation has a kink that decreases in field with increasing temperature until it disappears at high temperatures. The inset shows a close-up of the region where the kink appears. (b) Susceptibility $\mathrm{d}M\mathrm{d}H^{-1}$ calculated from the magnetisation data. In contrast to field along $\langle 111 \rangle$, the field driven transition shows no discontinuity. (c) Spontaneous magnetic moment M_0 as a function of temperature. The spontaneous magnetisation is temperature independent and vanishes discontinuously above the same transition temperature T_C observed in the temperature dependence of the magnetisation. The transition temperature in the limit of very small fields is marked in red, with the red shaded area representing the difference of the transition temperature upon heating and cooling.

and very high fields are required to reach saturation. This is a characteristic signature of systems with strong anisotropic interactions, which do not have rotational symmetry around the field axis. In this case, zero-point quantum fluctuations are present at all fields, reducing the magnetisation compared to the fully possible value, and the field only gradually polarises the system [144, 164].

A significant difference between the three field directions may be seen in the sponta-

Figure 4.15.: Magnetisation dependence of Yb$_2$Ti$_2$O$_7$ for field along $\langle 100 \rangle$. (a) Magnetisation as a function of internal magnetic field after zero-field cooling and correction for demagnetising fields. (b) Susceptibility $\mathrm{d}M\mathrm{d}H^{-1}$ calculated from the magnetisation data. (c) Spontaneous magnetic moment M_0 as a function of temperature. The spontaneous magnetisation is temperature independent and vanishes discontinuously above the same transition temperature T_C observed in the temperature dependence of the magnetisation. The transition temperature in the limit of very small fields is marked in red, with the red shaded area representing the difference of the transition temperature upon heating and cooling.

neous magnetisation. The spontaneous magnetic moment increases when going from the $\langle 111 \rangle$ via $\langle 110 \rangle$ to the $\langle 100 \rangle$ direction. Only at higher temperatures, i.e. above 3 K, the magnetisation as a function of internal field is essentially isotropic. A more detailed study of the spontaneous magnetisation including comparison with theory will be presented in Sec. 4.4.5.

The susceptibility calculated from the magnetisation data reveals differences in the field driven phase transition between field along $\langle 111 \rangle$ and $\langle 110 \rangle$. For field along $\langle 111 \rangle$, the magnetisation shows a smeared out jump, while for field along $\langle 110 \rangle$, the magnetisation displays a kink, rather than a jump. At 0.25 K, just below the phase transition found in
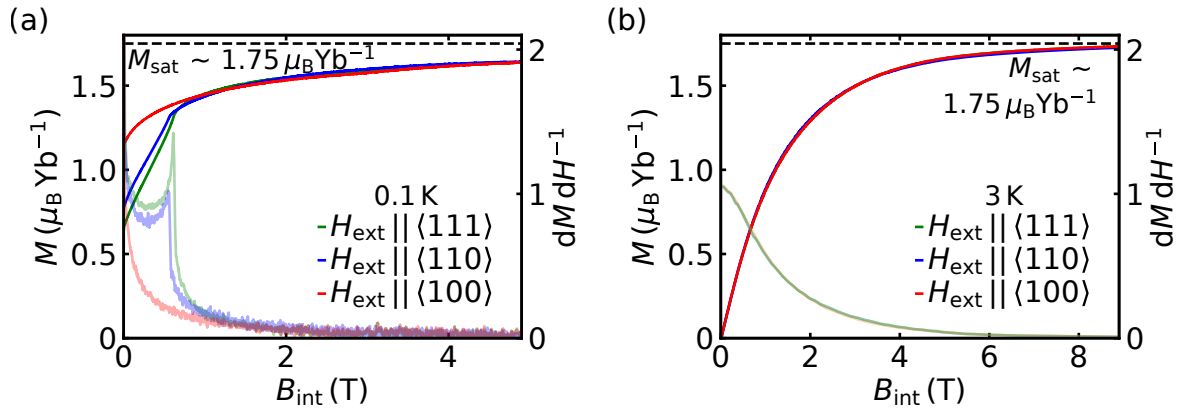
Figure 4.16.: Comparison of the magnetisation as a function of internal magnetic field of $Yb_2Ti_2O_7$ along $\langle 111 \rangle$, $\langle 110 \rangle$, and $\langle 100 \rangle$. (a) Data were recorded at $0.1\,\text{K}$ after zero-field cooling for applied fields up to $5\,\text{T}$. Data were featureless for field along $\langle 100 \rangle$. For fields along $\langle 111 \rangle$ and $\langle 110 \rangle$, data for fields above the change of slope are featureless and the magnetisation reaches the same value and slope as for field along $\langle 100 \rangle$. (b) Magnetisation measurements recorded with a vibrating sample magnetometer at $3\,\text{K}$ as a function of field up to $9\,\text{T}$ along $\langle 111 \rangle$, $\langle 110 \rangle$, and $\langle 100 \rangle$, respectively. All three magnetisation curves are essentially identical. At $9\,\text{T}$ the magnetisation is nearly saturated at $\sim 1.75\,\mu_\text{B}\text{Yb}^{-1}$.

the temperature dependence of the magnetisation, the initial jump in the magnetisation at the start of the sweep is smeared out for field along $\langle 111 \rangle$, while it is unchanged sharp for the other two field directions. At $0.3\,\text{K}$, the initial increase in magnetisation is no longer vertical, i.e. no spontaneous magnetic moment is observed, for any direction.

4.4.4. Magnetic Field Dependence of Hysteresis Loops

The magnetic field dependence of hysteresis loops was measured according to the protocol described in Sec. 4.3.2. While Sec. 4.4.3 focused on the zero-field cooled field dependence, hysteresis loops of the magnetisation for different temperatures will be presented in the following. Data were recorded following the sequence $0 \rightarrow +1\,\text{T} \rightarrow -1\,\text{T} \rightarrow +1\,\text{T}$. Zero-field cooled branches following the sequence $+1\,\text{T} \rightarrow -1\,\text{T} \rightarrow +1\,\text{T}$ are not shown.

Fig. 4.17(A1, B1, C1) show the field dependence of the magnetisation for different temperatures along $\langle 111 \rangle$, $\langle 110 \rangle$, and $\langle 100 \rangle$, respectively. Data are shown as a function of internal magnetic field, after correcting the effects of demagnetising fields. As the magnetic field dependence for fields along all three main symmetry directions is point symmetric with respect to the $B = 0$, only the first quadrant of the hysteresis loop is shown. The susceptibility calculated from the measured magnetisation are plotted in Fig. 4.17(A2, B2, C2). For better visibility, data are shifted vertically by a constant.

The field driven feature for field along $\langle 111 \rangle$ and $\langle 110 \rangle$, respectively, shows the same
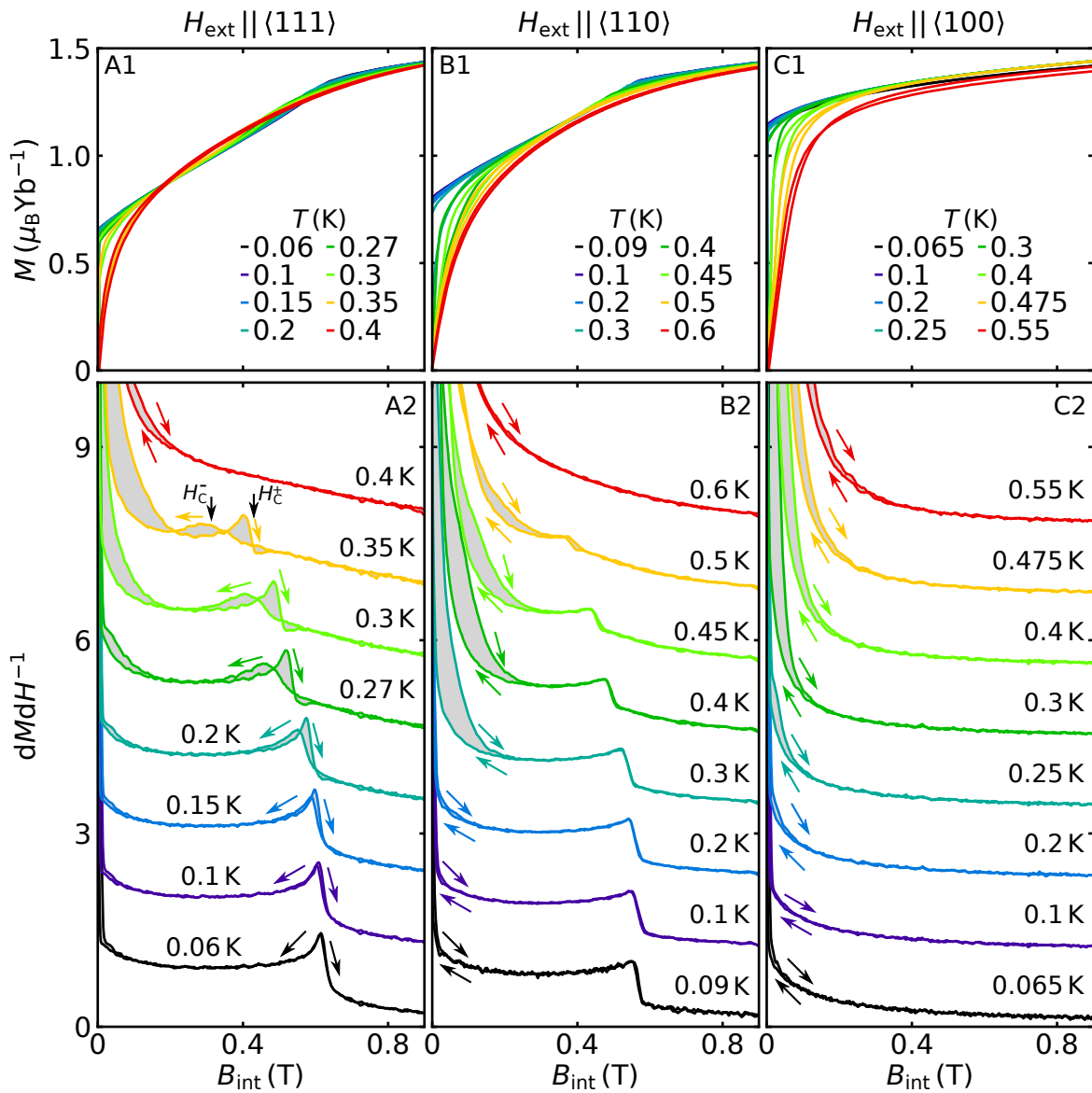
Figure 4.17.: First quadrant of the hysteresis loops for field along the three main symmetry directions in Yb$_2$Ti$_2$O$_7$. Field dependence of the magnetisation as function of internal magnetic field for field along $\langle 111 \rangle$ (A1), $\langle 110 \rangle$ (B1), and $\langle 100 \rangle$ (C1). The numerical derivative of the experimental data are shown in panels A2, B2, and C2. The curves are shifted with respect to each other to better illustrate the hysteretic behaviour. The coloured arrows indicate the direction of the field sweep, i.e. increasing and decreasing field sweeps. As an example, the measurement at $0.35\,\mathrm{K}$ shows where the transition field for increasing and decreasing sweeps were taken.

temperature dependence as for the zero-field cooled magnetisation. Namely, for field along $\langle 111 \rangle$, the feature shifts to smaller fields for increasing temperature, and eventually vanishes.

For field along $\langle 111 \rangle$, the discontinuity in the magnetisation shows hysteretic behaviour. For field sweeps up to $\pm 1\,\text{T}$, the phase transition is located at the same field as for the zero-field cooling. Further, the qualitative field dependence of the magnetisation is the same. In comparison, under decreasing field starting from $\pm 1\,\text{T}$, the transition shifts to lower fields with increasing temperature, and gets rounded and smeared out. The hysteresis is most pronounced for the highest temperature at which the transition can still be discerned. With decreasing temperatures the hysteresis is no longer visible below $\sim 0.1\,\text{K}$. This is counter-intuitive, as a first-order phase transition is expected to show hysteretic behaviour even in the low temperature limit. Interestingly, the temperatures where the hysteresis vanishes coincides with the spin freezing observed in the temperature dependence of the magnetisation. In comparison, the field driven feature for field along $\langle 110 \rangle$ shows no hysteretic behaviour at all.

All three directions show a small hysteresis with respect to zero field. This hysteresis vanishes for temperatures below $\sim 0.1\,\text{K}$. For increasing temperature, the hysteresis increases, and vanishes for temperatures where the system no longer enters the ferromagnetic state.

4.4.5. Comparison with Theory

The experimental data may be described to some extent by the theoretical model introduced in Sec. 4.2. Besides the general aspects of the Potts model summarised in Sec. 4.2, the experimental challenges applying the Potts model to an experimental realisation are discussed in Sec. 4.2.1. The model was found to describe the systems low field behaviour, and also predicts the first-order phase transition for field along $\langle 111 \rangle$, as well as a higher-order phase transition for field along $\langle 110 \rangle$. In the following, the experimental data are compared to the theoretical predictions.

Assuming cubic anisotropy selecting six ground states within the Potts model. This allows to predict the applied magnetic field necessary for reaching the spontaneous magnetisation M_0, i.e. without correcting for demagnetising fields, as well as the strength of M_0, as a function of field direction, cf. Eq. (4.25-4.26). This saturation field was obtained by the magnetisation data not corrected for demagnetising fields as shown in Fig. 4.18(a), where the zero-field cooled magnetisation data taken at $0.1\,\text{K}$ are plotted against applied field. The saturation field was defined where the initial increase in magnetisation ends, i.e. the spontaneous jump in magnetisation when correcting for demagnetising fields as

shown in Fig. 4.18(b). The spontaneous magnetic moment was obtained as described in Sec. 4.4.3, by extrapolating the low field behaviour of the zero-field cooled magnetisation data linearly to zero field.
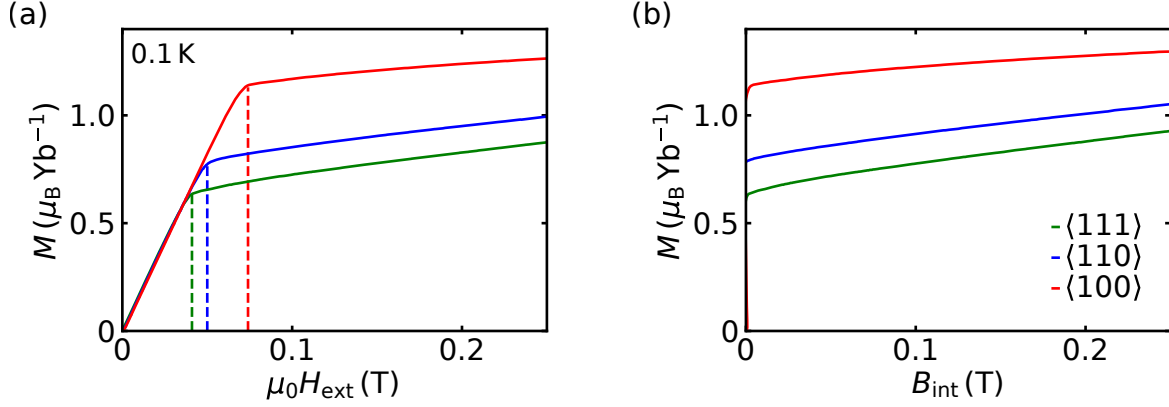
Figure 4.18.: Magnetic field dependence of the magnetisation of Yb$_2$Ti$_2$O$_7$ up to 0.25 T. Data were recorded at 0.1 K after zero-field cooling as a function of applied magnetic field along $\langle 111 \rangle$, $\langle 110 \rangle$, and $\langle 100 \rangle$. (a) Magnetisation data before correcting for demagnetising fields. The dashed lines mark the saturation fields, which are: 0.074 T for $\langle 100 \rangle$; 0.050 T for $\langle 110 \rangle$; 0.041 T for $\langle 111 \rangle$. (b) Magnetisation data after correction of demagnetisation effects. Adding the demagnetising field to the applied field turns the initial linear rise in (a) to a vertical line.

Tab. 4.2 summarises the spontaneous magnetic moment and the applied field to reach that moment, i.e. the saturation field, obtained from the experimental data, and compares them to the theoretical predictions. Relative relations between the spontaneous moments are found to be

$$M_{0,\langle 100 \rangle} : M_{0,\langle 110 \rangle} = 1 : 0.69,$$

$$M_{0,\langle 100 \rangle} : M_{0,\langle 111 \rangle} = 1 : 0.56,$$

and for the applied field necessary to reach the spontaneous moments

$$H_{\text{ext},\langle 100 \rangle} : H_{\text{ext},\langle 110 \rangle} = 1 : 0.68,$$

$$H_{\text{ext},\langle 100 \rangle} : H_{\text{ext},\langle 111 \rangle} = 1 : 0.55.$$

The ratios are in excellent agreement with the ratios predicted by the model given in Eq. (4.25) and Eq. (4.26).

Fig. 4.19 compares the experimental data of the magnetisation of Yb$_2$Ti$_2$O$_7$ recorded at 0.1 K, shown in panels (a) and (b), with mean-field calculations at $T = 0$ performed by Tchernyshyov [154], shown in panels (c) and (d). The model considers a simple statistical mechanical model based on a unit vector of magnetisation with fourth- and sixth-order

Table 4.2.: Spontaneous magnetic moment and saturation field required to reach this moment from the experimental data of $Yb_2Ti_2O_7$ for field along $\langle 100 \rangle$, $\langle 110 \rangle$, and $\langle 111 \rangle$. The ratios between the spontaneous moments and the corresponding saturation fields are in excellent agreement with the predicted ratios in Eq. (4.25) and Eq. (4.26).

field direction	M_0 $(\mu_{\mathrm{B}} \mathrm{Yb}^{-1})$	ratio $M_0/M_{0,100}$	$\mu_0 H_{\mathrm{ext}}$ (T)	ratio $H_{\mathrm{ext}}/H_{\mathrm{ext},100}$	ratio theory
$\langle 100 \rangle$	1.20	1	0.074	1	1
$\langle 110 \rangle$	0.83	0.69	0.05	0.68	$1/\sqrt{2}$
$\langle 111 \rangle$	0.68	0.56	0.041	0.55	$1/\sqrt{3}$

cubic anisotropies, as suggested by Cullen and Callen [165]. The approximation is based on a coarse-grained description in which spins of each tetrahedron were represented by a magnetic moment of fixed length. The length of these effective spins increases with increasing field, as microscopic ionic moments turn toward the direction of the field. This realises the $(q = 3)$-Potts model discussed in Sec. 4.2. Therefore, the model takes into account a cubic anisotropy and the Zeeman field. $\boldsymbol{M}$ is treated as a unit vector and the scale of $\boldsymbol{H}$ is arbitrary. The mean-field calculation shown in Fig. 4.19(c) uses parameters obtained by Ross *et al.* [103].

Regarding the theoretical magnetisation, a field along the $\langle 100 \rangle$ polarises the system featureless. Magnetising along $\langle 111 \rangle$ and $\langle 110 \rangle$ are accompanied by a distinct change of slope. The field strength of this change of slope along $\langle 111 \rangle$ is lower than for $\langle 110 \rangle$. The latter is not in agreement with the experimental data, were the upper critical field for $\langle 111 \rangle$ is higher than for $\langle 110 \rangle$. Even at higher fields, a finite susceptibility is observed experimentally, characteristic of an increasing magnetisation. This is not accounted for in the theoretical model, as additional fluctuations are not included. Overall, the trends at low temperatures are described rather well by the model.

The discontinuous onset of saturation for field along $\langle 111 \rangle$ is in accord with Landau theory of this transition, cf. Sec. 4.2. This also could explain the hysteresis observed in magnetisation at high fields for temperatures above $0.1\,\mathrm{K}$, but not the absence of the hysteresis at lowest temperatures which, empirically, may be related to the spin freezing process, cf. Fig. 4.4.4 A2.

The transition in the magnetisation for field along $\langle 110 \rangle$ is continuous in theory, again consistent with Landau theory, and no hysteresis is expected at high fields. The data show a kink in the magnetisation. This is consistent with theory, as well as the absence of a hysteresis, cf. Fig. 4.4.4 B2.

Only the wrong sorting of the upper critical field for $\langle 111 \rangle$ and $\langle 110 \rangle$ is inconsistent with
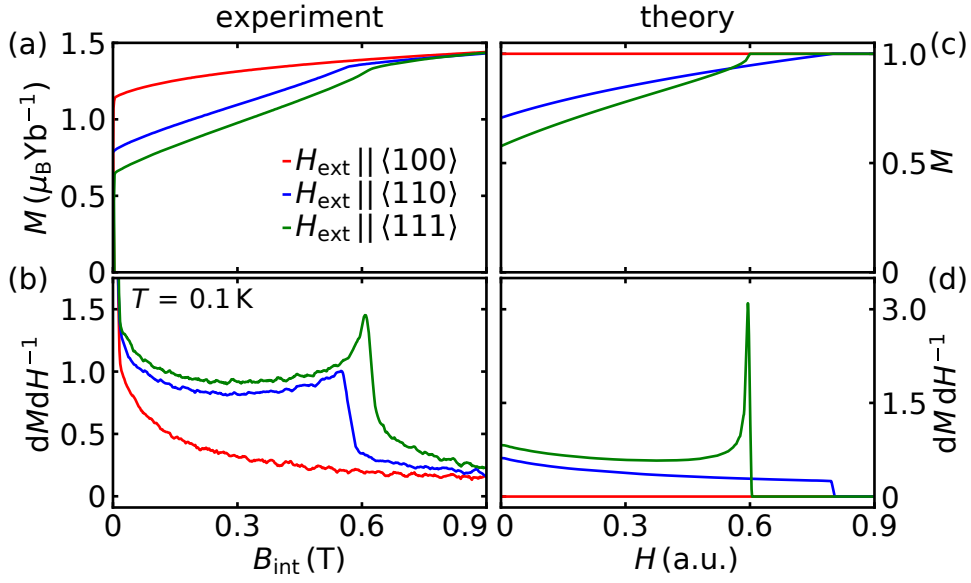
Figure 4.19.: Experimental and theoretical magnetisation of $Yb_2Ti_2O_7$. (a) Magnetic field dependence of the magnetisation of $Yb_2Ti_2O_7$ at $0.1\,\mathrm{K}$ for field along $\langle 111 \rangle$, $\langle 110 \rangle$, and $\langle 100 \rangle$. (b) Susceptibility $\mathrm{d}M\mathrm{d}H^{-1}$ calculated from the magnetisation data. (c) Mean-field calculation at $T = 0$, taking into account a cubic anisotropy and the Zeeman field. $\boldsymbol{M}$ is treated as a unit vector and the scale of $\boldsymbol{H}$ is arbitrary. (d) Susceptibility calculated from the theoretical model of the magnetisation shown in panel (c). Calculations in (c) and (d) are taken from Ref. [154].

the theoretical model. A recent study by Changlani discusses the influence of quantum mechanical effects on the properties of $Yb_2Ti_2O_7$ [166]. Changlani showed that frustrated interactions and quantum effects significantly renormalise the critical field and, hence, quantum calculations are necessary to describe the discrepancies between experiment and classical theories [166]. Comparing the experimental data for upper critical field with theoretical calculations including quantum effects [166, 167] gives for

$$\text{field along } \langle 111 \rangle : \quad H_{\mathrm{C, exp.}} \sim 0.63\,\mathrm{T} \quad \text{and} \quad H_{\mathrm{C, theo.}} \sim 0.58\,\mathrm{T},$$
$$\text{field along } \langle 110 \rangle : \quad H_{\mathrm{C, exp.}} \sim 0.57\,\mathrm{T} \quad \text{and} \quad H_{\mathrm{C, theo.}} \sim 0.30\,\mathrm{T}.$$

The calculations show fields which are significantly lower than classical estimations, and account for a higher critical field along $\langle 111 \rangle$ than along $\langle 110 \rangle$, which both is in good agreement with the experimental data.

4.5. Conclusions and Outlook

The magnetic phase diagram of $Yb_2Ti_2O_7$ for applied magnetic field shows an unusual field dependence of a first-order phase boundary, wherein an applied field initially increases the

ordering temperature, giving a reentrant type phase diagram. Thereby, the direction of the applied field strongly influences the phase diagram.

In zero field, the phase transition from the paramagnet to the splayed ferromagnet was found to be of first-order. A first-order nature is supported by the strong hysteresis found in the temperature dependence of the magnetisation, and also by the fact that the phase transition is observed in finite fields. If the phase transition would be of second-order within Landau theory, applying a magnetic field would break time reversal symmetry. Since applying a magnetic field also breaks time reversal symmetry, a second-order phase transition would strictly only occur for zero field. If the transition is of first-order, however, the transition would survive for finite fields, which is consistent with the experimental data in the present work and Ref. [144].

For applying higher fields along $\langle 111 \rangle$ and $\langle 110 \rangle$, the phase boundary sweeps back until it terminates at $T = 0$, indicating a field driven quantum phase transition. This was confirmed in theoretical calculations, were the reorganisation of the energy levels was found as evidence for a quantum phase transition [166, 167]. Between field along $\langle 111 \rangle$ and $\langle 110 \rangle$, the phase boundary is distorted along the field axis and stretched along the temperature axis. Whereas for field along $\langle 100 \rangle$, the upper phase boundary is absent.
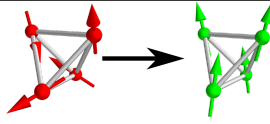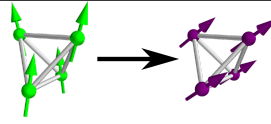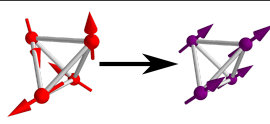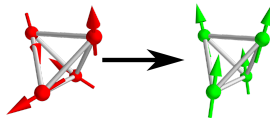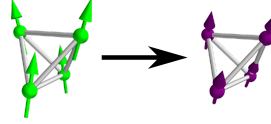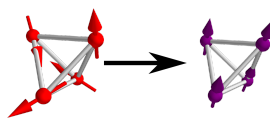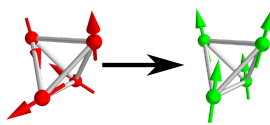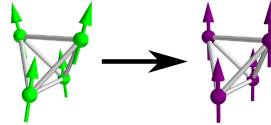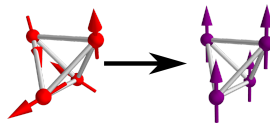
The ground state was found to be of ferromagnetic like order. Applying a magnetic field spontaneously selects the direction of the ferromagnetic polarisation along one of the six cubic axes. The canting of the magnetic moments is towards the local 3-fold $\langle 111 \rangle$ axes, forming the splayed ferromagnetic state. For field along $\langle 100 \rangle$ the paramagnet and the ordered phase have the same symmetry without a phase transition needed [144], consistent with the high spontaneous moment and the absence of a field driven phase transition in the data.

For fields as high as observed during the present work, i.e. up to $5\,\mathrm{T}$ at low temperatures, and up to $9\,\mathrm{T}$ at higher temperatures, the data show an increasing magnetisation. The field gradually polarises the system with spins along the applied magnetic field, struggling additional fluctuations.

Tab. 4.3 summarises the observed phase transitions in $\mathrm{Yb_2Ti_2O_7}$ for field along $\langle 111 \rangle$, $\langle 110 \rangle$, and $\langle 100 \rangle$. The schematics in Tab. 4.3 illustrate the spin arrangement on one tetrahedron for the different phases found in $\mathrm{Yb_2Ti_2O_7}$.

Further, a simple classical model based on the Potts model for cubic ferromagnets describes the low temperature behaviour of $\mathrm{Yb_2Ti_2O_7}$ to some extent. The model predicts the first-order field driven phase transition along $\langle 111 \rangle$, and a higher-order phase transition for field along $\langle 110 \rangle$, as well as the absence of a field driven phase transition along $\langle 100 \rangle$. However, the classical estimates of the field strength of these phase transitions are inconsistent with the experimental data found in the present work. Frustrated interac-

Table 4.3.: Phase transitions in Yb$_2$Ti$_2$O$_7$ for field applied along $\langle 111 \rangle$, $\langle 110 \rangle$, and $\langle 100 \rangle$. The type of transition from paramagnetic (PM) to splayed ferromagnetic (FM) state, from splayed ferromagnetic to the field polarised (FP) state, and from paramagnetic to field polarised state are shown.

$H_{\text{ext}} \parallel$	PM $\rightarrow$ s-FM	s-FM $\rightarrow$ FP	PM $\rightarrow$ FP
$\langle 111 \rangle$	1st-order	1st-order	crossover
$\langle 110 \rangle$	1st-order	2nd-order	crossover
$\langle 100 \rangle$	1st-order	crossover	crossover

tions and quantum effects significantly renormalise the critical field, making it necessary to take quantum effects into account [166]. Including quantum calculations explains the discrepancies between experimental data and classical calculations [166, 167]. These renormalisation effects might also be responsible for the reentrant type phase diagram [166].

5. Critical Spin Wave Dynamics in Iron

Iron is one of the archetypical ferromagnets, and allows to study the critical fluctuations at a continuous phase transition. In a recent study the behaviour of the critical dynamics at the transition from the para- to the ferromagnetic phase in iron was reported, employing the high resolution spin echo technique MIEZE [47]. Thereby, the focus was on temperatures above the Curie temperature, i.e. $T > T_C$, where the spin echo signal is described by a single exponential decay, characteristic for critical fluctuations in the paramagnetic regime. The study in the present work continues the previous investigation of the critical phenomena at continuous phase transitions for temperatures below T_C, in the ferromagnetic phase in iron. When going below T_C, inelastic scattering of spin waves in the ferromagnetic phase drastically alters the excitation spectrum. The spin echo signal takes the form of a cosine oscillation damped by an exponential decay, where the frequency of the oscillation is a measure for the energy of the excitation. The MIEZE technique is ideally suited for investigating magnetic phase transitions, as it allows measuring under depolarising conditions with spin echo energy resolution. A position sensitive detector further allows covering a large region in reciprocal space. Experiments were performed at the beamline RESEDA at the MLZ using the longitudinal MIEZE option. The chapter starts with a brief introduction into the critical dynamics of dipolar ferromagnets, cf. Sec. 5.1. The introduction is followed by the experimental set-up in Sec. 5.2, and the experimental results in Sec. 5.3. The chapter concludes with a summary of the present study, and an outlook, cf. Sec. 5.4.

5.1. Critical Dynamics of Dipolar Ferromagnets

The foundation to study critical dynamics at continuous phase transitions are the concepts of scaling laws [168], universality [168], and renormalisation [169]. In scaling theory, one important quantity is the correlation length ξ of the order parameter, which diverges at the transition. The inverse correlation length $\kappa = \frac{2\pi}{\xi}$ was used by Halperin and Hohenberg to define three regions for the critical behaviour of a system [170], as shown in the (q, T)-diagram in Fig. 5.1: (i) the spin wave region: the ordered phase below the Curie temperature and for $q < \kappa$; (ii) the transition region: for $q > \kappa$ which extends

to $q = 0$ at T_{C}, as ξ diverges; (iii) the hydrodynamic region: the paramagnetic phase above the Curie temperature and for $q < \kappa$. In each of these regions, different correlation functions describe the behaviour of the system.
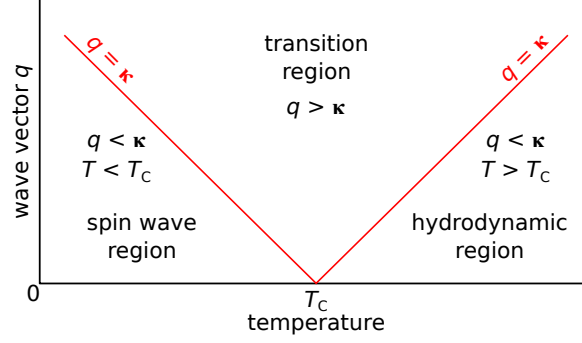

Figure 5.1.: Schematic diagram describing the three regions for different critical phenomena near the Curie temperature. (i) spin wave region: $T < T_{\mathrm{C}}$ and $q < \kappa$; (ii) transition region: $q > \kappa$; (iii) hydrodynamic region: $T > T_{\mathrm{C}}$ and $q < \kappa$. Figure adapted from Ref. [170, 171].

(i). Spin Wave Region

At low temperatures $T < T_{\mathrm{C}}$, and for $q < \kappa$, the system is in the ferromagnetically ordered spin wave region. In this region propagating spin wave modes are observed. Spin waves in dipolar ferromagnets can be described by taking exchange and dipolar interactions into account. In the absence of an external magnetic field, the classical Heisenberg ferromagnet is described by the isotropic nearest-neighbour exchange Hamiltonian

$$\mathcal{H}_{\mathrm{exchange}} = -J \sum_{\langle ij \rangle} \boldsymbol{S}_i \cdot \boldsymbol{S}_j, \tag{5.1}$$

with three components of the spin $\boldsymbol{S}$, and the nearest-neighbour exchange constant $J > 0$ for ferromagnetic interactions. With dipolar interactions the Hamiltonian takes the form

$$\mathcal{H} = \mathcal{H}_{\mathrm{exchange}} + \mathcal{H}_{\mathrm{dipolar}}. \tag{5.2}$$

A full Hamiltonian including dipolar interactions was introduced within the spin wave theory by Holstein and Primakoff [172], and summarised by Keffer [173]. From the Hamiltonian follows the spin wave energy

$$E_{\mathrm{sw}}(\boldsymbol{q}) = \sqrt{A_{\boldsymbol{q}}^2 - |B_{\boldsymbol{q}}|^2}, \tag{5.3}$$

where $A_{\boldsymbol{q}}$ describes exchange interactions and interactions between the local dipolar field and the spin waves, and $B_{\boldsymbol{q}}$ contains further dipolar contributions. Including only nearest-neighbour and next-nearest-neighbour interactions, and for small $\boldsymbol{q}$, the exchange interaction part of $A_{\boldsymbol{q}}$ takes the isotropic form

$$E_{\text{exchange}}(\boldsymbol{q}) \; = \; D\boldsymbol{q}^2, \tag{5.4}$$

where D is the spin wave stiffness. With the dipolar contributions, the spin wave energy takes the form

$$E_{\text{sw}}(\boldsymbol{q}) \; = \; \sqrt{D\boldsymbol{q}^2(D\boldsymbol{q}^2 + E_{\text{dipolar}})}, \tag{5.5}$$

with the energy of the dipolar exchange

$$E_{\text{dipolar}} \; = \; g\mu_{\text{B}}\mu_0\langle\sin^2\theta_{\boldsymbol{q}}\rangle M(T), \tag{5.6}$$

the Landé factor g, the Bohr magneton μ_{B}, the magnetic field constant μ_0, the angle $\theta_{\boldsymbol{q}}$ between $\boldsymbol{q}$ and the direction of the magnetisation, and the temperature dependent magnetisation $M(T)$. The determination of the dipolar energy in iron is described in App. B.3.2. From dynamical scaling theory follows the temperature dependence of the spin wave stiffness D close to the critical point

$$D \; = \; D_0\left(1 - \frac{T}{T_{\text{C}}}\right)^{\beta}; \quad \beta = \frac{1}{3}. \tag{5.7}$$

Approaching T_{C} from the ordered phase, the spin wave energy E_{sw} and stiffness D decrease. Further, more and more spin waves are thermally excited, reducing the magnetisation $M(T)$, hence also the dipolar energy E_{dipolar}.

The neutron scattering cross section for spin wave scattering was derived by Lowde [174] from the cross section for magnetic scattering of unpolarised neutrons given in Eq. (3.18). The delta function in the scattering function, cf. Eq. (3.19), links the energy loss/gain of the neutron to the energy of the created/annihilated excitation, implying that scattering only occurs at discrete energy transfers $\Delta E = \pm\hbar\omega$ [174]. Following Sec. 3.3.1, the scattering function for inelastic scattering of spin waves in the ferromagnetic regime shows a double Lorentzian centred at finite energy transfer of the created/annihilated excitation. This signal changes at T_{C}. The scattering function for critical fluctuations in the paramagnetic regime is described by a Lorentzian centred at zero energy transfer. The scattering function is hence given by

$$S(\boldsymbol{q},\omega) \; \propto \; \begin{cases} \frac{1}{\Gamma_q}\left(\frac{\Gamma_q^2}{(\omega-\omega_q)^2+\Gamma_q^2} + \frac{\Gamma_q^2}{(\omega+\omega_q)^2+\Gamma_q^2}\right), & \text{for } T < T_{\text{C}} \\ \frac{1}{\Gamma_q}\left(\frac{\Gamma_q^2}{\omega^2+\Gamma_q^2}\right), & \text{for } T \geq T_{\text{C}}, \end{cases} \tag{5.8}$$

with the energy $E(q) = \hbar\omega_q$ and the width Γ_q of the excitation. The expected spin echo signal, i.e. the intermediate scattering function $S(\boldsymbol{q}, \tau)$ corresponding to the scattering function $S(\boldsymbol{q}, \omega)$, for inelastic scattering of spin waves is a cosine oscillation damped by an exponential decay, where the frequency of the oscillation gives the energy of the excitation. For quasielastic scattering of critical fluctuations in the paramagnetic regime, the signal changes to a single exponential decay. The intermediate scattering function is therefore given by

$$S(\boldsymbol{q}, \tau) \propto \begin{cases} \exp\{-\Gamma_q \tau\} \cos(\omega_q \tau), & \text{for } T < T_{\mathrm{C}} \\ \exp\{-\Gamma_q \tau\}, & \text{for } T \geq T_{\mathrm{C}}. \end{cases} \tag{5.9}$$

With increasing temperature, the spin waves renormalise until the correlation length ξ becomes infinite, which defines the critical point T_{C}, and spin waves cease to exist. Further, the linewidth of the spin waves increases upon approaching T_{C}. The latter makes a high energy resolution necessary, as otherwise close to T_{C} the spin waves appear as a single, quasielastic-like excitation.

(ii). Transition Region

At the critical point spin waves are no longer present, and the critical behaviour is described by diffusive modes. Scaling theory predicts that the inverse lifetime of the critical fluctuations is given by

$$\Gamma = Aq^z, \tag{5.10}$$

with a material specific constant A expressing the energy scale of the exchange interaction, and the critical exponent $z = 2.5$.

(iii). Hydrodynamic Region

In the hydrodynamic region diffusive modes describe the critical fluctuations, and dynamical scaling theory predicts that the inverse lifetime of these critical fluctuations is given by

$$\Gamma = f(\kappa/q, q_D/\kappa)Aq^z, \tag{5.11}$$

with the dynamical scaling function $f(\kappa/q, q_D/\kappa)$ and q_D being the dipolar wave number, the material specific constant A, and the critical exponent $z = 2.5$.

In the hydrodynamic regime of the itinerant ferromagnet iron, systematic deviations of the dynamic scaling function $f(\kappa/q, q_D/\kappa)$ from the expectation for isotropic critical behaviour are observed [47]. To retain isotropic critical behaviour, a temperature dependence of the dipolar wave number q_D was introduced by Kindervater *et al.*, allowing to describe the hydrodynamic behaviour in iron within dynamical scaling theory. The deviation of the dipolar wave number from the literature value $q_D = 0.033\,\mathring{A}^{-1}$ due to the temperature dependence may be understood as an additional damping of the transverse magnetic fluctuations by spin-flip excitation of the conduction electrons [47].

The goal of the present work was to investigate the spin wave dynamics in the ferromagnetically ordered phase in iron. Thereby, the focus was on temperatures below and close to T_{C}, and small scattering vectors.

5.2. Experimental Set-up

Spin echo measurements were performed at RESEDA in the MIEZE mode, cf. Sec. 3.4. The distance between the first and second NRSE coil was 1.875 m, the distance between the second NRSE coil and the detector 3.700 m. With the sample as close to the primary spectrometer arm as possible, the sample detector distance was 2.250 m. For a high neutron flux and to cover the desired dynamic range, the wavelength was set to 6 Å with a wavelength spread $\Delta\lambda/\lambda = 0.12$. With this configuration, and frequency differences in the resonant coils between $\sim 1\,\mathrm{Hz}$ and 600 kHz, a dynamic range from $\sim 6 \cdot 10^{-6}\,\mathrm{ns}$ to 2 ns was accessible.

Measurements were performed between room temperature and $\sim 1125\,\mathrm{K}$. The sample was heated using a high temperature furnace, with a resistive niobium double cylinder heating element. Temperature was controlled with a Eurotherm 2404 controller. The furnace covers a temperature range between room temperature and $\sim 2200\,\mathrm{K}$. The temperature stability was about $\sim 0.05\,\mathrm{K}$ and no hysteresis effects were observed. Both was verified by means of several temperature scans.

The sample used in the present study is a bcc iron single crystal of cylindrical shape with a diameter of $\sim 9\,\mathrm{mm}$ and a length of $\sim 25\,\mathrm{mm}$. A $\langle 110 \rangle$ axis is aligned approximately 10° off the cylinder axis. The bcc α-Fe structure is stable for temperatures up to $\sim 1180\,\mathrm{K}$, before undergoing a phase transition into the fcc γ-Fe. Therefore, temperatures above 1180 K must be avoided in order to preserve the bcc structure. The sample was mounted vertically in the neutron beam, and a circular aperture with a diameter of 7 mm defined the illuminated sample volume. This study uses the very same single crystal as previous studies by Collins *et al.* in 1969 [171], Wicksted *et al.* in 1984 [175], and Kindervater *et al.* in 2017 [47].

5.3. Experimental Results

The following sections present the experimental results of the neutron scattering measurements in iron. Sec. 5.3.1 discusses the temperature dependence of the critical scattering, which was used to identify the Curie temperature. Further, temperature scans were used to assess temperature stability and hysteresis effects due to sweeping the temperature. The results of the spin echo measurements are presented in Sec. 5.3.2.

5.3.1. Temperature Dependence of the Critical Scattering

The temperature dependence of the small angle scattering was used to identify the Curie temperature T_C of iron, and to examine temperature stability and hysteresis effects. The detector image was evaluated according to the masks shown in Fig. 5.2(a). The masks define circular ring-segments centred at the direct beam with an opening of 60° and a width of 5 pixels, hence describing regions of constant 2θ.

  The temperature dependence of the critical scattering is shown in Fig. 5.3. Panel Fig. 5.3(a) shows the critical small angle scattering, evaluated in the different q-regions. In panel Fig. 5.3(b), the transmission through the sample is shown. A sharp, q independent peak in the scattered intensity, and a sharp minimum in the transmission through the sample at $T_C = 1045.15\,\mathrm{K}$ are the characteristic signatures of the Curie temperature. The very narrow peak at T_C suggests that there is no temperature gradient in the sample. However, the observed Curie temperature has an offset of $\sim 2\,\mathrm{K}$ to the literature value of $1043\,\mathrm{K}$ [89], that originates from a small temperature gradient between sample and thermocouple. Temperature scans were performed first while heating and subsequently during cooling the sample at the same rate, thereby, no hysteretic effects were observed. The very pronounced suppression of the transmission at T_C in Fig. 5.3(b) is a vivid example of critical opalescence at a continuous phase transition, where critical fluctuations on all time- and length-scales tremendously increase the scattering cross section, making the sample almost opaque. A broadened peak at a temperature $T^\star < T_C$ in the ferromagnetic phase is observed. This feature shifts to lower temperatures with increasing scattering vector, and may presumably be attributed to elastic small angle scattering from shrinking ferromagnetic domains when approaching the Curie temperature [47]. A similar effect was observed in EuO by Als-Nielsen *et al.* [176].

5.3.2. Quasi- and Inelastic Measurements

Measurements were performed in the SANS geometry with the direct beam in the lower right corner of the CASCADE detector, as shown in Fig. 5.2(c) and (d). With a wavelength
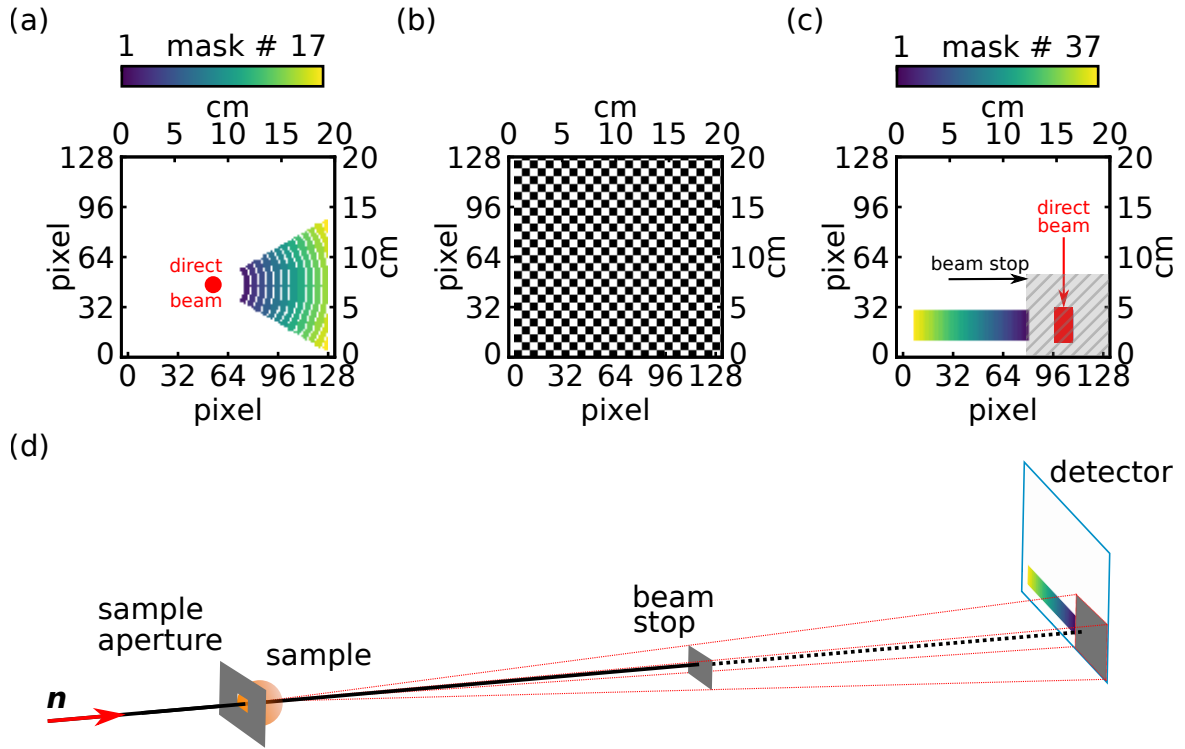
Figure 5.2.: Detector Mask used for evaluating the experimental data. (a) Masks used for the evaluation of the elastic scattering, representing circular ring-segments around the direct beam with an opening angle of $60°$ and a width of 5 pixels. Transmission through the direct beam was evaluated in a mask centred at the direct beam with a radius of 4 pixels. (b) Pre-grouping masks. The 128×128 pixels of the detector are combined in regions of $n \times n$ pixels (black and white squares). (c) Masks used for the evaluation of the MIEZE scans. The masks are segments with a width of 2 pixels and a height of 20 pixels, centred at the direct beam, and starting at the edge of the beam stop indicated by the grey hatched area. (d) Schematic of the set-up during MIEZE scans, showing how the beam stop blocks the view on the grey hatched area on the detector in (c).

of $6\,\text{Å}$, and taking into account the blocked view on the detector by the beam stop, this configuration allows covering a q-range of:

$$\text{horizontal}: \quad 0.018\,\text{Å}^{-1} \leq q \leq 0.075\,\text{Å}^{-1}$$
$$\text{vertical}: \quad 0.021\,\text{Å}^{-1} \leq q \leq 0.078\,\text{Å}^{-1}$$
$$\text{diagonal}: \quad 0.026\,\text{Å}^{-1} \leq q \leq 0.108\,\text{Å}^{-1}.$$

Data were taken in the ferro- and paramagnetic regime, in the temperature range $T_\text{C} - 21\,\text{K} \leq T \leq T_\text{C}$. The spin echo data reduction to extract the normalised intermediate scattering function follows Sec. 3.3. Comparing data evaluation using different masks showed, that choosing masks with a width of 2 pixels and a height of 20 pixels, i.e. approximately

(a)

(b)
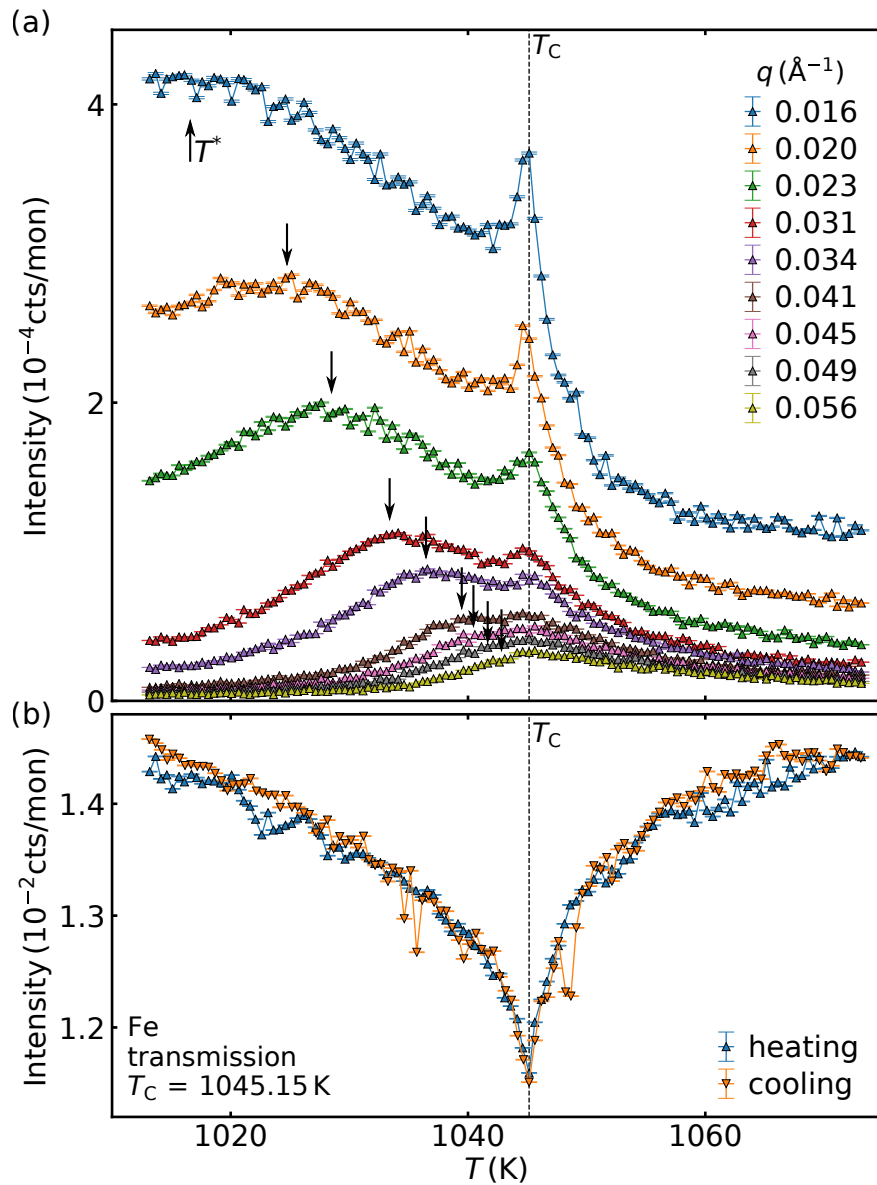
Figure 5.3.: Temperature dependence of the critical scattering around the Curie temperature in iron. (a) Critical small angle scattering for different q-regions as function of temperature. A sharp peak identifies the Curie temperature $T_C = 1045.15\,\text{K}$, marked by the dashed line. (b) Transmission through the sample as function of temperature. The sharp minimum of the transmission defines the Curie temperature, and is at the same temperature as the maximum of the critical scattering in panel (a).

the height of the illuminated sample at the detector, allows to evaluate very narrow q-regions while simultaneously retaining high statistics in the region of interest. At low spin echo times, as used in the present study, phase changes generally extend over large spatial regions. Hence, the phase within one mask does not change, and pre-grouping the detector pixels is not necessary. The procedure of pre-grouping the detector is described in Sec. 3.3.4. A comparison between evaluating the data using a pre-grouping of the detector pixels, as seen in Fig. 5.2(b), and without pre-grouping showed no significant difference. Therefore, data were evaluated using the masks shown in Fig. 5.2(c), without pre-grouping the detector. A previous study revealed that at small q the influence of the dipolar interactions on the critical fluctuations above T_C are strongest [47]. Due to the geometry of the sample and the position of the beam stop, the smallest q-values can be evaluated horizontally, cf. Fig. 5.2(c). Data from the iron sample were normalised to the measurement of a standard graphite sample, using the very same sample environment, sample shape, and apertures. The process of normalisation is explained in detail in Sec. 3.3.3.

Fig. 5.4 shows the normalised intermediate scattering functions for temperatures between $T_C - 21\,\mathrm{K} \leq T \leq T_C$ for five selected q-values, $0.018\,\mathrm{\mathring{A}}^{-1} \leq q \leq 0.041\,\mathrm{\mathring{A}}^{-1}$. Statistics did not allow for reliable data treatment of higher q-values. Also due to statistics, data taken at $T_C - 21\,\mathrm{K}$ were only analysed for up to $\sim 0.035\,\mathrm{\mathring{A}}^{-1}$. The normalised intermediate scattering functions of all other data sets discussed in this chapter are shown in App. B.3.1, Fig. B.8-B.2. The experimental data were fitted by taking into account the wavelength distribution $f(\lambda)$ of the incoming neutron beam, the intensity measured at the detector $I(t_D)$, and the scattering function of the scattering process $S(\boldsymbol{q}, \omega)$, given in Eq. (5.8). Since at high temperatures, where $k_\mathrm{B}T \gg \hbar\omega$, the probabilities for neutron energy gain and loss during the scattering event are equal, the detailed balance factor could be neglected for measurements close to T_C in iron. From now on $S(\boldsymbol{q}, \omega) = S(\boldsymbol{q}, E)$ will be used, as the energy transfer during the scattering process $\pm\hbar\omega$ corresponds to the energy of the excited/annihilated excitation $\pm E$. A numerical integration over the wavelength distribution and all possible energy transfers, ranging from $-E_\lambda$, i.e. the maximum energy the incoming neutrons can lose during scattering, to infinity, gives the intermediate scattering function describing the scattering process

$$S(\boldsymbol{q}, \tau) = \int_{\lambda_0(1-\Delta\lambda/\lambda_0)}^{\lambda_0(1+\Delta\lambda/\lambda_0)} \int_{-E(\lambda)}^{\infty} f(\lambda) I(t_D) S(\boldsymbol{q}, E) \, \mathrm{d}E \, \mathrm{d}\lambda. \tag{5.12}$$

The determination of the intermediate scattering function for spin waves in iron relies

on the explicit calculation of the spin phase as discussed in Sec. 3.3.2. The triangular wavelength distribution is described by

$$
f(\lambda) = \begin{cases}
\frac{2(\lambda - a)}{(b-a)(\lambda_0 - a)}, & \text{for } a \leq \lambda < \lambda_0 \\
\frac{2}{b-a}, & \text{for } \lambda = \lambda_0 \\
\frac{2(b-\lambda)}{(b-a)(b-\lambda_0)}, & \text{for } \lambda_0 < \lambda \leq b \\
0, & \text{otherwise,}
\end{cases}
\tag{5.13}
$$

with the mean value of the incoming neutron beam $\lambda_0 = 6\,\text{Å}$ and the width of the wavelength distribution $\Delta\lambda/\lambda_0 = 0.12$ defining the lower boundary $a = \lambda_0(1 - \Delta\lambda/\lambda_0)$ and the upper boundary $b = \lambda_0(1 + \Delta\lambda/\lambda_0)$. The fit to the data are shown as solid lines in Fig. 5.4 and Fig. B.8-B.2. From the obtained fit results, the scattering function $S(q, E)$ was calculated, and plotted in Fig. 5.5.

For $T < T_\text{C}$, in the ferromagnetic phase, well-defined spin waves are present, cf. Fig. 5.4(a-f). Increasing the temperature, Fig. 5.4(a) to (f), the oscillation shifts to longer times, i.e. the frequency of the oscillation, associated with the energy of the spin waves, decreases. Regarding the intermediate scattering function at one temperature, the frequency of the oscillation increases, for increasing scattering vector q. Hence, the energy of the spin waves decreases for increasing temperature and for decreasing scattering vector.

When crossing the Curie temperature from the ferro- to the paramagnetic phase, as can be seen in Fig. 5.4(f) to (g), the intermediate scattering function changes. In the ferromagnetic phase, the signal is an exponentially damped oscillation, as expected for inelastic scattering of spin waves, cf. Eq. (5.9). For temperatures $T \geq T_\text{C}$ the intermediate scattering function changes to a single exponential decay, typical for quasielastic scattering at critical fluctuations.

However, as can be seen in Fig. 5.4(g), a weak inelastic signal is still observable at T_C. This becomes even more apparent when regarding the scattering function $S(q, E)$ in Fig. 5.5(g). This signal indicates propagating modes in the critical region close to the critical point. As found in literature, Collins *et al.* were not able to observe this weak signal of a double peak close to and at T_C, due their instrumental resolution [171]. The instrumental resolution for the measurements by Collins *et al.* was calculated from their instrumental set-up given in Ref. [171] via the approach by Cooper and Nathans [177], and is indicated as horizontal bars in Fig. 5.5. The existence of a double peak at T_C was also discussed in further literature. Theoretical work by Beeby and Hubbard [178], and Lowde [179] discussed the existence of spin wave like excitations at T_C. Görlitz *et al.* [180] observed a crossover from a single Lorentzian to a double peak structure in EuS when approaching T_C from high temperatures. This crossover was only observed
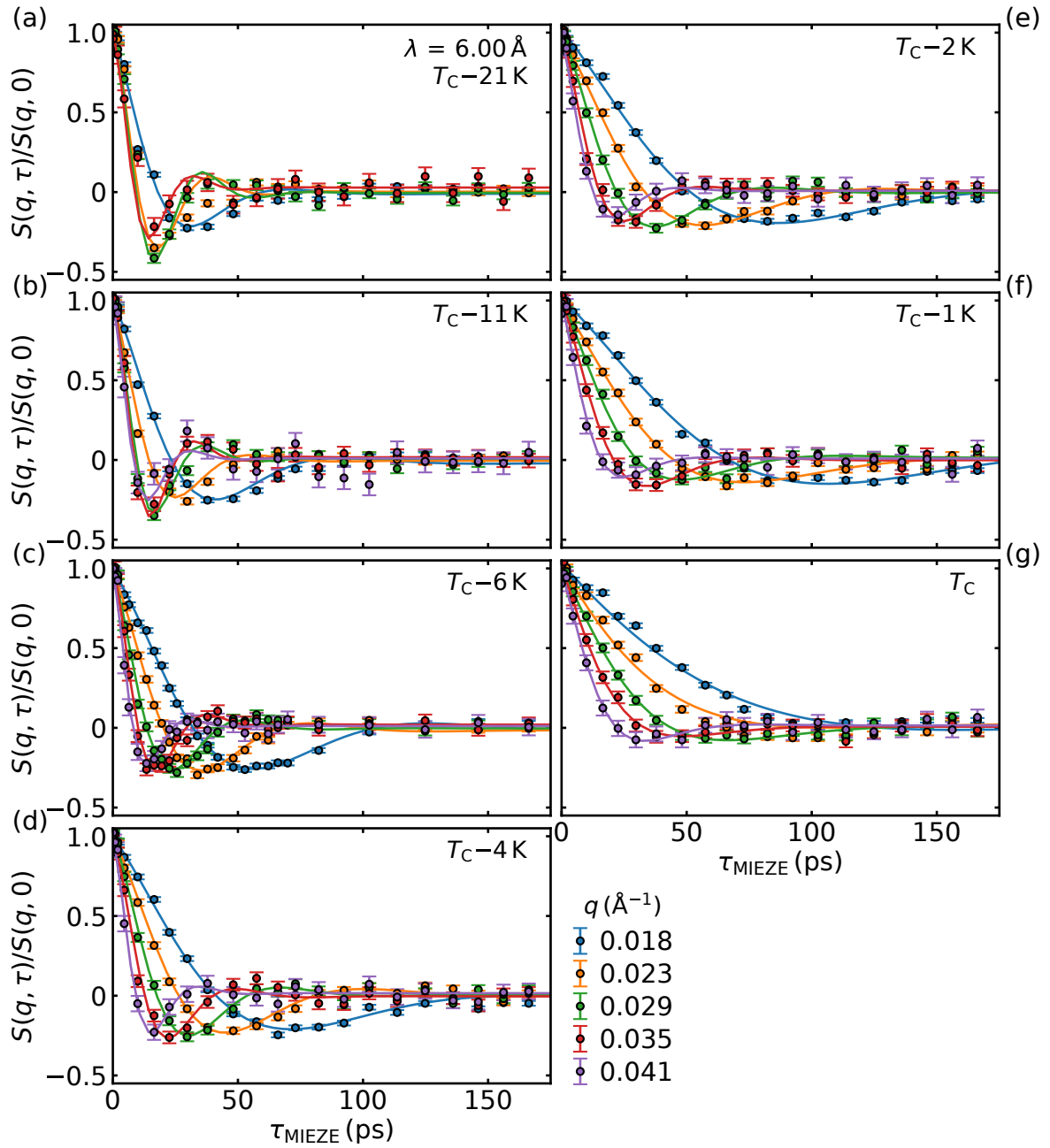
Figure 5.4.: Normalised intermediate scattering function as measured at T_C, and in the ferromagnetic phase in iron. Data were recorded using neutrons with a mean wavelength of $\lambda = 6.0\,\text{Å}$. Data are shown for (a) $T_C - 21\,\text{K}$, (b) $T_C - 11\,\text{K}$, (c) $T_C - 4\,\text{K}$, (d) $T_C - 2\,\text{K}$, (e) $T_C - 6\,\text{K}$, (f) $T_C - 1\,\text{K}$, and (g) T_C. The solid lines are fits to the data using Eq. (5.12).
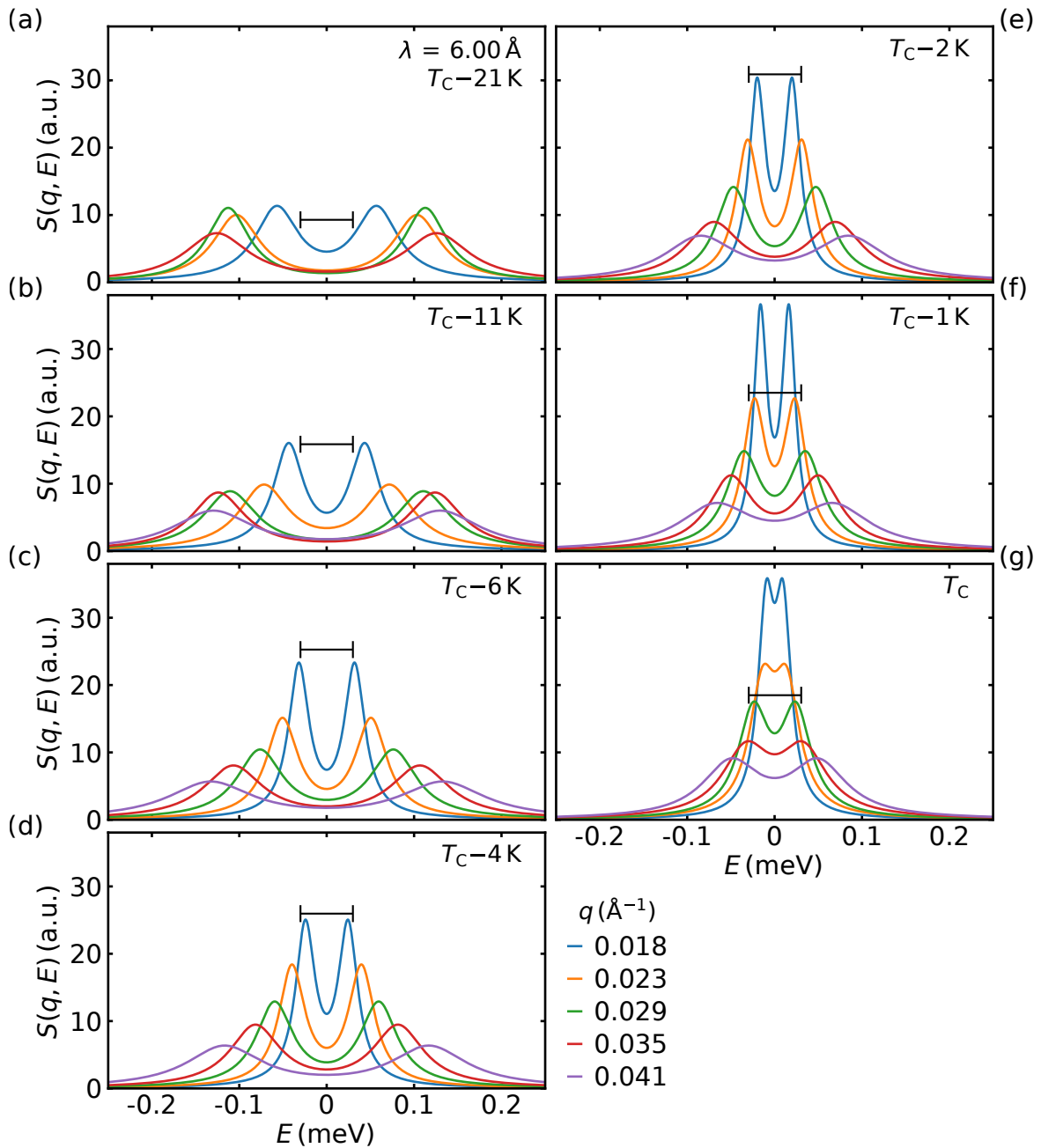
Figure 5.5.: Scattering function $S(q, E)$ as a function of energy transfer $\hbar\omega = E$. The scattering function is the Fourier transform of the intermediate scattering function in time, and was calculated from the fit results in Fig. 5.4. The scattering function is shown for (a) $T_C - 21\,\mathrm{K}$, (b) $T_C - 11\,\mathrm{K}$, (c) $T_C - 4\,\mathrm{K}$, (d) $T_C - 2\,\mathrm{K}$, (e) $T_C - 6\,\mathrm{K}$, (f) $T_C - 1\,\mathrm{K}$, and (g) T_C. The black horizontal bars indicate the highest energy resolution used by Collins *et al.* close to T_C.

after maximum entropy deconvolution of the experimental data obtained by Böni *et al.* [181]. This double shape corresponds to the longitudinal paramagnetic spin fluctuations predicted by mode-coupling theory [180, 182], and is not associated to spin waves.

Collins *et al.* discussed the possibility of a third peak in the spin wave region due to the diffusive longitudinal component of the static susceptibility near the critical temperature [171]. Such a peak would be centred at zero energy transfer, but was not observed during their study. Fitting the data of the present work with a third peak did not improve χ^2, and showed no evidence for the existence of such a diffusive component. This is hardly surprising as it is impossible to separate this longitudinal component from the transverse component, i.e. spin waves, without polarisation analysis [176]. Experimental evidence of the longitudinal and transverse spin fluctuations below T_C was found with polarised neutrons, e.g. in Ni [183], MnSi [184], and EuS [185].

(i). Spin Wave Energy and Spin Wave Stiffness

The spin wave energy E_sw as function of the scattering vector q is shown in Fig. 5.6(a). It was obtained by fitting the intermediate scattering function as described in the first part of Sec. 5.3.2. The data quantitatively show the decrease of the spin wave energy with increasing temperature and decreasing scattering vector.

The grey shaded area in Fig. 5.6(a) shows the region in (q, E) where the spectrometer is not able to measure. This region is determined by all combinations of (q, E) where the scattering triangle is not closed, that is where the momentum and energy transfer given in Eq. (3.1) and Eq. (3.2), respectively, are not conserved. The boundary of the grey shaded area is the maximum energy transfer that the spectrometer can reach with a wavelength of the incoming neutrons of $\lambda = 6$ Å and a wavelength spread of $\Delta\lambda/\lambda = 0.12$. The determination of this limit is described in App. B.1. Data taken at $T_\mathrm{C} - 21$ K are entirely beyond the limit of maximum energy transfer observable. Data taken at $T_\mathrm{C} - 11$ K are partially in this limit. It should be noted that it can be possible to measure the observed energies just beyond the limit, as the spectrometer used a finite wavelength spread. This cross-over region is indicated by the grey hatched area in Fig. 5.6(a). Further, the calculation for the maximum energy transfer does not take into account the instrumental resolution, which will be discussed later on. Data points for $T_\mathrm{C} - 21$ K at higher energies and wave vectors show a trend towards the boundary, while data taken at $T_\mathrm{C} - 11$ K entirely lie in the hatched cross-over region. Therefore, data taken at these two temperatures are fitted, but excluded from the following discussion of the spin wave stiffness.

The spin wave energy was fitted using Eq. (5.5), taking into account dipolar interactions, and convolved with the instrumental momentum resolution of the spectrometer. The

(a)

(b)
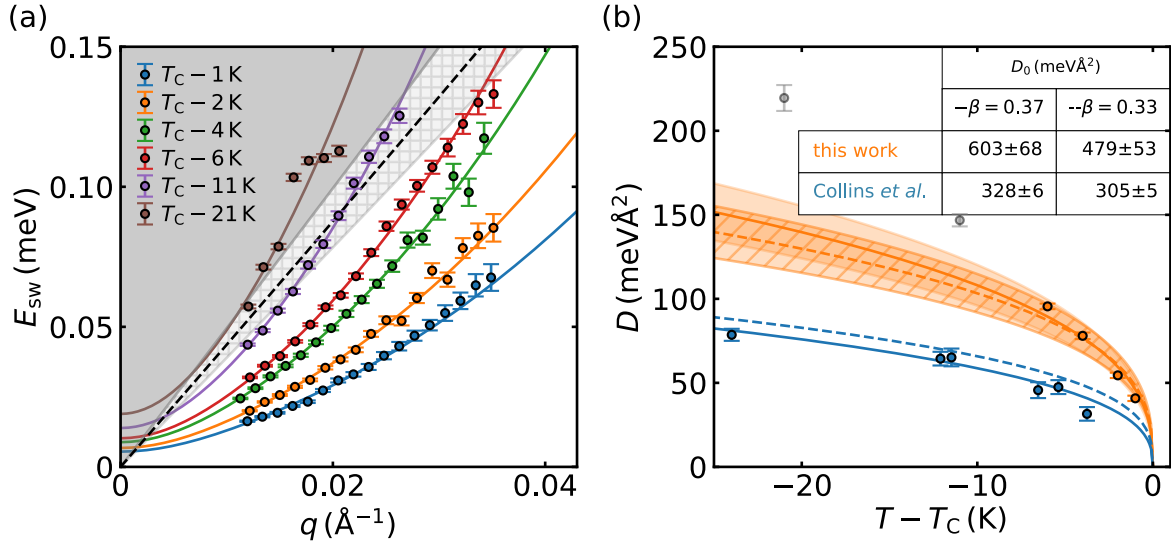
Figure 5.6.: Spin wave dispersion in iron at different temperatures. (a) Spin wave energy E_{sw} as function of scattering vector q. Data are corrected for direct beam offset. The solid lines are fits to the data using Eq. (5.14). The grey shaded area gives the maximum energy transfer described in App. B.1, taking into account the wavelength spread around $\lambda = 6\,\text{Å}$. (b) Spin wave stiffness D as function of temperature. The solid and dashed lines are fits to the data using Eq. (5.7) with $\beta = 0.37$ and $\beta = 0.33$, respectively. The shaded and hatch-shaded areas denote the 1σ standard deviation of the fit for $\beta = 0.37$ and $\beta = 0.33$, respectively. Data were fitted only for $T > T_C - 11\,\text{K}$ due to the maximum energy transfer shown in panel (a). The blue data are taken from Ref. [171].

instrumental resolution was analytically derived by taking into account the two main contributions to the resolution of a small angle neutron scattering instrument, following the theoretical work by Pedersen *et al.* [186], and Hammouda and Mildner [187]: (i) resolution due to a finite wavelength spread, and (ii) resolution due to finite collimation. The derivation of the instrumental resolution function for RESEDA is given in App. B.2.

Finally, a direct beam offset was taken into account. The direct beam, defined by the sample aperture, is absorbed by the beam stop as shown in Fig. 5.2(d). Therefore, it is impossible to define the precise position where the direct beam would hit the detector, making it necessary to include a direct beam offset q_0 in the model.

The fit function is then given by

$$(E_{sw} * R)(q - q_0) = \int_{\mathbb{D}} E_{sw}(q' - q_0) R(q - q' - q_0, \sigma_{q-q'-q_0})\, \mathrm{d}q', \qquad (5.14)$$

with the spin wave energy E_{sw} in Eq. (5.5), and the resolution function R in App. B.2, Eq. (B.17). As expected, the offset of the direct beam was found to be small and temperature independent with $\bar{q}_0 \approx 0.0046\,\text{Å}^{-1}$. Data shown in Fig. 5.6(a) are corrected for this offset.

Regarding the model it becomes apparent that the spin wave energy at $q = 0$ is not zero, as would be expected from theory. This is due to the convolution of the spin wave energy with the instrumental resolution: at $q = 0$ the instrument measures contributions from finite q. These contributions should be equal for energy gain and energy loss, hence level out to $E = 0$. However, spin echo is unable to distinguish between energy gain and energy loss, hence a finite instrumental resolution leads to a finite measured energy at $q = 0$.

Fig. 5.6(b) shows the spin wave stiffness as a function of temperature, obtained from fitting the spin wave energy in (a). Data from the present work (orange) are compared to the temperature dependent spin wave stiffness in iron obtained by Collins *et al.* (blue) [171]. A more detailed discussion of the spin wave data of Collins *et al.* is given in App. B.3.3.

The data points in Fig. 5.6(b) were fitted with the power law in Eq. (5.7), using a fixed parameter $\beta = 0.33$ (dashed lines) from theory. Since Collins *et al.* observed a deviation from the theoretical critical exponent $\beta = 0.33$ to $\beta = 0.37 \pm 0.03$, data were also fitted using a fixed parameter $\beta = 0.37$ (solid lines). The orange hatch-shaded and shaded areas denote the 1σ standard deviation of the fit due to the error for D for $\beta = 0.33$ and $\beta = 0.37$, respectively. Tab. 5.1 summarises the obtained fit results, and compares them with the results from Collins *et al.*

The power law behaviour for the spin wave stiffness in Eq. (5.7) describes the data within 1σ standard deviation for temperatures above $T_{\mathrm{C}} - 11\,\mathrm{K}$ for both $\beta = 0.33$ and $\beta = 0.37$. Comparing the material specific spin wave stiffness D_0 in Tab. 5.1, shows that D_0 found in the present work is significantly larger than reported by Collins *et al.*

Table 5.1.: Comparison of the spin wave stiffness given by Collins *et al.* (i), to the results obtained by fitting their data with Eq. (5.7) (ii), and to the results of the present study (iii). While the critical exponent β is within the margin of errors, the spin wave stiffness D_0 differs significantly.

	(i) Collins *et al.*	(ii) own fit of Collins data		(iii) this work	
β	0.37 ± 0.03	0.37 (fixed)	0.33 (fixed)	0.37 (fixed)	0.33 (fixed)
$D_0\,(\mathrm{meV\mathring{A}}^2)$	281 ± 10	328 ± 6	305 ± 5	603 ± 68	479 ± 53

5.4. Conclusions and Outlook

The present study continued the investigation of continuous phase transitions, following up on a previous study of the critical dynamics close to the transition temperature in the hydrodynamic and transition region in iron [47]. The focus was on critical phenomena in the transition and spin wave region in iron, especially focusing on the inelastic excitations of spin waves. The elastic data in Sec. 5.3.1 show how the critical fluctuations on all time- and length-scales increase upon approaching the Curie temperature, providing a textbook example of critical opalescence at a continuous phase transition. The quasi- and inelastic spin echo data discussed in Sec. 5.3.2 show the presence of spin waves in the ferromagnetic phase.

The temperature and q dependence of the spin wave energy shows the expected behaviour: with increasing temperature, the energy of the spin waves decreases. The energy of the spin waves increases with increasing q, when going from the centre to the boundary of the Brillouin zone. There is a clear deviation from the classical Heisenberg ferromagnet, where the spin wave energy depends quadratic on q. Due to the large magnetic moment of iron, dipolar interactions were taken into account to describe the observed spin wave energy. Eq. (5.5) is based on the theory by Holstein and Primakoff [172], and includes dipolar interaction. This model for the spin wave energy describes the data very well.

The temperature dependence of the spin wave stiffness fits the power law behaviour predicted by scaling theory. Data were fitted with a critical exponent of $\beta = 0.33$, as theoretically predicted, as well as with $\beta = 0.37$, as experimentally found by Collins *et al.* Both critical exponents fit the data within 1σ standard deviation. It should be noted that only data taken at temperatures between $T_{\mathrm{C}} - 1\,\mathrm{K}$ and $T_{\mathrm{C}} - 6\,\mathrm{K}$ were included in the fit. The combination of (q, E) at lower temperatures does not close the scattering triangle, hence is not observable with RESEDA in the used configuration. This limitation can be circumvented by using a smaller wavelength of $\sim 4.5\,\text{Å}$. This would decrease the upper limit of the dynamic range of the instrument, but allow to investigate higher energies at smaller q.

The temperature dependent spin wave stiffnesses D was found to be larger by a factor of ~ 2 as compared to what was reported by Collins *et al.* Hence, also the material specific spin wave stiffness constant D_0 is significantly larger than what was found by Collins *et al.*

Due to energy resolution, Collins *et al.* observed over-critical damping of the spin waves for temperatures above $T_{\mathrm{C}} - 3\,\mathrm{K}$. Therefore, they were unable to say whether D goes to zero at T_{C}, as predicted by scaling theory, cf. Eq. (5.7). The high energy resolution of RESEDA allowed to observe spin waves until just below T_{C}. Fitting the spin wave

stiffness with the power law within scaling theory, the data suggest that the spin wave stiffness goes to zero at the Curie temperature.

The present study shows the advantages of the NRSE MIEZE technique for the investigation of critical phenomena. MIEZE allows to investigate in the small angle scattering regime under depolarising conditions with sub-µeV energy resolution. Thus, resolving very weak signals that were not accessible before, cf. double peak Lorentzian at the Curie temperature in iron. Compared to triple-axis spectroscopy, spin echo is not limited to a very narrow wavelength band to retain high energy resolution. Spin echo allows to use a broad wavelength band, yielding much higher intensities. With the position sensitive CASCADE detector, a large region in reciprocal space can be measured simultaneously, further reducing measurement time. The present study proved that the MIEZE method at RESEDA is ideally suited to study quasi- and inelastic excitations in the vicinity of magnetic phase transitions.

(i). Deviations from Literature

In inelastic neutron scattering, differing results within an order of magnitude are often reported, especially close to critical points as it is the case in the present work. For example Böni *et al.* [188] reported a linewidth of the critical fluctuations at T_C in EuO a factor of two higher than observed by Passell *et al.* [189]. Another example is the critical exponent z for the linewidth $\Gamma \sim q^z$ in EuS, which was reported to be $z = 2.09 \pm 0.6$ by Bohn *et al.* [190], and later found to be $z = 2.54 \pm 0.1$ in accordance with scaling theory for a Heisenberg ferromagnet by Böni *et al.* [191].

Although the dispersion of the spin waves in iron as observed with RESEDA is in accordance with spin wave theory including dipolar interactions, the resulting spin wave stiffness constant differs from the literature value. To address this issue, a second study on the very same bcc iron single crystal using the triple-axis spectrometer (TAS) MIRA at MLZ was performed. A more detailed description of the TAS study can be found in App. B.3.4. Fig. 5.7 shows the spin wave stiffness as a function of temperature as obtained with TAS. Data from the present work (red) are compared to data obtained by Collins *et al.* (blue). The data obtained from the present TAS study agree with the data from Collins *et al.* within 1σ standard deviation.

The cause of the discrepancy between data obtained with RESEDA and data obtained with MIRA and Collins *et al.*, respectively, was still an open question at the time the present thesis was submitted. The present study is the first extensive investigation of inelastic excitations using spin echo spectroscopy, leading to new challenges, with one of the greatest being data analysis of inelastic signals and signals with large energy transfers.
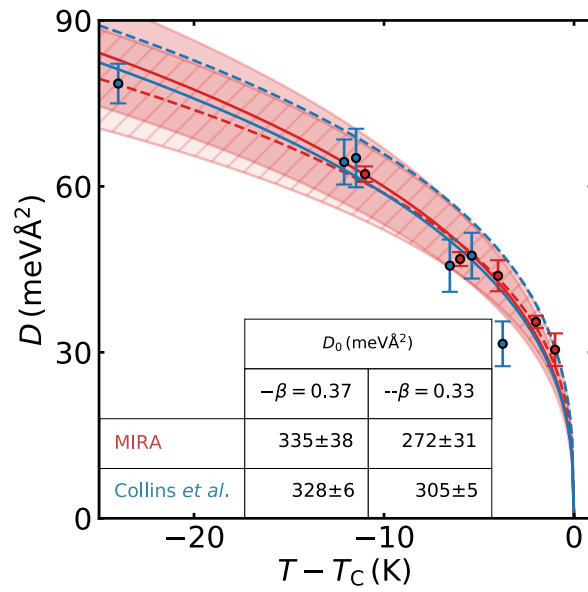
Figure 5.7.: Spin wave stiffness D as function of temperature. The solid and dashed lines are fits to the data using Eq. (5.7) with $\beta = 0.37$ and $\beta = 0.33$, respectively. The shaded and hatch-shaded areas denote the 1σ standard deviation of the fit for $\beta = 0.37$ and $\beta = 0.33$, respectively. The blue data are taken from Ref. [171].

Using the explicit calculation of the spin phase, cf. Ch. 3.3.2, the main difficulty lies in solving the integral in Eq. (5.12) numerically. With the recent developments at RESEDA, the code for data analysis is still under development, hence might be the cause of the discrepancy between the spin wave stiffness constant found at RESEDA and reported in literature.

6. Spin Relaxation in Fe$_x$Cr$_{1-x}$

In iron chromium alloys, Fe$_x$Cr$_{1-x}$, reentrant spin-glass behaviour is observed, where the spin-glass forms from a ferromagnetically or antiferromagnetically ordered high temperature state. The present study investigates the spin relaxation processes in Fe$_x$Cr$_{1-x}$ for different iron concentrations x. Depending on the iron concentration, the samples show either ferromagnetic, antiferromagnetic, or paramagnetic high temperature states. Measuring samples with different iron concentrations allows to compare the relaxation process depending on the particular state at high temperatures. A broad distribution of relaxation times, characteristic for spin-glasses, is found over a broad range of the phase diagram above and in the spin-glass dome. This behaviour suggests that clusters of different size and single spins in between the clusters are present, all fluctuating on different time scales. The chapter starts with a brief introduction into spin-glasses, in particular the reentrant spin-glass Fe$_x$Cr$_{1-x}$, cf. Sec. 6.1. The introduction is followed by the experimental set-up in Sec. 6.2, and the experimental results in Sec. 6.3. The chapter concludes with a summary of the present study and an outlook, cf. Sec. 6.4.

6.1. Introduction to Spin Glasses

A spin-glass is defined as a magnetic system where randomness or disorder, competing interactions, anisotropy, and frustration lead to a random, yet collective, freezing of the spins at a freezing temperature T_f. The frozen state below this temperature is highly irreversible and metastable, and long-range magnetic order is absent. The freezing into a metastable state can be seen as being analogue to the freezing in real glasses, hence the name spin-glass. A more detailed introduction into spin-glasses can be found in the textbook by Mydosh [27], on which this section is oriented.

The evolution of the cooperative freezing starts at high temperatures $T \gg T_f$, where all spins are independent due to dominant thermal fluctuations. Lowering the temperature leads to a formation of clusters, in which the spins are correlated. These clusters form in various shapes and sizes due to the random distribution of competing interactions. Since the fluctuation rate of a cluster depends on its size, a large distribution of relaxation times for the clusters formed already above T_f is observed. There are still spins remaining, which

do not belong to any of these clusters. These spins take part in interactions between the clusters. Further cooling towards T_f, the dynamics within the clusters slow down, until the system eventually finds one of its many ground states and freezes. The spins outside the clusters fluctuate rapidly, until slowing down too. However, even in the frozen state, single spins and small clusters are present, contributing to faster relaxation rates as compared to larger clusters. This cooperative phase transition is not yet fully understood. For temperatures $T < T_f$, the system is in a glassy, metastable state. This state shows neither ferromagnetic nor antiferromagnetic long-range order.

The most prominent example are diluted spin-glasses, such as Au$_{1-x}$Fe$_x$ or Cu$_{1-x}$Mn$_x$ [90, 91], where only a few atomic percent of magnetic ions are added to the alloys, i.e. $x \ll 1$. This yields a random distribution of the magnetic ions, what leads to a competition between ferromagnetic and antiferromagnetic interactions due to the oscillatory RKKY-interactions (Ruderman–Kittel–Kasuya–Yosida) between the Fe and Mn atoms, respectively [27, 92]. Diluted spin-glasses can be described by the Hamiltonian

$$\mathcal{H}_{\mathrm{RKKY}} = -\sum_{\langle ij \rangle} J\left(\boldsymbol{R}_i - \boldsymbol{R}_j\right) \boldsymbol{S}_i \cdot \boldsymbol{S}_j, \tag{6.1}$$

with Heisenberg spins $\boldsymbol{S}_{i,j}$ of the magnetic ions i, j at locations $\boldsymbol{R}_{i,j}$. The RKKY exchange interaction $J\left(\boldsymbol{R}\right)$ oscillates between ferromagnetic and antiferromagnetic interaction as a function of distance between the magnetic ions. Thereby, the frustration arises from the random distribution of competing interactions, and is different to the geometrically frustrated systems which were the topic of Ch. 4, cf. Sec. 4.1.1. Due to the frustration, spin-glasses possess a multidegenerate ground state.

Increasing the number of magnetic ions in the system, the spin can not be seen as diluted any more, and a concentrated spin-glass is formed, also known as cluster glass or mictomagnet. In such systems, a large number of interacting magnetic moments might lead to the formation of large clusters which then might dominate the magnetic behaviour. This leads to a spin-glass with incipient long-range magnetic order. Further increasing the concentration of magnetic ions eventually leads to the percolation limit, where each magnetic site has at least one magnetic nearest neighbour. Depending on the lattice and the type of interaction between the magnetic moments, beyond the percolation limit the system might show long-range magnetic order [27].

If the system is close to its percolation limit towards long-range ferromagnetic order, it is possible to observe spin-glass behaviour at low temperatures, with a ferromagnetically ordered state at higher temperatures. When cooling, these systems freeze without long-range magnetic order. The name reentrant spin-glasses comes from the reentering of a magnetically disordered state from an ordered state. In these systems either a temperature dependent random anisotropy appears, or some mechanism related to the freezing

temperature leads to the anisotropy, such as the freezing of transverse spin components [27, 192]. If this anisotropy grows strong enough, it leads to the formation of a spin-glass phase out of a magnetically ordered state.

One major question in spin-glasses is the dynamical behaviour over the whole cooperative freezing process. This was addressed mainly by neutron scattering, in particular by neutron spin echo spectroscopy [193–200]. An observation often found in the literature is a wide spectral distribution of relaxation times, which is found continuously from high to low temperatures [195]. This broad distribution of relaxation times is a result of different sized clusters, and spins surrounding these clusters, all fluctuating with different rates. Cooling down, the spin relaxation slows down continuously through the transition into the spin-glass phase.

The majority of the neutron scattering studies found in the literature were performed on conventional spin-glasses, where also a q-independence of the spin relaxation was observed. The absence of a dispersion was taken as evidence that spin conserving forces, such as dipolar or spin-orbit interactions, are crucial in spin-glasses [195, 196]. In 1985, Shapiro *et al.* employed neutron spin echo spectroscopy on two samples of the reentrant spin-glass $Eu_xSr_{1-x}S$ with a high temperature paramagnetic and ferromagnetic state, respectively [199]. In contrast to conventional spin-glasses, both samples showed a weak q-dependence of the spin relaxation. Apart from that, the behaviour of the spin relaxation over the freezing process in reentrant spin-glasses was found to be as in conventional spin-glasses.

In the ferromagnetic regime of the reentrant spin-glasses Fe_xAl_{1-x} and Fe_xCr_{1-x}, inelastic neutron scattering was used to investigate inelastic excitations in the ferromagnetic and spin-glass phases [201–205]. It was found that spin waves are present in the ferromagnetic phase of Fe_xAl_{1-x} and Fe_xCr_{1-x}, which vanish when entering the spin-glass phase. Applying a magnetic field to the Fe_xCr_{1-x} sample leads to an emergence of spin waves also in the spin-glass phase [202]. In contrast, in Fe_xAl_{1-x} no spin waves could be induced in the spin-glass phase [204]. This might be due to the fact that in Fe_xAl_{1-x} the spin-glass phase and the ferromagnetic phase are separated by a paramagnetic regime, while in Fe_xCr_{1-x} the ferromagnetic phase directly goes over into the spin-glass state [204].

6.1.1. Introduction to Fe_xCr_{1-x}

In iron chromium alloys, Fe_xCr_{1-x}, the magnetic order changes from itinerant ferromagnetism to itinerant antiferromagnetism by substituting iron atoms by chromium atoms. Pure iron shows a Curie temperature $T_C = 1043\,K$, which can be suppressed by adding chromium. Properties of pure iron were already discussed in Ch. 5. In contrast, pure chromium is a spin-density wave antiferromagnet with a Néel temperature of $T_N = 311\,K$

[206]. Its Néel temperature is reduced gradually by adding iron, retaining the spin-density wave antiferromagnetism until the antiferromagnetic order is fully suppressed [207, 208].

Fig. 6.1 shows the magnetic phase diagram of Fe$_x$Cr$_{1-x}$ as a function of the iron concentration x in zero field. Changing the iron content x might lead to disorder, anisotropy, and a deformation of the electronic band structure, hence influencing the magnetic behaviour of the system. By suppressing the ferromagnetic or antiferromagnetic order, respectively, a spin-glass dome emerges, covering a putative quantum critical point. At low temperatures, this spin-glass phase extends into both, the ferromagnetic and antiferromagnetic states. Fe$_x$Cr$_{1-x}$ crystallises in the body-centred cubic (bcc) crystal structure with $Im\bar{3}m$ symmetry, i.e. space group number 229, over the entire range from pure Fe to pure Cr.
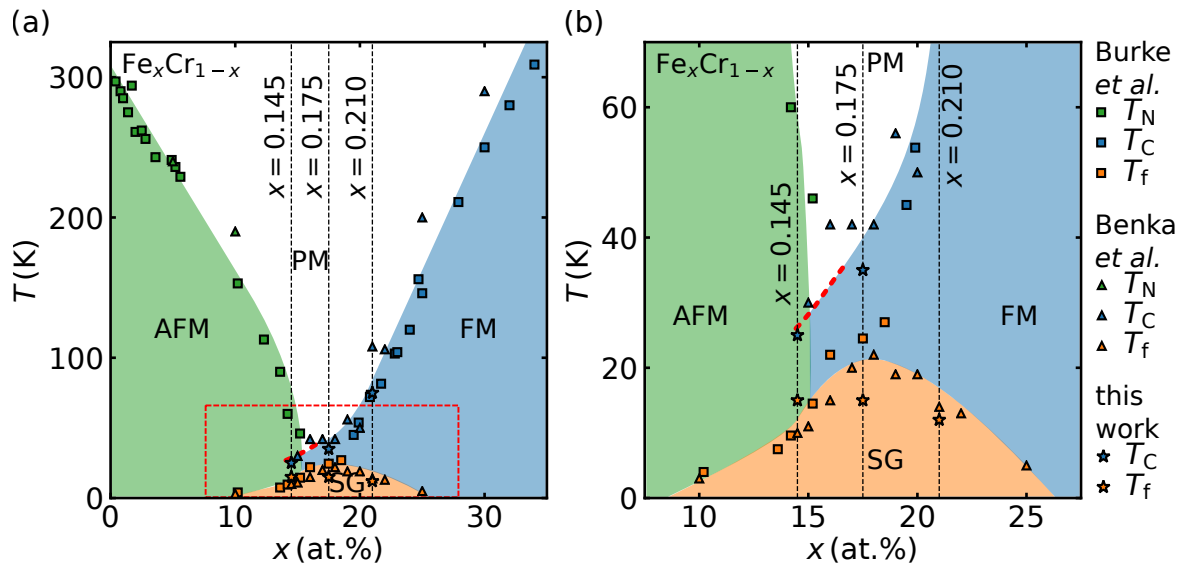
Figure 6.1.: Concentration dependence of the magnetic phase diagram of Fe$_x$Cr$_{1-x}$ in zero field. (a) Data shown were obtained by means of neutron scattering and low-field magnetisation by Burke *et al.* (square symbols) [209–211], via ac susceptibility and magnetisation measurements by Benka (triangular symbols) [212], and by neutron scattering in the present work (star symbols). With increasing iron concentration x, the system shows a transition from an itinerant antiferromagnet (AFM; green) to an itinerant ferromagnet (FM; blue). In the vicinity between these two phases, a dome showing spin-glass (SG; orange) behaviour covers a putative quantum critical point. The three dashed vertical lines indicate the iron concentrations investigated in the present work. The red marked area indicates the region of interest, which is enlarged in (b).

The ferromagnetic and antiferromagnetic transitions in Fe$_x$Cr$_{1-x}$ were mainly addressed by measurements of bulk properties [15, 213–215] and neutron scattering studies [216–218]. The first reports on spin-glass behaviour was by Shull *et al.* [14] and Loegel *et al.* [15], where magnetisation and transport measurements suggested a superparamagnetic phase. This behaviour is similar to what was found in AuFe [92]. In 1983, Burke *et al.*

reported the evolution of magnetic order in Fe_xCr_{1-x} over a wide composition range using neutron scattering and magnetisation measurements, mapping out the phase diagram in detail [209–211], cf. Fig. 6.1.

An extensive study of bulk properties on a wide range of Fe_xCr_{1-x} compositions by Benka found an extended ferromagnetic regime, spanning the concentration range from the ferromagnet to the antiferromagnet above the spin-glass phase, cf. Fig. 6.1. The study by Benka also suggest that the magnetic behaviour in the spin-glass phase in Fe_xCr_{1-x} with $x = 0.10$ to 0.25 is at the border between a superparamagnet and a cluster glass. Thus, a cluster glass is on the low and a superparamagnet on the high concentrated side.

In a recent study using neutron depolarisation imaging [219], Schmakat suggested a scenario for the evolution of the magnetism in a sample of Fe_xCr_{1-x} with a ferromagnetic high temperature phase. The suggested scenario is illustrated in Fig. 6.2. For $T < T_C$, cf. Fig. 6.2(a), ferromagnetic clusters form. These are surrounded by fluctuating magnetic moments, rather than developing domain walls. Cooling below the spin-glass temperature T_f, cf. Fig. 6.2(b), the fluctuating moments outside the clusters couple antiferromagnetically, thus enhancing the frustration between the ferromagnetic clusters. Cooling even further $T \ll T_f$, cf. Fig. 6.2(c), the antiferromagnetic surrounding stabilises, and the system slows down significantly, freezing the spin system.
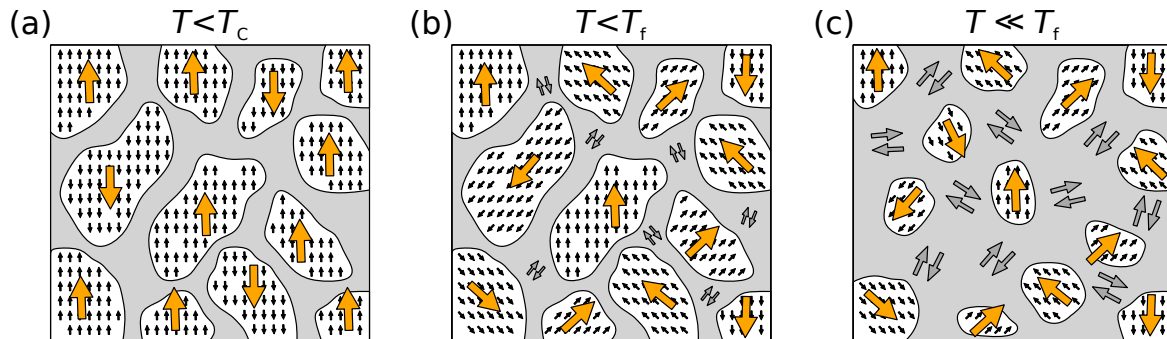
Figure 6.2.: Possible scenario for the magnetic behaviour in an Fe_xCr_{1-x} sample with a high temperature ferromagnetic state, as suggested by Schmakat [219]. (a) For $T < T_C$, ferromagnetic domains form, which are surrounded by fluctuating magnetic moments. (b) For $T < T_f$, the moments outside the clusters couple antiferromagnetically. (c) For $T \ll T_f$, the antiferromagnetic regions grow at the cost of the ferromagnetic clusters, leading to an effective freezing of the spin system due to frustration. Figure taken from Ref. [219].

The objective of the present work was to investigate the spin relaxation processes of the reentrant spin-glass Fe_xCr_{1-x} over the whole collective freezing process. Measurements were performed on samples with different iron concentrations, comparing the spin relaxation processes depending on the particular state at high temperatures.

6.2. Experimental Set-up and Samples

Spin relaxation processes in Fe$_x$Cr$_{1-x}$ were measured at RESEDA in the MIEZE mode, as introduced in Sec. 3.4. The distance between the first and second NRSE coil was 1.875 m, the distance between the second NRSE coil and the detector 3.700 m. With the sample as close to the primary spectrometer arm as possible, the sample detector distance was 2.335 m. For a high neutron flux and to cover the desired dynamic range, the wavelength was set to 6 Å with a wavelength spread $\Delta\lambda/\lambda = 0.12$. With this configuration, and frequency differences between the RF coils between $\sim$1 Hz and 600 kHz, a dynamic range from $\sim 6 \cdot 10^{-6}$ ns to 2 ns was accessible. For the present study, the dynamic range was limited to 10^{-4} ns to 1 ns.

Measurements were performed between $\sim$4 K and 300 K. The sample was cooled using a top-loading closed cycle refrigerator (CCR) with a diameter of the sample tube of 80 mm. The temperature was controlled using a Lakeshore 336 temperature controller with two Cernox sensors close to the sample. The temperature stability was about $\sim$0.05 K and no hysteresis effects were observed. Both was verified by means of several temperature scans.

The samples used in the present study were polycrystalline Fe$_x$Cr$_{1-x}$ specimens with iron concentrations of $x = 0.145; 0.175; 0.210$. The crystals are of cuboidal shape with a thickness of $\sim$8 mm. The samples were mounted vertically in the neutron beam, and a circular aperture with a diameter of $\sim$10 mm defined the illuminated sample volume. Tab. 6.1 lists the samples used in the present study alongside the samples used by Schmakat [219] and Benka [212] during their studies using neutron depolarisation, ac susceptibility, magnetisation, electrical transport, and heat capacity measurements.

Regarding the phase diagram in Fig. 6.1, the chosen samples provide different high temperature states according to the different iron concentrations. The sample with $x = 0.145$ and $x = 0.210$ enter the spin-glass phase from an antiferromagnetic and ferromagnetic phase, respectively. With an iron concentration of $x = 0.175$, Fe$_x$Cr$_{1-x}$ is a paramagnet for higher temperatures. In the study by Benka, samples between $x = 0.150 - 0.190$ were found to pass through a small temperature region with ferromagnetic order before entering the spin-glass phase, whereas the study of Burke *et al.* suggest that these samples enter the spin-glass state directly from a paramagnetic phase [209–212]. The elastic measurements in Sec. 6.3.1 confirm a small ferromagnetic phase in the sample with $x = 0.175$, consistent with the observations of Benka.

Table 6.1.: Sample overview for Fe_xCr_{1-x} studies conducted by Schmakat [219] and Benka [212], and in the present work. The studies contained measurements of the ac susceptibility and magnetisation (ACMS), ac electrical transport (ACT), heat capacity (HC), neutron depolarisation (depol), and NRSE MIEZE (MIEZE). The samples used in the present work, written in bold, were provided by Shapiro and grown by Motoya [202, 203].

at.% Fe	Sample from	ACMS	ACT	HC	depol	MIEZE
0	Benka	Benka	-	-	-	-
5.0	Benka	Benka	-	-	-	-
10.0	Benka	Benka	-	-	-	-
14.5	Shapiro/Motoya	Benka	-	-	-	this work
15.0	Benka	Benka	Benka	Benka	Schmakat	-
16.0	Benka	Benka	-	-	Schmakat	-
17.0	Benka	Benka	-	-	Schmakat	-
17.5	Shapiro/Motoya	-	-	-	-	this work
18.0	Benka	Benka	-	-	Schmakat	-
19.0	Benka	Benka	-	-	Schmakat	-
20.0	Benka	Benka	-	-	Schmakat	-
21.0	Benka	Benka	-	-	Schmakat	-
21.0	Shapiro/Motoya	-	-	-	-	this work
22.0	Benka	Benka	-	-	Schmakat	-
25.0	Benka	Benka	-	-	-	-
30.0	Benka	Benka	-	-	-	-

6.3. Experimental Results

In the following, the experimental results of the neutron scattering measurements in Fe_xCr_{1-x} will be presented for iron concentrations $x = 0.145;\ 0.175;\ 0.210$. Sec. 6.3.1 discusses the temperature and q-dependence of the small angle scattering, which was mainly used to identify the transition temperatures, and to assess the temperature stability and hysteresis effects due to sweeping the temperature. The results of the spin echo measurements are presented in Sec. 6.3.2. The discussions focus on similarities and differences between Fe_xCr_{1-x} with different iron concentrations, and thus different states above the spin-glass phase.

6.3.1. Elastic Scattering

The small angle scattering of Fe$_x$Cr$_{1-x}$ for the investigated iron concentrations, i.e. $x =$ 0.145; 0.175; 0.210, was evaluated using the masks shown in Fig. 6.3(a). As no magnetic scattering was observed at high temperatures, the measurements at $\sim$300 K were used as background and subtracted from the experimental data. The temperature dependence of the background corrected SANS data is shown in Fig. 6.4(a-c) for six selected q-values in the range $0.025\,\text{Å}^{-1} \leq q \leq 0.070\,\text{Å}^{-1}$. The data were used to identify the transition temperatures of the ferromagnetic state at T_C, and the onset of spin-glass behaviour at T_f. Since no antiferromagnetic scattering intensity can be observed in the vicinity of the [000]-Bragg peak, a transition into an antiferromagnetic state can not be identified by SANS. The shaded areas in Fig. 6.1 indicate the antiferromagnetic (green), ferromagnetic (blue), and spin-glass (orange) phases as observed with ac susceptibility and magnetisation measurements by Benka [212].

The scattering intensity as a function of temperature for iron concentrations $x = 0.145$ and $x = 0.175$ are very similar. Lowering the temperature leads to an increase in intensity as expected for a transition into a ferromagnetically ordered state. The point of inflection is used to define the transition temperature T_C. When entering the spin-glass phase, the system is static on the time-scales probed by SANS, hence the temperature T_f where the intensity has a change of slope towards a plateau defines the transition into the spin-glass state. In case of the sample with $x = 0.210$, a plateau region could not be observed,
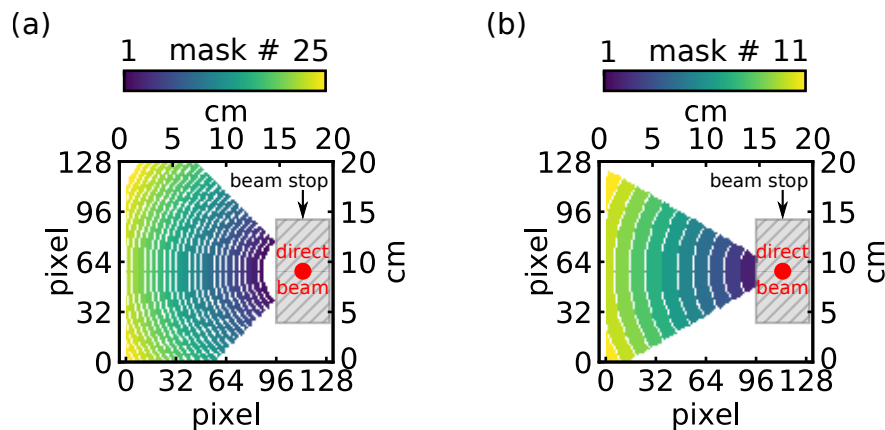
Figure 6.3.: Detector masks used for evaluating the experimental data. (a) Masks used for the evaluation of the elastic scattering, representing circular ring-segments around the direct beam with an opening angle of $90°$ and a width of 4 pixels. (b) Masks used for the evaluation of the MIEZE scans. The masks are circular ring-segments around the direct beam with an opening angle of $60°$ and a width of 10 pixels. The grey hatched area in (a) and (b) represents the blocked view on the detector due to the beam stop, cf. Fig. 5.2(d).
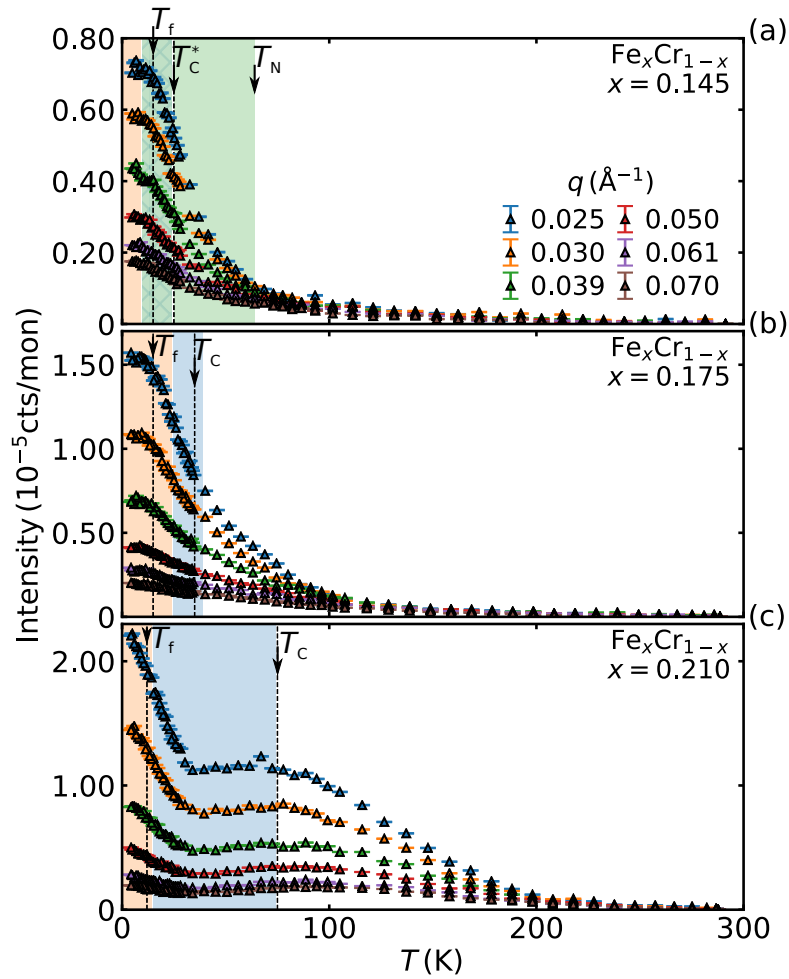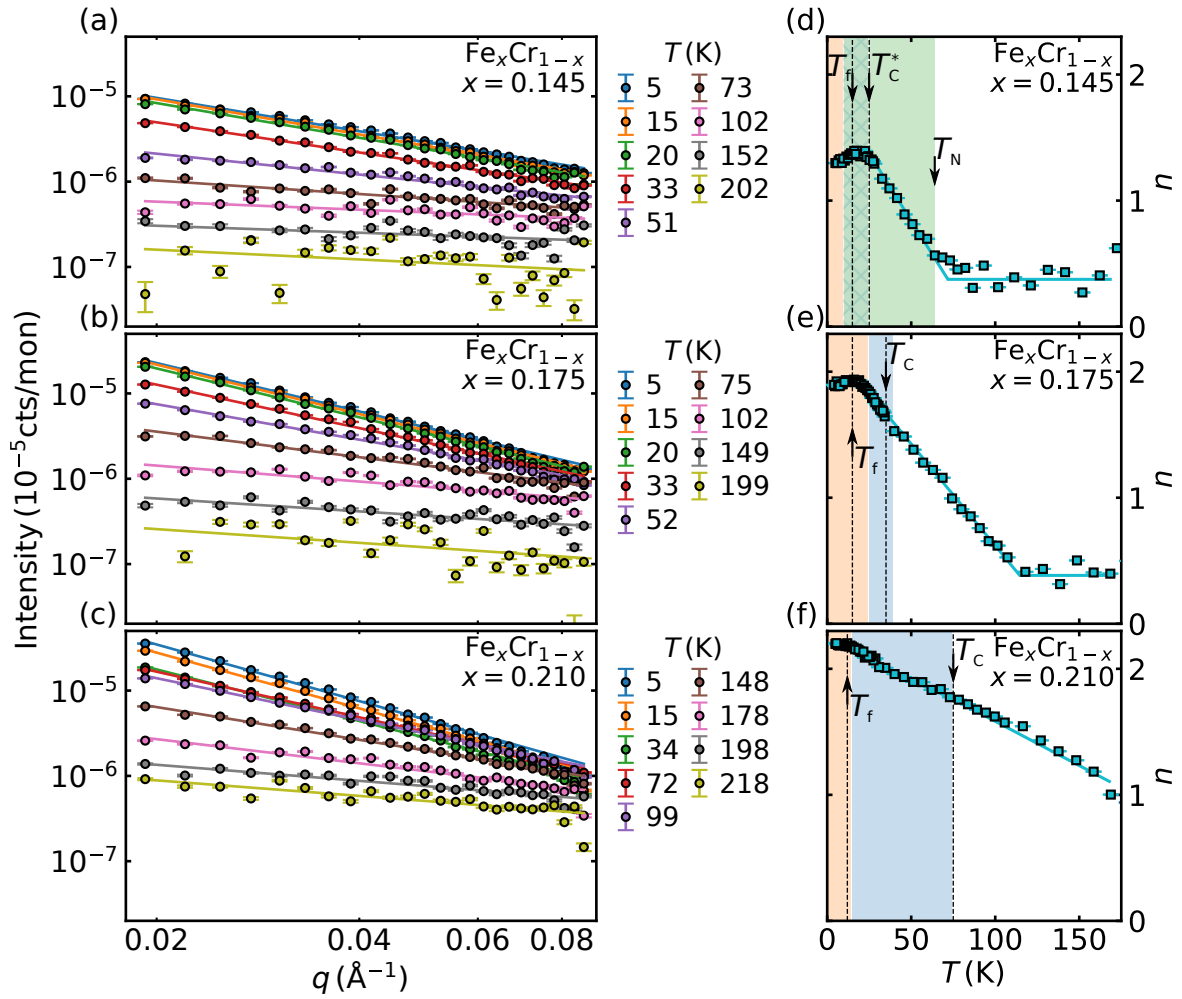
Figure 6.4.: Temperature dependence of the SANS data of Fe_xCr_{1-x}. Samples with iron concentrations of $x = 0.145$ (a), $x = 0.175$ (b), and $x = 0.210$ (c) were evaluated at different q-regions using the masks shown in Fig. 6.3(a). The shaded areas indicate the phases according to the phase diagram in Fig. 6.1: AFM (green), FM (blue), SG (orange). Dashed lines indicate the transitions observed with SANS.

but only a slight change of slope which is very close to the transition temperature found by Benka. As mentioned above, the transition into the antiferromagnetic state for the sample with $x = 0.145$ can not be detected. Even though the sample with $x = 0.145$ is supposed to enter the spin-glass state from an antiferromagnetic state, the increase in intensity suggests ferromagnetic order due to the formation of iron clusters. This is in accordance with Benka, who found an extended ferromagnetic transition down to $x = 0.15$, which is at the border to the antiferromagnetic regime. The red dotted line in Fig. 6.1 shows how the ferromagnetic transition might extend into the antiferromagnetic state as found for $x = 0.145$ in the present SANS data.

For the sample with $x = 0.210$ a broad feature with a maximum at $\sim 80\,\text{K}$ defines

T_C, followed by a sharp increase in intensity. As mentioned above, a slight change in the slope of the increase of the low temperature intensity was observed, which is very close to T_f from the study by Benka, and therefore was defined as T_f in the present work. The features found in neutron scattering are indicated by dashed lines in Fig. 6.4. The discrepancy between the features in neutron scattering from the present work, and the phase boundaries from ac susceptibility and magnetisation by Benka, might be due to the use of different samples and due to the different time-scales probed by the different measurement methods.

The q-dependence of the SANS data of Fe$_x$Cr$_{1-x}$ is shown in Fig. 6.5(a-c). Again, the data recorded at $\sim$300 K were used as background, and are subtracted from the experimental data recorded at low temperatures. With decreasing temperature, not only the intensity increases, but also the slope of the q-dependence of the scattering changes.

Long-range ferromagnetic order was inferred in SANS from Porod scattering from magnetic domains [220, 221]. The intensity as a function of scattering vector q thereby follows a power law behaviour

$$I \propto q^{-n}, \tag{6.2}$$

where, according to Porod, $n = 4$. It should be noted that the Porod law is only valid for rather large q, when $q \sim 2\pi/D$ with D being the size of the probed structure [222]. Deviations from the Porod law may give information on the surface of the probed structures.

Fig. 6.5(d-f) shows the exponent n as a function of the temperature, obtained from fitting the experimental data in Fig. 6.5(a-c) with the power law in Eq. (6.2). The exponents found in Fe$_x$Cr$_{1-x}$ are much smaller than the exponent expected for Porod scattering. For decreasing temperatures, the exponent n increases from $\sim$0.5 to $\sim$1.5 − 2 at T_f. In the spin-glass phase, and for $x = 0.175$ and $x = 0.210$, the exponent n was found to be constant with $n \sim 2$. For an iron concentration of $x = 0.145$ the exponent in the spin-glass phase was constant with $n \sim 1.5$.

An exponent of $n = 2$ was found in the perovskite manganite Pr$_{1-x}$Ca$_x$MnO$_3$, and it was attributed to sheets of inter-penetrating ferromagnetic and antiferromagnetic phases [223]. In the same material, Viret *et al.* found $n = 1.6 − 1.7$. In comparison to the literature on polymers, $n = 1.6 − 1.7$ was attributed to filamentary ferromagnetic chains [224].

6.3.2. Quasielastic Measurements

Data were recorded in the SANS geometry with the direct beam centred at the right hand side of the detector, cf. Fig. 6.3(b). Using a wavelength of 6 Å allowed to cover a q-range of

Figure 6.5.: q-dependence of the SANS data of Fe_xCr_{1-x}. Samples with iron concentrations of $x = 0.145$ (a,d), $x = 0.175$ (b,e), and $x = 0.210$ (c,f) were evaluated at different temperatures. (a-c) Intensity as a function of scattering angle q. The accessible q-range was $\sim 0.02\,\text{Å}^{-1} < q < \sim 0.08\,\text{Å}^{-1}$. Solid lines are fits to the data using the power law given by Eq. (6.2). (d-f) Temperature dependence of the exponent n obtained from fitting the experimental data in (a-c). Solid lines are guides to the eye. The shaded areas indicate the phases according to the phase diagram in Fig. 6.1: AFM (green), FM (blue), SG (orange). Dashed lines indicate the transitions observed with SANS.

$0.018\,\text{Å}^{-1} \leq q \leq 0.085\,\text{Å}^{-1}$ when evaluating the data horizontally. Data were recorded in the temperature range $4\,\text{K} \leq T \leq 300\,\text{K}$. The spin echo data reduction to extract the normalised intermediate scattering function follows Sec. 3.3. To retain high statistics over the investigated q-range, masks were defined as circular ring-segments with respect to the direct beam with an opening of 90° and a width of 4 pixels, cf. Fig. 6.3(b). At low spin echo times, as used in the present study, neutron spin phase changes generally extend over large spatial regions. Hence, the neutron spin phase within one mask does not change,

and pre-grouping the detector pixels is not necessary. The procedure of pre-grouping the detector is described in Sec. 3.3.4.

A comparison between evaluating the data using a pre-grouping of the detector pixels, and without pre-grouping showed no significant difference. Therefore, data were evaluated using the grouping masks shown in Fig. 6.3(b), without pre-grouping the detector. Data were normalised by means of data recorded at the base temperature, i.e. $\sim 4\,\mathrm{K}$, assuming that the spin dynamics in Fe$_x$Cr$_{1-x}$ is frozen at temperatures well below T_f [200]. This minimises systematic errors as the same sample environment, sample shape, and apertures are used for resolution and data measurements. The process of normalising spin echo spectra is explained in detail in Sec. 3.3.3.

The normalised intermediate scattering functions in the temperature range $4\,\mathrm{K} \leq T \leq 150\,\mathrm{K}$ at a selected $q = 0.044\,\mathrm{\mathring{A}}^{-1}$ for the three investigated concentrations are shown in Fig. 6.6(a-c) around the freezing temperature $T \sim T_\mathrm{f}$, and in Fig. 6.7(a-c) at higher temperatures $T > T_\mathrm{f}$. The intermediate scattering functions evaluated over the full measured q-range are shown in App. B.4, Fig. B.16-B.21. The experimental data were fitted with a stretched exponential decay of the form

$$S(\boldsymbol{q}, \tau) = (1 - A) + A \exp\left\{-\left(\Gamma \tau\right)^\beta\right\}; \quad 0 < \beta \leq 1, \tag{6.3}$$

with the decay rate Γ, i.e. the inverse spin relaxation time, and were $0 < \beta < 1$ stretches the usual exponential decay, i.e. $\beta = 1$. A stretched exponential decay accounts for the broad distribution of relaxation times expected in spin-glasses. Evaluating the data comparing different decay models found in literature, cf. Ref. [193, 195–197, 199, 200, 225], a stretched exponential decay was found to best describe the experimental data.

Regarding the intermediate scattering functions in Fig. 6.6(a-c) and Fig. 6.7(a-c), at first glance the three investigated samples show similar behaviour. At low temperatures, below $\sim 4\,\mathrm{K}$, the spin dynamics are frozen. For temperatures below the freezing temperature $T_\mathrm{f} \sim 15\,\mathrm{K}$, the systems are still almost static in the dynamic range investigated during the present study, i.e. $\sim 10^{-4}\,\mathrm{ns}$ to $\sim 1\,\mathrm{ns}$. The spin relaxation starts to decay for temperatures around the freezing temperature T_f. Increasing the temperature shifts the spin relaxation to shorter spin echo times in all samples. At high temperatures, $T \geq 150\,\mathrm{K}$, the spin relaxation remains constant for all three samples, cf. Fig. 6.7.

The spin echo curves for temperatures up to $34\,\mathrm{K}$ do not drop to zero, but drop to a finite, constant value. This indicates that there are parts of the sample, which are static on the time-scales probed during the measurements, i.e. clusters that might fluctuate on much longer time-scales. With increasing temperature, these clusters also start to fluctuate on time-scales observed during the measurements, hence further decreasing the intermediate scattering function, eventually reaching a minimum for temperatures above
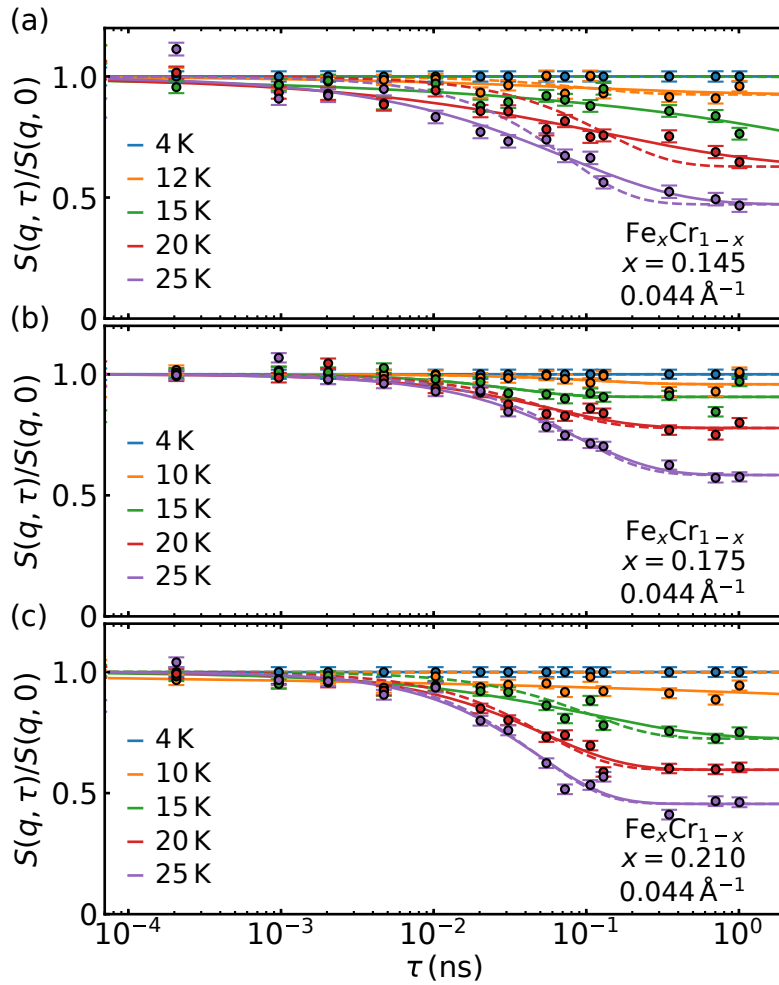
Figure 6.6.: Normalised intermediate scattering function as measured around the freezing temperature T_f in Fe_xCr_{1-x}. Data were recorded using neutrons with a mean wavelength of $\lambda = 6.0\,\text{Å}$. Data are shown for (a) $x = 0.145$, (b) $x = 0.175$, (c) $x = 0.210$, at $q = 0.044\,\text{Å}^{-1}$. The solid lines are fits to the data using Eq. (6.3). The dashed lines show usual exponential decays calculated from the fit results of the corresponding stretched exponential decay, showing the deviations from a stretched behaviour.

34 K. It should be noted that the different samples show different elastic background, as can be seen in the limited drop of the spin echo signal at the highest temperatures, cf. Fig. 6.7. The spin echo signal drops to a minimal value of ∼0.25 for $x = 0.145$, ∼0.15 for $x = 0.175$, and ∼0.1 for $x = 0.210$. This might have its reason in the magnetic signal to noise ratio, which is better for higher iron concentrations. This is also in accordance with the temperature scans in Fig. 6.4, where the intensity of the magnetic scattering is strongest for $x = 0.210$, and weakest for $x = 0.145$.

Also directly visible from the intermediate scattering functions is the different shape of the exponential decay. The usual exponential behaviour is calculated from the fit
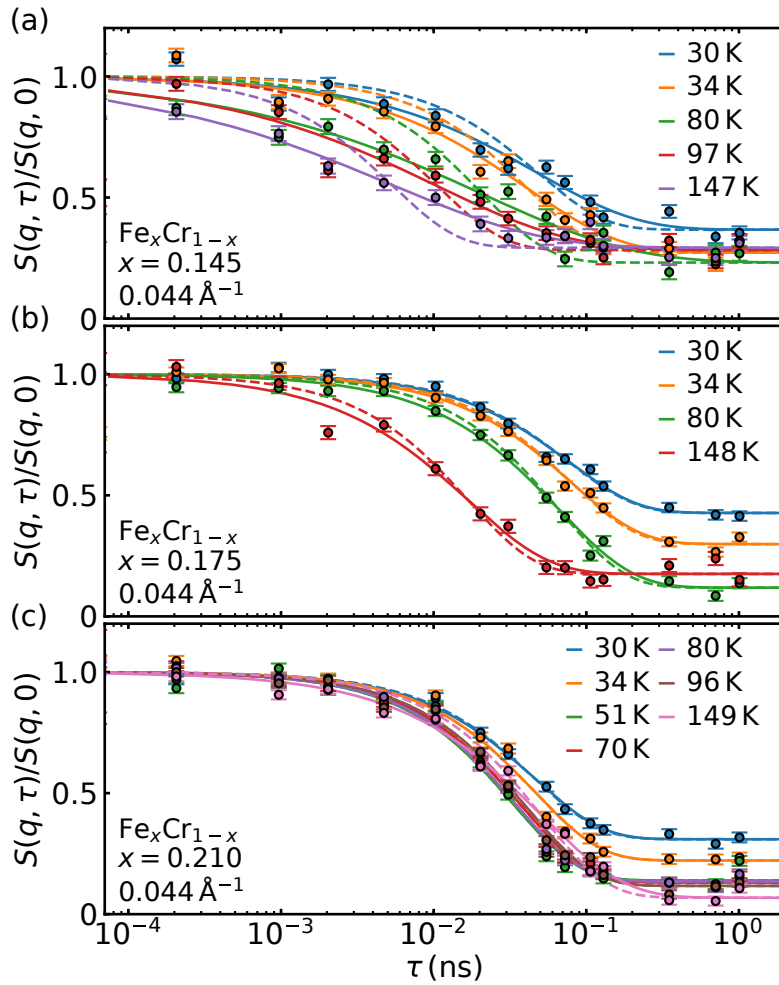
Figure 6.7.: Normalised intermediate scattering function as measured above the spin-glass phase $T > T_f$ in Fe_xCr_{1-x}. Data were recorded using neutrons with a mean wavelength of $\lambda = 6.0\,\text{Å}$. Data are shown for (a) $x = 0.145$, (b) $x = 0.175$, (c) $x = 0.210$, at $q = 0.044\,\text{Å}^{-1}$. The solid lines are fits to the data using Eq. (6.3). The dashed lines show usual exponential decays calculated from the fit results of the corresponding stretched exponential decay, showing the deviations from a stretched behaviour.

results of the stretched exponential decay, and shown as dashed lines in Fig. 6.6(a-c) and Fig. 6.7(a-c). For the sample with $x = 0.145$, the decay strongly deviates from a normal exponential over the entire temperature range. For the samples with $x = 0.175$ and $x = 0.210$, respectively, the exponential decay is stretched around T_f, and rather exponential for higher temperatures. A discussion of the stretched exponential constant β follows below.

When considering the decay rate Γ, shown in Fig. 6.8(a-c), more differences between the three samples become apparent. Data are shown for temperatures where the fit of the intermediate scattering function in Fig. 6.6 and Fig. 6.7 delivered a physical meaningful Γ.

There are two main reasons for when this is not the case. First, when a very broad distribution of relaxation times is present, hence the exponential decay is strongly stretched. Therefore, a single dominant relaxation time, i.e. a single dominant Γ, does not represent the decay. Second, when a poor signal to noise ratio does not allow for proper fitting, as it may be the case for highest temperatures. The data where these two reasons prevent extracting a physical meaningful Γ are shown in App. B.4, Fig. B.22.

The solid lines in Fig. 6.8(a-c) are fits to the data using a power law dependence

$$\Gamma \propto q^z, \tag{6.4}$$

with the exponent z as a free fit parameter. For all three samples, the exponential decay is strongly stretched around and below the freezing temperature, hence a single dominant Γ is not observed for $T \sim T_\mathrm{f}$. For $x = 0.145$, Γ could be extracted for temperatures where a ferromagnetic signal was observed, i.e. $25\,\mathrm{K} \leq T \leq 34\,\mathrm{K}$. At even higher temperatures, the exponential decay is strongly stretched and a single dominant relaxation time could not be determined. The sample with $x = 0.175$ allows to analyse Γ for temperatures between $25\,\mathrm{K} \leq T < 150\,\mathrm{K}$. For $x = 0.210$, Γ could be extracted for all temperatures above the freezing temperature T_f. For all concentrations, Γ depends on q according to the relation given in Eq. (6.4). Thereby, the exponent z in Eq. (6.4) was found to be below 2 with $z = 1.30 - 1.76$. Fig. 6.9(a-c) shows the exponent z as a function of temperature. A q-dependence seems to be present, as long as there is some ferromagnetic order.

The dashed lines in Fig. 6.8(a-c) are fits to the data using Eq. (6.4) with a fixed $z = 2.0$. The spin diffusion model $\Gamma \propto q^{2.0}$ was found by Tajima *et al.* to describe the q-dependence of Γ in the Invar alloy $\mathrm{Fe_{65}Ni_{35}}$ in a rather wide q-range [226]. A $z = 2.0$ was explained by impurity scattering of the electrons. The exponent z found for $\mathrm{Fe_xCr_{1-x}}$ in the present study will be addressed in more detail in the following discussion at the end of this chapter.

In Fig. 6.9(d-f), the stretched exponential constant β, cf. Eq. (6.3), is shown as a function of temperature for $x = 0.145$ (a), $x = 0.175$ (b), and $x = 0.210$ (c). The constant β provides an estimate how broadened the spectrum of relaxation times is. The solid lines in Fig. 6.9(d-f) are guides to the eye. For the sample with $x = 0.145$, the exponent $\beta \sim 0.5$ indicates a wide spread of relaxation times at high temperatures above T_N. In the antiferromagnetic regime, below T_N, $\beta > 0.6$ is observed. It should be noted again, that no antiferromagnetic scattering intensity can be observed in the vicinity of the [000]-Bragg peak, hence during the present study. The Néel temperature T_N is taken from literature [212, 217]. Approaching T_f, β drops drastically, indicating a very wide spectrum of relaxation times. For $x = 0.175$, $\beta \sim 0.9$ at high temperatures, dropping to $\beta \sim 0.7$ upon approaching T_f. The sample with $x = 0.210$ has $\beta \sim 1.0$ throughout the ferromagnetic phase until $\sim 20\,\mathrm{K}$ when cooling close to T_f. All samples show a drastic drop of β upon approaching T_f, indicating a wide spectrum of relaxation times.
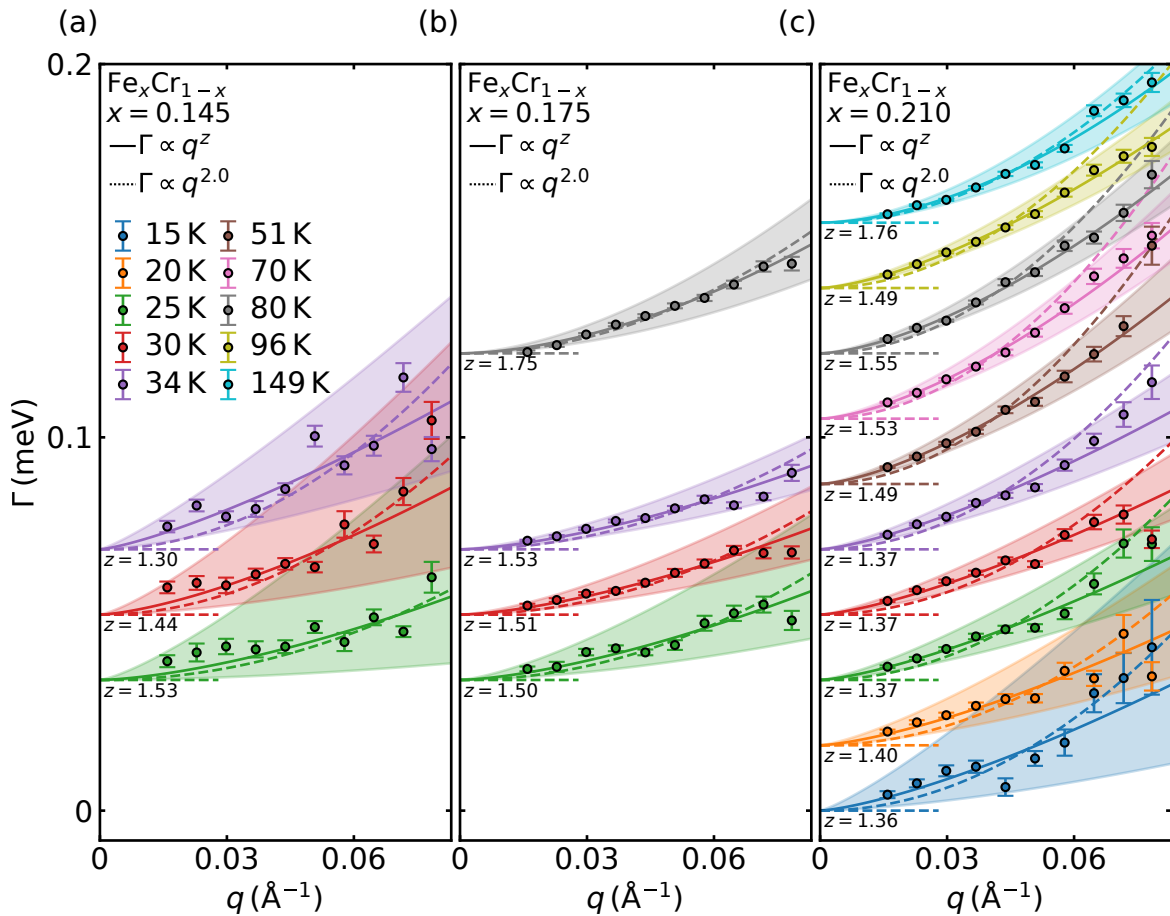
Figure 6.8.: Decay rate Γ as function of scattering vector q. Data are shown for (a) $x = 0.145$, (b) $x = 0.175$, (c) $x = 0.210$, and temperatures where the fit of the intermediate scattering function in Fig. 6.6 and Fig. 6.7 delivered meaningful Γ (for details see text). The solid lines are fits to the data using Eq. (6.4). The shaded areas indicate the 1σ standard deviation of the fit. The dashed lines are fits to the data using Eq. (6.4) with $z = 2.0$. Data are shifted by $0.0175\,\mathrm{meV}$ as indicated by the horizontal dashed lines.

6.4. Conclusions and Outlook

The present study focused on the investigation of the spin relaxation processes in a set of Fe$_x$Cr$_{1-x}$ samples with $x = 0.145$, $x = 0.175$, and $x = 0.210$. The samples were chosen so that the study allows to compare the spin relaxation at high temperatures and down into the spin-glass state with different high temperature phases. The sample with $x = 0.145$ and $x = 0.210$ enter the spin-glass phase from an antiferromagnetic and ferromagnetic phase, respectively. With an iron concentration of $x = 0.175$, Fe$_x$Cr$_{1-x}$ shows ferromagnetic signal in a small gap between the spin-glass and the paramagnet.

In a first step, the elastic SANS data in Sec. 6.3.1 gave insight into the magnetic structure of the different samples. Surprisingly, the sample with $x = 0.145$ shows ferromag-
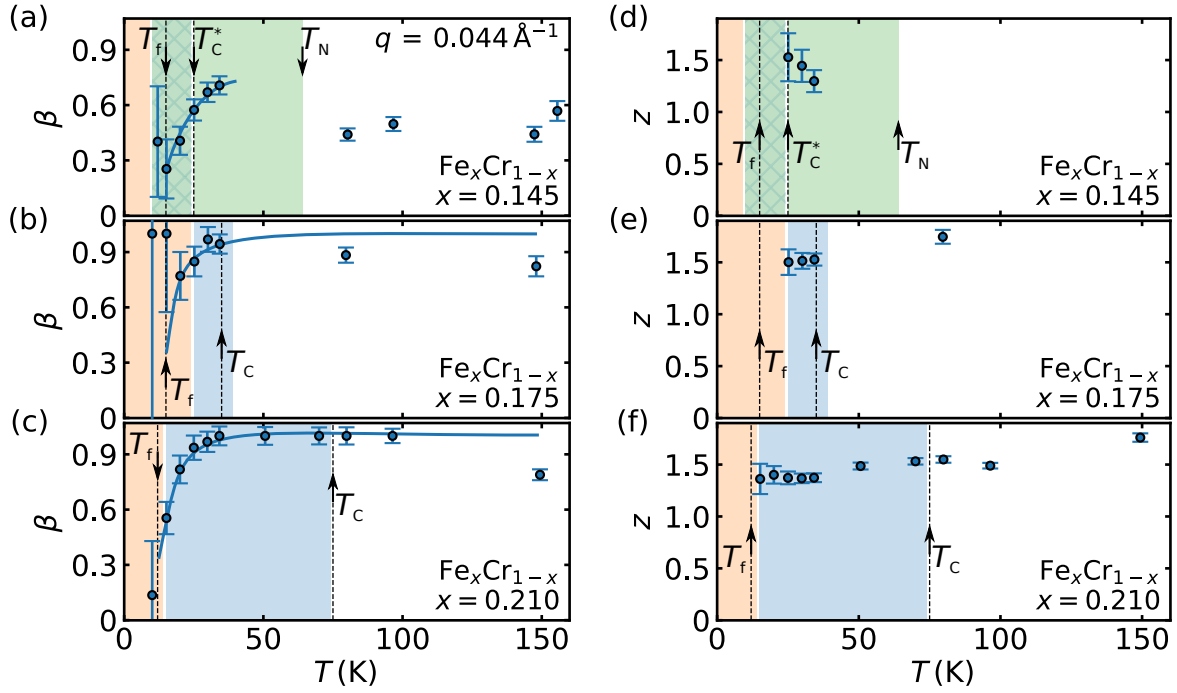
Figure 6.9.: Temperature dependence of the fit parameters z and β. (a-c) Exponent z from the model in Eq. (6.4) as function of temperature. (d-f) Stretched exponential constant β from the model in Eq. (6.3) as function of temperature. Data are shown for (a,d) $x = 0.145$, (b,e) $x = 0.175$, (c,f) $x = 0.210$. The shaded areas indicate the phases according to the phase diagram in Fig. 6.1: AFM (green), FM (blue), SG (orange). Dashed lines indicate the transitions observed with SANS. The solid lines in (a-c) are guides to the eye.

netic intensity, even though the sample is expected to have an antiferromagnetic high temperature state. Benka found an extended ferromagnetic transition down to $x = 0.15$ [212]. Clustering of Fe might lead to a formation of ferromagnetic domains, explaining the observed ferromagnetic signal for the sample with $x = 0.145$.

Further explained by the extended ferromagnetic transition is the similarity between the samples with $x = 0.145$ and $x = 0.175$, both showing ferromagnetic ordering. The sample with $x = 0.210$ clearly shows the ferromagnetic transition at high temperatures, as expected from the literature.

The q-dependence of the SANS data indicates that the magnetic structure in the spin-glass phase of the three samples is rather complex. A comparison with studies on the perovskite manganite $\mathrm{Pr}_{1-x}\mathrm{Ca}_x\mathrm{MnO}_3$ might suggest that the magnetic structure in the spin-glass phase of $\mathrm{Fe}_x\mathrm{Cr}_{1-x}$ is either composed of sheets of inter-penetrating ferromagnetic and antiferromagnetic phases [223], or has separated phases with filaments of ferromagnetic order [224]. A recent study by Wagner *et al.* characterised the microstructure of a $\mathrm{Fe}_x\mathrm{Cr}_{1-x}$ sample with $x = 0.175$ by means of atomically resolved atomic probe tomog-

raphy, and found local concentration fluctuations of Fe and Cr on length scales between 2 nm and 5 nm [227].

The quasielastic spin echo data are discussed in Sec. 6.3.2, addressing differences and similarities of the spin relaxation process in Fe$_x$Cr$_{1-x}$ for different iron concentrations. The q-dependence of the decay rate Γ can be extracted from the experimental data for temperatures above the freezing temperature T_f. Very broad distributions of relaxation times, as it is the case for $T \sim T_f$, lead to a strongly stretched exponential decay. Therefore, a single dominant relaxation time, i.e. a single dominant Γ, does not represent the decay.

The q-dependence of the decay rate Γ is proportional to q^z, with an exponent $z \sim 1.30 - 1.76$. The experimental data were also fitted with a fixed $z = 2.0$, which fits the data to some extent of the q-range. According to dynamic scaling theory, the spin diffusion in the hydrodynamic region is described by $\Gamma \propto q^{2.0}$, where the spins move without correlation. When the system is critical, theory predicts the critical exponent to be $z = 2.5$ for ferromagnetic and $z = 1.5$ for antiferromagnetic correlation, respectively.

A heuristic explanation for the critical exponent found in Fe$_x$Cr$_{1-x}$ might be the importance of the Cr atoms for the development of a spin-glass phase. Due to the presence of Cr atoms in ferromagnetic Fe clusters, the system might never reach criticality, and a $z = 2.0$ would be expected. The spin diffusion model $\Gamma \propto q^{2.0}$ was found by Tajima *et al.* to describe the q-dependence of Γ in the Invar alloy Fe$_{65}$Ni$_{35}$ in a rather wide q-range [226]. Tajima *et al.* argued, that the system never reaches criticality, i.e. $z = 2.5$ for ferromagnetically correlated spins, due to impurity scattering of the electrons. However, this explanation does not account for $z < 2.0$, as found in the present study. As frustration in Fe$_x$Cr$_{1-x}$ arises from the competition between antiferromagnetic correlations due to Cr and ferromagnetic correlations due to Fe, a certain amount of Cr needs to be present in the sample. A dominance of Cr might lead to a critical exponent of $z = 1.5$, according to dynamic scaling theory. It appears that the spins in Fe$_x$Cr$_{1-x}$ might be weakly correlated antiferromagnetically, hence reducing the exponent z further below $z = 2.0$. This might give an effective critical exponent between $z = 1.5$ for antiferromagnetic correlations and $z = 2.0$ as expected in the hydrodynamic regime.

The exponential decay of the intermediate scattering function was further investigated in terms of how strongly the exponential is stretched, i.e. how broad is the spectrum of relaxation times. For all iron concentrations, a very broad range of relaxation times is present in the vicinity of the spin-glass regime. This indicates the formation of different sized domains, fluctuating on different time scales, before freezing out at lowest temperatures. Thereby, a broad distribution of relaxation times is already present at high temperatures in the sample with $x = 0.145$. For the sample with $x = 0.210$, on the

other hand, a single relaxation time describes the exponential decay at high temperatures. For all samples, the exponent β drops drastically when approaching T_f, indicating the development of a very broad range of relaxation times. The non-exponential decay in spin-glasses and glassy systems was discussed by Campbell *et al.* in terms of percolation theory [228, 229]. Their calculation showed that the stretched exponent β approaches $\beta = 1/3$ at T_f when the system is close to its percolation limit. The stretched exponent observed in the present work is close to $\beta = 1/3$ at T_f for all samples. But as the drop is very sharp, and the density of data points around T_f rather scarce, a quantitative agreement with the predictions by Campbell *et al.* can not be made.

In the literature, spin waves were reported in the ferromagnetic phase of $Fe_x Cr_{1-x}$ for samples with $x = 0.240 - 0.340$, where the spin wave stiffness decreases drastically with decreasing iron concentration [201, 202]. Thereby, the spin wave stiffness extrapolates to zero at an iron concentration $x = 0.217$ [202]. In accordance with the literature, the sample with $x = 0.210$, which is just below the threshold of $x = 0.217$, shows no signs of spin waves. As a side note, the spin wave energies reported in literature would be measurable at RESEDA.

To summarise, $Fe_x Cr_{1-x}$ shows a broad distribution of relaxation times characteristic for spin-glasses. The stretched behaviour close to the freezing temperature further suggests that $Fe_x Cr_{1-x}$ is close to its percolation limit. The sample with antiferromagnetic order, i.e. $x = 0.145$, shows a broad distribution of relaxation times already at high temperature. For increasing iron content, hence increasing ferromagnetic order, a single relaxation time is observed to describe the exponential decay at high temperatures. The q-dependence of Γ was found to agree the power law behaviour in Eq. (6.4) with $z \sim 1.30 - 1.76$. The exponent $z < 2.0$ might be explained by Cr dissolved in Fe-clusters, giving rise to a weakly antiferromagnetically system. The present study shows that the MIEZE technique allows to perform high resolution spin-echo spectroscopy despite the presence of ferromagnetic domains that may depolarise the neutron beam in conventional spin echo. Samples with ferromagnetic, antiferromagnetic, or paramagnetic high temperature states above the spin-glass state can therefore be investigated with the very same instrument and sample environment. The very high energy resolution of RESEDA resolves the spin relaxation processes for the different samples down to lowest q-values.

7. Concluding Remarks

In the present work, ultraslow magnetisation dynamics were addressed by means of vibrating coil magnetometry and neutron resonance spin echo spectroscopy. Thereby, the spin echo beamline RESEDA was improved in terms of increased dynamic and momentum range, reduced instrumental background, and new development of instrumental control and data analysis software. The main focus was on the low-temperature magnetisation processes in the pyrochlore oxide $Yb_2Ti_2O_7$, spin wave excitations and dispersions in the archetypal ferromagnet iron, and spin relaxation processes in the spin-glass Fe_xCr_{1-x}.

7.1. Conclusion

One part the present work focused on the magnetic phase diagram and the ground state of $Yb_2Ti_2O_7$ as inferred from magnetisation measurements at millikelvin temperatures. Ch. 2 gave a brief introduction into vibrating coil magnetometry.

In the magnetic pyrochlore oxide $Yb_2Ti_2O_7$, the topic of Ch. 4, frustration arises from the geometry of the lattice, suppressing the development of magnetic order to lowest temperatures. Over the last years, experimental inconsistencies of different samples concerning the low-temperature magnetic properties of $Yb_2Ti_2O_7$ were reported. It turned out, that these inconsistencies are linked to systematic material discrepancy, making very high quality single crystals necessary [126]. Moreover, as the system is believed to be influenced by strong transverse quantum fluctuations, $Yb_2Ti_2O_7$ is still under debate to host a quantum spin-liquid at low temperatures [28, 37, 38]. Hence, the open question remained: What is the true nature of the ground state of $Yb_2Ti_2O_7$? The present work presents a detailed study of the low-temperature magnetisation processes in a high-quality single crystal of $Yb_2Ti_2O_7$ as inferred from vibrating coil magnetometry. The ground state was found to be of ferromagnetic like order, where applying a magnetic field selects the direction of the ferromagnetic polarisation along one of the six $\langle 100 \rangle$ cubic directions. Thereby, the magnetic moments are not perfectly aligned along these axes, but slightly canted towards the local 3-fold $\langle 111 \rangle$ axes, forming a splayed ferromagnetic state. The magnetic phase diagram was mapped out for applied magnetic field along the three main symmetry directions, i.e. $\langle 111 \rangle$, $\langle 110 \rangle$, and $\langle 100 \rangle$. The phase diagram shows an unusual

field dependence of a first-order phase boundary. Applying field along $\langle 111 \rangle$ and $\langle 110 \rangle$, respectively, initially increases the ordering temperature before sweeping back and eventually terminating at $T = 0$. For field along $\langle 100 \rangle$, this unusual field dependence is absent. Further, a classical model based on the Potts model for cubic ferromagnets describes the low temperature behaviour of $Yb_2Ti_2O_7$ to some extent. However, the classical estimates of the field strength of these phase transitions are inconsistent with the experimental data found in the present work. A recent study by Changlani revealed that frustrated interactions and quantum effects significantly renormalise the critical field, making it necessary to take quantum effects into account [166]. These renormalisation effects are also responsible for the reentrant type phase diagram [166].

The critical phenomena in the vicinity of magnetic phase transitions were investigated with high-resolution neutron spectroscopy. An ultra-high energy resolution is indispensable for such studies, as the addressed energy scales are very small. Neutron spin echo (NSE) spectrometers possess the highest energy resolution among neutron spectroscopy. However, in classical NSE it is not possible to measure under depolarising conditions such as ferromagnetic samples or applied magnetic fields. The neutron resonance spin echo (NRSE) technique modulation of intensity with zero effort (MIEZE) circumvents this problem by completing all spin manipulation prior to the sample position. Combining spin echo resolution with depolarising samples and sample environments makes the MIEZE technique ideally suited to study magnetisation dynamics in the vicinity of magnetic phase transitions. Ch. 3 gave a brief introduction into the fundamentals of neutron scattering, and a more detailed introduction on neutron spin echo techniques. Since instrumental development of the spin echo spectrometer RESEDA was part of the present work, Ch. 3 further contains a description of the advancements made to RESEDA. With the establishment of the longitudinal NRSE and MIEZE methods in the last years, RESEDA was reconstructed as a permanent longitudinal NRSE/MIEZE instrument. Besides the technical progress, software for instrumental control and data analysis were developed. Further, a major focus was on the reduction of background signal.

Ch. 5 reports a MIEZE study of the spin wave excitations and dispersions in the ferromagnetic phase of iron. The present study continued a recent study of the prototypical continuous phase transition from the para- to the ferromagnetic phase in iron, for $T \geq T_{\mathrm{C}}$ [47]. Going below the Curie temperature, the results of the present work are in good agreement with spin wave theory, when including dipolar interactions. There is a clear deviation from the classical Heisenberg ferromagnet, where the spin wave energy depends quadratic on q. The large magnetic moment of iron makes it necessary to include dipolar interaction to describe the observed spin wave dispersion. Although the spin wave dispersion is in accordance with spin wave theory, the resulting spin wave stiffness constant

obtained with RESEDA differs from the value observed during a triple axis spectroscopy (TAS) measurement performed in course of the present work, as well as from the value found in literature [171]. The cause for this discrepancy is still an open question. As the present study is the first extensive investigation of inelastic excitations using spin echo spectroscopy, data analysis proofed to be a great challenge. The code for data analysis at RESEDA when it comes to higher energy transfers is still under development, harbouring an unresolved issue which might account for the discrepancy between data measured at RESEDA and data obtained with TAS and found in literature, respectively.

Ch. 6 discussed a MIEZE study of the spin relaxation processes in a series of Fe_xCr_{1-x} alloys. Fe_xCr_{1-x} shows a transition from itinerant antiferromagnetism to itinerant ferromagnetism by substituting Cr by iron atoms. By changing the iron content x, the ferromagnetic phase transition of iron, and the antiferromagnetic phase transition of chromium, respectively, can be suppressed to lowest temperatures. Thereby, a putative quantum critical point is covered by a dome of emerging order showing spin-glass behaviour. The present study investigated three sample concentrations, where the different samples show antiferromagnetic, paramagnetic, and ferromagnetic order above the spin-glass phase, respectively. The spin echo measurement showed a broad distribution of relaxation times in all samples. This indicates the formation of different-sized domains, fluctuating on different time scale, before freezing out at lowest temperatures. This behaviour is characteristic for spin relaxations in spin-glasses. At higher temperatures, the distribution of spin relaxation times depends on the iron concentration. The distribution of relaxation time thereby is broadest for the samples with the lowest iron concentration, i.e. on the antiferromagnetic site. The broadness of the distribution close to the freezing temperature further suggests that Fe_xCr_{1-x} is close to its percolation limit. The q-dependence of the decay rate Γ was found to show a power law behaviour $\Gamma \propto q^z$ with $z \sim 1.30 - 1.76$. As frustration in Fe_xCr_{1-x} arises from the competition of antiferromagnetic correlations due to Cr and ferromagnetic correlations due to Fe, a dominance of Cr might lead to a critical exponent of $z = 1.5$. It appears that the spins in Fe_xCr_{1-x} are weakly correlated antiferromagnetically, giving an effective critical exponent between an antiferromagnetic $z = 1.5$ and $z = 2.0$ as expected in the hydrodynamic regime.

In conclusion, the present work investigated ultraslow magnetisation dynamics on different time-scales, employing two measurement methods. Millikelvin magnetometry allowed to investigate and better understand the low-temperature magnetisation processes in $Yb_2Ti_2O_7$. The present work further demonstrated that the MIEZE technique allows performing high resolution spin-echo spectroscopy despite the presence of depolarising conditions such as ferromagnetic domains or applied magnetic fields. This allowed the study of low-energy inelastic excitations in the ferromagnetic state of iron with spin echo

resolution. Further, the study of Fe_xCr_{1-x} samples with ferromagnetic, antiferromagnetic, or paramagnetic high temperature states above the spin-glass state could be performed with the very same instrument and sample environment.

7.2. Outlook

With the instrumental developments over the last years, RESEDA improved significantly. Besides the ultra-high energy and momentum resolution, RESEDA covers a huge dynamic range from time-of-flight over triple axis to spin echo methods. The possibility to use MIEZE to investigate under depolarising conditions with spin echo resolution allows to address exotic forms of magnetic and electronic order under extreme conditions. Examples are the spin dynamics arising from geometric frustration in the pyrochlore oxides, such as $Yb_2Ti_2O_7$, over a wide temperature range. In a most recent study, MIEZE was employed to measure crystal field excitations in $Ho_2Ti_2O_7$ [230], which are much higher in energy as compared to the spin waves in iron, making data analysis even more challenging.

Spin echo data analysis will remain a big topic in the future, especially for high energy transfers and inelastic signals. Further developments on the software are necessary to keep track with the increasing potential of the spectrometer. This is crucial to understand discrepancies such as the one observed in iron in the present study.

In Fe_xCr_{1-x}, a question to address would be the atomic short range correlations in comparison to the magnetic correlations. Depending on the orientation and clustering of the Fe and Cr, a neutron diffraction study, for example, would allow investigate the short range correlations. Another approach would be electron diffraction in an electron microscope with a nanometre sized beam, focusing on the concentrations of Fe and Cr, hence gaining information of short range order. This might allow to quantitatively assign the spin relaxation processes to certain structural clusters and concentrations of Fe and Cr.

The study in $Yb_2Ti_2O_7$ in the present work showed that the behaviour of the system is highly sensitive to slight misalignment of the sample with respect to the applied magnetic field. Further investigations of $Yb_2Ti_2O_7$ should include a study of the magnetisation using a vector magnet. Such a study would be able to reveal the transition from the field driven phase transition for field applied along $\langle 111 \rangle$ towards field along $\langle 110 \rangle$, and whether there is a tricritical point as proposed by the Potts model.

A. Magnetisation of Yb₂Ti₂O₇

This appendix chapter comprises additional information on the magnetisation measurements in $Yb_2Ti_2O_7$, cf. Ch. 2 and Ch. 4. The measurement protocols are given in App. A.1, and the plots of all measured temperature and field dependence data are shown in App. A.2.

A.1. Measurement Protocols

Three temperature versus field histories were used: (i) After cooling at zero magnetic field starting at ~1 K, the magnetic field was applied at base temperature and data collected while heating monotonically at a rate between $5\,\mathrm{mK\,min^{-1}}$ and $10\,\mathrm{mK\,min^{-1}}$, depending on the desired measurement. This is referred to as zero-field cooled / field heated (zfc-fh). (ii) Data were recorded while cooling in the same unchanged applied magnetic field starting at ~1 K. This is referred to as field cooled (fc). (iii) Following initial cool down in the applied magnetic field, data were recorded while heating monotonically at a rate of $5\,\mathrm{mK\,min^{-1}}$ and $10\,\mathrm{mK\,min^{-1}}$, respectively, in the same unchanged magnetic field. These data are referred to as field cooled / field heated (fc-fh). Measurement protocols of the temperature dependence of the magnetisation for field along the three main symmetry directions are summarised in Tab. A.1, Tab. A.3, and Tab. A.3.

Similarly, the magnetic field dependence was determined according to one of the following three different protocols: (iv) After zero-field cooling, field sweeps were carried out either from $0 \rightarrow 1\,\mathrm{T}$ or $0 \rightarrow 5\,\mathrm{T}$. They are denoted (A1) and (A1'), respectively. (v) Field sweeps starting at a high field, notably from $1\,\mathrm{T} \rightarrow -1\,\mathrm{T}$ or $1\,\mathrm{T} \rightarrow 0$, are denoted (A2) and (A2'), respectively. (vi) Related field sweeps from $-1\,\mathrm{T} \rightarrow 1\,\mathrm{T}$ are denoted (A3). Measurement protocols of field dependence of the magnetisation for field along the three main symmetry directions are summarised in Tab. A.2, Tab. A.4, and Tab. A.6.

Table A.1.: Temperature dependence of the magnetisation for fields along $\langle 111 \rangle$. The table lists applied fields, covered temperature ranges, and sweep rates.

$\mu_0 H_{\text{ext}}$ (T)	sweep protocol T (K)	sweep rate (mK min^{-1})
0.01	0.050 $\underset{②}{\overset{①}{\rightleftarrows}}$ 0.9	5
0.02	0.050 $\underset{②}{\overset{①}{\rightleftarrows}}$ 0.9	10
0.02	0.055 $\underset{②}{\overset{①}{\rightleftarrows}}$ 0.9	5
0.05	0.050 $\underset{②}{\overset{①}{\rightleftarrows}}$ 0.9	5
0.75	0.060 $\underset{②}{\overset{①}{\rightleftarrows}}$ 0.6	5
0.15	0.050 $\underset{②}{\overset{①}{\rightleftarrows}}$ 0.9	5
0.2	0.050 $\underset{②}{\overset{①}{\rightleftarrows}}$ 0.9	5
0.3	0.100 $\underset{②}{\overset{①}{\rightleftarrows}}$ 0.9	5
0.37	0.150 $\underset{②}{\overset{①}{\rightleftarrows}}$ 0.9	5
0.45	0.100 $\underset{②}{\overset{①}{\rightleftarrows}}$ 0.9	5
0.6	0.060 $\underset{②}{\overset{①}{\rightleftarrows}}$ 0.9	5
0.9	0.100 $\underset{②}{\overset{①}{\rightleftarrows}}$ 0.9	5

Table A.2.: Field dependence of the magnetisation for fields along $\langle 111 \rangle$. The table lists temperatures, covered field ranges, and sweep rates.

T (K)	sweep protocol $\mu_0 H_{\text{ext}}$ (T)	sweep rate (mT min^{-1})
0.028	$0 \rightarrow 1$	1.5
0.06	$0 \rightarrow 1 \rightarrow -1 \rightarrow 1$	15
0.1	$0 \rightarrow 1 \rightarrow -1 \rightarrow 1$	15
0.1	$0 \rightarrow 5$	15
0.15	$0 \rightarrow 1 \rightarrow -1 \rightarrow 1$	15
0.2	$0 \rightarrow 1 \rightarrow -1 \rightarrow 1$	15
0.25	$0 \rightarrow 1 \rightarrow -1 \rightarrow 1$	15
0.27	$0 \rightarrow 1 \rightarrow -1 \rightarrow 1$	15
0.3	$0 \rightarrow 1 \rightarrow -1 \rightarrow 1$	15
0.35	$0 \rightarrow 1 \rightarrow -1 \rightarrow 1$	15
0.4	$0 \rightarrow 1 \rightarrow -1 \rightarrow 1$	15
0.5	$0 \rightarrow 1$	15
0.6	$0 \rightarrow 1 \rightarrow -1 \rightarrow 1$	15
0.9	$0 \rightarrow 1 \rightarrow -1 \rightarrow 1$	15
2	$0 \rightarrow 5$	30
3	$0 \rightarrow 5$	30

Table A.3.: Temperature dependence of the magnetisation for fields along $\langle 110 \rangle$. The table lists applied fields, covered temperature ranges, and sweep rates.

$\mu_0 H_{\text{ext}}$ (T)	sweep protocol T (K)	sweep rate (mK min^{-1})
0.01	$0.090 \;{}^{①}_{②}\!\rightleftharpoons\; 0.9$	10
0.75	$0.100 \;{}^{①}_{②}\!\rightleftharpoons\; 0.9$	10
0.3	$0.250 \;{}^{①}_{②}\!\rightleftharpoons\; 0.9$	10
0.4	$0.250 \;{}^{①}_{②}\!\rightleftharpoons\; 0.9$	10
0.45	$0.100 \;{}^{①}_{②}\!\rightleftharpoons\; 0.9$	10
0.5	$0.100 \;{}^{①}_{②}\!\rightleftharpoons\; 0.9$	10
0.55	$0.100 \;{}^{①}_{②}\!\rightleftharpoons\; 0.9$	10
0.6	$0.100 \;{}^{①}_{②}\!\rightleftharpoons\; 0.9$	10
0.8	$0.080 \;{}^{①}_{②}\!\rightleftharpoons\; 0.9$	10

Table A.4.: Field dependence of the magnetisation for fields along $\langle 110 \rangle$. The table lists temperatures, covered field ranges, and sweep rates.

T (K)	sweep protocol $\mu_0 H_{\text{ext}}$ (T)	sweep rate (mT min^{-1})
0.09	$0 \rightarrow 1 \rightarrow 0$	15/30/60
0.1	$0 \rightarrow 1 \rightarrow 0$	15/30/60
0.2	$0 \rightarrow 1 \rightarrow 0$	15/30/60
0.27	$0 \rightarrow 1 \rightarrow 0$	15/30/60
0.3	$0 \rightarrow 1 \rightarrow 0$	15/30/60
0.4	$0 \rightarrow 1 \rightarrow 0$	15/30/60
0.45	$0 \rightarrow 1 \rightarrow 0$	15/30/60
0.5	$0 \rightarrow 1 \rightarrow 0$	15/30/60
0.6	$0 \rightarrow 1 \rightarrow 0$	15
0.9	$0 \rightarrow 1 \rightarrow 0$	50
2	$0 \rightarrow 5$	30
3	$0 \rightarrow 5$	30
5	$0 \rightarrow 5$	30

Table A.5.: Temperature dependence of the magnetisation for fields along $\langle 100 \rangle$. The table lists applied fields, covered temperature ranges, and sweep rates.

$\mu_0 H_\text{ext}$ (T)	sweep protocol T (K)	sweep rate (mK min^{-1})
0.01	0.05 ①⇄② 0.9	10
0.05	0.05 ①⇄② 0.9	10
0.7	0.05 ①⇄② 0.9	10
0.15	0.10 ①⇄② 0.9	10
0.3	0.10 ①⇄② 0.9	10
0.6	0.10 ①⇄② 0.9	10

Table A.6.: Field dependence of the magnetisation for fields along $\langle 100 \rangle$. The table lists temperatures, covered field ranges, and sweep rates.

T (K)	sweep protocol $\mu_0 H_\text{ext}$ (T)	sweep rate (mT min^{-1})
0.065	$0 \to 1 \to -1 \to 1$	10
0.065	$0 \to 5$	10
0.1	$0 \to 1 \to -1 \to 1$	15
0.1	$0 \to 5$	15
0.15	$0 \to 1$	15
0.2	$0 \to 1 \to -1 \to 1$	15
0.25	$0 \to 1 \to -1 \to 1$	15
0.3	$0 \to 1 \to -1 \to 1$	15
0.4	$0 \to 1 \to -1 \to 1$	15
0.475	$0 \to 1 \to -1 \to 1$	15
0.55	$0 \to 1 \to -1 \to 1$	15
0.9	$0 \to 1 \to -1 \to 1$	10
1.5	$0 \to 3$	30
2	$0 \to 5$	30
3	$0 \to 5$	30

A.2. Temperature and Field Dependence

All measured temperature and field dependence of the magnetisation for field along the three main symmetry directions are plotted in Fig. A.1-A.6.
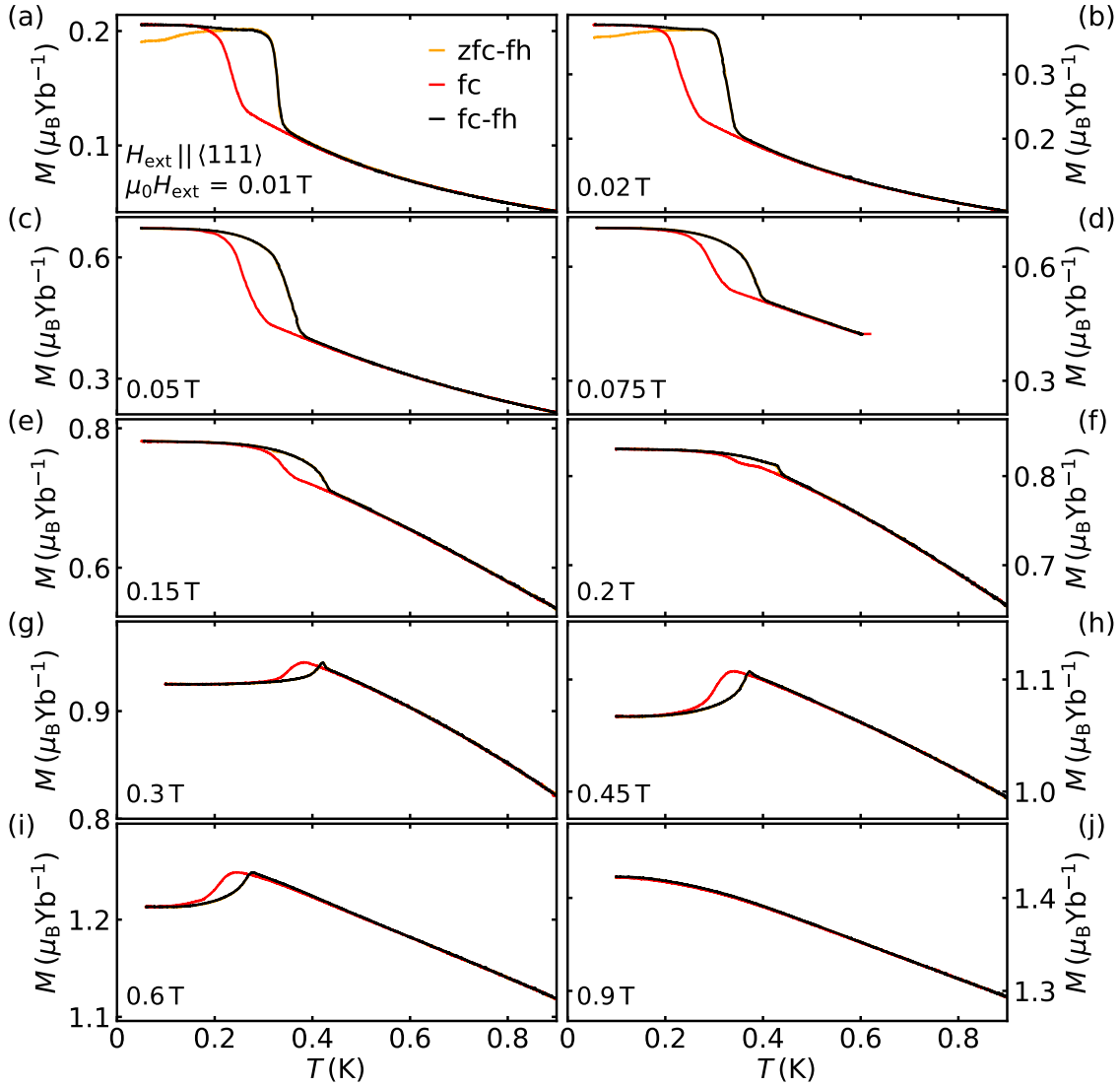
Figure A.1.: Temperature dependence of the magnetisation of $Yb_2Ti_2O_7$ in applied magnetic fields between $0.01\,T$ and $0.9\,T$ along the crystallographic $\langle 111 \rangle$ direction. In small applied fields, i.e. below $0.05\,T$ (panels (a) and (b)) a distinct difference between data recorded under zero-field cooling (zfc) and field cooling (fc) emerges below $T \sim 0.25\,K$. For fields higher than $0.05\,T$ zfc and fc data are identical.
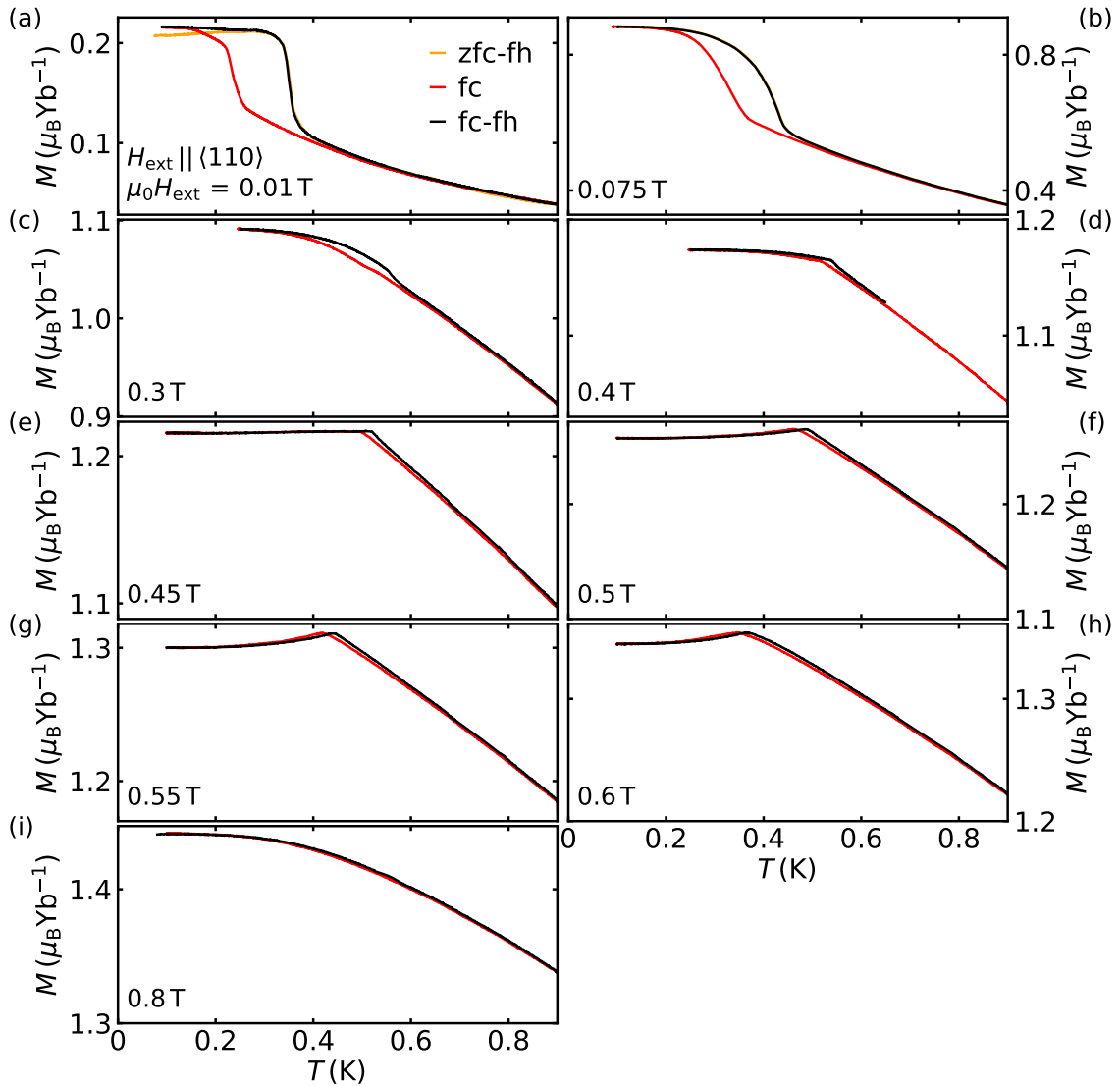
Figure A.2.: Temperature dependence of the magnetisation of Yb$_2$Ti$_2$O$_7$ in applied magnetic fields between $0.01\,\mathrm{T}$ and $0.8\,\mathrm{T}$ along the crystallographic $\langle 110 \rangle$ direction. In small applied fields, i.e. below $0.075\,\mathrm{T}$ (panel (a)) a distinct difference between data recorded under zero-field cooling (zfc) and field cooling (fc) emerges below $T \sim 0.25\,\mathrm{K}$. For higher fields zfc and fc data are identical.
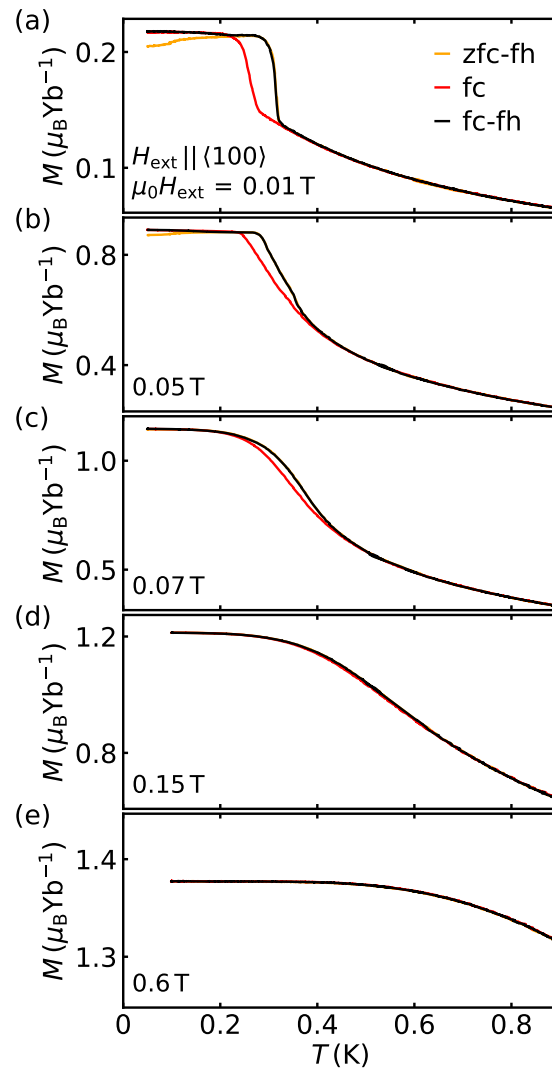
Figure A.3.: Temperature dependence of the magnetisation of $Yb_2Ti_2O_7$ in applied magnetic fields between $0.01\,\mathrm{T}$ and $0.6\,\mathrm{T}$ along $\langle 100\rangle$.
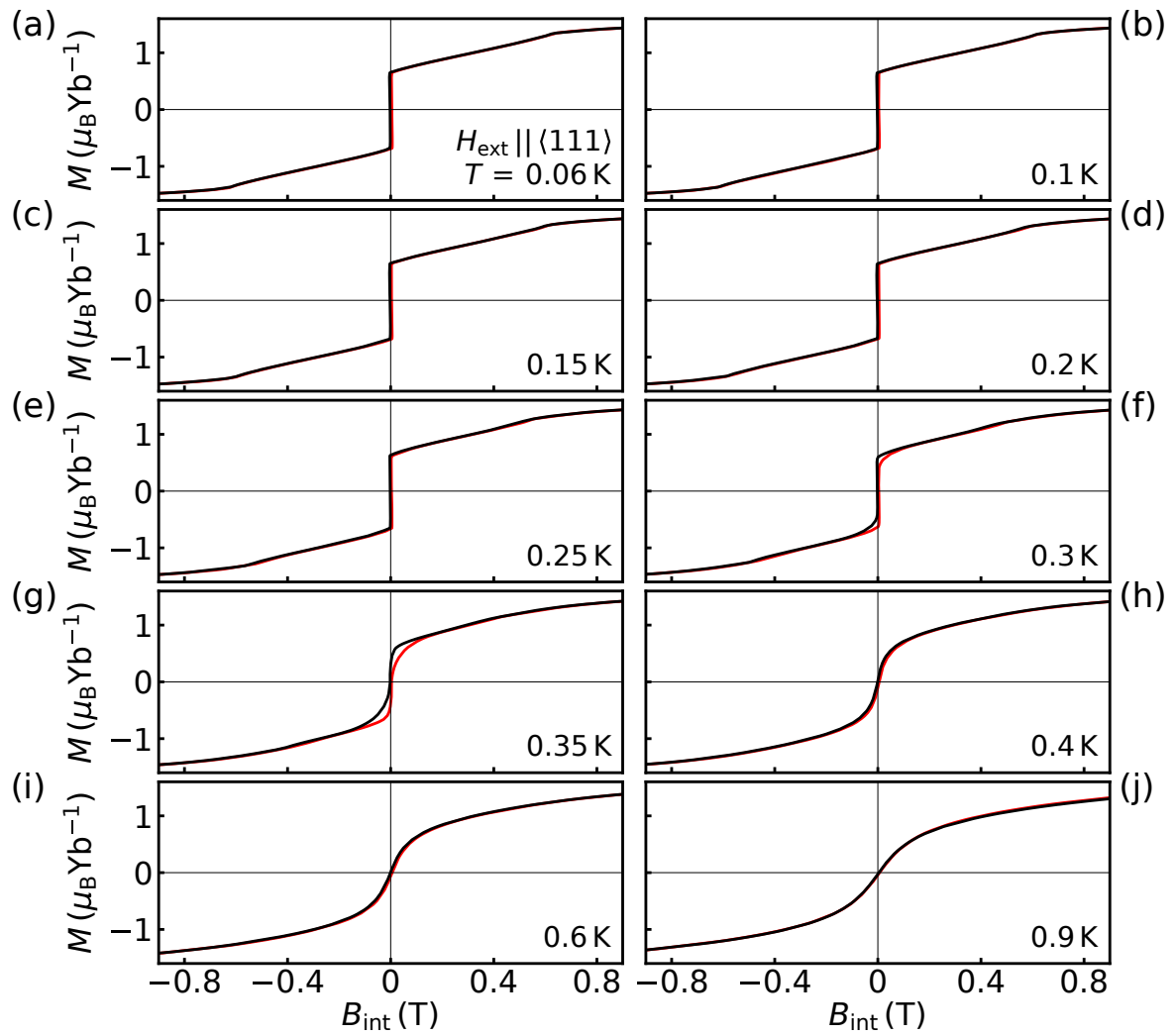
Figure A.4.: Magnetisation of Yb$_2$Ti$_2$O$_7$ as a function of internal magnetic field along $\langle 111 \rangle$ after correction for demagnetisation fields for temperatures in the range 0.06 K to 0.9 K. Field sweeps were measured according to the following protocol: $0 \to +1$ T $\to -1$ T $\to +1$ T with zfc from ambient. Data shown is the hysteresis loop without the zfc branch.
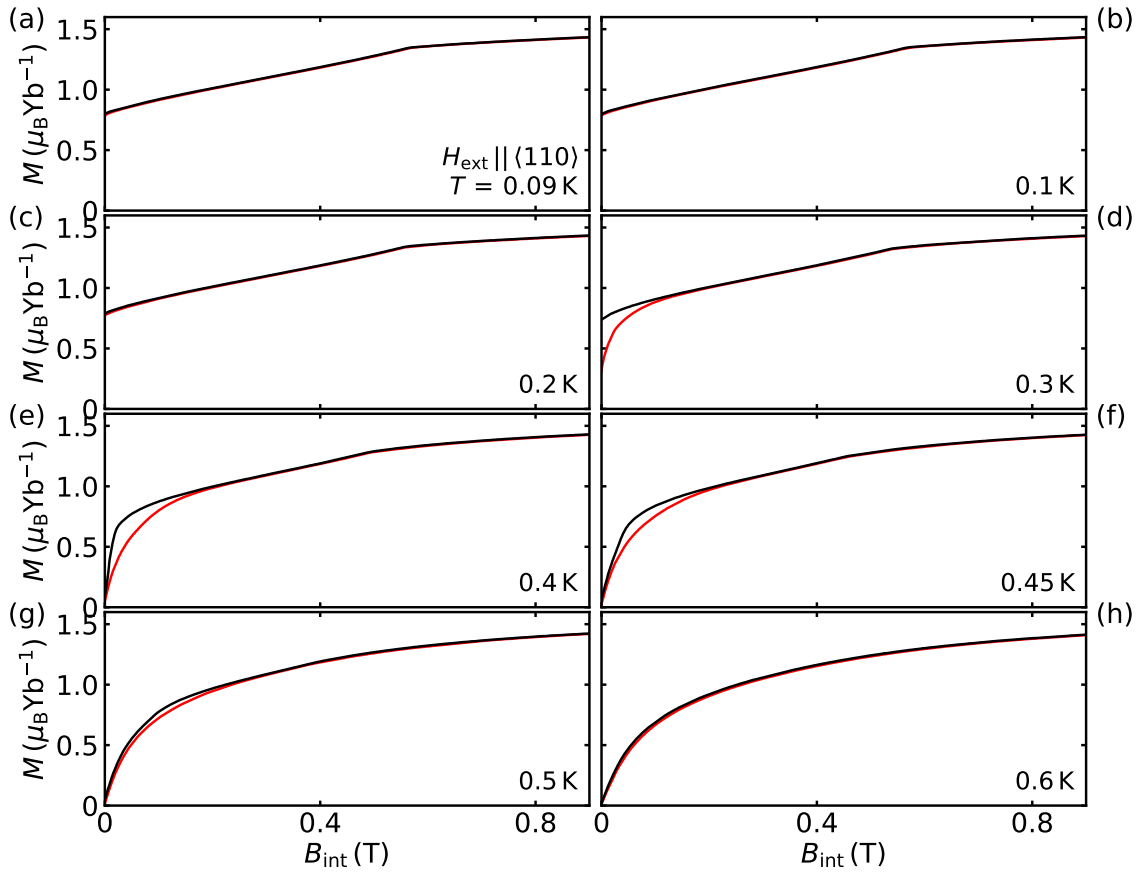
Figure A.5.: Magnetisation of $Yb_2Ti_2O_7$ as a function of internal magnetic field along $\langle 110 \rangle$ after correction for demagnetisation fields for temperatures in the range $0.09\,\text{K}$ to $0.6\,\text{K}$. Field sweeps were measured according to the following protocol: $0 \rightarrow +1\,\text{T} \rightarrow 0$. Data shown is the hysteresis loop without the zfc branch.
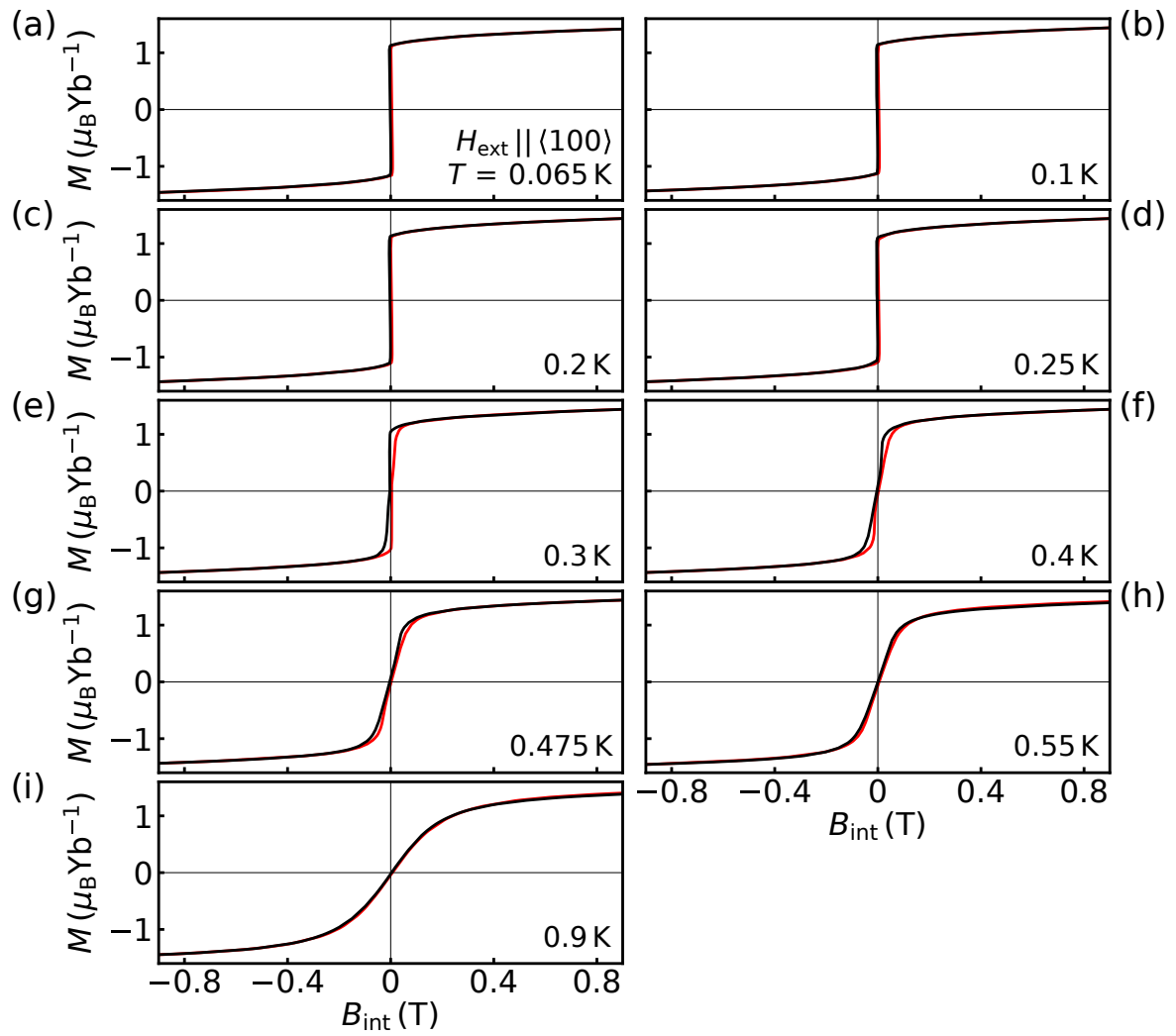
Figure A.6.: Magnetisation of $Yb_2Ti_2O_7$ as a function of internal magnetic field along $\langle 100 \rangle$ after correction for demagnetisation fields for temperatures in the range $0.065\,\mathrm{K}$ to $0.9\,\mathrm{K}$. Field sweeps were measured according to the following protocol: $0 \rightarrow +1\,\mathrm{T} \rightarrow 0$. Data shown is the hysteresis loop without the zfc branch.

B. Neutron Scattering

This appendix chapter comprises additional information on the neutron scattering performed in the present work, cf. Ch. 3 and Ch. 5-6. The maximum energy transfer achievable with neutron scattering is discussed in App. B.1. In App. B.2, details of the instrumental resolution of the spin echo spectrometer RESEDA are given. Additional information on the measurements in iron are given in App. B.3, and on the measurements in Fe_xCr_{1-x} in App. B.4.

B.1. Maximum Energy Transfer

The maximum energy transfer that can be realised by neutron scattering can be determined from the equations for momentum and energy transfer:

$$\boldsymbol{Q} = (\boldsymbol{k}_i - \boldsymbol{k}_f), \tag{B.1}$$

and

$$\hbar\omega = \frac{\hbar^2}{2m}\left(k_i^2 - k_f^2\right), \tag{B.2}$$

to

$$|Q|^2 = |k_f|^2 + |k_i|^2 - 2|k_f||k_i|\cos(2\theta). \tag{B.3}$$

From Eq. (B.1) follows

$$\boldsymbol{k}_f = -\boldsymbol{Q} + \boldsymbol{k}_i \tag{B.4}$$

$$|k_f|^2 = Q^2 + k_i^2 - 2|Q||k_i|\cos(\measuredangle(Q, k_i)), \tag{B.5}$$

which has its maximum for $\angle(Q, k_i) = 0$. This is the case for $k_f \parallel k_i$, and $|Q|^2$ follows to

$$|Q|^2 = |k_f|^2 + |k_i|^2 - 2|k_f||k_i| \tag{B.6}$$

$$= \frac{2m_{\mathrm{n}}}{\hbar^2} E_f + \frac{2m_{\mathrm{n}}}{\hbar^2} E_i - 2\frac{2m_{\mathrm{n}}}{\hbar^2}\sqrt{E_f}\sqrt{E_i} \tag{B.7}$$

$$= \frac{2m_{\mathrm{n}}}{\hbar^2}\left(E_f + E_i - 2\sqrt{E_f}\sqrt{E_i}\right) \tag{B.8}$$

$$= \frac{2m_{\mathrm{n}}}{\hbar^2}\left(\sqrt{E_f} - \sqrt{E_i}\right)^2 \tag{B.9}$$

$$= \frac{2m_{\mathrm{n}}}{\hbar^2}\left(\sqrt{E_i + \Delta E} - \sqrt{E_i}\right)^2 \tag{B.10}$$

$$= \frac{2m_{\mathrm{n}}}{\hbar^2}\left(\sqrt{E_i}\sqrt{1 + \frac{\Delta E}{E_i}} - \sqrt{E_i}\right)^2. \tag{B.11}$$

This gives for ΔE:

$$\Delta E = \left(\frac{|Q|^2\hbar^2}{2E_i m_{\mathrm{n}}} + \frac{\sqrt{2}|Q|\hbar}{\sqrt{E_i m_{\mathrm{n}}}} + 1\right)E_i - E_i \tag{B.12}$$

$$= \frac{|Q|^2\hbar^2}{2m_{\mathrm{n}}} + \frac{\sqrt{2E_i}|Q|\hbar}{\sqrt{m_{\mathrm{n}}}} + E_i - E_i \tag{B.13}$$

$$= \frac{|Q|^2\hbar^2}{2m_{\mathrm{n}}} + \frac{\sqrt{2E_i}|Q|\hbar}{\sqrt{m_{\mathrm{n}}}} \tag{B.14}$$

$$= |Q|^2\frac{E_i}{k_i^2} + |Q|\frac{2\sqrt{E_i}\hbar^2}{\sqrt{2m_{\mathrm{n}}}} \tag{B.15}$$

$$= E_i|Q|\left(\frac{|Q|}{k_i^2} + \frac{2}{k_i}\right). \tag{B.16}$$

Fig. B.1 shows the observable $(q/k_i, E/E_i)$-space during a neutron scattering experiment. A constant angle $\angle(Q, k_i)$ corresponds to a parabolic trajectory. The observable q, E-spaces for RESEDA during the iron measurements (red), as well as for Collins set-up (blue) are shown in Fig. B.1.

B.2. Instrumental Resolution of RESEDA

The resolution was analytically derived by taking into account the two main contribution to the resolution of a small angle neutron scattering instrument, following the theoretical work by Pedersen *et al.* [186], and Hammouda and Mildner [187]: (i) resolution due to a finite wavelength spread; (ii) resolution due to finite collimation. The SANS resolution
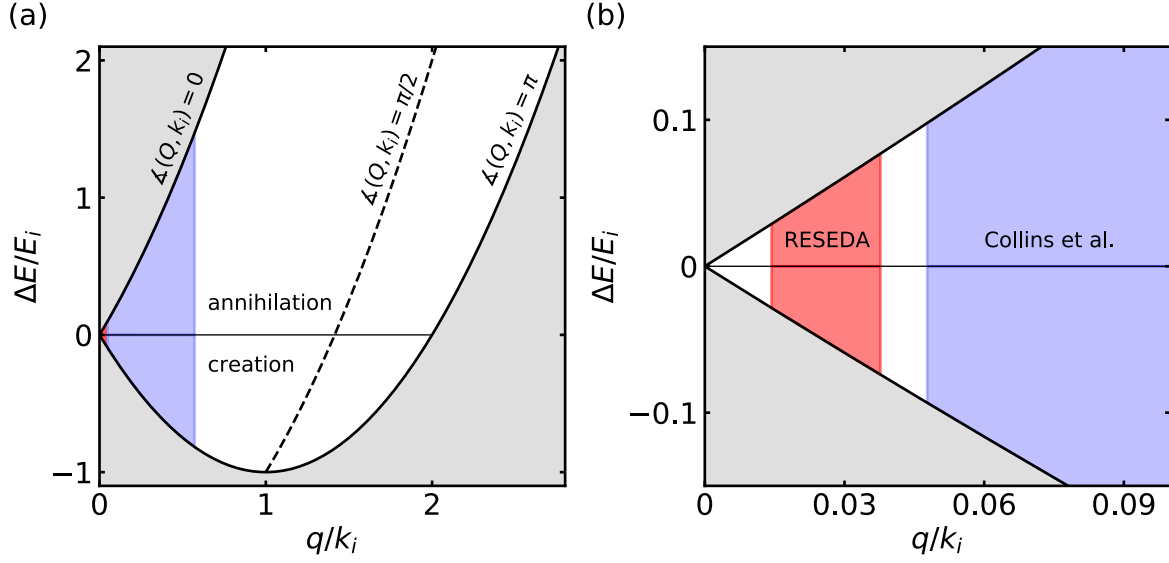
Figure B.1.: Observable $(q/k_i, E/E_i)$-space during a neutron scattering experiment. (a) Scattering parabolas for $\sphericalangle(Q, k_i) = 0$, $\pi/2$, and π are shown as solid and dashed lines, respectively. The grey shaded area shows the (q, E)-space which is inaccessible during neutron scattering. The red and blue shaded areas show the (q, E)-space of RESEDA and Collins *et al.* [171], respectively. (b) shows a zoom of the region of interest during the investigations in iron.

function is represented by a Gaussian distribution of standard deviation σ_q, where q is the scattering vector:

$$R(q, \sigma_q) = \sqrt{\frac{1}{2\pi\sigma_q^2}} \exp\left\{-\frac{q^2}{2\sigma_q^2}\right\}, \tag{B.17}$$

with

$$\sigma_q^2 = (\sigma_q^2)_\lambda + (\sigma_q^2)_{\text{coll.}} \tag{B.18}$$

$$= q^2 \left(\frac{\sigma_\lambda}{\lambda}\right)^2 + \frac{4\pi^2}{\lambda^2}\frac{\sigma_x^2 + \sigma_y^2}{L_{\text{SS}}^2} \tag{B.19}$$

$$= q^2 \left(\frac{\Delta\lambda}{\sqrt{6}\lambda}\right)^2 + \left(\frac{2\pi}{\lambda}\right)^2 \frac{\sigma_x^2 + \sigma_y^2}{L_{\text{SS}}^2}. \tag{B.20}$$

In the last step, a triangular wavelength distribution was assumed. The spatial variance is divided in a horizontal contribution

$$\sigma_x^2 = \left(\frac{L_{\text{SD}}}{L_{\text{SS}}}\right)^2 \frac{r_1^2}{4} + \left(\frac{L_{\text{SS}} + L_{\text{SD}}}{L_{\text{SD}}}\right)^2 \frac{r_2^2}{4} + \frac{1}{3}\left(\frac{\Delta x_3}{2}\right)^2, \tag{B.21}$$

and a vertical contribution

$$\sigma_x^2 = \left(\frac{L_{\text{SD}}}{L_{\text{SS}}}\right)^2 \frac{r_1^2}{4} + \left(\frac{L_{\text{SS}} + L_{\text{SD}}}{L_{\text{SD}}}\right)^2 \frac{r_2^2}{4} + \frac{1}{3}\left(\frac{\Delta y_3}{2}\right)^2. \tag{B.22}$$

The instrumental configuration at RESEDA was:

radius source aperture:	$r_1 = 0.02\,\mathrm{m}$
radius sample aperture:	$r_1 = 0.005\,\mathrm{m}$
source-sample distance:	$L_{\mathrm{SS}} = 3.0\,\mathrm{m}$
sample-detector distance:	$L_{\mathrm{SD}} = 2.25\,\mathrm{m}$
horizontal pixel width:	$\Delta x = 0.003125\,\mathrm{m}$
vertical pixel width:	$\Delta y = 0.003125\,\mathrm{m}$
wavelength:	$\lambda = 6.0\,\text{Å}$
wavelength spread:	$\Delta\lambda/\lambda = 0.12.$

B.3. Measurements in Iron

This appendix section comprises additional information on the measurements in iron, cf. Ch. 5. The plots of all measured temperatures are shown in App. B.3.1. In App. B.3.2, the calculations of the dipolar energy of iron is given. App. B.3.3 summarises the results obtained on iron by Collins *et al.* in 1969 [171]. The data obtained via triple-axis spectroscopy (TAS) at the beamline MIRA are presented in App. B.3.4.

B.3.1. MIEZE Results

MIEZE scans in iron for all measured temperatures are shown in Fig. B.2-B.8.
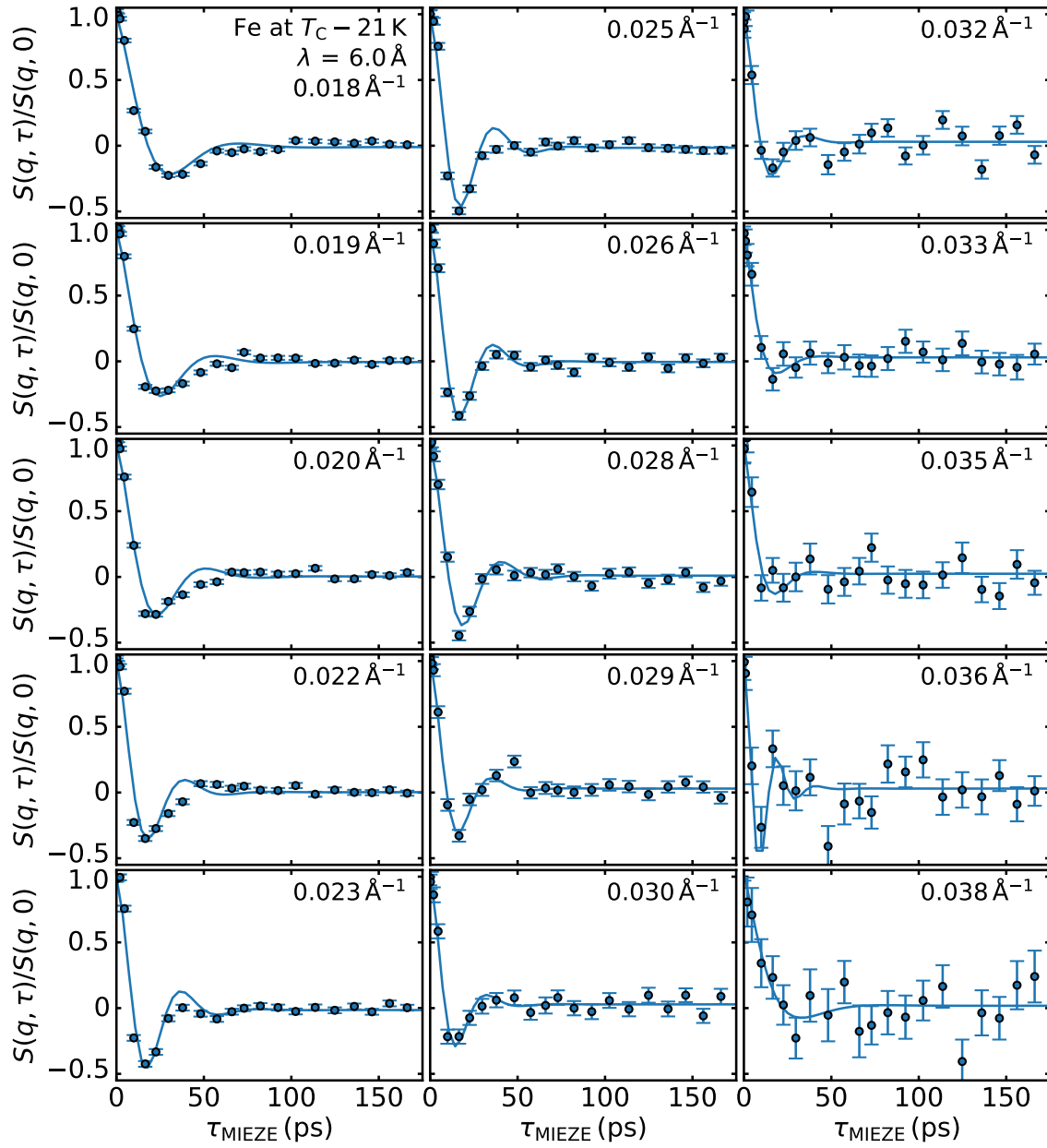
Figure B.2.: Normalised intermediate scattering function as measured in iron at $T_{\mathrm{C}} - 21\mathrm{K}$. Data was recorded using neutrons with a mean wavelength of $\lambda = 6.0\,\text{Å}$. Data is shown for the evaluated q-region, i.e. $0.018\,\text{Å}^{-1}$ to $0.042\,\text{Å}^{-1}$. The solid lines are fits to the data using Eq. (5.12).
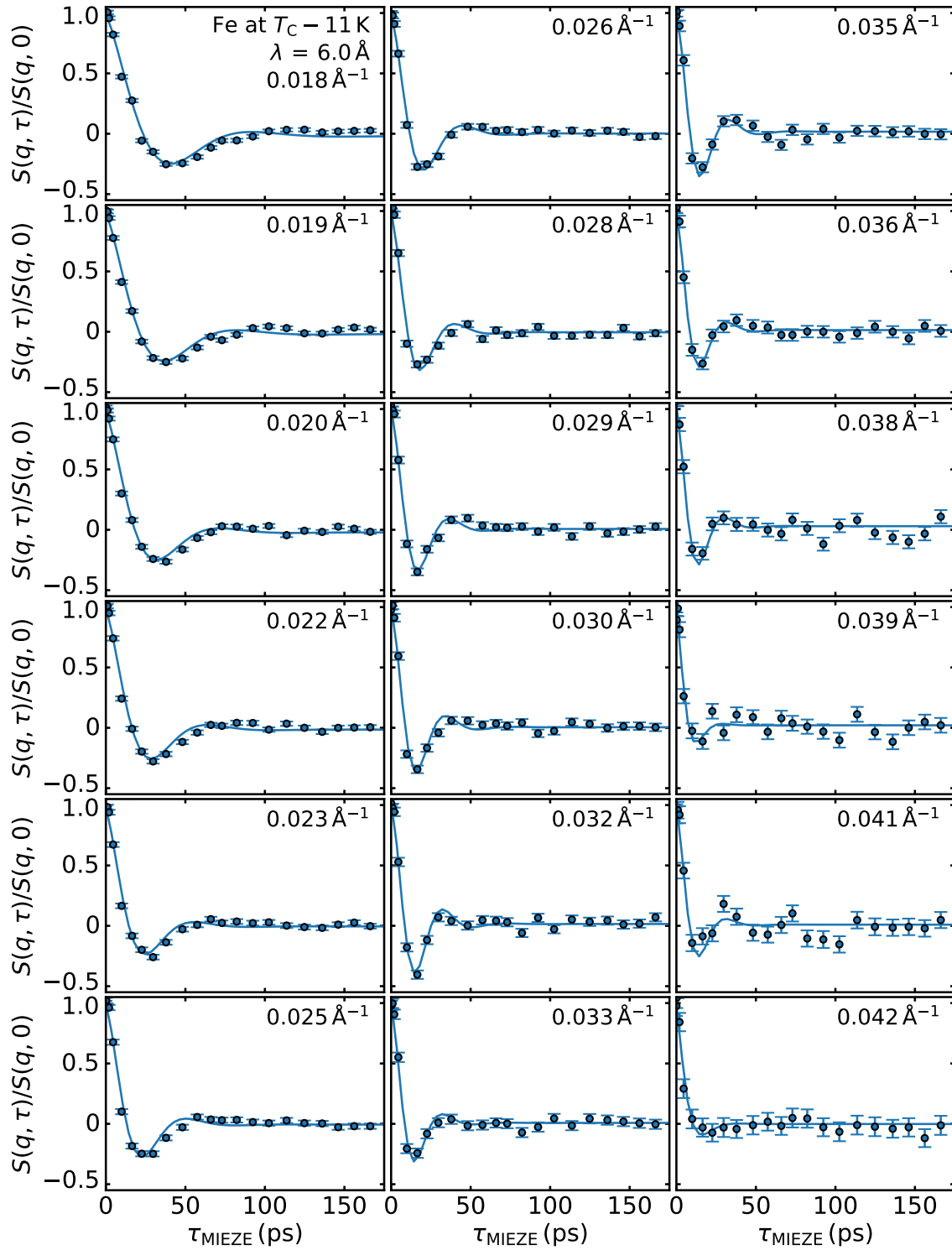
Figure B.3.: Normalised intermediate scattering function as measured in iron at $T_{\mathrm{C}} - 11\mathrm{K}$. Data was recorded using neutrons with a mean wavelength of $\lambda = 6.0\,\text{Å}$. Data is shown for the evaluated q-region, i.e. $0.018\,\text{Å}^{-1}$ to $0.042\,\text{Å}^{-1}$. The solid lines are fits to the data using Eq. (5.12).
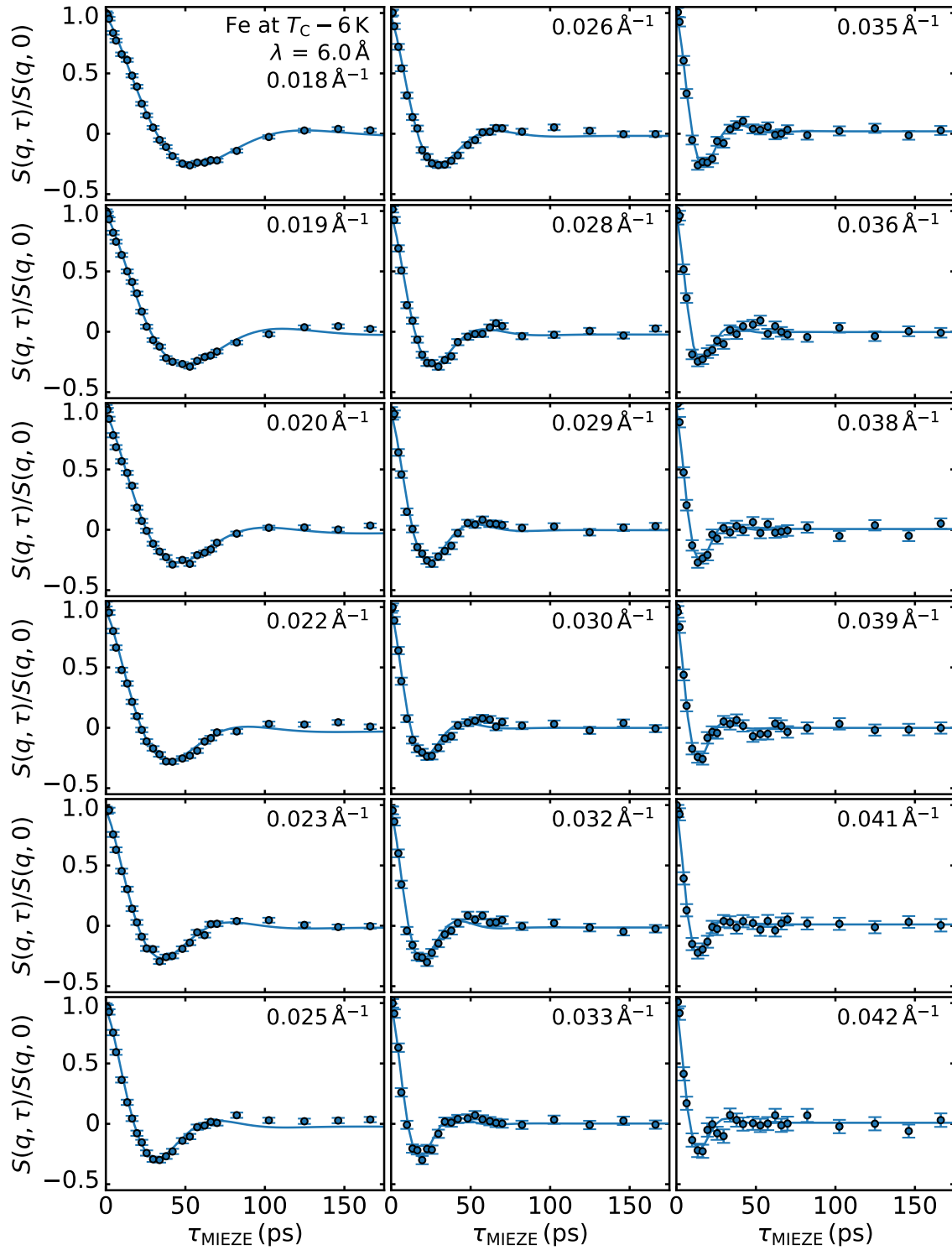
Figure B.4.: Normalised intermediate scattering function as measured in iron at $T_C - 6$K. Data was recorded using neutrons with a mean wavelength of $\lambda = 6.0$ Å. Data is shown for the evaluated q-region, i.e. 0.018 Å^{-1} to 0.042 Å^{-1}. The solid lines are fits to the data using Eq. (5.12).
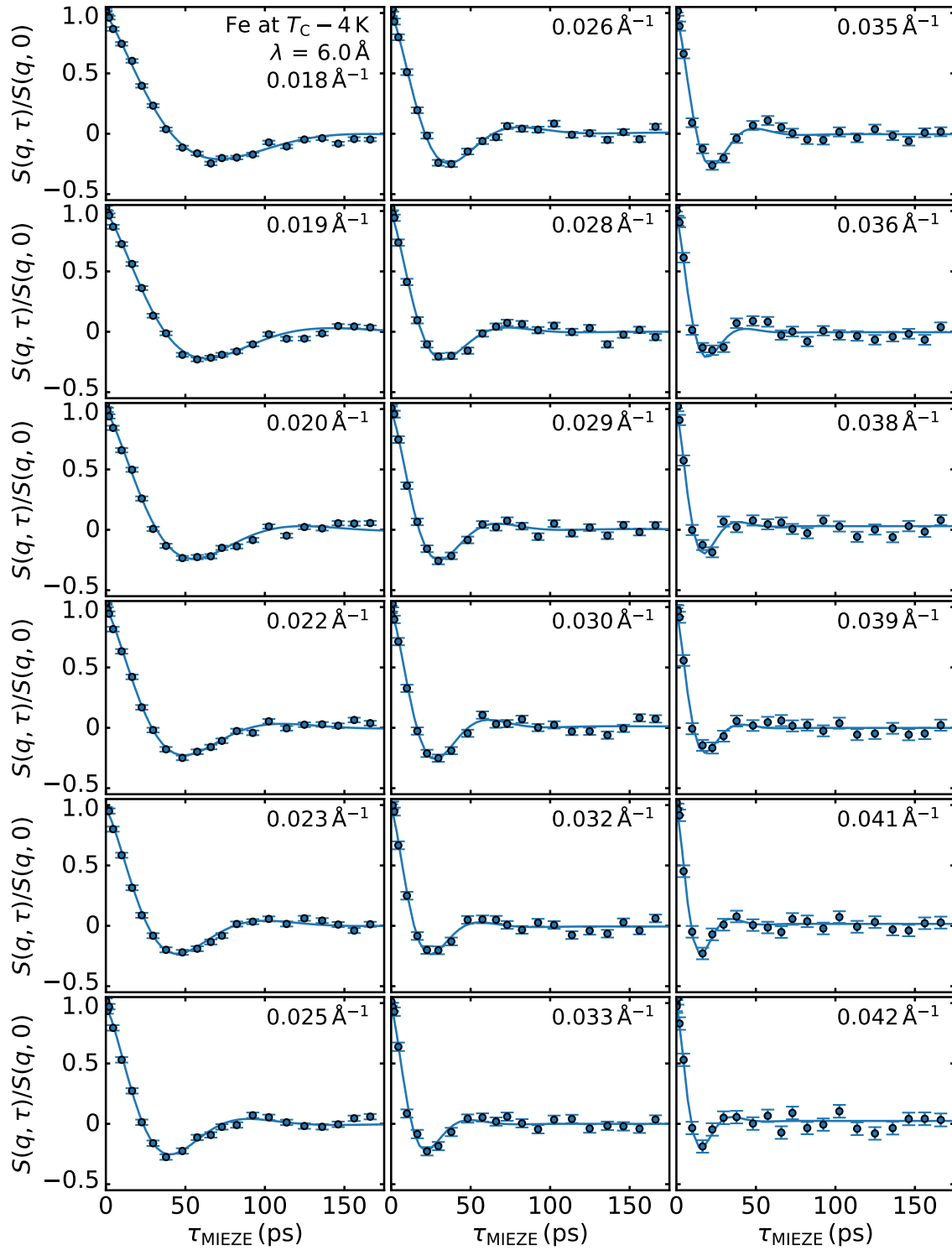
Figure B.5.: Normalised intermediate scattering function as measured in iron at $T_C - 4\,\text{K}$. Data was recorded using neutrons with a mean wavelength of $\lambda = 6.0\,\text{Å}$. Data is shown for the evaluated q-region, i.e. $0.018\,\text{Å}^{-1}$ to $0.042\,\text{Å}^{-1}$. The solid lines are fits to the data using Eq. (5.12).
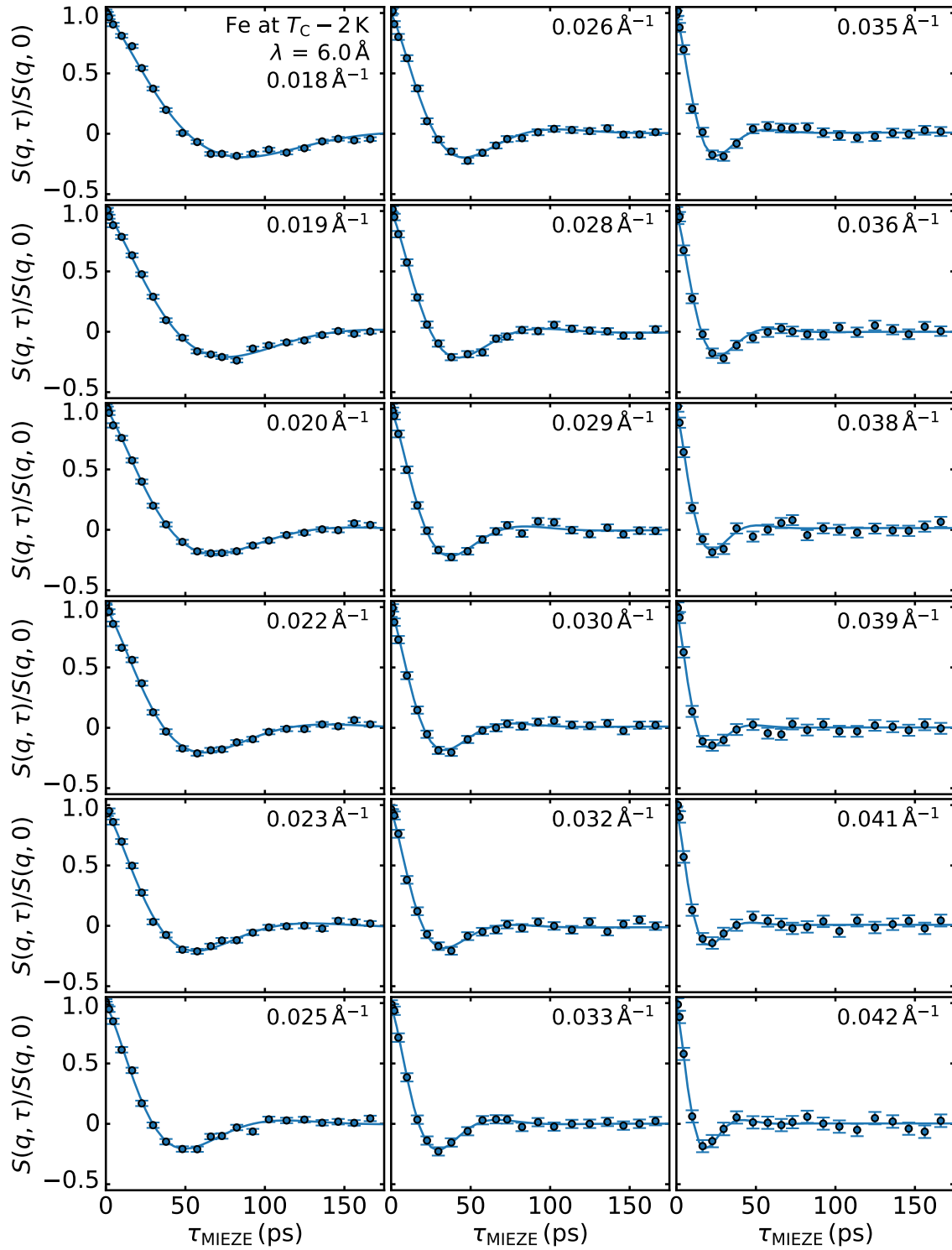
Figure B.6.: Normalised intermediate scattering function as measured in iron at $T_C - 2\,\mathrm{K}$. Data was recorded using neutrons with a mean wavelength of $\lambda = 6.0\,\text{Å}$. Data is shown for the evaluated q-region, i.e. $0.018\,\text{Å}^{-1}$ to $0.042\,\text{Å}^{-1}$. The solid lines are fits to the data using Eq. (5.12).
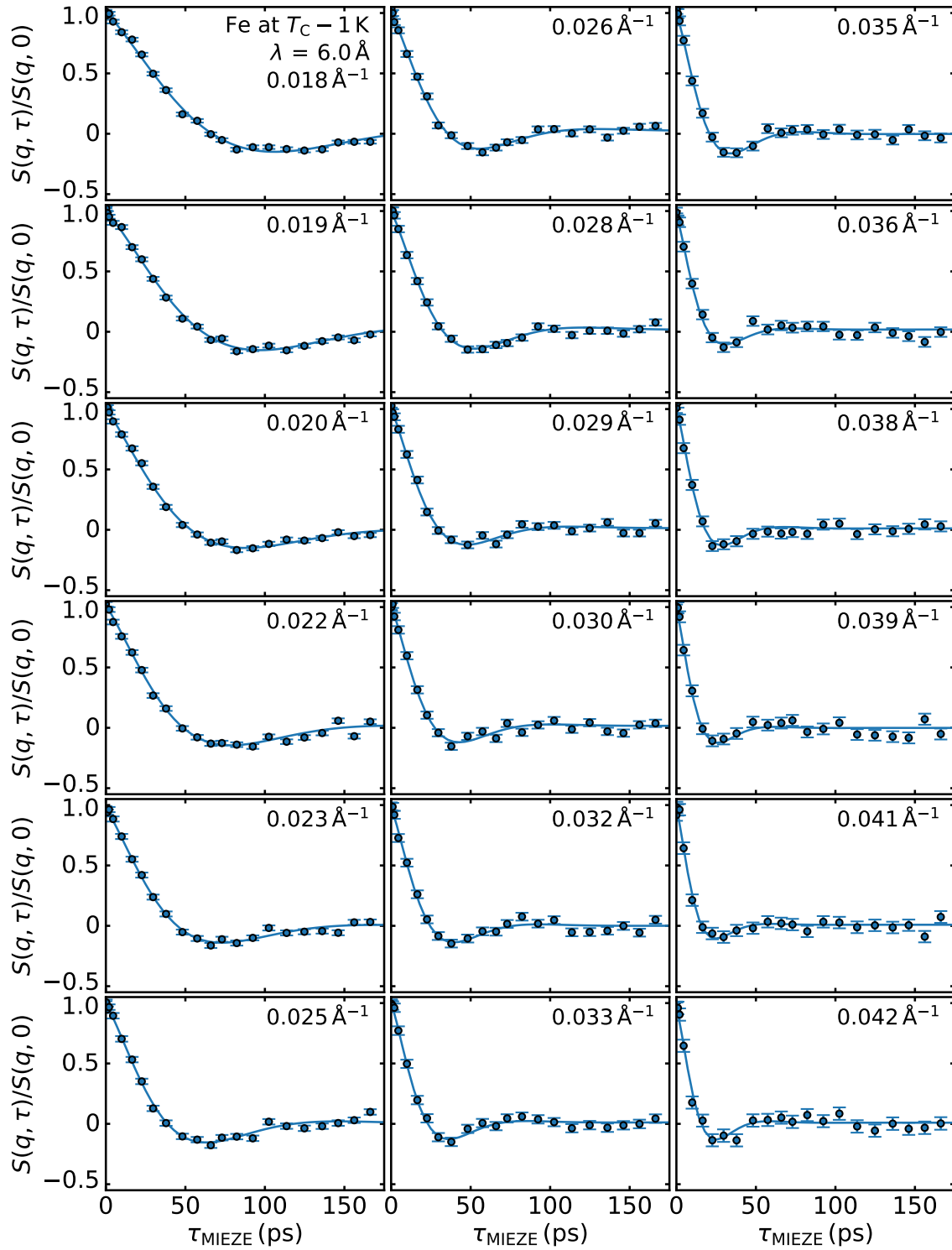
Figure B.7.: Normalised intermediate scattering function as measured in iron at $T_\mathrm{C} - 1\,\mathrm{K}$. Data was recorded using neutrons with a mean wavelength of $\lambda = 6.0\,\text{Å}$. Data is shown for the evaluated q-region, i.e. $0.018\,\text{Å}^{-1}$ to $0.042\,\text{Å}^{-1}$. The solid lines are fits to the data using Eq. (5.12).
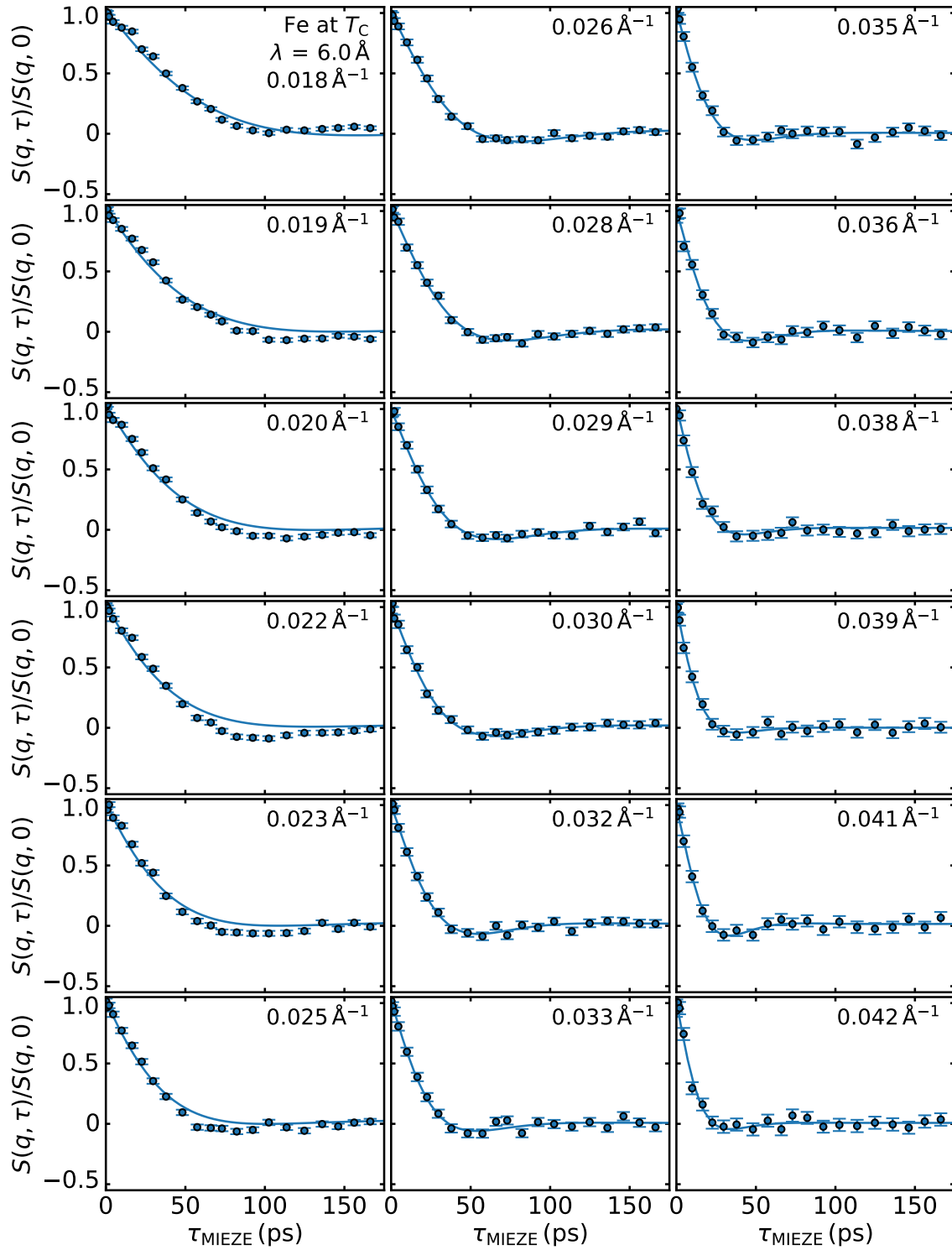
Figure B.8.: Normalised intermediate scattering function as measured at the Curie point in iron. Data was recorded using neutrons with a mean wavelength of $\lambda = 6.0\,\text{Å}$. Data is shown for the evaluated q-region, i.e. $0.018\,\text{Å}^{-1}$ to $0.042\,\text{Å}^{-1}$. The solid lines are fits to the data using Eq. (5.12).

B.3.2. Dipolar Energy

The dipolar exchange energy for iron was calculated by

$$E_{\mathrm{dipolar}} \;=\; g\mu_{\mathrm{B}}\mu_0 \sin^2\theta_{\boldsymbol{q}} M(T), \tag{B.23}$$

with the Landé factor for iron $g = 2$, the Bohr magneton μ_{B}, the magnetic constant μ_0, and the temperature dependent magnetisation $M(T)$. The temperature dependent magnetisation was determined using the experimental data from Ref. [231–235], shown in Fig. B.9(a). Since during the experiment the iron sample was not magnetised, the domains in the sample were assumed to be randomly distributed and, hence, the angle between scattering vector and magnetisation can take any value:

$$\langle \sin^2\theta_{\boldsymbol{q}} \rangle \;=\; \frac{1}{4\pi} \int_0^{2\pi}\int_0^\pi \sin\theta_{\boldsymbol{q}} \sin^2\theta_{\boldsymbol{q}} \mathrm{d}\theta_{\boldsymbol{q}}\mathrm{d}\phi \tag{B.24}$$

$$= \frac{1}{2}\int_0^\pi \sin^3\theta_{\boldsymbol{q}} \mathrm{d}\theta_{\boldsymbol{q}} \tag{B.25}$$

$$= \frac{2}{3}. \tag{B.26}$$

The dipolar energy, shown in Fig. B.9(b), used for determining the spin wave energy was calculated by using the fit to the experimental data, rather than the strict power law behaviour introduced in Sec. 5.1.
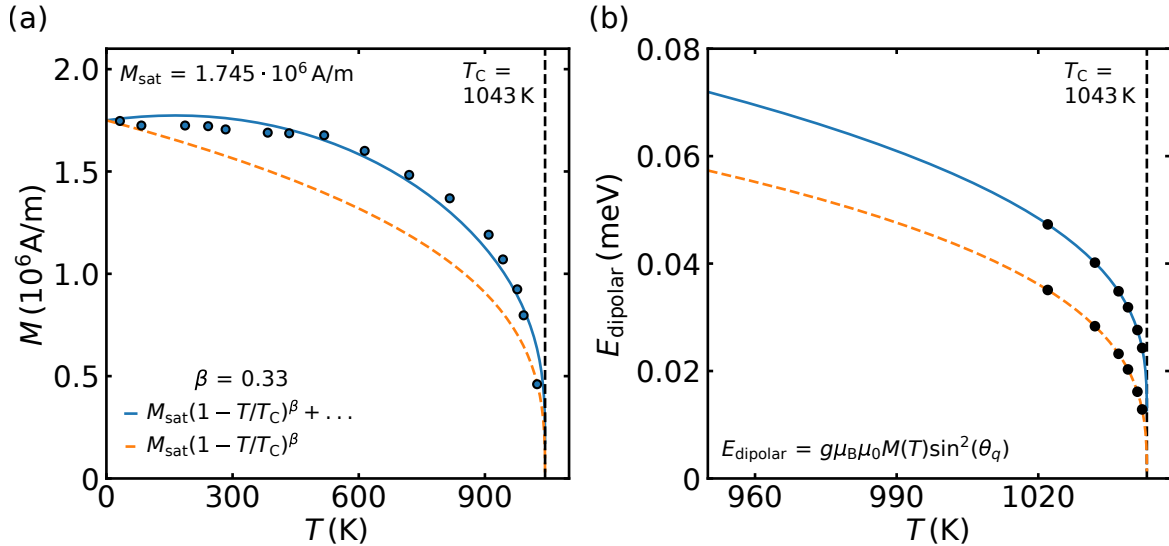
Figure B.9.: Magnetisation and dipolar energy of iron. (a) Magnetisation as function of temperature. Experimental data taken from Ref. [231–235]. The blue solid line is a fit to the data. The dashed orange line describes the power law behaviour, cf. Sec. 5.1. (b) Calculated dipolar energy for the fit to the data, and the power law behaviour from (a), respectively. Black dots indicate at what temperatures data was taken during the present study.

B.3.3. Data Collins *et al.*

In 1969, Collins *et al.* [171] studied the critical scattering in iron for a wide temperature range in the spin wave and transition region introduced in Sec. 5.1. As compared to the model describing the dispersion relation of the spin waves in the present work, cf. Eq. (5.5), Collins *et al.* included a higher order term:

$$E_{sw}(\boldsymbol{q}) = \sqrt{\left(D\boldsymbol{q}^2 + E\boldsymbol{q}^4\right)\left(\left(D\boldsymbol{q}^2 + E\boldsymbol{q}^4\right) + E_{\text{dipolar}}\right)}, \qquad (B.27)$$

with an additional exchange constant E. Since this higher order term becomes important only for larger q, it was neglected in the data treatment of the present study. Collins *et al.* show their constant q scans and the fit results for the spin stiffness D, without showing the dispersion relations for all investigated temperatures. Fig. B.10 shows the spin stiffness D from Ref. [171] Fig. 7 as a function of temperature. Data is plotted as in Ref. [171], cf. Fig. B.10(a, c, e), and plotted as during the present work, cf. Fig. B.10(b, d, f).

Data from Collins *et al.* was fitted with fixed parameter $\beta = 0.33$ (a, b), with fixed parameter $\beta = 0.37$ (c, d), and with leaving β free (e, f). Tab. B.1 compares the different fit results for β and D_0. Collins *et al.* reported $\beta = 0.37 \pm 0.03$ and $D_0 = 281 \pm 10 \, \text{meV\AA}^2$. Fitting their data and leaving β free gives $\beta = 0.38$, which is within the margin of error of $\beta = 0.37 \pm 0.03$. The spin wave stiffness constant, however, is with $D_0 = 334 \pm 6 \, \text{meV\AA}^2$ significantly larger than what was reported by Collins *et al.*

Table B.1.: Comparison of the fit results for the spin wave stiffness given by Collins *et al.* to the results obtained by fitting their data for the spin wave stiffness. While the critical exponent β is within the margin of errors, the spin wave stiffness D differs significantly.

	Collins *et al.*	own fit of Collins data		
β	0.37 ± 0.03	0.33 (fixed)	0.37 (fixed)	0.38 (free)
$D_0 \, (\text{meV\AA}^2)$	281 ± 10	305 ± 5	328 ± 6	334 ± 6
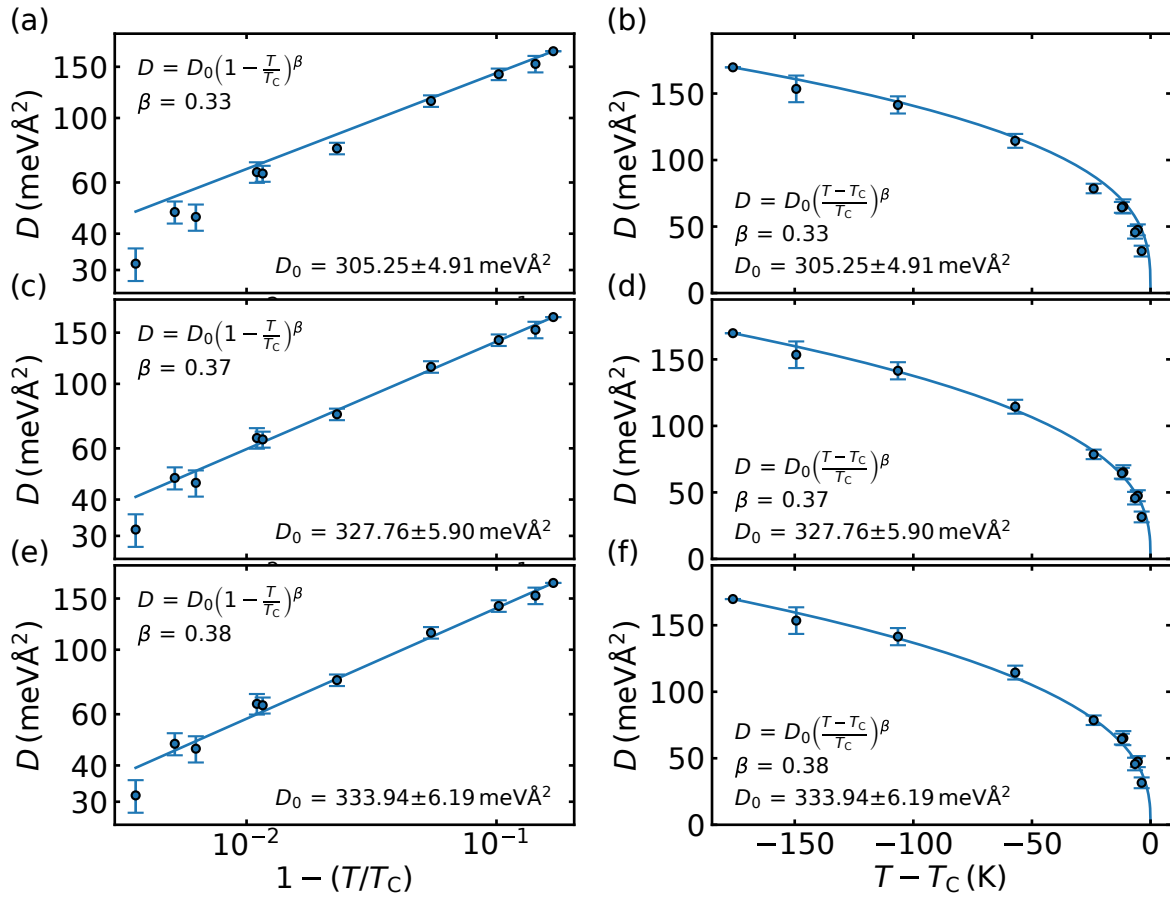
Figure B.10.: Spin wave stiffness obtained by Collins *et al.* The left row (a, c, e) is plotted on a log-log scale, while the right row (b, d, f) is plotted on a linear scale. (a, b) β fixed to 0.33. (c, d) β fixed to 0.37, as obtained by Collins *et al.* (e, f) β fitted as a free parameter, giving $\beta = 0.38$.

B.3.4. TAS Results

Triple-axis spectroscopy (TAS) was performed at the MIRA beamline, MLZ [236, 237]. Data was taken in the vicinity of the [000]-Bragg peak, with a fixed final wave-vector $k_\mathrm{f} = 1.36\,\text{Å}^{-1}$. The neutron beam was collimated before and after the sample with a 30' collimator.

Measurements were performed between room temperature and $\sim$1125 K. The sample was heated using a high temperature furnace, with a resistive niobium double cylinder heating element. It should be noted that this experiment used the HTF-03, while the spin echo studies used the HTF-01, both from the sample environment of FRM II. Temperature was controlled with a Eurotherm 2404 controller. The furnace covers a temperature range between room temperature and $\sim$2200 K. The temperature stability was about $\sim$0.05 K and no hysteresis effects were observed. Both was verified by means of several temperature scans.

The sample used in the present study is the same bcc iron single crystal as used for the spin echo measurements, cf. Ch. 5. Data was analysed using the Convofit tool from the Takin software package [238, 239]. Thereby, the physical model

$$E_\mathrm{sw}(\boldsymbol{q}) = \sqrt{D\boldsymbol{q}^2(D\boldsymbol{q}^2 + E_\mathrm{dipolar})}, \tag{B.28}$$

describing the dispersion relation of the spin wave energy, cf. Ch. 5.1, was convolved with the instrumental resolution of the spectrometer using the Popovici algorithm [240].
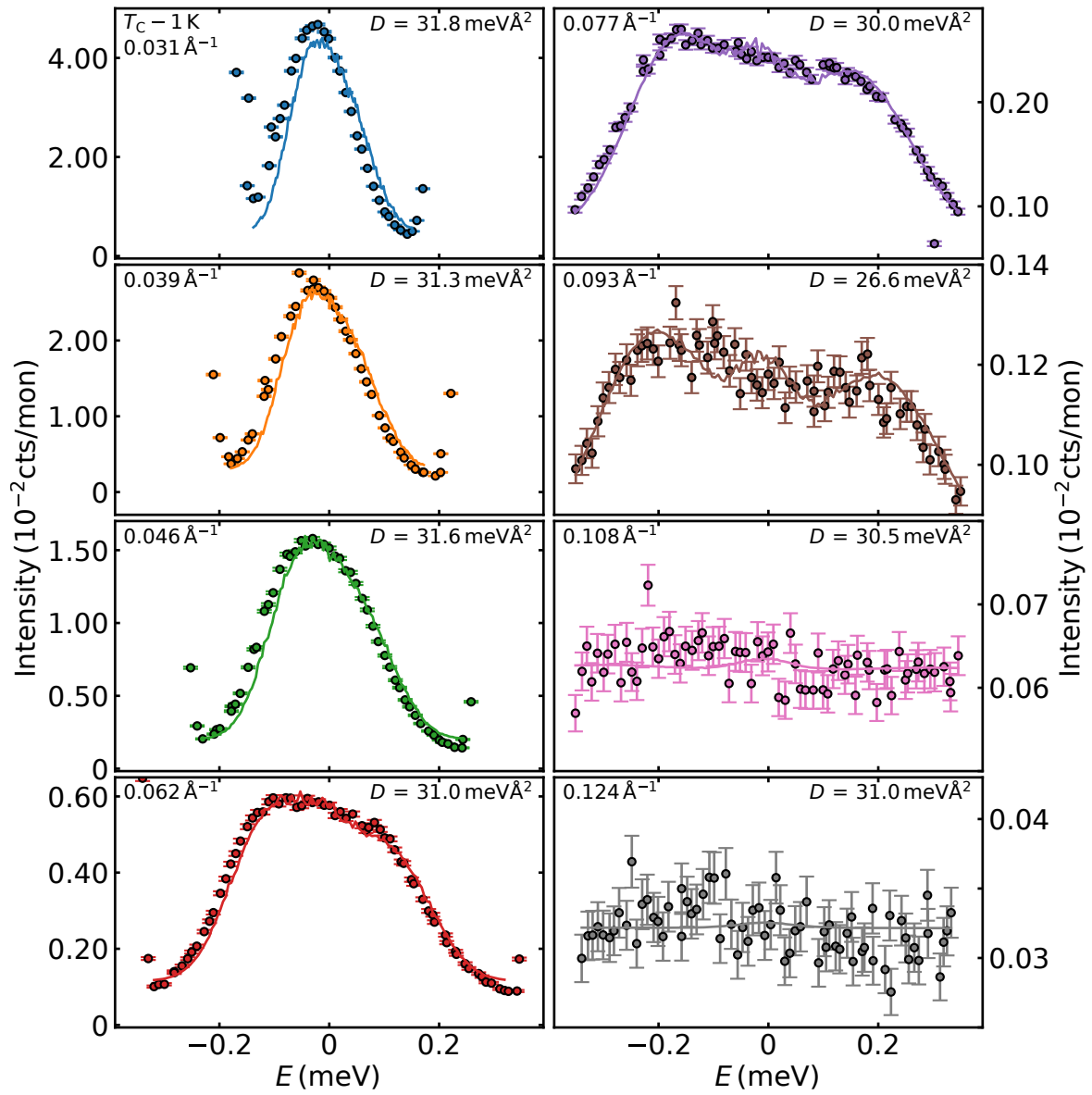
Figure B.11.: Spin-waves in iron at $T_C - 1\,\mathrm{K}$. Constant q scans with a fixed final wave-vector $k_{\mathrm{f}} = 1.36\,\text{Å}^{-1}$. Solid lines are fits to the data using Eq. (B.28) convolved with the instrumental resolution.
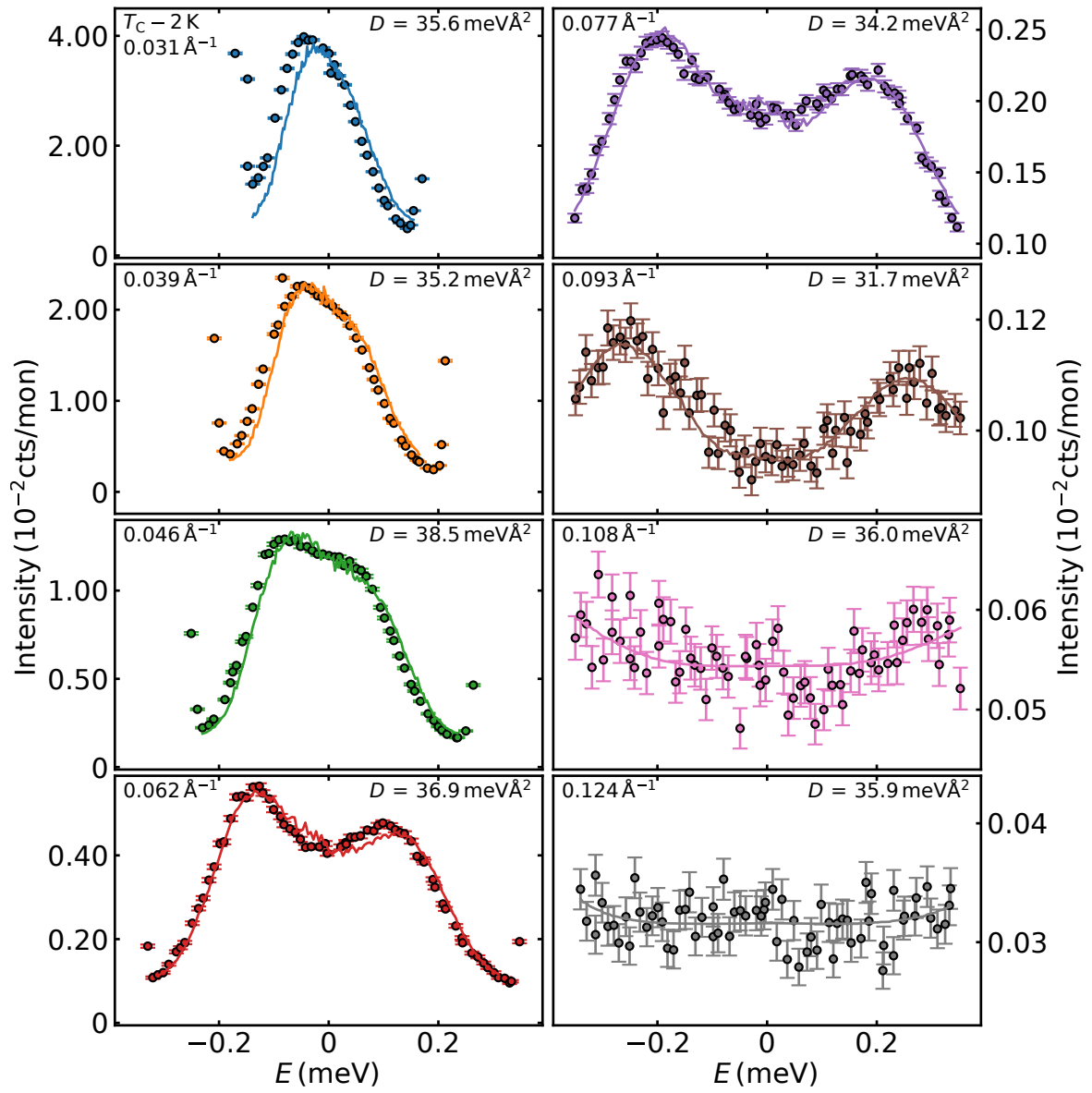
Figure B.12.: Spin-waves in iron at $T_C - 2\,\mathrm{K}$. Constant q scans with a fixed final wave-vector $k_\mathrm{f} = 1.36\,\text{Å}^{-1}$. Solid lines are fits to the data using Eq. (B.28) convolved with the instrumental resolution.
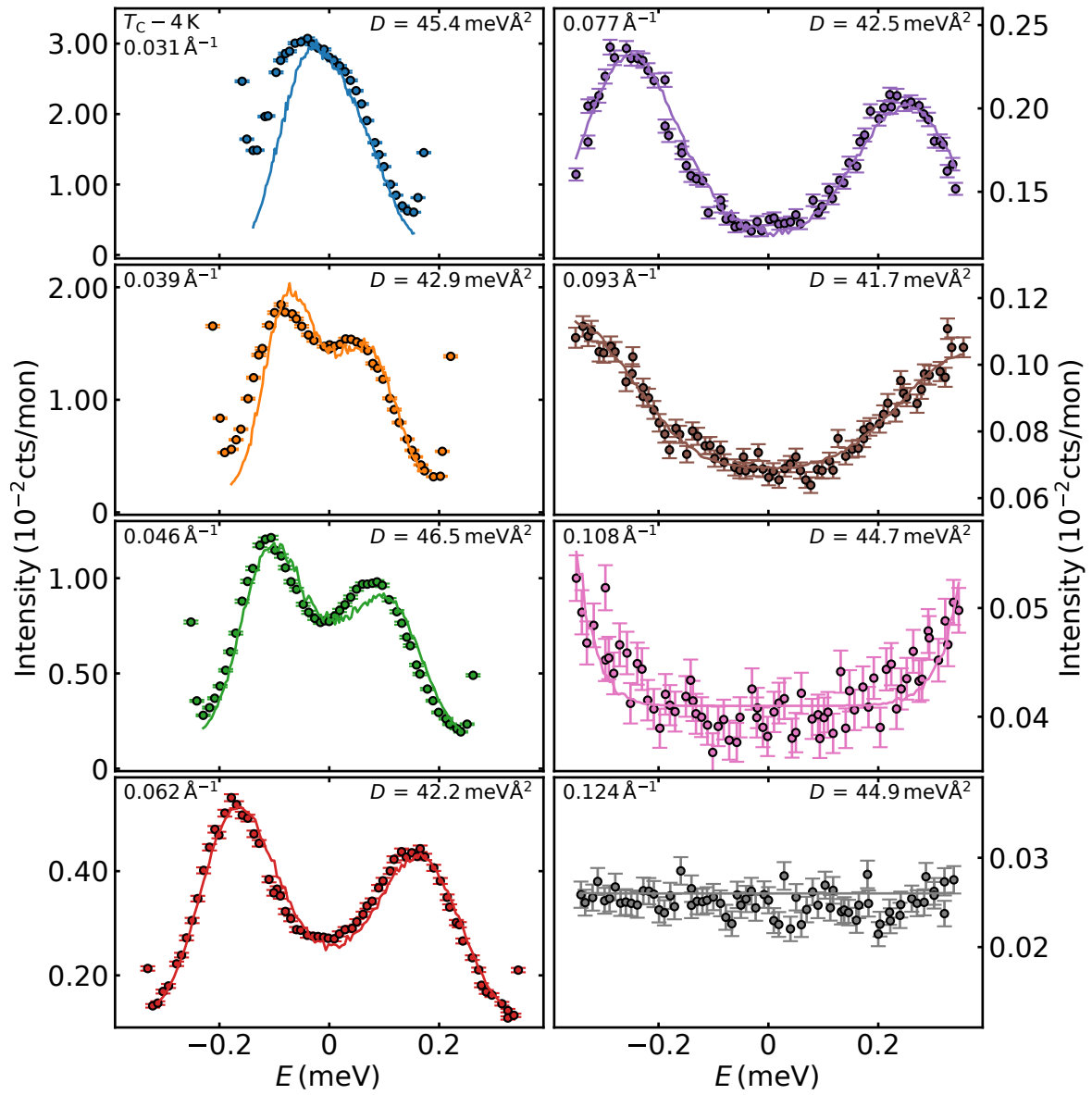
Figure B.13.: Spin-waves in iron at $T_C - 4\,\mathrm{K}$. Constant q scans with a fixed final wave-vector $k_\mathrm{f} = 1.36\,\mathrm{\mathring{A}}^{-1}$. Solid lines are fits to the data using Eq. (B.28) convolved with the instrumental resolution.
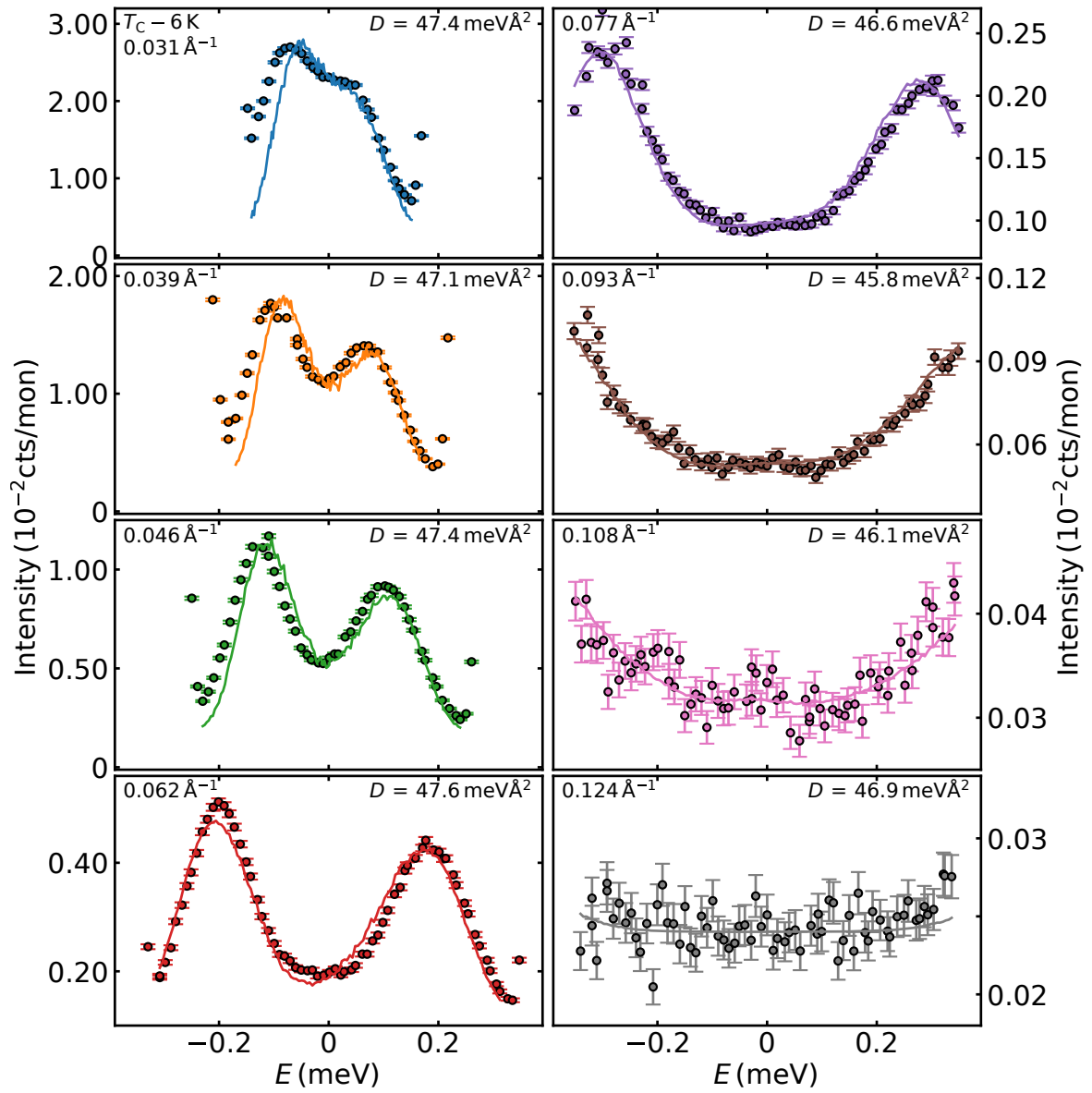
Figure B.14.: Spin-waves in iron at $T_C - 6\,\text{K}$. Constant q scans with a fixed final wave-vector $k_f = 1.36\,\text{Å}^{-1}$. Solid lines are fits to the data using Eq. (B.28) convolved with the instrumental resolution.
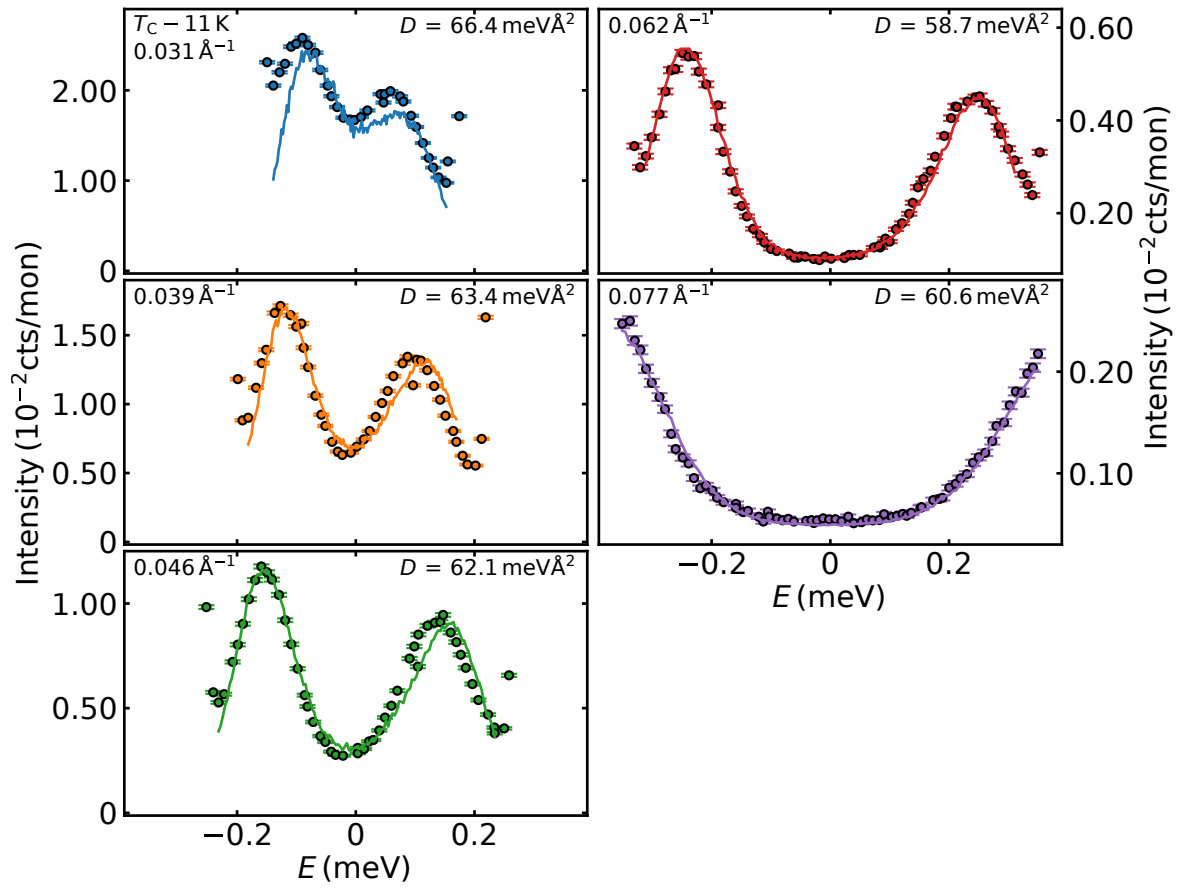
Figure B.15.: Spin-waves in iron at $T_C - 11\,\mathrm{K}$. Constant q scans with a fixed final wave-vector $k_\mathrm{f} = 1.36\,\mathring{\mathrm{A}}^{-1}$. Solid lines are fits to the data using Eq. (B.28) convolved with the instrumental resolution.

B.4. Measurements in Fe$_x$Cr$_{1-x}$

This appendix section comprises additional information on the measurements in Fe$_x$Cr$_{1-x}$, cf. Ch. 6. The plots of all measured MIEZE scans are shown in App. B.4.1.

B.4.1. MIEZE Results

MIEZE scans in Fe$_x$Cr$_{1-x}$ for all measured temperatures are shown in Fig. B.16-B.21. In Fig. B.22, the decay rate Γ is shown for temperatures, where the extraction of a physical meaningful Γ was not possible.
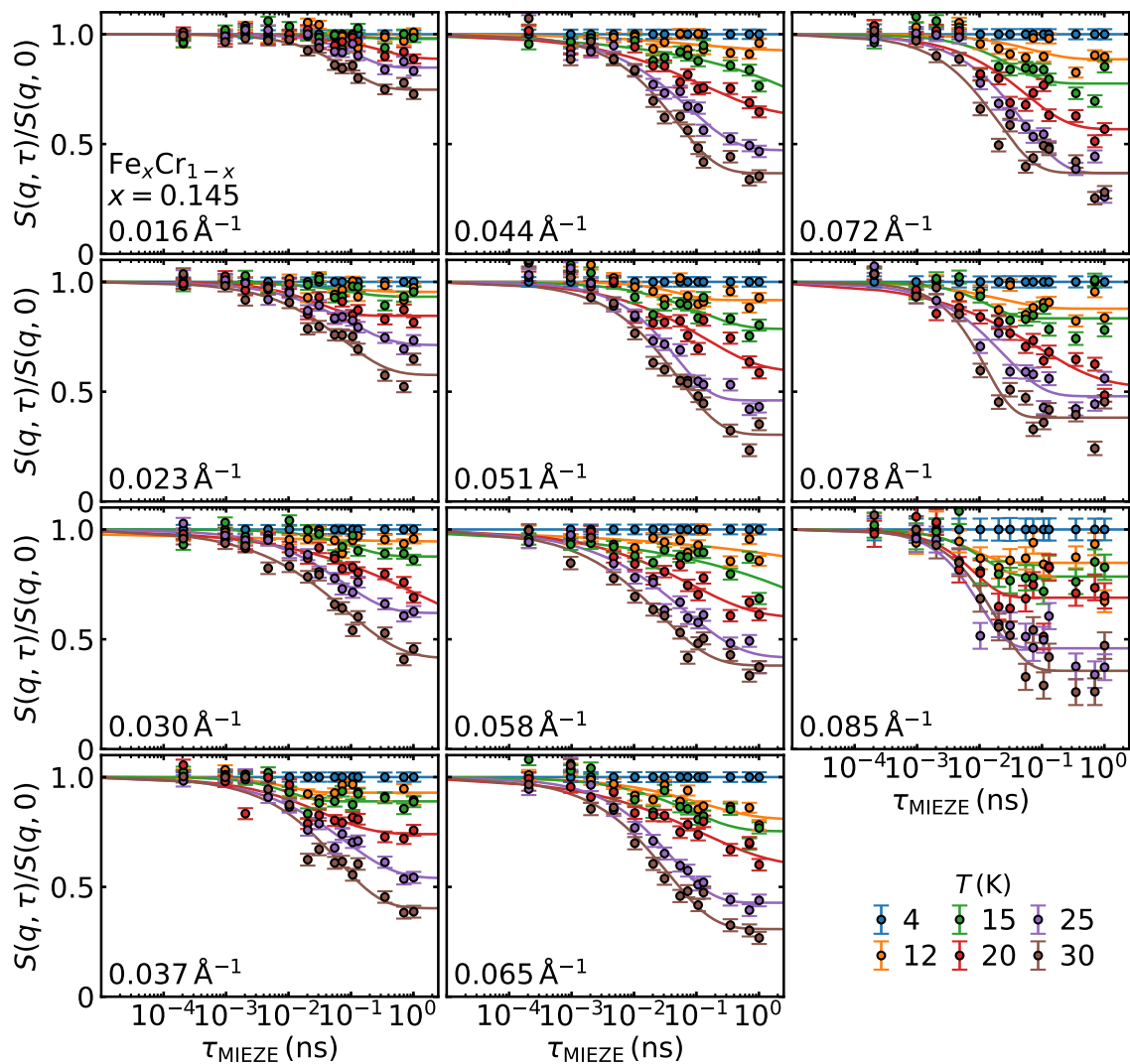
Figure B.16.: Normalised intermediate scattering function as measured in Fe_xCr_{1-x} with $x = 0.145$ for temperatures between $4\,K$ and $30\,K$. Data was recorded using neutrons with a mean wavelength of $\lambda = 6.0\,\text{Å}$. Data is shown for the evaluated q-region, i.e. $0.016\,\text{Å}^{-1}$ to $0.085\,\text{Å}^{-1}$. The solid lines are fits to the data using Eq. (6.3).
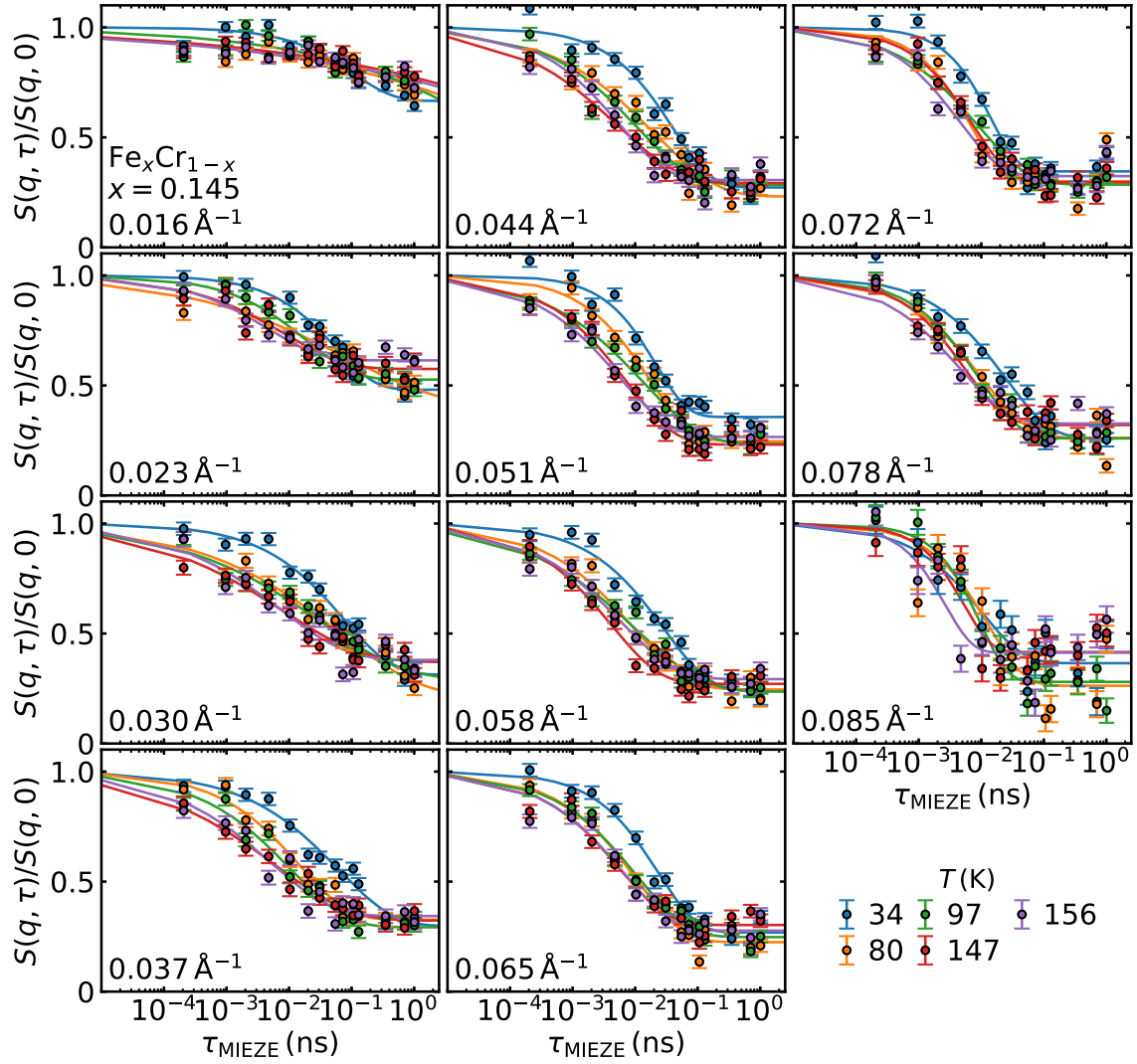
Figure B.17.: Normalised intermediate scattering function as measured in Fe$_x$Cr$_{1-x}$ with $x = 0.145$ for temperatures between $34\,\mathrm{K}$ and $295\,\mathrm{K}$. Data was recorded using neutrons with a mean wavelength of $\lambda = 6.0\,\text{Å}$. Data is shown for the evaluated q-region, i.e. $0.016\,\text{Å}^{-1}$ to $0.085\,\text{Å}^{-1}$. The solid lines are fits to the data using Eq. (6.3).
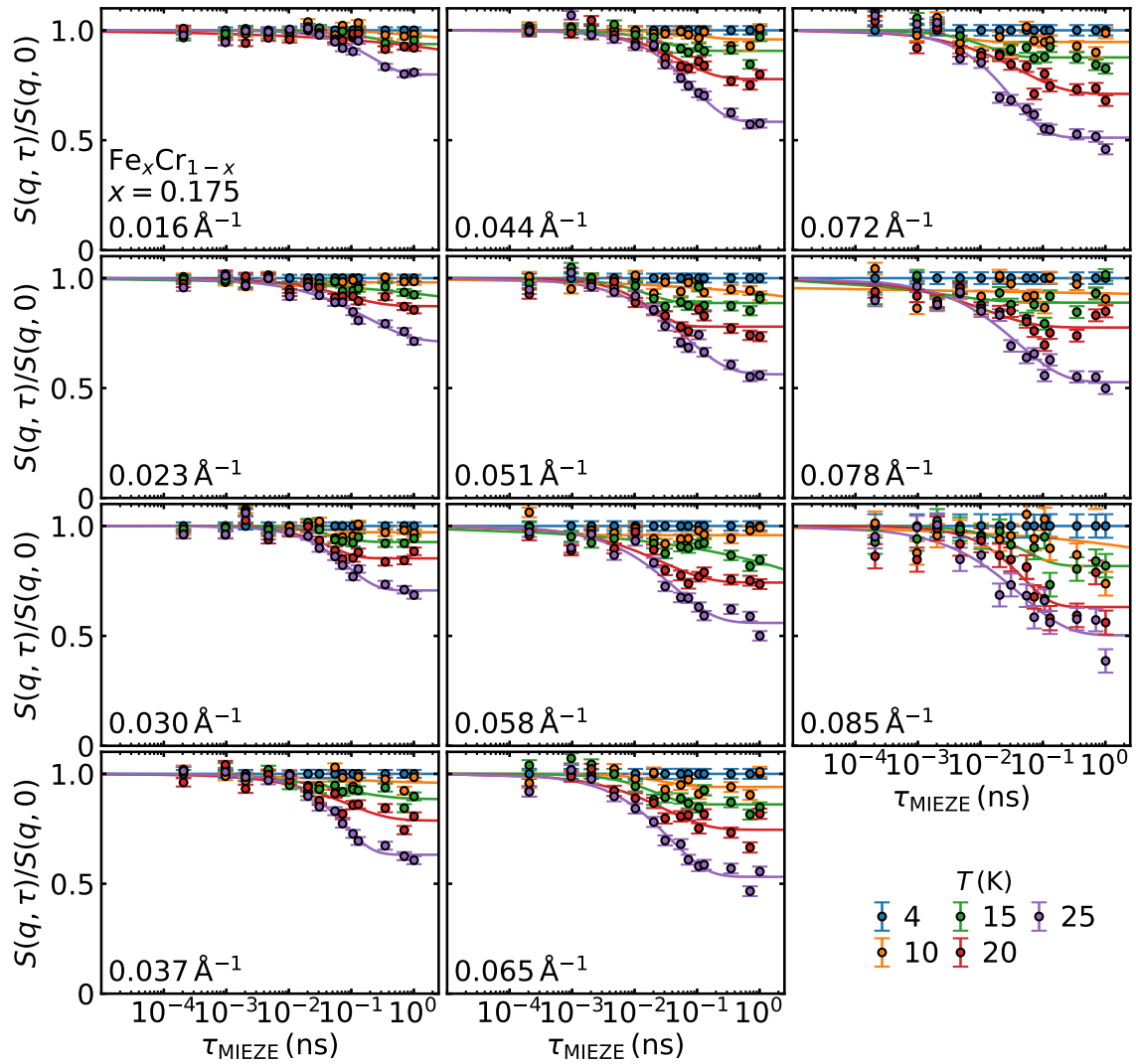
Figure B.18.: Normalised intermediate scattering function as measured in Fe_xCr_{1-x} with $x = 0.175$ for temperatures between $4\,K$ and $25\,K$. Data was recorded using neutrons with a mean wavelength of $\lambda = 6.0\,\text{Å}$. Data is shown for the evaluated q-region, i.e. $0.016\,\text{Å}^{-1}$ to $0.085\,\text{Å}^{-1}$. The solid lines are fits to the data using Eq. (6.3).
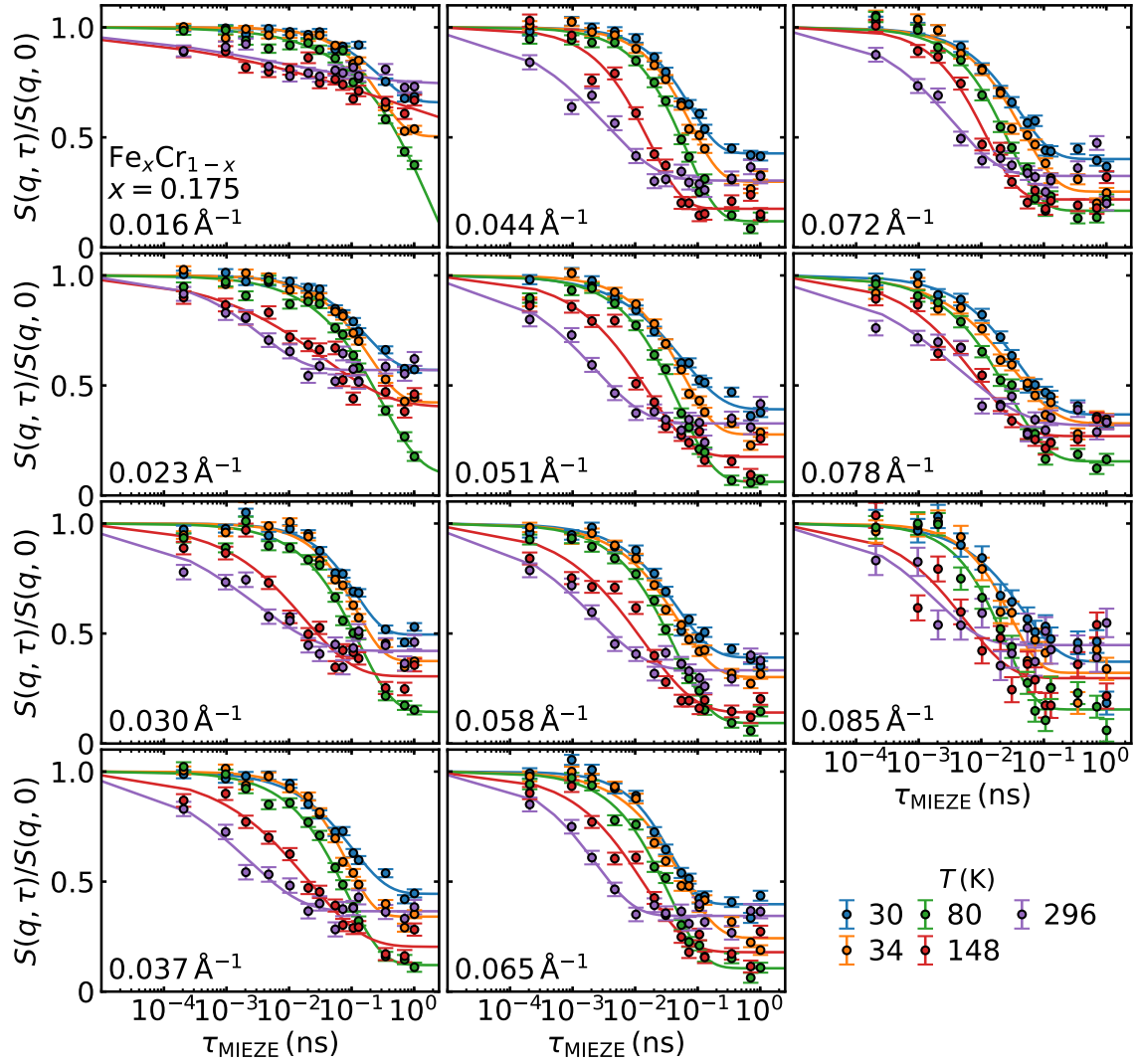
Figure B.19.: Normalised intermediate scattering function as measured in Fe_xCr_{1-x} with $x = 0.175$ for temperatures between $30\,K$ and $295\,K$. Data was recorded using neutrons with a mean wavelength of $\lambda = 6.0\,\text{Å}$. Data is shown for the evaluated q-region, i.e. $0.016\,\text{Å}^{-1}$ to $0.085\,\text{Å}^{-1}$. The solid lines are fits to the data using Eq. (6.3).
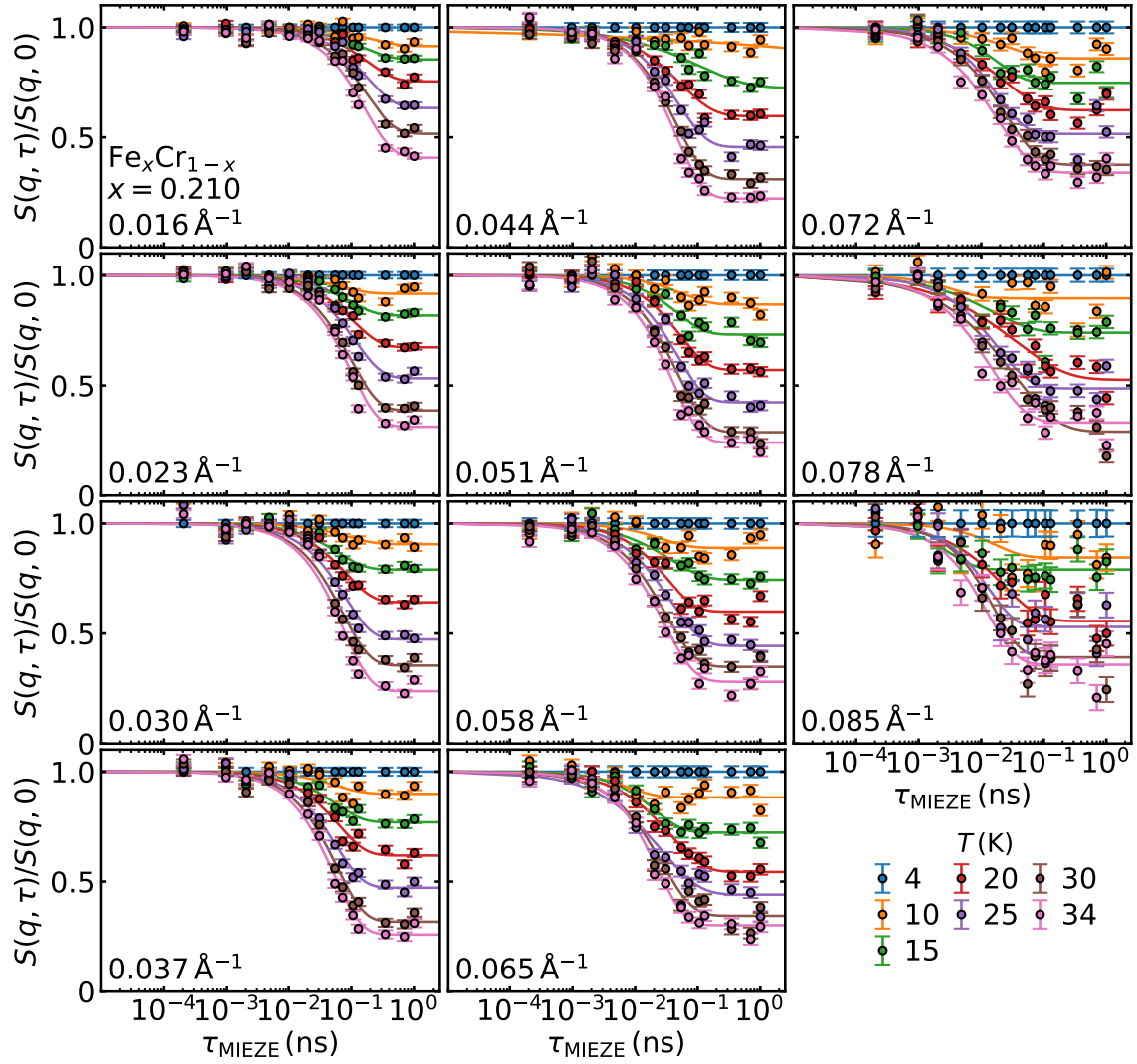
Figure B.20.: Normalised intermediate scattering function as measured in Fe_xCr_{1-x} with $x = 0.210$ for temperatures between $4\,K$ and $34\,K$. Data was recorded using neutrons with a mean wavelength of $\lambda = 6.0\,Å$. Data is shown for the evaluated q-region, i.e. $0.016\,Å^{-1}$ to $0.085\,Å^{-1}$. The solid lines are fits to the data using Eq. (6.3).
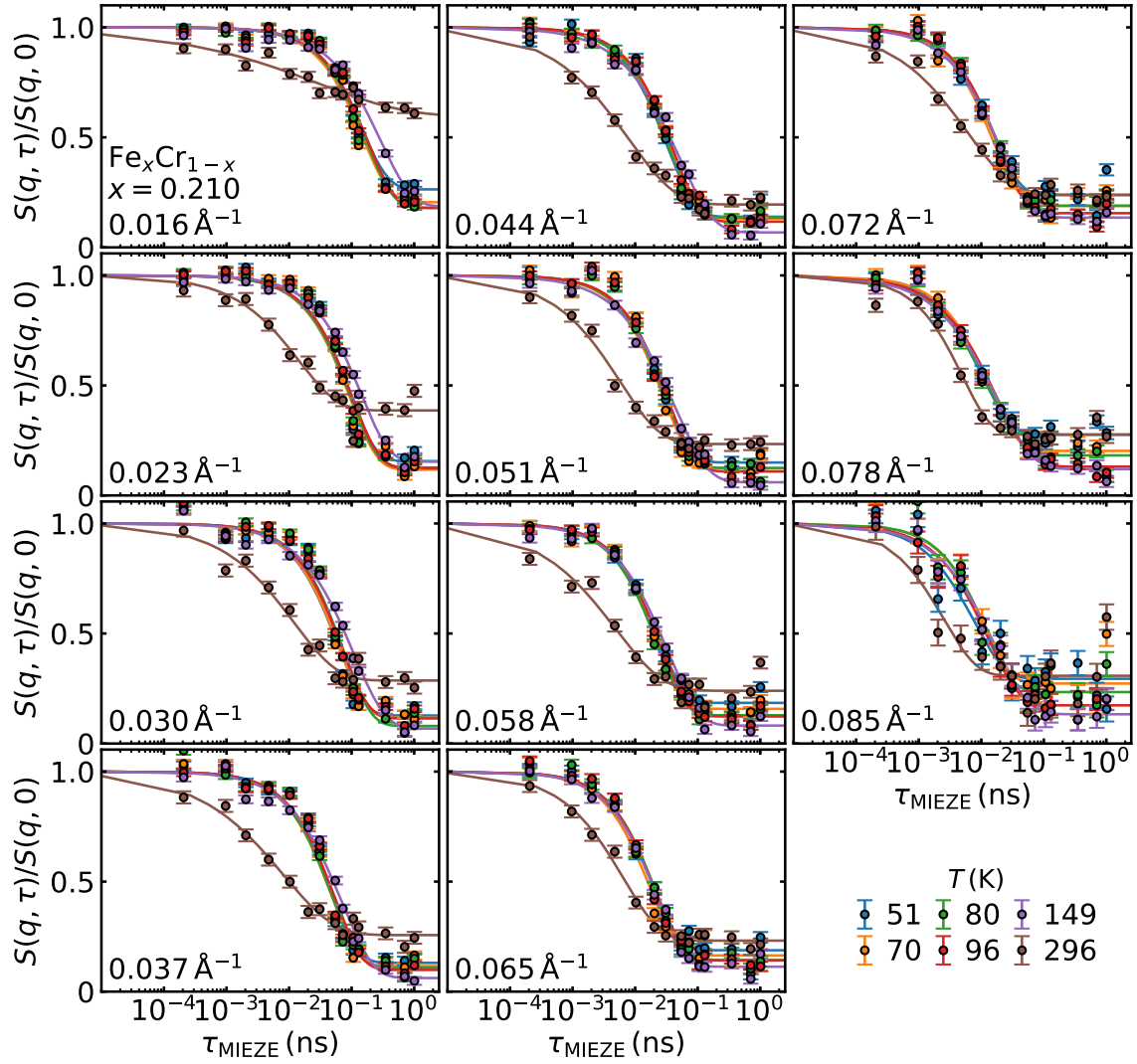
Figure B.21.: Normalised intermediate scattering function as measured in Fe$_x$Cr$_{1-x}$ with $x = 0.210$ for temperatures between $50\,\text{K}$ and $295\,\text{K}$. Data was recorded using neutrons with a mean wavelength of $\lambda = 6.0\,\text{Å}$. Data is shown for the evaluated q-region, i.e. $0.016\,\text{Å}^{-1}$ to $0.085\,\text{Å}^{-1}$. The solid lines are fits to the data using Eq. (6.3).
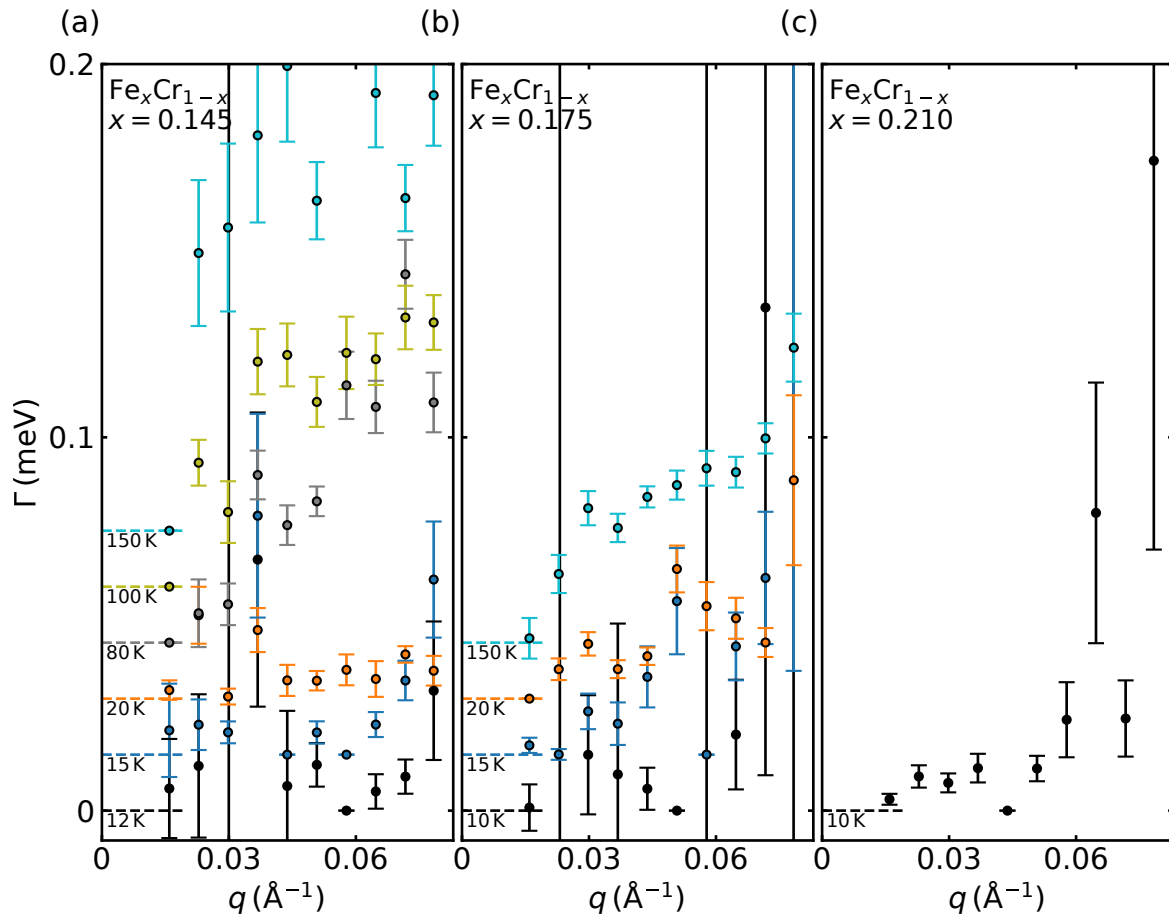
Figure B.22.: Decay rate Γ as function of scattering vector q. Data is shown for (a) $x = 0.145$, (b) $x = 0.175$, (c) $x = 0.210$, and temperatures where the fit of the intermediate scattering function in Fig. 6.6 and Fig. 6.7 did not deliver meaningful Γ. There are two main reasons for when the fit fails to deliver a meaningful Γ. First, when a very broad distribution of relaxation times is present, hence the exponential decay is strongly stretched. Therefore, a single relaxation time, i.e. a single Γ, does not represent represent the decay. Second, when a poor signal to noise ratio does not allow for proper fitting, as it may be the case for highest temperatures. Data is shifted by $0.015\,\mathrm{meV}$ as indicated by the horizontal dashed lines.

Bibliography

[1] S.-K. Kim, Micromagnetic Computer Simulations of Spin Waves in Nanometre-Scale Patterned Magnetic Elements, J. Phys. D: Appl. Phys. **43**, 264004 (2010).

[2] A. Barman and A. Haldar, Chapter One - Time-Domain Study of Magnetization Dynamics in Magnetic Thin Films and Micro- and Nanostructures, in *Solid State Physics*, Vol. 65, edited by R. E. Camley and R. L. Stamps (Academic Press, 2014) p. 1.

[3] L. Landau, The Theory of Phase Transitions, Nature **138**, 840 (1936).

[4] J.-C. Tolédano and P. Tolédano, *The Landau Theory of Phase Transitions: Application to Structural, Incommensurate, Magnetic and Liquid Crystal Systems* (World Scientific, 1987).

[5] S. L. Sondhi, S. M. Girvin, J. P. Carini, and D. Shahar, Continuous Quantum Phase Transitions, Rev. Mod. Phys. **69**, 315 (1997).

[6] T. Vojta, Quantum Phase Transitions in Electronic Systems, Ann. Phys. **9**, 403 (2000).

[7] M. Vojta, Quantum Phase Transitions, Rep. Prog. Phys. **66**, 2069 (2003).

[8] C. Pfleiderer, Why First Order Quantum Phase Transitions Are Interesting, J. Phys.: Condens. Matter **17**, S987 (2005).

[9] D. M. Broun, What Lies beneath the Dome? Nat. Phys. (2008), 10.1038/nphys909.

[10] S. Sachdev, Quantum Magnetism and Criticality, Nat. Phys. **4**, 173 (2008).

[11] S. Sachdev and B. Keimer, Quantum Criticality, Physics Today **64**, 29 (2011).

[12] S. Sachdev, *Quantum Phase Transitions*, second edition ed. (Cambridge University Press, 2011).

[13] S. S. Saxena, P. Agarwal, K. Ahilan, F. M. Grosche, R. K. W. Haselwimmer, M. J. Steiner, E. Pugh, I. R. Walker, S. R. Julian, P. Monthoux, G. G. Lonzarich, A. Huxley, I. Sheikin, D. Braithwaite, and J. Flouquet, Superconductivity on the Border of Itinerant-Electron Ferromagnetism in UGe_2, Nature **406**, 587 (2000).

[14] R. D. Shull and P. A. Beck, Mictomagnetic to Ferromagnetic Transition in Cr-Fe Alloys, in *AIP Conf. Proc.*, Vol. 24 (AIP, 1975) p. 95.

[15] B. Loegel, Magnetic Transitions in the Chromium-Iron System, J. Phys. F: Met. Phys. **5**, 497 (1975).

[16] J. G. Bednorz and K. A. Müller, Possible High T_C Superconductivity in the Ba-La-Cu-O System, Z. Phys. B **64**, 189 (1986).

[17] P. A. Lee, N. Nagaosa, and X.-G. Wen, Doping a Mott Insulator: Physics of High-Temperature Superconductivity, Rev. Mod. Phys. **78**, 17 (2006).

[18] F. Steglich, J. Aarts, C. D. Bredl, W. Lieke, D. Meschede, W. Franz, and H. Schäfer, Superconductivity in the Presence of Strong Pauli Paramagnetism: $CeCu_2Si_2$, Phys. Rev. Lett. **43**, 1892 (1979).

[19] N. D. Mathur, F. M. Grosche, S. R. Julian, I. R. Walker, D. M. Freye, R. K. W. Haselwimmer, and G. G. Lonzarich, Magnetically Mediated Superconductivity in Heavy Fermion Compounds, Nature **394**, 39 (1998).

[20] C. Pfleiderer, Superconducting Phases of f-Electron Compounds, Rev. Mod. Phys. **81**, 1551 (2009).

[21] G. R. Stewart, Unconventional Superconductivity, Adv. Phys. **66**, 75 (2017).

[22] C. Pfleiderer, S. R. Julian, and G. G. Lonzarich, Non-Fermi-Liquid Nature of the Normal State of Itinerant-Electron Ferromagnets, Nature **414**, 427 (2001).

[23] G. R. Stewart, Non-Fermi-Liquid Behavior in d- and f-Electron Metals, Rev. Mod. Phys. **73**, 797 (2001).

[24] G. R. Stewart, Addendum: Non-Fermi-Liquid Behavior in d- and f-Electron Metals, Rev. Mod. Phys. **78**, 743 (2006).

[25] H. v. Löhneysen, A. Rosch, M. Vojta, and P. Wölfle, Fermi-Liquid Instabilities at Magnetic Quantum Phase Transitions, Rev. Mod. Phys. **79**, 1015 (2007).

[26] R. Ritz, M. Halder, M. Wagner, C. Franz, A. Bauer, and C. Pfleiderer, Formation of a Topological Non-Fermi Liquid in MnSi, Nature **497**, 231 (2013).

[27] J. A. Mydosh, *Spin Glasses: An Experimental Introduction* (Taylor & Francis, 1993).

[28] J. S. Gardner, M. J. P. Gingras, and J. E. Greedan, Magnetic Pyrochlore Oxides, Rev. Mod. Phys. **82**, 53 (2010).

[29] L. Balents, Spin Liquids in Frustrated Magnets, Nature **464**, 199 (2010).

[30] M. J. Harris, S. T. Bramwell, D. F. McMorrow, T. Zeiske, and K. W. Godfrey, Geometrical Frustration in the Ferromagnetic Pyrochlore $Ho_2Ti_2O_7$, Phys. Rev. Lett. **79**, 2554 (1997).

[31] M. J. Harris, S. T. Bramwell, T. Zeiske, D. F. McMorrow, and P. J. C. King, Magnetic Structures of Highly Frustrated Pyrochlores, J. Magn. Magn. Mater. **177-181**, 757 (1998).

[32] A. P. Ramirez, A. Hayashi, R. J. Cava, R. Siddharthan, and B. S. Shastry, Zero-Point Entropy in 'Spin Ice', Nature **399**, 333 (1999).

[33] S. T. Bramwell and M. J. P. Gingras, Spin Ice State in Frustrated Magnetic Pyrochlore Materials, Science **294**, 1495 (2001).

[34] M. J. P. Gingras, Spin Ice, in *Introduction to Frustrated Magnetism: Materials, Experiments, Theory* (Springer, 2011).

[35] C. Castelnovo, R. Moessner, and S. L. Sondhi, Magnetic Monopoles in Spin Ice, Nature **451**, 42 (2008).

[36] L. D. C. Jaubert and P. C. W. Holdsworth, Signature of Magnetic Monopole and Dirac String Dynamics in Spin Ice, Nat. Phys. **5**, 258 (2009).

[37] M. J. P. Gingras and P. A. McClarty, Quantum Spin Ice: A Search for Gapless Quantum Spin Liquids in Pyrochlore Magnets, Rep. Prog. Phys. **77**, 056501 (2014).

[38] L. Savary and L. Balents, Quantum Spin Liquids: A Review, Rep. Prog. Phys. **80**, 016502 (2016).

[39] R. Sibille, N. Gauthier, H. Yan, M. C. Hatnean, J. Ollivier, B. Winn, U. Filges, G. Balakrishnan, M. Kenzelmann, N. Shannon, and T. Fennell, Experimental Signatures of Emergent Quantum Electrodynamics in Pr 2 Hf 2 O 7, Nat. Phys. , 1 (2018).

[40] F. Mezei, Neutron Spin Echo: A New Concept in Polarized Thermal Neutron Techniques, Z. Physik **255**, 146 (1972).

[41] F. Mezei and Institut Laue-Langevin, eds., *Neutron Spin Echo: Proceedings of a Laue-Langevin Institut Workshop, Grenoble, October 15 - 16, 1979* (Springer, 1980) oCLC: 59819226.

[42] R. Golub and R. Gähler, A Neutron Resonance Spin Echo Spectrometer for Quasi-Elastic and Inelastic Scattering, Phys. Lett. A **123**, 43 (1987).

[43] R. Gähler, R. Golub, and T. Keller, Neutron Resonance Spin Echo - a New Tool for High Resolution Spectroscopy, Physica B Condens. Matter **180-181**, 899 (1992).

[44] P. Hank, W. Besenböck, R. Gähler, and M. Köppe, Zero-Field Neutron Spin Echo Techniques for Incoherent Scattering, Physica B Condens. Matter **234-236**, 1130 (1997).

[45] W. Besenböck, R. Gähler, P. Hank, R. Kahn, M. Köppe, C.-H. D. Novion, W. Petry, and J. Wuttke, First Scattering Experiment on MIEZE: A Fourier Transform Time-of-Flight Spectrometer Using Resonance Coils, J. Neutron Res. **7**, 65 (1998).

[46] J. Kindervater, N. Martin, W. Häußler, M. Krautloher, C. Fuchs, S. Mühlbauer, J. A. Lim, E. Blackburn, P. Böni, and C. Pfleiderer, Neutron Spin Echo Spectroscopy under 17 T Magnetic Field at RESEDA, EPJ Web of Conferences **83**, 03008 (2015).

[47] J. Kindervater, S. Säubert, and P. Böni, Dipolar Effects on the Critical Fluctuations in Fe: Investigation by the Neutron Spin-Echo Technique MIEZE, Phys. Rev. B **95**, 014429 (2017).

[48] S. Legl, C. Pfleiderer, and K. Krämer, Vibrating Coil Magnetometer for Milli-Kelvin Temperatures, Rev. Sci. Instrum. **81**, 043911 (2010).

[49] S. Legl, *Entwicklung eines Spulen-Vibrationsmagnetometers zur Untersuchung korrelierter Elektronensysteme bei ultratiefen Temperaturen*, PhD Thesis, Technische Universität München (TUM) (2010).

[50] O. V. Lounasmaa, *Experimental Principles and Methods below 1 K* (Academic Press, 1974).

[51] D. S. Betts, *An Introduction to Millikelvin Technology* (Cambridge University Press, 1989).

[52] C. Enss and S. Hunklinger, *Low-Temperature Physics* (Springer, 2010) oCLC: 837781387.

[53] C. Krey, *Spulen-Vibrationsmagnetometrie an Frustrierten Magneten Bei mK-Temperaturen*, Diploma Thesis, Karlsruhe Institute of Technology (KIT) (2011).

[54] G. Batey and V. Mikheev, Adsorption Pumping for Obtaining ULT in ^{3}He Cryostats and ^{3}He-^{4}He Dilution Refrigerators, J. Low Temp. Phys. **113**, 933 (1998).

[55] H. London, Proc. Int. Conf. Low-Temp. Phys. (1951).

[56] C. Duvinage, *No Title*, PhD Thesis, Technische Universität München (TUM) (unpublished).

[57] S. Foner, Versatile and Sensitive Vibrating-Sample Magnetometer, Rev. Sci. Instrum. **30**, 548 (1959).

[58] D. O. Smith, Development of a Vibrating-Coil Magnetometer, Rev. Sci. Instrum. **27**, 261 (1956).

[59] D. U. Gubser and D. E. Mapother, Remotely Controlled Piezoelectric Vibrator for Low Temperature Applications, Rev. Sci. Instrum. **40**, 843 (1969).

[60] S. Legl, C. Krey, S. R. Dunsiger, H. A. Dabkowska, J. A. Rodriguez, G. M. Luke, and C. Pfleiderer, Vibrating-Coil Magnetometry of the Spin Liquid Properties of $Tb_2Ti_2O_7$, Phys. Rev. Lett. **109**, 047201 (2012).

[61] C. Krey, S. Legl, S. R. Dunsiger, M. Meven, J. S. Gardner, J. M. Roper, and C. Pfleiderer, First Order Metamagnetic Transition in $Ho_2Ti_2O_7$ Observed by Vibrating Coil Magnetometry at Milli-Kelvin Temperatures, Phys. Rev. Lett. **108**, 257204 (2012).

[62] G. L. Squires, *Introduction to the Theory of Thermal Neutron Scattering* (Dover Publications, 1996).

[63] T. Keller, R. Golub, and R. Gähler, Chapter 2.8.6 - Neutron Spin Echo - a Technique for High-Resolution Neutron Scattering, in *Scattering*, edited by R. Pike and P. Sabatier (Academic Press, 2002) p. 1264, 10.1016/B978-012613760-6/50068-1.

[64] J. Schweizer, Polarized Neutrons and Polarization Analysis, in *Neutron Scattering from Magnetic Materials* (Elsevier, 2005) p. 155.

[65] A. Furrer, J. Mesot, and T. Strässle, *Neutron Scattering in Condensed Matter Physics*, Vol. 0 (WORLD SCIENTIFIC, 2009).

[66] L. Van Hove, Correlations in Space and Time and Born Approximation Scattering in Systems of Interacting Particles, Phys. Rev. **95**, 249 (1954).

[67] D. F. Johnston, On the Theory of the Electron Orbital Contribution to the Scattering of Neutrons by Magnetic Ions in Crystals, Proc. Phys. Soc. **88**, 37 (1966).

[68] F. Haslbeck, *Neutron Resonance Spin-Echo Spectroscopy in MnSi*, Masters Thesis, Technische Universität München (TUM) (2015).

[69] J. Kindervater, W. Häußler, A. Tischendorf, and P. Böni, Neutron-Spin-Echo from Polarizing Samples, J. Phys.: Conf. Ser. **340**, 012030 (2012).

[70] F. Bloch and A. Siegert, Magnetic Resonance for Nonrotating Fields, Phys. Rev. **57**, 522 (1940).

[71] M. Monkenbusch, R. Schätzler, and D. Richter, The Jülich Neutron Spin-Echo Spectrometer - Design and Performance, Nucl. Instr. Meth. Phys. Res. A **399**, 301 (1997).

[72] F. Mezei, C. Pappas, and T. Gutberlet, *Neutron Spin Echo Spectroscopy: Basics, Trends and Applications* (Springer Science & Business Media, 2002).

[73] M. Ohl, M. Monkenbusch, N. Arend, T. Kozielewski, G. Vehres, C. Tiemann, M. Butzek, H. Soltner, U. Giesen, R. Achten, H. Stelzer, B. Lindenau, A. Budwig, H. Kleines, M. Drochner, P. Kaemmerling, M. Wagener, R. Möller, E. B. Iverson, M. Sharp, and D. Richter, The Spin-Echo Spectrometer at the Spallation Neutron Source (SNS), Nucl. Instr. Meth. Phys. Res. A **696**, 85 (2012).

[74] C. Franz and T. Schröder, RESEDA: Resonance Spin Echo Spectrometer, JLSRF **1**, 14 (2015).

[75] W. Häussler, B. Gohla-Neudecker, R. Schwikowski, D. Streibl, and P. Böni, RESEDA - The New Resonance Spin Echo Spectrometer Using Cold Neutrons at the FRM-II, Physica B Condens. Matter **397**, 112 (2007).

[76] M. Krautloher, *Implementation of a LNRSE Option into RESEDA / MLZ*, Masters Thesis, Ludwig-Maximilians-Universität München (LMU) (2014).

[77] M. Krautloher, J. Kindervater, T. Keller, and W. Häußler, Neutron Resonance Spin Echo with Longitudinal DC Fields, Rev. Sci. Instrum. **87**, 125110 (2016).

[78] W. Häussler, U. Schmidt, G. Ehlers, and F. Mezei, Neutron Resonance Spin Echo Using Spin Echo Correction Coils, Chemical Physics **292**, 501 (2003).

[79] W. Häussler, G. Ehlers, and U. Schmidt, Field Integral Correction in Neutron Resonance Spin Echo, Physica B Condens. Matter **350**, E807 (2004).

[80] W. Häussler and U. Schmidt, Effective Field Integral Subtraction by the Combination of Spin Echo and Resonance Spin Echo, Phys Chem Chem Phys **7**, 1245 (2005).

[81] M. Klein and C. J. Schmidt, CASCADE, Neutron Detectors for Highest Count Rates in Combination with ASIC/FPGA Based Readout Electronics, Nucl. Instr. Meth. Phys. Res. A **628**, 9 (2011).

[82] W. Häussler, P. Böni, M. Klein, C. J. Schmidt, U. Schmidt, F. Groitl, and J. Kindervater, Detection of High Frequency Intensity Oscillations at RESEDA Using the CASCADE Detector, Rev. Sci. Instrum. **82**, 045101 (2011).

[83] M. Köhli, F. Allmendinger, W. Häußler, T. Schröder, M. Klein, M. Meven, and U. Schmidt, Efficiency and Spatial Resolution of the CASCADE Thermal Neutron Detector, Nucl. Instr. Meth. Phys. Res. A **828**, 242 (2016).

[84] J. Kindervater, *Fluctuation-Induced Magnetic Phase Transitions in Fe and MnSi Studied by Neutron Scattering*, PhD Thesis, Technische Universität München (TUM) (2015).

[85] F. Haslbeck, *Untitled*, PhD Thesis, Technische Universität München (TUM) (unpublished).

[86] F. Haslbeck, S. Säubert, M. Seifert, C. Franz, M. Schulz, A. Heinemann, T. Keller, P. Das, J. D. Thompson, E. D. Bauer, C. Pfleiderer, and M. Janoschek, Interplay of Itinerant and Localized Spin Fluctuations in the Ferromagnetic Superconductor UGe_2, arXiv:1801.10278 [cond-mat] (2018), arXiv:1801.10278 [cond-mat] .

[87] S. T. Bramwell, M. J. P. Gingras, and J. N. Reimers, Order by Disorder in an Anisotropic Pyrochlore Lattice Antiferromagnet, J. Appl. Phys. **75**, 5523 (1994).

[88] N. W. Ashcroft and N. D. Mermin, *Solid State Physics* (Holt, Rinehart and Winston, 1976).

[89] C. Kittel, *Introduction to Solid State Physics*, 8th ed. (Wiley, 2005).

[90] V. Cannella, J. A. Mydosh, and J. I. Budnick, Magnetic Susceptibility of Au-Fe Alloys, J. Appl. Phys. **42**, 1689 (1971).

[91] L. E. Wenger and P. H. Keesom, Calorimetric Investigation of a Spin-Glass Alloy: CuMn, Phys. Rev. B **13**, 4053 (1976).

[92] A. P. Murani, Ferromagnet or Spin Glass? Magnetic Ordering in Au-Fe Alloys, J. Phys. F: Met. Phys. **4**, 757 (1974).

[93] G. H. Wannier, Antiferromagnetism. The Triangular Ising Net, Phys. Rev. **79**, 357 (1950).

[94] G. H. Wannier, Errata: Antiferromagnetism. The Triangular Ising Net, Phys. Rev. B **7**, 5017 (1973).

[95] A. P. Ramirez, Strongly Geometrically Frustrated Magnets, Annu. Rev. Mater. Sci. **24**, 453 (1994).

[96] P. W. Anderson, Ordering and Antiferromagnetism in Ferrites, Phys. Rev. **102**, 1008 (1956).

[97] J. Villain, Insulating Spin Glasses, Z. Phys. B **33**, 31 (1979).

[98] J. N. Reimers, A. J. Berlinsky, and A.-C. Shi, Mean-Field Approach to Magnetic Ordering in Highly Frustrated Pyrochlores, Phys. Rev. B **43**, 865 (1991).

[99] J. N. Reimers, Absence of Long-Range Order in a Three-Dimensional Geometrically Frustrated Antiferromagnet, Phys. Rev. B **45**, 7287 (1992).

[100] R. Moessner and J. T. Chalker, Properties of a Classical Spin Liquid: The Heisenberg Pyrochlore Antiferromagnet, Phys. Rev. Lett. **80**, 2929 (1998).

[101] R. Moessner and J. T. Chalker, Low-Temperature Properties of Classical Geometrically Frustrated Antiferromagnets, Phys. Rev. B **58**, 12049 (1998).

[102] J. E. Greedan, M. Sato, X. Yan, and F. S. Razavi, Spin-Glass-like Behavior in $Y_2Mo_2O_7$, a Concentrated, Crystalline System with Negligible Apparent Disorder, Solid State Commun. **59**, 895 (1986).

[103] K. A. Ross, L. Savary, B. D. Gaulin, and L. Balents, Quantum Excitations in Quantum Spin Ice, Phys. Rev. X **1**, 021002 (2011).

[104] R. Siddharthan, B. S. Shastry, A. P. Ramirez, A. Hayashi, R. J. Cava, and S. Rosenkranz, Ising Pyrochlore Magnets: Low-Temperature Properties, "ice Rules," and Beyond, Phys. Rev. Lett. **83**, 1854 (1999).

[105] B. C. den Hertog and M. J. P. Gingras, Dipolar Interactions and Origin of Spin Ice in Ising Pyrochlore Magnets, Phys. Rev. Lett. **84**, 3430 (2000).

[106] W. F. Giauque and M. F. Ashley, Molecular Rotation in Ice at 10°K. Free Energy of Formation and Entropy of Water, Phys. Rev. **43**, 81 (1933).

[107] J. D. Bernal and R. H. Fowler, A Theory of Water and Ionic Solution, with Particular Reference to Hydrogen and Hydroxyl Ions, J. Chem. Phys. **1**, 515 (1933).

[108] L. Pauling, The Structure and Entropy of Ice and of Other Crystals with Some Randomness of Atomic Arrangement, J. Am. Chem. Soc. **57**, 2680 (1935).

[109] M. J. Gingras and B. C. den Hertog, Origin of Spin-Ice Behavior in Ising Pyrochlore Magnets with Long-Range Dipole Interactions: An Insight from Mean-Field Theory, Can. J. Phys. **79**, 1339 (2001).

[110] R. G. Melko and M. J. P. Gingras, Monte Carlo Studies of the Dipolar Spin Ice Model, J. Phys.: Condens. Matter **16**, R1277 (2004).

[111] I. A. Ryzhkin, Magnetic Relaxation in Rare-Earth Oxide Pyrochlores, J. Exp. Theor. Phys. **101**, 481 (2005).

[112] T. Sakakibara, T. Tayama, Z. Hiroi, K. Matsuhira, and S. Takagi, Observation of a Liquid-Gas-Type Transition in the Pyrochlore Spin Ice Compound $Dy_2Ti_2O_7$ in a Magnetic Field, Phys. Rev. Lett. **90**, 207205 (2003).

[113] T. Fennell, P. P. Deen, A. R. Wildes, K. Schmalzl, D. Prabhakaran, A. T. Boothroyd, R. J. Aldus, D. F. McMorrow, and S. T. Bramwell, Magnetic Coulomb Phase in the Spin Ice $Ho_2Ti_2O_7$, Science **326**, 415 (2009).

[114] M. Hermele, M. P. A. Fisher, and L. Balents, Pyrochlore Photons: The $U(1)$ Spin Liquid in a $S = 1/2$ Three-Dimensional Frustrated Magnet, Phys. Rev. B **69**, 064404 (2004).

[115] P. A. McClarty, S. H. Curnoe, and M. J. P. Gingras, Energetic Selection of Ordered States in a Model of the $Er_2Ti_2O_7$ Frustrated Pyrochlore XY Antiferromagnet, J. Phys.: Conf. Ser. **145**, 012032 (2009).

[116] S. H. Curnoe, Structural Distortion and the Spin Liquid State in $Tb_2Ti_2O_7$, Phys. Rev. B **78**, 094418 (2008).

[117] L. Savary and L. Balents, Coulombic Quantum Liquids in Spin-1/2 Pyrochlores, Phys. Rev. Lett. **108**, 037202 (2012).

[118] S. Lee, S. Onoda, and L. Balents, Generic Quantum Spin Ice, Phys. Rev. B **86**, 104412 (2012).

[119] L. Savary and L. Balents, Spin Liquid Regimes at Nonzero Temperature in Quantum Spin Ice, Phys. Rev. B **87**, 205130 (2013).

[120] R. Applegate, N. R. Hayre, R. R. P. Singh, T. Lin, A. G. R. Day, and M. J. P. Gingras, Vindication of $Yb_2Ti_2O_7$ as a Model Exchange Quantum Spin Ice, Phys. Rev. Lett. **109**, 097205 (2012).

[121] N. R. Hayre, K. A. Ross, R. Applegate, T. Lin, R. R. P. Singh, B. D. Gaulin, and M. J. P. Gingras, Thermodynamic Properties of $Yb_2Ti_2O_7$ Pyrochlore as a Function of Temperature and Magnetic Field: Validation of a Quantum Spin Ice Exchange Hamiltonian, Phys. Rev. B **87**, 184423 (2013).

[122] L. Pan, N. J. Laurita, K. A. Ross, B. D. Gaulin, and N. P. Armitage, A Measure of Monopole Inertia in the Quantum Spin Ice $Yb_2Ti_2O_7$, Nat. Phys. **12**, 361 (2016).

[123] Y. Tokiwa, T. Yamashita, M. Udagawa, S. Kittaka, T. Sakakibara, D. Terazawa, Y. Shimoyama, T. Terashima, Y. Yasui, T. Shibauchi, and Y. Matsuda, Possible Observation of Highly Itinerant Quantum Magnetic Monopoles in the Frustrated Pyrochlore $Yb_2Ti_2O_7$, Nat. Commun. **7**, 10807 (2016).

[124] H. R. Molavian, M. J. P. Gingras, and B. Canals, Dynamically Induced Frustration as a Route to a Quantum Spin Ice State in $Tb_2Ti_2O_7$ via Virtual Crystal Field Excitations and Quantum Many-Body Effects, Phys. Rev. Lett. **98**, 157204 (2007).

[125] A. M. Hallas, J. Gaudet, and B. D. Gaulin, Experimental Insights into Ground-State Selection of Quantum XY Pyrochlores, Annu. Rev. Condens. Matter Phys. **9**, null (2018).

[126] K. E. Arpino, B. A. Trump, A. O. Scheie, T. M. McQueen, and S. M. Koohpayeh, Impact of Stoichiometry of $Yb_2Ti_2O_7$ on Its Physical Properties, Phys. Rev. B **95**, 094407 (2017).

[127] J. A. Hodges, P. Bonville, A. Forget, M. Rams, K. Królas, and G. Dhalenne, The Crystal Field and Exchange Interactions in $Yb_2Ti_2O_7$, J. Phys.: Condens. Matter **13**, 9301 (2001).

[128] A. Bertin, Y. Chapuis, P. D. de Réotier, and A. Yaouanc, Crystal Electric Field in the $R_2Ti_2O_7$ Pyrochlore Compounds, J. Phys.: Condens. Matter **24**, 256003 (2012).

[129] H. W. J. Blöte, R. F. Wielinga, and W. J. Huiskamp, Heat-Capacity Measurements on Rare-Earth Double Oxides $R_2M_2O_7$, Physica **43**, 549 (1969).

[130] L. D. C. Jaubert, O. Benton, J. G. Rau, J. Oitmaa, R. R. P. Singh, N. Shannon, and M. J. P. Gingras, Are Multiphase Competition and Order by Disorder the Keys to Understanding $Yb_2Ti_2O_7$? Phys. Rev. Lett. **115**, 267208 (2015).

[131] J. Robert, E. Lhotel, G. Remenyi, S. Sahling, I. Mirebeau, C. Decorse, B. Canals, and S. Petit, Spin Dynamics in the Presence of Competing Ferromagnetic and Antiferromagnetic Correlations in $Yb_2Ti_2O_7$, Phys. Rev. B **92**, 064425 (2015).

[132] A. Mostaed, G. Balakrishnan, M. R. Lees, Y. Yasui, L.-J. Chang, and R. Beanland, Atomic Structure Study of the Pyrochlore $Yb_2Ti_2O_7$ and Its Relationship with Low-Temperature Magnetic Order, Phys. Rev. B **95**, 094431 (2017).

[133] K. A. Ross, T. Proffen, H. A. Dabkowska, J. A. Quilliam, L. R. Yaraskavitch, J. B. Kycia, and B. D. Gaulin, Lightly Stuffed Pyrochlore Structure of Single-Crystalline $Yb_2Ti_2O_7$ Grown by the Optical Floating Zone Technique, Phys. Rev. B **86**, 174424 (2012).

[134] Y. Yasui, M. Soda, S. Iikubo, M. Ito, M. Sato, N. Hamaguchi, T. Matsushita, N. Wada, T. Takeuchi, N. Aso, and K. Kakurai, Ferromagnetic Transition of Pyrochlore Compound $Yb_2Ti_2O_7$, J. Phys. Soc. Jpn. **72**, 3014 (2003).

[135] L.-J. Chang, S. Onoda, Y. Su, Y.-J. Kao, K.-D. Tsuei, Y. Yasui, K. Kakurai, and M. R. Lees, Higgs Transition from a Magnetic Coulomb Liquid to a Ferromagnet in $Yb_2Ti_2O_7$, Nat. Commun. **3**, 992 (2012).

[136] L.-J. Chang, M. R. Lees, I. Watanabe, A. D. Hillier, Y. Yasui, and S. Onoda, Static Magnetic Moments Revealed by Muon Spin Relaxation and Thermodynamic Measurements in the Quantum Spin Ice $Yb_2Ti_2O_7$, Phys. Rev. B **89**, 184416 (2014).

[137] E. Lhotel, S. R. Giblin, M. R. Lees, G. Balakrishnan, L. J. Chang, and Y. Yasui, First-Order Magnetic Transition in $Yb_2Ti_2O_7$, Phys. Rev. B **89**, 224419 (2014).

[138] J. Gaudet, K. A. Ross, E. Kermarrec, N. P. Butch, G. Ehlers, H. A. Dabkowska, and B. D. Gaulin, Gapless Quantum Excitations from an Icelike Splayed Ferromagnetic Ground State in Stoichiometric $Yb_2Ti_2O_7$, Phys. Rev. B **93**, 064406 (2016).

[139] A. Scheie, J. Kindervater, S. Säubert, C. Duvinage, C. Pfleiderer, H. J. Changlani, S. Zhang, L. Harriger, K. Arpino, S. M. Koohpayeh, O. Tchernyshyov, and C. Broholm, Reentrant Phase Diagram of $Yb_2Ti_2O_7$ in a $\langle 111 \rangle$ Magnetic Field, Phys. Rev. Lett. **119**, 127201 (2017).

[140] J. A. Hodges, P. Bonville, A. Forget, A. Yaouanc, P. Dalmas de Réotier, G. André, M. Rams, K. Królas, C. Ritter, P. C. M. Gubbens, C. T. Kaiser, P. J. C. King, and C. Baines, First-Order Transition in the Spin Dynamics of Geometrically Frustrated $Yb_2Ti_2O_7$, Phys. Rev. Lett. **88**, 077204 (2002).

[141] J. S. Gardner, G. Ehlers, N. Rosov, R. W. Erwin, and C. Petrovic, Spin-Spin Correlations in $Yb_2Ti_2O_7$: A Polarized Neutron Scattering Study, Phys. Rev. B **70**, 180404 (2004).

[142] P. Bonville, J. A. Hodges, E. Bertin, J.-P. Bouchaud, P. D. de Réotier, L.-P. Regnault, H. M. Rønnow, J.-P. Sanchez, S. Sosin, and A. Yaouanc, Transitions and Spin Dynamics at Very Low Temperature in the Pyrochlores $Yb_2Ti_2O_7$ and $Gd_2Sn_2O_7$, in *ICAME 2003* (Springer, Dordrecht, 2004) p. 103.

[143] K. A. Ross, J. P. C. Ruff, C. P. Adams, J. S. Gardner, H. A. Dabkowska, Y. Qiu, J. R. D. Copley, and B. D. Gaulin, Two-Dimensional Kagome Correlations and Field Induced Order in the Ferromagnetic *XY* Pyrochlore $Yb_2Ti_2O_7$, Phys. Rev. Lett. **103**, 227202 (2009).

[144] J. D. Thompson, P. A. McClarty, D. Prabhakaran, I. Cabrera, T. Guidi, and R. Coldea, Quasiparticle Breakdown and Spin Hamiltonian of the Frustrated Quantum Pyrochlore $Yb_2Ti_2O_7$ in a Magnetic Field, Phys. Rev. Lett. **119**, 057203 (2017).

[145] J. Gaudet, D. D. Maharaj, G. Sala, E. Kermarrec, K. A. Ross, H. A. Dabkowska, A. I. Kolesnikov, G. E. Granroth, and B. D. Gaulin, Neutron Spectroscopic Study of Crystalline Electric Field Excitations in Stoichiometric and Lightly Stuffed $Yb_2Ti_2O_7$, Phys. Rev. B **92**, 134420 (2015).

[146] H. Yan, O. Benton, L. Jaubert, and N. Shannon, Theory of Multiple-Phase Competition in Pyrochlore Magnets with Anisotropic Exchange with Application to $Yb_2Ti_2O_7, Er_2Ti_2O_7$, and $Er_2Sn_2O_7$, Phys. Rev. B **95**, 094422 (2017).

[147] A. W. C. Wong, Z. Hao, and M. J. P. Gingras, Ground State Phase Diagram of Generic XY Pyrochlore Magnets with Quantum Fluctuations, Phys. Rev. B **88**, 144402 (2013).

[148] A. Yaouanc, P. Dalmas de Réotier, P. Bonville, J. A. Hodges, V. Glazkov, L. Keller, V. Sikolenko, M. Bartkowiak, A. Amato, C. Baines, P. J. C. King, P. C. M. Gubbens, and A. Forget, Dynamical Splayed Ferromagnetic Ground State in the Quantum Spin Ice $Yb_2Ti_2O_7$, Phys. Rev. Lett. **110**, 127207 (2013).

[149] G. Chen, "Magnetic Monopole" Condensation of the Pyrochlore Ice U(1) Quantum Spin Liquid: Application to $Pr_2Ir_2O_7$ and $Yb_2Ti_2O_7$, Phys. Rev. B **94**, 205107 (2016).

[150] R. B. Potts, Some Generalized Order-Disorder Transformations, Math. Proc. Camb. Philos. Soc. **48**, 106 (1952).

[151] D. Mukamel, M. E. Fisher, and E. Domany, Magnetization of Cubic Ferromagnets and the Three-Component Potts Model, Phys. Rev. Lett. **37**, 565 (1976).

[152] B. Barbara, M. F. Rossignol, and P. Bak, First-Order Transitions and Tricritical Points in DyAl 2 : A Realisation of the Three-State Potts Model, J. Phys. C: Solid State Phys. **11**, L183 (1978).

[153] O. Tchernyshyov, Written Communication: Potts Model for $Yb_2Ti_2O_7$, (2016).

[154] O. Tchernyshyov, Written Communication: Mean-Field Calculations $Yb_2Ti_2O_7$, (2017).

[155] C. Domb, Configurational Studies of the Potts Models, J. Phys. A: Math. Nucl. Gen. **7**, 1335 (1974).

[156] R. J. Baxter, Potts Model at the Critical Temperature, J. Phys. C: Solid State Phys. **6**, L445 (1973).

[157] J. P. Straley and M. E. Fisher, Three-State Potts Model and Anomalous Tricritical Points, J. Phys. A: Math. Nucl. Gen. **6**, 1310 (1973).

[158] G. R. Golner, Investigation of the Potts Model Using Renormalization-Group Techniques, Phys. Rev. B **8**, 3419 (1973).

[159] D. J. Amit and A. Shcherbakov, The Phase Transition in the Continuous Potts Model, J. Phys. C: Solid State Phys. **7**, L96 (1974).

[160] J. Rudnick, Epsilon Expansion for the Free Energy of the Continuous Three-State Potts Model: Evidence for a First-Order Transition, J. Phys. A: Math. Gen. **8**, 1125 (1975).

[161] H.-G. Purwins, E. Walker, B. Barbara, M. F. Rossignol, and A. Furrer, Single Crystal Magnetization of $ErAl_2$ and Interpretation in Terms of the Crystalline Field, J. Phys. C: Solid State Phys. **9**, 1025 (1976).

[162] T. M. McQueen, Personal Communication, (2017).

[163] Y. Yasui, N. Hamachi, Y. Kono, S. Kittaka, and T. Sakakibara, First-Order Ferromagnetic Transition of Quantum Spin Ice System $Yb_2Ti_2O_7$, SPIN **05**, 1540002 (2015).

[164] R. Coldea, J. D. Thompson, P. McClarty, D. Prabhakaran, I. Cabrera, and T. Guidi, Field Dependence of the Spin Dynamics and Heat Capacity in the Frustrated Pyrochlore $Yb_2Ti_2O_7$, (2015).

[165] J. Cullen and E. Callen, Potts Models and the Critical Behavior of a Cubic Ferromagnet with Fourth- and Sixth-Order Anisotropy, Phys. Rev. B **30**, 181 (1984).

[166] H. J. Changlani, Quantum versus Classical Effects at Zero and Finite Temperature in the Quantum Pyrochlore $Yb_2Ti_2O_7$, arxiv (2017), arXiv:1710.02234 [cond-mat] .

[167] H. J. Changlani, Written Communication: Finite Temperature Lanczos and Classical Monte Carlo Method on $Yb_2Ti_2O_7$ along 110, (2017).

[168] L. P. Kadanoff, W. Götze, D. Hamblen, R. Hecht, E. A. S. Lewis, V. V. PALCIAUSKAS, M. RAYL, J. SWIFT, D. ASPNES, and J. KANE, Static Phenomena near Critical Points: Theory and Experiment, Rev. Mod. Phys. **39**, 395 (1967).

[169] K. G. Wilson, Renormalization Group and Critical Phenomena. i. Renormalization Group and the Kadanoff Scaling Picture, Phys. Rev. B **4**, 3174 (1971).

[170] B. I. Halperin and P. C. Hohenberg, Generalization of Scaling Laws to Dynamical Properties of a System near Its Critical Point, Phys. Rev. Lett. **19**, 700 (1967).

[171] M. F. Collins, V. J. Minkiewicz, R. Nathans, L. Passell, and G. Shirane, Critical and Spin-Wave Scattering of Neutrons from Iron, Phys. Rev. **179**, 417 (1969).

[172] T. Holstein and H. Primakoff, Field Dependence of the Intrinsic Domain Magnetization of a Ferromagnet, Phys. Rev. **58**, 1098 (1940).

[173] F. Keffer, Spin Waves, in *Ferromagnetism / Ferromagnetismus*, Vol. 4 / 18 / 2, edited by S. Flügge and H. P. J. Wijn (Springer Berlin Heidelberg, 1966) p. 1.

[174] R. D. Lowde, Spin Waves and Neutron Scattering, J. Appl. Phys. **36**, 884 (1965).

[175] J. P. Wicksted, P. Böni, and G. Shirane, Polarized-Beam Study of the Paramagnetic Scattering from Bcc Iron, Phys. Rev. B **30**, 3655 (1984).

[176] J. Als-Nielsen, O. W. Dietrich, and L. Passell, Neutron Scattering from the Heisenberg Ferromagnets EuO and EuS. II. Static Critical Properties, Phys. Rev. B **14**, 4908 (1976).

[177] M. J. Cooper and R. Nathans, The Resolution Function in Neutron Diffractometry. I. The Resolution Function of a Neutron Diffractometer and Its Application to Phonon Measurements, Acta Cryst. **23**, 357 (1967).

[178] J. L. Beeby and J. Hubbard, Spin-Waves in the Paramagnetic Phase, Phys. Lett. A **26**, 376 (1968).

[179] R. D. Lowde and C. G. Windsor, On the Magnetic Excitations in Nickel, Adv. Phys. **19**, 813 (1970).

[180] D. Görlitz, J. Kötzler, F. J. Bermejo, P. Böni, and J. L. Martínez, Maximum Entropy Analysis of Dipolar Anisotropic Magnetic Scattering above T_C in EuS, Physica B Condens. Matter **180-181**, 214 (1992).

[181] P. Böni, D. Görlitz, J. Kötzler, and J. L. Martnez, Dynamics of Longitudinal and Transverse Fluctuations above T_C in EuS, Phys. Rev. B **43**, 8755 (1991).

[182] E. Frey, F. Schwabl, and S. Thoma, Shape Functions of Dipolar Ferromagnets at and above the Curie Point, Phys. Rev. B **40**, 7199 (1989).

[183] P. Böni, J. L. Martnez, and J. M. Tranquada, Longitudinal Spin Fluctuations in Nickel, Phys. Rev. B **43**, 575 (1991).

[184] S. Tixier, P. Böni, Y. Endoh, B. Roessli, and G. Shirane, Polarisation Dependence of the Magnetic Fluctuations in the Weak Itinerant Ferromagnet MnSi below T_C, Physica B Condens. Matter **241-243**, 613 (1997).

[185] P. Böni, B. Roessli, D. Görlitz, and J. Kötzler, Damping of Spin Waves and Singularity of the Longitudinal Modes in the Dipolar Critical Regime of the Heisenberg Ferromagnet EuS, Phys. Rev. B **65**, 144434 (2002).

[186] J. S. Pedersen, D. Posselt, and K. Mortensen, Analytical Treatment of the Resolution Function for Small-Angle Scattering, J. Appl. Cryst. **23**, 321 (1990).

[187] B. Hammouda and D. F. R. Mildner, Small-Angle Neutron Scattering Resolution with Refractive Optics, J. Appl. Cryst. **40**, 250 (2007).

[188] P. Böni and G. Shirane, Paramagnetic Neutron Scattering from the Heisenberg Ferromagnet EuO, Phys. Rev. B **33**, 3012 (1986).

[189] L. Passell, O. W. Dietrich, and J. Als-Nielsen, Neutron Scattering from the Heisenberg Ferromagnets EuO and EuS. I. The Exchange Interactions, Phys. Rev. B **14**, 4897 (1976).

[190] H. G. Bohn, A. Kollmar, and W. Zinn, Spin Dynamics in the Cubic Heisenberg Ferromagnet EuS, Phys. Rev. B **30**, 6504 (1984).

[191] P. Böni, G. Shirane, H. G. Bohn, and W. Zinn, Critical Magnetic Scattering from the Heisenberg Ferromagnet EuS, J. Appl. Phys. **61**, 3397 (1987).

[192] S. Blundell, *Magnetism in Condensed Matter*, reprint ed. (Oxford Univ. Press, 2014) oCLC: 898266646.

[193] F. Mezei and A. P. Murani, Combined Three-Dimensional Polarization Analysis and Spin Echo Study of Spin Glass Dynamics, J. Magn. Magn. Mater. **14**, 211 (1979).

[194] A. P. Murani, F. Mezei, and J. L. Tholence, Neutron Spin Echo, Polarisation Analysis and A.C. Susceptibility Measurements of Spin Glass Dynamics, Physica B+C **108**, 1283 (1981).

[195] A. P. Murani, Spectral Distribution of Relaxation Times in Spin Glasses, J. Magn. Magn. Mater. **22**, 271 (1981).

[196] F. Mezei, Neutron Spin Echo Study of Spin Glass Dynamics (Invited), J. Appl. Phys. **53**, 7654 (1982).

[197] F. Mezei, The Dynamical Behaviour Associated with the Spin Glass Transition, J. Magn. Magn. Mater. **31-34**, 1327 (1983).

[198] R. H. Heffner and D. E. MacLaughlin, Comparison of Spin-Glass Dynamics Determined by the Muon-Spin-Relaxation and Neutron Spin-Echo Techniques, Phys. Rev. B **29**, 6048 (1984).

[199] S. M. Shapiro, H. Maletta, and F. Mezei, Neutron-Spin-Echo Study of the Reentrant Spin Glass $Eu_xSr_{1-x}S$, J. Appl. Phys. **57**, 3485 (1985).

[200] C. Pappas, F. Mezei, G. Ehlers, P. Manuel, and I. A. Campbell, Dynamic Scaling in Spin Glasses, Phys. Rev. B **68**, 054431 (2003).

[201] C. R. Fincher, S. M. Shapiro, A. H. Palumbo, and R. D. Parks, Spin-Wave Evolution Crossing from the Ferromagnetic to Spin-Glass Regime of Fe_xCr_{1-x}, Phys. Rev. Lett. **45**, 474 (1980).

[202] S. M. Shapiro, C. R. Fincher, A. C. Palumbo, and R. D. Parks, Anomalous Spin-Wave Behavior in the Magnetic Alloy Fe_xCr_{1-x}, Phys. Rev. B **24**, 6661 (1981).

[203] K. Motoya, S. M. Shapiro, and Y. Muraoka, Neutron Scattering Studies of the Anomalous Magnetic Alloy $Fe_{0.7}Al_{0.3}$, Phys. Rev. B **28**, 6183 (1983).

[204] P. Böni, S. M. Shapiro, and K. Motoya, Magnetic Field Dependence of the Spin Dynamics in the Reentrant Spin Glass $Fe_{70.4}Al_{29.6}$, Phys. Rev. B **37**, 243 (1988).

[205] W. Bao, S. Raymond, S. M. Shapiro, K. Motoya, B. Fåk, and R. W. Erwin, Unconventional Ferromagnetic and Spin-Glass States of the Reentrant Spin Glass $Fe_{0.7}Al_{0.3}$, Phys. Rev. Lett. **82**, 4711 (1999).

[206] E. Fawcett, Spin-Density-Wave Antiferromagnetism in Chromium, Rev. Mod. Phys. **60**, 209 (1988).

[207] J. O. Strom-Olsen, D. F. Wilford, S. K. Burke, and B. D. Rainford, The Coexistence of Spin Density Wave Ordering and Spin Glass Ordering in Chromium Alloys Containing Iron, J. Phys. F: Met. Phys. **9**, L95 (1979).

[208] E. Fawcett, H. L. Alberts, V. Y. Galkin, D. R. Noakes, and J. V. Yakhmi, Spin-Density-Wave Antiferromagnetism in Chromium Alloys, Rev. Mod. Phys. **66**, 25 (1994).

[209] S. K. Burke and B. D. Rainford, The Evolution of Magnetic Order in CrFe Alloys. I. Antiferromagnetic Alloys Close to the Critical Concentration, J. Phys. F: Met. Phys. **13**, 441 (1983).

[210] S. K. Burke, R. Cywinski, J. R. Davis, and B. D. Rainford, The Evolution of Magnetic Order in CrFe Alloys. II. Onset of Ferromagnetism, J. Phys. F: Met. Phys. **13**, 451 (1983).

[211] S. K. Burke and B. D. Rainford, The Evolution of Magnetic Order in CrFe Alloys. III. Ferromagnetism Close to the Critical Concentration, J. Phys. F: Met. Phys. **13**, 471 (1983).

[212] G. Benka, *Untitled*, PhD Thesis, Technische Universität München (TUM) (unpublished).

[213] M. V. Nevitt and A. T. Aldred, Ferromagnetism in V-Fe and Cr-Fe Alloys, J. Appl. Phys. **34**, 463 (1963).

[214] S. Arajs and G. R. Dunmyre, Electrical Resistivity of Chromium-rich Chromium-iron Alloys between 4° and 320°K, J. Appl. Phys. **37**, 1017 (1966).

[215] M. A. Mitchell and J. F. Goff, Electrical Resistivity and the Depression of the Néel Temperature in Cr-Mo and Cr-Fe, Phys. Rev. B **5**, 1163 (1972).

[216] Y. Ishikawa, S. Hoshino, and Y. Endoh, Antiferromagnetism in Dilute Iron Chromium Alloys, J. Phys. Soc. Jpn. **22**, 1221 (1967).

[217] S. K. Burke and B. D. Rainford, Determination of the Antiferromagnetic Phase Boundary in Cr-Fe Alloys, J. Phys. F: Met. Phys. **8**, L239 (1978).

[218] S. K. Burke, R. Cywinski, and B. D. Rainford, Superparamagnetism and the Character of Magnetic Order in Binary Cr-Fe Alloys near the Critical Concentration, J. Appl. Cryst. **11**, 644 (1978).

[219] P. Schmakat, *Neutron Depolarisation Measurements of Ferromagnetic Quantum Phase Transitions & Wavelength-Frame Multiplication Chopper System for the Imaging Instrument ODIN at the ESS*, PhD Thesis, Technische Universität München (TUM) (2015).

[220] G. Porod, Die Röntgenkleinwinkelstreuung von Dichtgepackten Kolloiden Systemen, Kolloid-Zeitschrift **124**, 83 (1951).

[221] G. Porod, General Theory, Small Angle X-Ray Scatt. (1982).

[222] B. T. M. Willis and C. J. Carlile, *Experimental Neutron Scattering* (Oxford University Press, 2009) oCLC: ocn213301925.

[223] S. Mercone, V. Hardy, C. Martin, C. Simon, D. Saurel, and A. Brûlet, Field Dependence of the Electronic Phase Separation in $Pr_{0.67}Ca_{0.33}MnO_3$ by Small-Angle Magnetic Neutron Scattering, Phys. Rev. B **68**, 094422 (2003).

[224] M. Viret, F. Ott, J. P. Renard, H. Glättli, L. Pinsard-Gaudart, and A. Revcolevschi, Magnetic Filaments in Resistive Manganites, Phys. Rev. Lett. **93**, 217402 (2004).

[225] R. M. Pickup, R. Cywinski, C. Pappas, B. Farago, and P. Fouquet, Generalized Spin-Glass Relaxation, Phys. Rev. Lett. **102**, 097202 (2009).

[226] K. Tajima, P. Böni, G. Shirane, Y. Ishikawa, and M. Kohgi, Paramagnetic Spin Fluctuations in an $Fe_{65}Ni_{35}$ Invar Alloy, Phys. Rev. B **35**, 274 (1987).

[227] J. N. Wagner, W. Häußler, O. Holderer, A. Bauer, S. M. Shapiro, and P. Böni, Influence of Concentration Fluctuations on Relaxation Processes in Spin Glasses, submitted (2018).

[228] I. A. Campbell, J. M. Flesselles, R. Jullien, and R. Botet, Random Walks on a Hypercube and Spin Glass Relaxation, J. Phys. C: Solid State Phys. **20**, L47 (1987).

[229] I. A. Campbell, J. M. Flesselles, R. Jullien, and R. Botet, Nonexponential Relaxation in Spin Glasses and Glassy Systems, Phys. Rev. B **37**, 3825 (1988).

[230] A. Wendl, *Neutron Spin Echo Spectroscopy on Geometrically Frustrated Magnets*, Masters Thesis, Technische Universität München (TUM) (2018).

[231] M. Peschard, Contribution à l'étude des Ferros-nickels, Rev. Met. Paris **22**, 581 (1925).

[232] P. Weiss and R. Forrer, La saturation absolue des ferromagnétiques et les lois d'approche en fonction du champ et de la température, Ann. Phys. **10**, 279 (1929).

[233] H. H. Potter, The Magneto-Caloric Effect and Other Magnetic Phenomena in Iron, Proc. Roc. Soc. A **146**, 362 (1934).

[234] R. Pauthenet, Aimantation spontanée des ferrites, Ann. Phys. **12**, 710 (1952).

[235] H. Danan, A. Herr, and A. J. P. Meyer, New Determinations of the Saturation Magnetization of Nickel and Iron, J. Appl. Phys. **39**, 669 (1968).

[236] R. Georgii and K. Seemann, MIRA: Dual Wavelength Band Instrument, JLSRF **1**, 3 (2015).

[237] R. Georgii, T. Weber, G. Brandl, M. Skoulatos, M. Janoschek, S. Mühlbauer, C. Pfleiderer, and P. Böni, The Multi-Purpose Three-Axis Spectrometer (TAS) MIRA at FRM II, Nucl. Instrum. Methods Phys. Res. A **881**, 60 (2018).

[238] T. Weber, R. Georgii, and P. Böni, Takin: An Open-Source Software for Experiment Planning, Visualisation, and Data Analysis, SoftwareX **5**, 121 (2016).

[239] T. Weber, R. Georgii, and P. Böni, Update 1.5 to "Takin: An Open-Source Software for Experiment Planning, Visualisation, and Data Analysis", (PII: S2352711016300152), SoftwareX **6**, 148 (2017).

[240] M. Popovici, On the Resolution of Slow-Neutron Spectrometers. IV. The Triple-Axis Spectrometer Resolution Function, Spatial Effects Included, Acta Cryst. A **31**, 507 (1975)

List of publications

- **Interplay of Itinerant and Localized Spin Fluctuations in the Ferromagnetic Superconductor UGe$_2$**
  F. Haslbeck, <u>S. Säubert</u>, M. Seifert, C. Franz, M. Schulz, A. Heinemann, T. Keller, P. Das, J. D. Thompson, E. D. Bauer, C. Pfleiderer, and M. Janoschek
  arXiv:1801.10278 [cond-mat] (2018)

- **Reentrant Phase Diagram of Yb$_2$Ti$_2$O$_7$ in a $\langle 111 \rangle$ Magnetic Field**
  A. Scheie, J. Kindervater, <u>S. Säubert</u>, C. Duvinage, C. Pfleiderer, H. J. Changlani, S. Zhang, L. Harriger, K. Arpino, S. M. Koohpayeh, O. Tchernyshyov, and C. Broholm
  Phys. Rev. Lett. 119, 127201 (2017)

- **Dipolar Effects on the Critical Fluctuations in Fe: Investigation by the Neutron Spin-Echo Technique MIEZE**
  J. Kindervater, <u>S. Säubert</u>, and P. Böni
  Phys. Rev. B 95, 014429 (2017)

- **Neutron and Hard X-ray Diffraction Studies of the Isothermal Transformation Kinetics in the Research Reactor Fuel Candidate U−8wt%Mo**
  <u>S. Säubert</u>, R. Jungwirth, T. Zweifel, M. Hofmann, M. Hoelzel, and W. Petry
  J. Appl. Cryst. 49, 923-933 (2016)

Acknowledgments/Danksagungen

An dieser Stelle möchte ich mich bei all denjenigen bedanken, die zu dieser Dissertation beigetragen und mich während meiner Arbeit unterstützt haben.

Allen voran möchte ich mich bei Prof. Christian Pfleiderer für die Möglichkeit bedanken, in einer so hervorragenden Arbeitsgruppe promovieren zu können. Vielen Dank für die unzähligen Gespräche, Diskussionen, Ratschläge, sowie die vielen Möglichkeiten an Konferenzen, Summer-/Winterschools, Workshops, etc. teilzunehmen. Es macht wirklich Spaß, in deinem Team zu arbeiten.

Besonderer Dank gilt auch Prof. Peter Böni. Da ein großer Teil meiner Projekte in Zusammenarbeit mit dir entstanden sind, habe ich sehr von der großartigen Zusammenarbeit der beiden Lehrstühle Pfleiderer/Böni profitiert. Vielen Dank für die vielen Lehrstunden in Neutronenstreuung sowie die stets guten Gespräche und Diskussionen.

Bei der gesamten Bunga-Bunga Crew: Gorck Benka, FXH, Andi Wendl, Stefan Giemsa, Fonsi Chacon, Pau Cabre, Marco Halder, Wolle Simeth, Andi Bauer, Felix Rucker, Markus Kleinhans, Alex Engelhardt, Jan Spallek, Christopher Duvinage, Aggl Regnat, Tomek Schulz, Marc Seifert, Chris Franz, alle die ich vergessen hab aufzuzählen (SORRY!), allen Stundenten... für all die Dinge, die Garching dann doch ganz schön machten. Danke natürlich auch an die Alumni und dem restlichen Lehrstuhl, Christoph Morkel, Astrid Mühlberg, Martina Michel, Tim Adams, Robert Ritz, Michael Wagner, Christoph Schnarri,...

Meinen beiden Mitstreitern im Vergnügungstriumvirat, die wir stets versucht haben das Partyherz des Lehrstuhls am Leben zu halten. Danke Marc und Franz. Sowie meinen Prokrastinerbrüdern Wolle und Felix. Durch unsere Treffen und Diskussionen (oder eher auf alles schimpfen...) war die Zeit des Schreibens super angenehm.

Meinem Mentor Marc Janoschek, der sich immer für mich Zeit genommen hat, sei es Proposals/Bewerbungen/sonstige Texte korrigieren, Physik diskutieren, Ratschläge erteilen,... dein super Mentoring hat mir durch meine Promotion geholfen und trägt sicher dazu bei, dass aus meiner "Karriere" was wird!

Natürlich der RESEDA Mannschaft: Chris Franz, Olaf Soltwedel, Thorsten Schröder (a.D.), Jonas Kindervater (a.D.), Franz Haslbeck, Andi Wendl, Christian Fuchs, sowie